Magnetic Bearing Stages for Electron Beam Lithography

by

Paul Thomas Konkola

Bachelor of Science in Mechanical Engineering
University of California at Berkeley
May 1995

Submitted to the Department of Mechanical Engineering
in partial fulfillment of the requirements for the degree of

Master of Science in Mechanical Engineering

at the

MASSACHUSETTS INSTITUTE OF TECHNOLOGY

February 1998

Author .....
Department of Mechanical Engineering
January 16, 1998

Certified by .....
David L. Trumper
Rockwell International Associate Professor
Thesis Supervisor

Accepted by .....
Ain A. Sonin
Chairman, Department Committee on Graduate Students

Magnetic Bearing Stages for Electron Beam Lithography

by

Paul Thomas Konkola

Submitted to the Department of Mechanical Engineering
on January 16, 1998, in partial fulfillment of the
requirements for the degree of
Master of Science in Mechanical Engineering

Abstract

This thesis investigates the feasibility of a magnetically suspended stage that can satisfy requirements for next generation electron beam lithography machines.

In the work of this thesis, I:

- analyze and formulate linear-motor-driven magnetic bearing stage topologies, magnet arrays, and coil designs that produce low fringing magnetic fields (less than $\pm 2 \times 10^{-7}$T) while satisfying electron beam tool requirements
- model the associated magnetic fields
- perform a thermal stability analysis
- design, build, and test a prototype magnetic bearing linear motor that implements analytical concepts
- design, test, and evaluate a single-axis stage position control system
- identify vacuum compatibility issues and indicate probable solutions
- develop design methodologies for electron beam lithography magnetically suspended stages

This research leads to the development of a highly promising magnetic bearing that is based on a synchronous motor design. This magnetic bearing, which produces all required suspension and translation forces, can be readily incorporated into a six degree of freedom stage. Various stage topologies are formulated and described. Novel permanent magnet array and coil array technologies form the heart of the designs where the stage fringing field is designed to have negligible influence on the electron beam trajectory in a lithography machine.

Magnetic bearing stages are thus shown to be a promising alternative for precision motion control in electron beam lithography systems. I also discuss the many advantages of such stages over current electron beam stage designs, which rely on many mechanical components. The magnetic bearing stages offer potential benefits

of a simpler and more reliable mechanical system, higher natural frequencies, smaller footprint, better controller performance, lower particle generation, and lower loads on the vacuum system. The system-level benefits and the advanced performance of the magnetic bearing stage technology become increasingly compelling as electron beam lithography machines are scaled for tough next-generation requirements.

Thesis Supervisor: David L. Trumper
Title: Rockwell International Associate Professor

Acknowledgments

Above all, I must thank my thesis advisor, Professor David Trumper. He taught me much of what I know about electromagnetism, controls, electrical engineering, and precision engineering. His teachings opened up new worlds of design possibilities that will enrich my life. He is truly a great advisor both on a technical and personal level. Without his support, encouragement, and contributions I could never have completed this work.

I must thank all my cohorts in the Precision Motion Control Laboratory. It has been an honor to work with these talented and generous students. There are some instances that I must note more specifically. I would like to thank Won-jong Kim (now graduated) for the discussions and advice on magnetic bearings. Pradeep Subramanyan was of instrumental importance for the controls aspect of this thesis. The discussions that I had with Mike Liebman on motor design and many other technical aspects were very helpful. Steve Ludwick was always willing to answer my questions and proved a great source of advice on numerous occasions.

I thank all the people at Etec Systems Incorporated who helped make this project a success. David Trost was a great supporter of this project from the beginning. It was a pleasure to absorb his technical expertise and his advice on stage design greatly strengthened this project. Mark Gesley was of instrumental importance in starting this project. His leadership serves as a great competitive advantage for Etec. Also, Frank Chilese was very supportive during my summer at Etec, Bill DeVore discussed the electromagnetic issues of electron beam lithography with me, Glen Howard helped me procure a magnetometer, and Phil Arnold allocated the interferometer system to me and has been a generous source of help during my time at Etec.

I thank my parents John and Mirjam Konkola for their undying support. They always entertained my curiosities and encouraged me to explore.

This work was sponsored by Etec Systems Incorporated

Contents

List of Figures

List of Tables

Symbols

Note: Vectors appear in bold face type.

a	separation constant (NA)
$\mathbf{A}$	magnetic vector potential (T m)
A	area (m^2)
A_{wire}	wire area (m^2)
b	dashpot constant (Ns/m)
$\mathbf{B}$	magnetic flux density (T)
B_w	magnetic flux density at the write plane (T)
c	speed of light ($3.00\times$ 10^8 m/s)
C	contour for integration (m)
C_p	specific heat at constant pressure (J/ K/Kg)
C_i	constant derived from boundary conditions (NA)
d	multipole moment arm (m)
$\mathbf{D}$	electric displacement (C/m^2)
$\mathbf{E}$	electric field intensity (Volts/m)
$\mathbf{F}$	force (N)
$\mathbf{f}$	force density (N/m^3)
G	motor geometrical constant (m^3)
G	transfer function (NA)
G_b	power booster gain (NA)
h	height (m)
$\mathbf{H}$	magnetic field intensity (Amps/m)
I	current (Amps)
I_L	current limit (Amps)
$\mathbf{J_f}$	free current density ($Amps/m^2$)
k	spring constant (N/m)
k_{eff}	effective thermal conductivity (W/m/K)
$\mathbf{K_f}$	free surface current density (Amps/m)
$\mathbf{l}$	length for integration (m)
l	length of a magnet pole face (m)
l	length (m)
$l_{effective}$	effective length (m)
l_g	length between the last column aperture and the write plane (m)
l_o	length between the nominal objective lens position and the last column aperture (m)
l_{wire}	wire length (m)
L	contour for integration (m)
L	inductance (H)
m	integer (NA)
m_e	mass of an electron (9.11×10^{-31} kg)
$\mathbf{M}$	magnetization density (A/m)

$\mathbf{n}$	normal vector to surface (NA)
n	integer used in separation of variables (NA)
N	integer (NA)
N_m	number of magnet spatial periods (NA)
p	separation constant (NA)
$\mathbf{P}$	coordinate of point 'P' in space (m)
P_d	power dissipation (W)
P_n	ordinary Legendre polynomial (NA)
q	electrical charge (C)
q	heat transfer (W)
q	separation constant (NA)
q_e	charge of an electron (1.60×10^{-19} C)
q'	heat flow (W/m)
Q_n	ordinary Legendre function of the second kind (NA)
r	distance in spherical coordinates (m)
R	autocorrelation function (NA)
R	thermal resistance (Ω)
R_s	Resistance of a stator phase (Ω)
R_w	distance from a multipole's center to the write plane (m)
s	number of superpositions
$\mathbf{S}$	surface for integration (m^2)
t	thickness (m)
T	temperature (K)
T_c	temperature of chamber (K)
T_s	temperature of stator (K)
$\mathbf{v}$	velocity (m/s)
V	volume for integration (m^3)
V_e	voltage describing the kinetic energy of the electron beam (V)
w	width of a magnet pole face (m)
w_m	depth of synchronous motor magnet array
$w_{effective}$	effective width (m)
z_0	gap between magnet array and stator
X	x component of separation distance between multipoles(m)
Y	y component of separation distance between multipoles(m)
Z	z component of separation distance between multipoles(m)
$Z(z)$	solution to the Legendre wave equation (NA)
α	coefficient of thermal expansion (1/K)
Δ_e	deflection of the ebeam (m)
Δ_m	height of synchronous motor magnet array (m)
Δ_m	a determinant (NA)
ϵ	emissivity (NA)
η	turns density (turns/m^2)
γ	magnet spatial frequency (rad/m)
Γ	stator thickness (m)
λ	magnet spatial period (m)

μ	permeability (H/m)
μ_0	permeability of free space ($4\ \pi \times 10^{-7}$ H/m)
μ_r	relative permeability (NA)
ω_n	natural frequency (rad/s)
ω_c	bandwidth (rad/s)
Φ	magnetic scalar potential (Amps)
ρ	density (kg/m^3)
ρ_f	free charge density (C/m^3)
σ	conductivity (5.60×10^7 1/Ohms/m, for copper)
σ	standard deviation (NA)
σ	Stefan Boltzman constant ($\sigma = 5.67 \times 10^{-8} W/m^2/K^4$)
σ_f	free surface charge density (C/m^2)
τ	characteristic time (s)
χ	separation constant (NA)
ζ	damping factor (NA)
$\mathcal{P}_p^q$	generalized Legendre function of the first kind (NA)
$\mathcal{Q}_p^q$	generalized Legendre function of the second kind (NA)

Chapter 1

Introduction

Magnetic bearing stages are a promising motion control alternative in electron beam (ebeam) lithography systems. A magnetic bearing stage can be a mechanically simple yet highly functional design, where a single moving part is controlled in six degrees of freedom. This design can achieve large-scale planar motion and small-scale focusing and rotational alignments. Since the stage is not limited by precision bearing surfaces, friction, or backlash, the positioning performance can be extended to the limits of control and metrology. This translates not only into more precise motion but many difficult disturbance sources that induce substrate vibration are also eliminated. The positioning performance is likely to be further improved since a single moving part can be designed for high natural frequencies.

Since no lubrication is required, a magnetic bearing stage is highly suited to the vacuum environment. Particle generation is also lowered since the suspended stage does not generate wear particles – making these stages highly suited for clean room use. Additionally, stringent thermal stability requirements for the substrate are possible since there is no heat dissipation on the moving part and there is large thermal resistance between the part and the power dissipating components.

From the system-level perspective, magnetic bearing stages have the potential for huge benefits. A single moving part is a highly reliable mechanical system, thereby improving the machine up-time and maintainability. Additionally, the cabling to the moving part is minimal – perhaps consisting of only a ground lead. Thus, a

troubling disturbance is largely removed. There is also the potential for a smaller stage footprint, thus reducing the size of the vacuum chamber. This leads to lower loads on the vacuum system, less demand on chamber shielding, better column-to-chamber structural properties, and in general a less expensive and higher performance system. Furthermore, the small chamber should experience less vibration disturbances from the lower capacity vacuum machinery and from acoustic air vibrations.

However, a stage suitable for ebeam lithography must be carefully designed to meet the requirements for low fringing magnetic fields. In this thesis, I analyze and formulate magnetic bearing stage topologies, magnet arrays, and coil designs that produce low fringing magnetic fields. I approach the analysis from fundamental electromagnetic field theory and develop tools and methodologies to aid the design.

Because the magnetic bearing stage must meet the overall ebeam tool requirements, I also evaluate the other major engineering issues, which include thermal stability, vacuum compatibility, controller performance, and structural dynamics.

After evaluating candidate actuation methods, I select a promising magnetic bearing subsystem for detailed prototyping. The design is based on a synchronous motor architecture that provides forces in both suspension and translation. Experimental observations are reported with reference to the analytical concepts. I also design, build, and evaluate a single axis position control system. The controller performance as well as electromechanical data is presented. The positioning noise is viewed in light of substrate-to-interferometer mirror dynamics.

In the rest of this chapter, I review electron beam lithography and introduce the technical requirements. In Chapter 2, prior art in ebeam stages and electromagnetic actuation is discussed. I select synchronous motor magnetic bearings in Chapter 3 as the most promising candidate for low fringing field designs that would also be suitable for ebeam lithography requirements. Chapter 4 details the physics of low fringing field magnetic bearing design. The design and implementation of a low fringing field magnetic bearing is described in Chapter 5. In Chapter 6, I present the design and implementation of a single degree of freedom position control system. Heat transfer analysis for thermal stability and the stator thermal current limit is described in

Chapter 7. Finally, I conclude that magnetic bearing stages are feasible for next generation electron beam lithography and make suggestions for further research in Chapter 8.

1.1 Description of electron beam lithography

A schematic of an electron beam lithography machine is found in Figure 1-1[1]. In this machine, electrons are emitted from an electron gun at high energies. Then a series of lenses, apertures, and blanking plates magnify, shape, and deflect the ebeam respectively [12]. At the base of the column, the electrons strike the resist-coated substrate, which may be a fused silica photomask or in the case of direct write, a silicon wafer. Because the deflection range of the ebeam is limited, a stage is used to steer the substrate under the beam such that large patterns can be exposed.

The electron beam acts much like very sharp pencil, transferring a desired pattern to the substrate. The pattern emerges because the ebeam's energy alters the molecular weight of the resist. After exposure, the substrate is removed from the ebeam machine and developed with a chemical solution that selectively removes the resist depending on its molecular weight. The resulting pattern then becomes the template for further processing operations that yield the finished photomask or integrated circuit.

1.2 Introduction to the technical requirements for an ebeam stage

The technical requirements for electron beam lithography parallel those of the world semiconductor industry. The National Technology Roadmap for Semiconductors, published by the Semiconductor Industry Association, serves as a prediction of the demands for the semiconductor equipment market [35]. I have repeated the data on the relevant critical-level mask requirements in Table 1.1.

[1]Courtesy of Etec Systems Inc. 26460 Corporate Avenue, Hayward, CA 94545

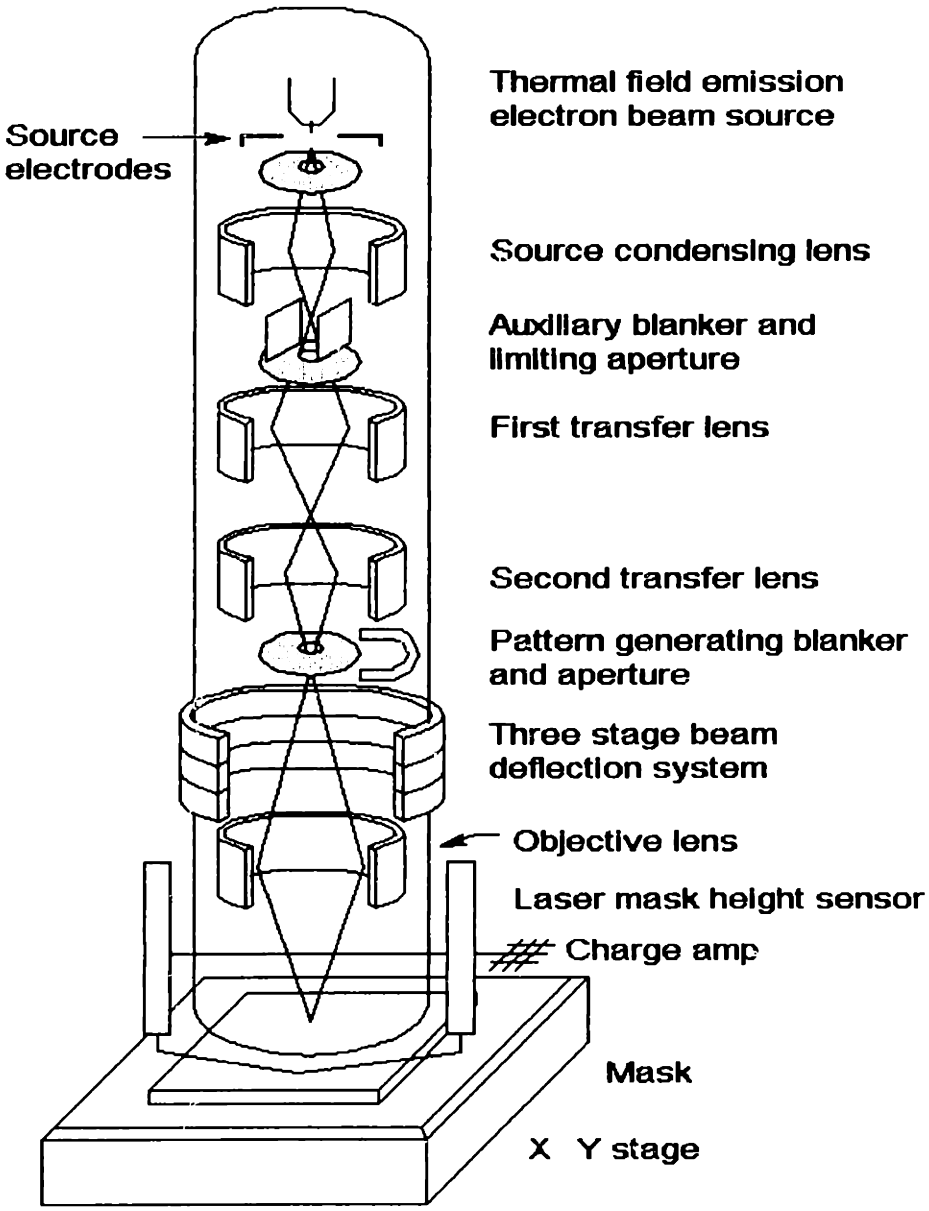

Figure 1-1: Architecture of an ebeam lithography machine

Year of First Product Shipment	1997	1999	2001	2003		2006		2009		2012	
Technology Generation (nm)	250	180	150	130		100		70		50	
Wafer Minimum Feature Size (nm)	200	140	120	100		70		50		35	
Magnification	4	4	4	4	1	4	1	4	1	4	1
Mask Minimum Image Size (nm)	800	560	480	400	100	280	70	200	50	140	35
Mask Optical Proximity Correction Feature Size (nm)	400	280	210	200	100	140	70	100	50	70	35
Image Placement (nm, multi-point)	52	36	32	28	14	20	10	16	8	12	6

Table 1.1: Critical level mask requirements

The toughest requirement relevant to the stage's design is the placement accuracy. By inspecting Table 1.1, you can see that in about 5 years (2003) the required placement accuracy will be 14nm and in 8 years (2008) the placement accuracy will reduce to only 10 nm for production machines. Needless to say, the stage will have demanding requirements. Considering that an ebeam lithography machine has many systems that contribute to its error budget and a practical system must be designed with margin, the actual error budget for the stage may be about half these figures. One should recognize that the placement accuracy and the stage positional accuracy are very different. Because the ebeam can deflect to compensate for measured stage position errors, the positional accuracy can be much worse than the placement accuracy. Thus, the error terms of interest are those not accurately measured and subsequently corrected by ebeam deflection.

The stage will have its own sub-error budget that drives the requirements for the magnitude of magnetic field variations, controller performance, thermal stability, and structural performance. To complicate matters, the chamber of an ebeam system operates at high vacuum ($< 10^{-6}$ Torr). Thus, the stage must also meet stringent vacuum compatibility requirements.

For my design purposes, it is reasonable to assign a nanometer or two of allowable

error to each of the following error contributors: magnetic field variations, controller performance, thermal stability, and structural performance. I will discuss the more specific requirements for these categories in their corresponding sections.

Chapter 2

Prior Art

2.1 Ebeam stages

Ebeam lithography stages have been designed and implemented in a variety of forms. Often the system architecture yields fundamental constraints on the stage design. If the pattern is written on the fly, then a scanning stage is required. If the pattern is written while the stage is stationary, then the stage is designated as a stepper. Scanning stage requirements are generally more difficult to achieve because disturbances during motion lead to vibration. Meanwhile, a stepper stage has significant time overhead associated with step and settle. At present, most of the commercial mask writers are scanners, indicating suppliers have preferred the higher throughput at the expense of tougher stage requirements. Another factor influencing stage design includes whether a lower pole piece is beneath the stage. For this configuration, the stage must be extremely non conductive to prevent the influences of eddy currents. Furthermore, the height of the stage may limited by the magnetic lens design.

The suppliers of commercial ebeam lithography systems include Etec Systems Incorporated, Hitachi, JEOL, Leica, and Lepton [8]. All of these suppliers but JEOL have systems that incorporate scanning stages. Also, at least AT&T Bell Labs (now operated by Lucent Technologies) and IBM have built machines for internal use.

Etec Systems' mask making machines incorporate a scanning stage that uses cylindrical air bearings in orthogonal pairs. Bellows separate air bearings, DC motors, and

ball screws from vacuum. Motion is transferred through the bellows to the platen, which is cantilevered in the chamber.

Reference [5] discusses several vacuum stage topologies. Most notable is an X–Y scanning stage shown incorporated into Lepton's EBES4. Two drive shafts, shrouded by bellows and forced by ball screws or linear motors push a stacked X–Y stage. It is not clear from the publication what type of bearing system is used to constrain the stage motion.

Reference [6] discusses a scanning stage used for an ebeam inspection machine. The stage is designed for the requirements of the KLA SEMSpec wafer and x-ray mask inspector. While the stage's H-frame is very large for the travel, the open geometry is well suited for material handling. The vacuum compatible linear motors are located as far from the ebeam's optical axis as the architecture allows. The stage uses linear crossed roller bearings riding on highly polished ways. The ways are lubricated with perfluoropolyether (Fomblin) grease.

At AT&T, the EBES4 mask making machine incorporates a scanning stage that uses hydrostatic bearings and hydraulic actuators on a cantilevered T structure [30]. The hydrostatic bearings and actuators are separated from vacuum by welded metal bellows evacuated to 50mTorr. A narrow distillate of perflourinated polyether vacuum pump oil is the hydraulic fluid, which provides good lubrication and low vapor pressure.

Reference [17] discusses a stage suitable for both scanning and step applications. This stage is guided by cylindrical hydrostatic bearings in orthogonal pairs. The lubricant for the hydrostatic bearings is diffusion pump oil. Hydraulic cylinders, sealed by bellows, provide actuation.

Leica Lithography's scanning stage incorporates ceramic ball linear bearings and a cross structure for guiding the stage plate [33]. There is a groove on the base plate and an orthogonal groove on the stage plate for accepting the cross. Pushing the cross along the base plate yields one axis of linear motion. Pushing the stage plate along the cross yields the second axis. The stage is supported by balls or sliding pads moving on the upper plane of the base plate. The driving mechanism incorporates a

special drive bar that pushes on the stage's center of mass for the scanning direction axis. Servo motors are located outside the vacuum and rotate the ball screws or a friction capstan drive assembly.

At IBM, the EL3 stage utilizes PTFE bearing pads sliding on a ferrite ceramic disc [20]. Three pivoting capstan drives provide actuation for $X - Y - \theta$ control. DC motors are located outside the vacuum by using ferrofluidic vacuum feedthroughs. This stepping stage is for a direct write machine. In the EL3 architecture, the lower pole piece of a magnetic lens is beneath the stage.

Reference [41] discusses a high-speed flat guide ceramic stage. This stage is designed to be nonconducting and thus would be suitable for the architecture where the pole piece is beneath the stage. The stage slides on pads, while ways shaped like a cross guide the stage motion. Drive bars, forced by DC motors and roller screws outside the vacuum, push the stage. A piezo drive mechanism at the end of one of the drive bars decouples that drive bar when the other axis transmits motion.

At Hitachi [27], a stepper stage slides on PTFE pads while a cross guides the stage motion. The drive arms pass through Teflon vacuum seals. DC motors and ball screws provide for coarse motion while piezo actuators and a flexure stage provide for fine positioning. The ball screws are housed in a sub vacuum environment while the DC motors are in atmosphere, separated by a rotary ferrofluidic feedthroughs.

My review above is by no means comprehensive, but only represents those stages for which I found published information. Just from the cases that I have cited, one sees that many stage architectures have been designed for ebeam lithography. However, I am unaware of any magnetically suspended stages for charged particle systems.

With the ever-increasing performance requirements for ebeam lithography and the growing pattern sizes, the demands on ebeam stages are becoming more challenging. The requirements for low fringing fields, thermal stability, controller performance, structural dynamics, vacuum compatibility, and contamination are difficult at best for many of the previous architectures. Therefore, a new stage paradigm that can be comfortably scaled to meet tough future requirements is worthy of exploration.

2.2 Magnetoquasistatic forces

In this thesis, I focus on a new approach to ebeam stages. I consider stage designs where a single moving part is electromagnetically suspended. Since these stages must be carefully designed to reduce the stage fringing field, I consider the fundamental physics before selecting a stage topology.

In the rest of this chapter, I consider basic ways to electromagnetically suspend and translate a part. This investigation prepares us for Chapter 3 where I select a magnetic bearing topology for detailed prototyping.

While I include the basic physics for forces in this section, the reader may want to refer to my review of the fundamentals of electromagnetic fields in Section 4.1 before proceeding. A fundamental derivation for electromagnetic forces can be found in [42] and [25]. In this thesis, I am primarily interested in magnetoquasistatic (MQS) forces, which arise when magnetic fields (as opposed to electrical) are present. The force density, $\mathbf{f}$, in a continuum [25] is given by

$$\mathbf{f} = (\mathbf{J_f} \times \mathbf{B}) - \left(\frac{1}{2}\mathbf{H} \cdot \mathbf{H}\nabla\mu\right) + \nabla\left(\frac{1}{2}\rho\frac{\partial\mu}{\partial\rho}\mathbf{H} \cdot \mathbf{H}\right) \tag{2.1}$$

where $\mathbf{J_f}$ is the free current density, $\mathbf{B}$ is the magnetic flux density, $\mathbf{H}$ is the magnetic field intensity, μ is the permeability, and ρ is the density. The first force term on the left is commonly referred to as the Lorentz force. The middle term is the magnetic polarization force. The last term is the magnetostrictive force. I will not consider magnetostrictive forces further since the magnetostrictive force density in solid engineering materials is so small it can usually be neglected for practical purposes.

A Lorentz force actuator arises when a magnetic field is directed across moving electrical charge. In practice, a current-carrying conductor crossing a magnetic field produces a Lorentz force. Polarization forces arise between magnetically polarized media. Common examples of polarization forces include attraction/repulsion between permanent magnets, attraction between a permanent magnet and iron, and attraction between an electromagnet and iron.

2.3 Basic types of actuators

Electromagnetic actuators are well documented in literature. For a review of linear motion devices, [21] and [2] are good references. The basic types of motors for linear motion include induction, synchronous, variable reluctance (Sawyer), and commutationless DC. All these motors operate on the basis of the fundamental MQS forces.

For a review of magnetic suspension techniques, [19] and [37] are good references. Suspension techniques using Lorentz forces and magnetic polarization forces are documented. Also, [19] gives an excellent review of the prior art in planar positioners, with an emphasis on those used for photolithography.

Chapter 3

Selection of a magnetic bearing topology for low fringing fields

Although there are many architectures for suspending and translating parts, few meet the requirements for ebeam lithography. The first question that I ask in the selection process is whether the architecture can be designed to meet low fringing field requirements. The low fringing field criteria is derived in Section 4.7 and requires the stage to produce less than $\pm 2 \times 10^{-7}$T ($\pm$2mGauss) in the ebeam trajectory.

The design tools for low fringing stage design include field cancellation, large spacing between the magnetic components and the location where large attenuation is desired, and shielding. I applied these tools at a high level early in the design process. After considering variations of the many possible suspension and linear motion techniques, I whittled through the candidate topologies. I then pursued the most promising topology for detailed engineering.

The first conclusion that I made is that, in general, it is good design practice to not have moving iron in a low fringing field stage. I will illustrate why with the example depicted in Figure 3-1. Although electromagnetic theory is reviewed in Section 4.1, I will include the result for this problem here since it is relevant to the selection of a stage topology. In the example, the permeable sphere is in the presence of an externally supplied, z directed flux density B_o. The magnetic scalar potential outside

the permeable sphere is given by

$$\Phi = H_0 \cos(\theta) \left(r + \frac{R^3}{r^2} \frac{\frac{\mu_0}{\mu} - 1}{\frac{2\mu_0}{\mu} + 1} \right). \tag{3.1}$$

The flux density outside the sphere is given by

$$\mathbf{B} = \mu_0 H_0 \left(\left(-1 + \frac{2R^3}{r^3} \frac{\frac{\mu_0}{\mu} - 1}{\frac{2\mu_0}{\mu} + 1} \right) \cos(\theta) \hat{\mathbf{i}}_r + \left(1 + \frac{R^3}{r^3} \frac{\frac{\mu_0}{\mu} - 1}{\frac{2\mu_0}{\mu} + 1} \right) \sin(\theta) \hat{\mathbf{i}}_\theta \right). \tag{3.2}$$

Now if we are conservative and take the maximum field change due to the dipole field induced by the sphere, we can eliminate θ and obtain

$$\Delta B = \mu_0 H_0 \left(\frac{2R^3}{r^3} \frac{1 - \frac{\mu_0}{\mu}}{\frac{2\mu_0}{\mu} + 1} \right) \tag{3.3}$$

and for $\mu >> \mu_0$,

$$\Delta B = \mu_0 H_0 \frac{2R^3}{r^3}. \tag{3.4}$$

Here ΔB is the difference in field magnitude with the sphere versus without it. The field changes that the ebeam experiences due to the moving sphere can be minimized by attenuating the ambient field and spacing the permeable material far away from the column. While the chamber is likely to be very highly shielded from the stray fields in the environment, it is likely that the objective lens in the column will produce significant fields in the chamber that the stage must tolerate. Also, changes in the objective lens' field due to regular pattern writing activity and noise from the electronics would make it difficult to map out the deflections as repeatable errors. Furthermore, since it is highly desirable to have a stage with a small footprint for structural and for many system-level reasons, I will assume that spacing the moving iron far from the ebeam is not an attractive solution. Thus, I rule out magnetic bearings that utilize moving iron. The class of motors eliminated by this decision is variable reluctance motors. It can also be argued that high force density induction motors require moving iron. However, induction machines do not inherently require moving iron and I instead rule them out because of power dissipation on the platen.

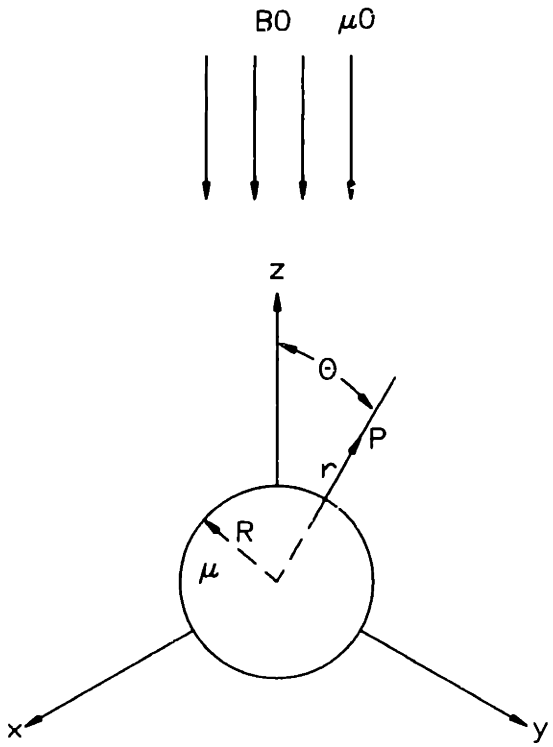

Figure 3-1: Permeable sphere in a uniform magnetic field

The basic propulsion methods left are forms of synchronous and commutationless DC motors. I select synchronous motors for detailed design because all of the following properties can be met

- forces in multiple directions can be precisely controlled
- high chance of achieving low fringing fields since opposing dipoles allow field cancellation topologies
- rare earth magnets have strong intrinsic magnetization and no hysteresis during normal use
- rare earth magnets and coils very closely approximate the permeability of free space
- force output of low permeability material based motor designs are relatively insensitive to the size of the "air" gap

- synchronous motors have been proven in precision motion control systems for six degree of freedom positioning

The basic architecture of the synchronous motor that I analyze in detail in this thesis is shown in Figure 3-2. It consists of a Halbach magnet array and multiple phases of currents. The figure shows a section of stator with three phases designated by A, B, and C. The current returns (end turns not shown) in the reverse direction through phases designated A', B', and C'. The Halbach array shown is a block array with four magnets per period as designated by the rotation period of the magnetization. One should note that additional phases or magnets per period could be used for a synchronous motor. Because the Halbach array creates strong field components in the translation and suspension directions, within the stator coils, forces in both suspension and translation can be generated. As the magnet array translates relative to the stator, the phases are commutated in a sinusoidal manner to achieve the desired force output. A small gap is maintained between the magnet array and the stator to prevent mechanical interference. Having settled on the synchronous motor magnetic bearings, I consider the tools for reducing the fringing fields in further detail.

One idea for attenuating the fields of magnetic bearings is shielding. Unfortunately, since I have ruled out moving high permeability material, shielding a planar motion stage becomes especially difficult. One topology that might be implemented is shown in Figure 3-3.

This shielded topology has a shield layer interlocked with the moving part. All the moving magnetic components and the stator are located on the bottom side of the shield. Meanwhile, the substrate and the ebeam are located on the top side. Holes in the shield layer allow connection between these two halves of the moving stage. The holes must be spaced far enough from the magnetic components for the shield to be effective.

This topology has many drawbacks. First of all, it requires a large structure, which gives it relatively poor dynamic properties. Furthermore, the structure would be relatively heavy which would put an even heavier burden on the shielding performance because of the additional magnetic material required to suspend it. At the system

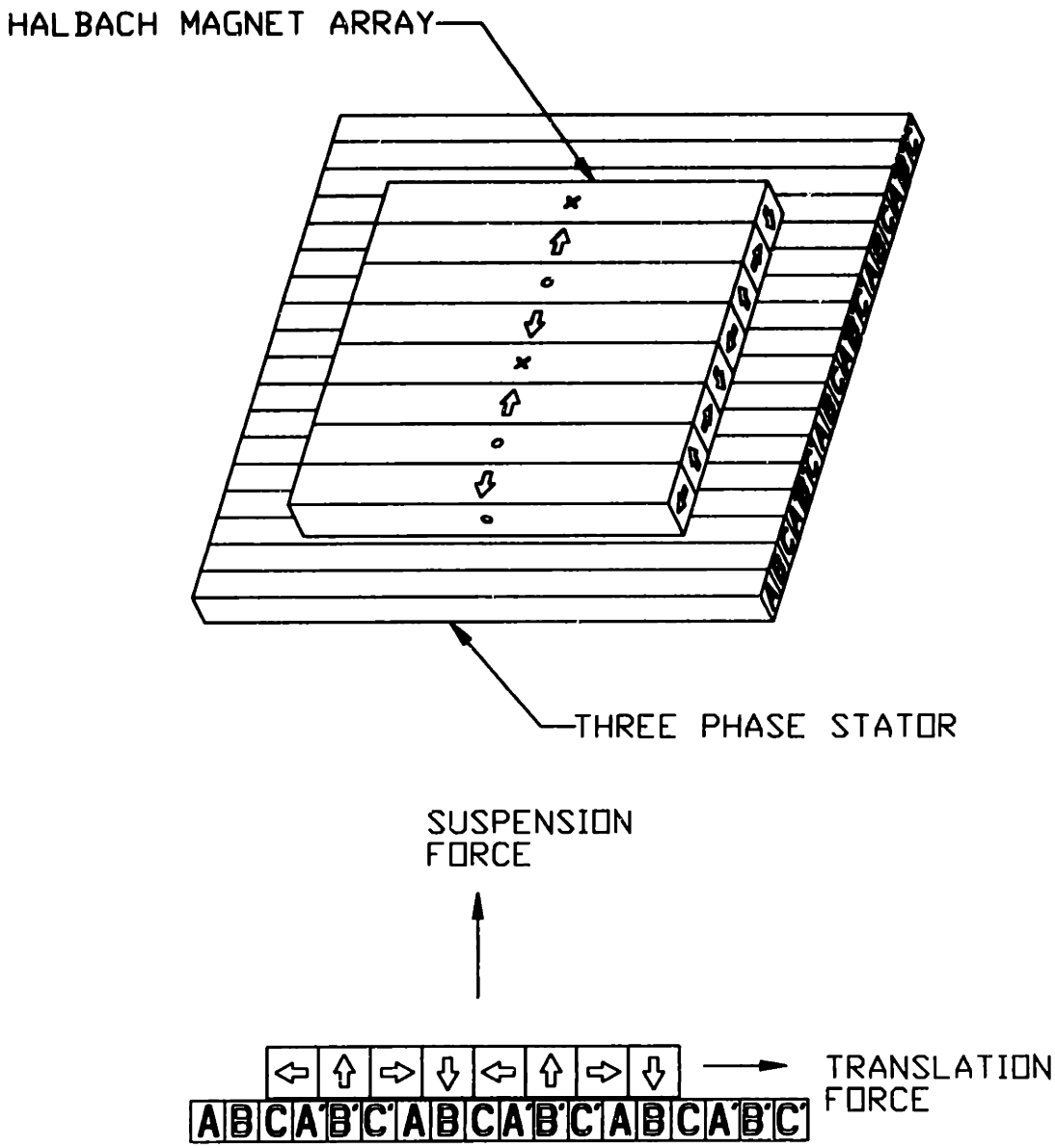

Figure 3-2: Schematic of a synchronous motor

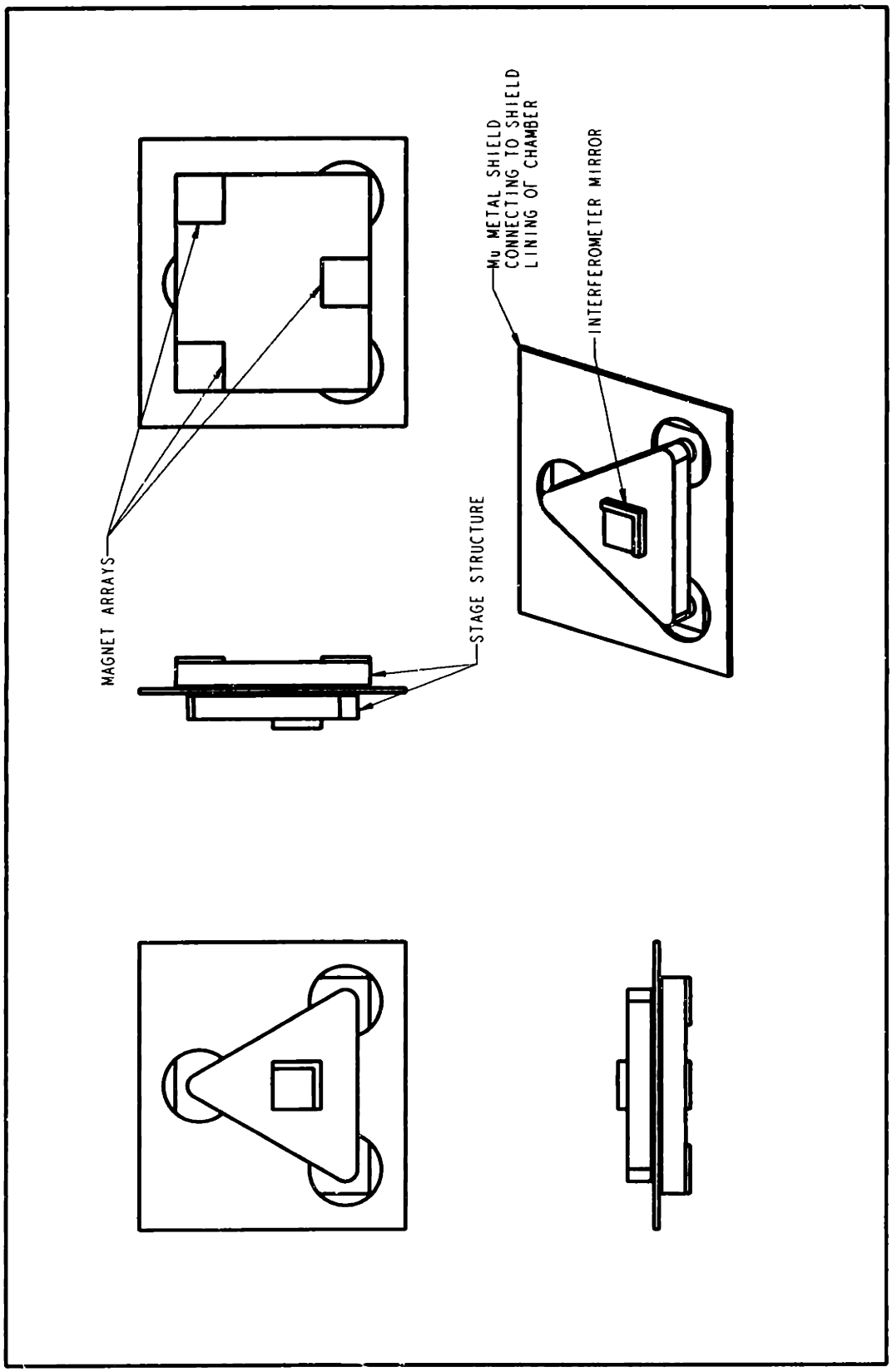

Figure 3-3: A shielded stage topology

level, the large amount of surface area and the large footprint of this design is not ideal for the vacuum environment. Similarly, I did not consider this topology to be promising for future generation ebeam lithography machines and I did not pursue its detailed design.

While shielding can be very effective in closed geometries, shielding is not a promising method of field attenuation in planar stage design. However, there are shielding effects that must be considered in any stage for ebeam lithography. These effects arise because of interaction between the highly shielded vacuum chamber and the magnetic components inside the chamber. Incidentally, the chamber is required to be highly shielded to attenuate stray fields from the environment. I will consider shielding further in Section 4.6 where I study the fields induced by multipoles in a spherical shield enclosure.

Another idea for reducing fringing fields is field cancellation. This is the method that I explore in detail in this thesis. It has the potential to achieve very fast-falling fringing fields and thus the spacing between the magnetic components and the ebeam can be a reasonable distance. Among other reasons, this is important if a high natural frequency structure is desired. Also, by avoiding heavy structures altogether the amount of magnetic material can be held to a minimum.

3.1 Proposed stage topologies using synchronous motors that provide suspension and translation forces

Before proceeding with the detailed design of low fringing field synchronous motor bearings, I considered a number of stage topologies that could achieve large scale planar motion along with small scale motions for focus and rotational alignment. This investigation was necessary to convince myself that an elegant stage design that met all the requirements for ebeam lithography could be achieved with the synchronous motors. In our Precision Motion Control Laboratory at MIT, Won-jong Kim has

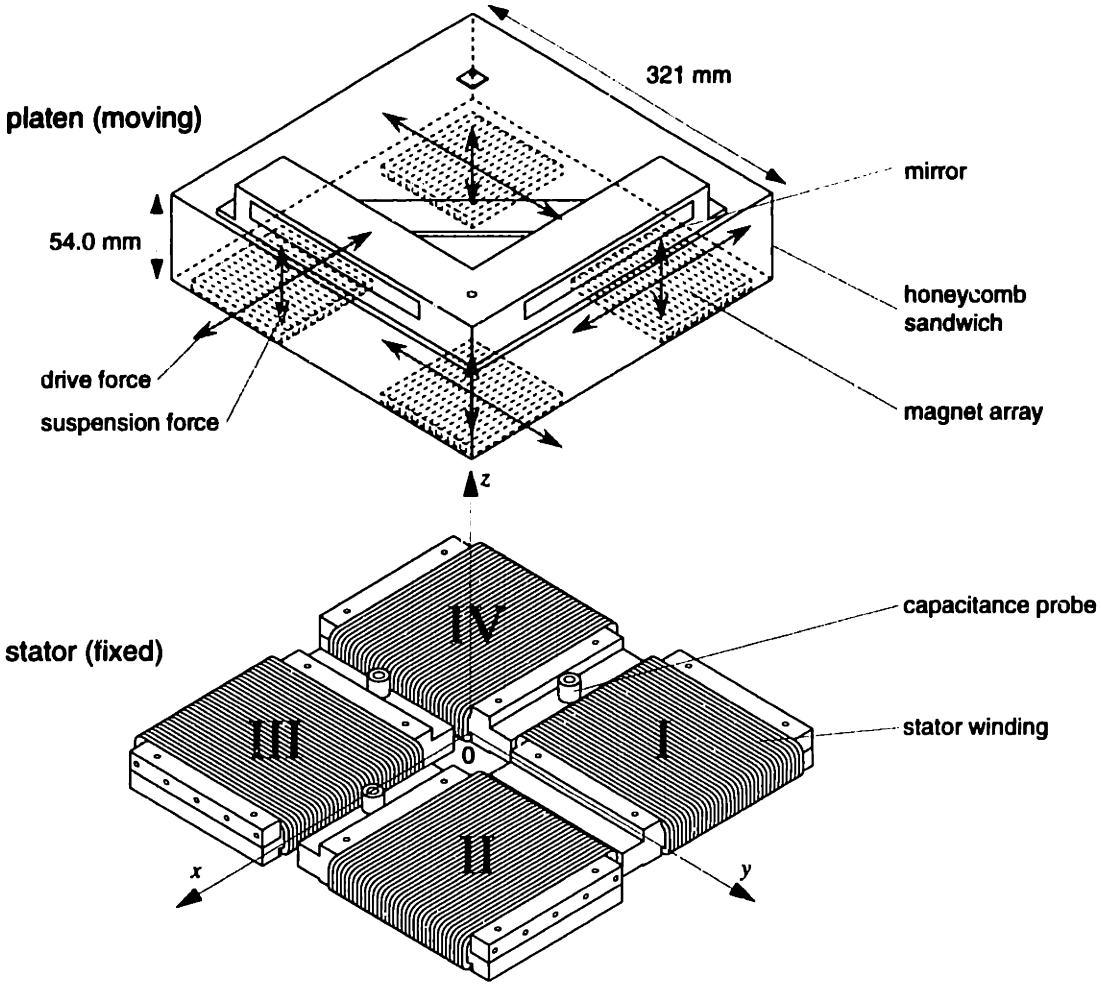

Figure 3-4: Selected design for prototyping, from Won-jong Kim's doctoral thesis

implemented a six degree of freedom magnetically levitated stage using synchronous motor bearings. The design is shown in Figure 3-4 [19].

This stage incorporates four linear synchronous motors with each producing forces in suspension and translation. Since these synchronous motor bearings can output an equal amount of force in both suspension and translation, the maximum translation force is half the maximum suspension force. A nice aspect of this design is that it is kinematically simple. A drawback of the design is that it has eight input forces, where six could be used. Also, the footprint is very large for the amount of travel. The minimum footprint of the coils is two times the travel plus the sum of the magnet lengths for each side. The magnet lengths are not insignificant. In the prototype shown in Figure 3-4, the magnet lengths are 3.7 times the 5 cm travel. However,

this magnet length to travel ratio is not a good comparison for an actual ebeam lithography stage. The magnet length to travel ratio must be considered in light the requirements for suspended weight, acceleration, thermal current limit, and a variety of motor parameters.

In Chapter 5, I consider the magnet array size requirements for a platen that would be suitable for an ebeam stage with $13'' \times 13''$ travel and a suspended mass of 21kg. The thermal current limit results found in Chapter 7 are used in the calculations. It turns out that it would not be surprising for a design to require magnet lengths close to the travel length. Even at this ratio, there is motivation for exploring alternative stage topologies. A stage footprint that is equal to the travel plus the size of the part that is moved is the fundamental limit on the compactness of any stage. In the ideal case, a topology would be restricted by this fundamental limit and not a larger space requirement imposed by actuator placement.

While [19] evaluates other stage topologies, I propose additional stage concepts that are appealing. Figure 3-5 shows a design that uses a more complicated commutation scheme but achieves a smaller footprint. Only two magnet arrays are used but six degrees of freedom are achieved by commutating sections of coils not only along the stack but across stacks. The forces and torques are designated by the directions of the arrows in the figure. The minimum footprint of the coils is the travel plus the sum of the magnet lengths for one side and two times the travel plus the sum of the magnet lengths for the other. The kinematics of this stage require the linear motors to counteract the torque when the platen is accelerated in the direction of the short platen axis. Depending on the actual geometry used, this is likely to limit the accelerations in this axis. But since ebeam lithography requires translational acceleration of only about 0.1g, the reduction in translational acceleration is acceptable. A drawback of this design is that there is ripple force associated with crossing the stacks. Also, many coils are required and the minimum stage footprint is still not achieved.

Another stage concept is shown in Figure 3-6. In this design, an inner stator is buried within an outer stator. The outer stator couples with the x -- z force arrays to

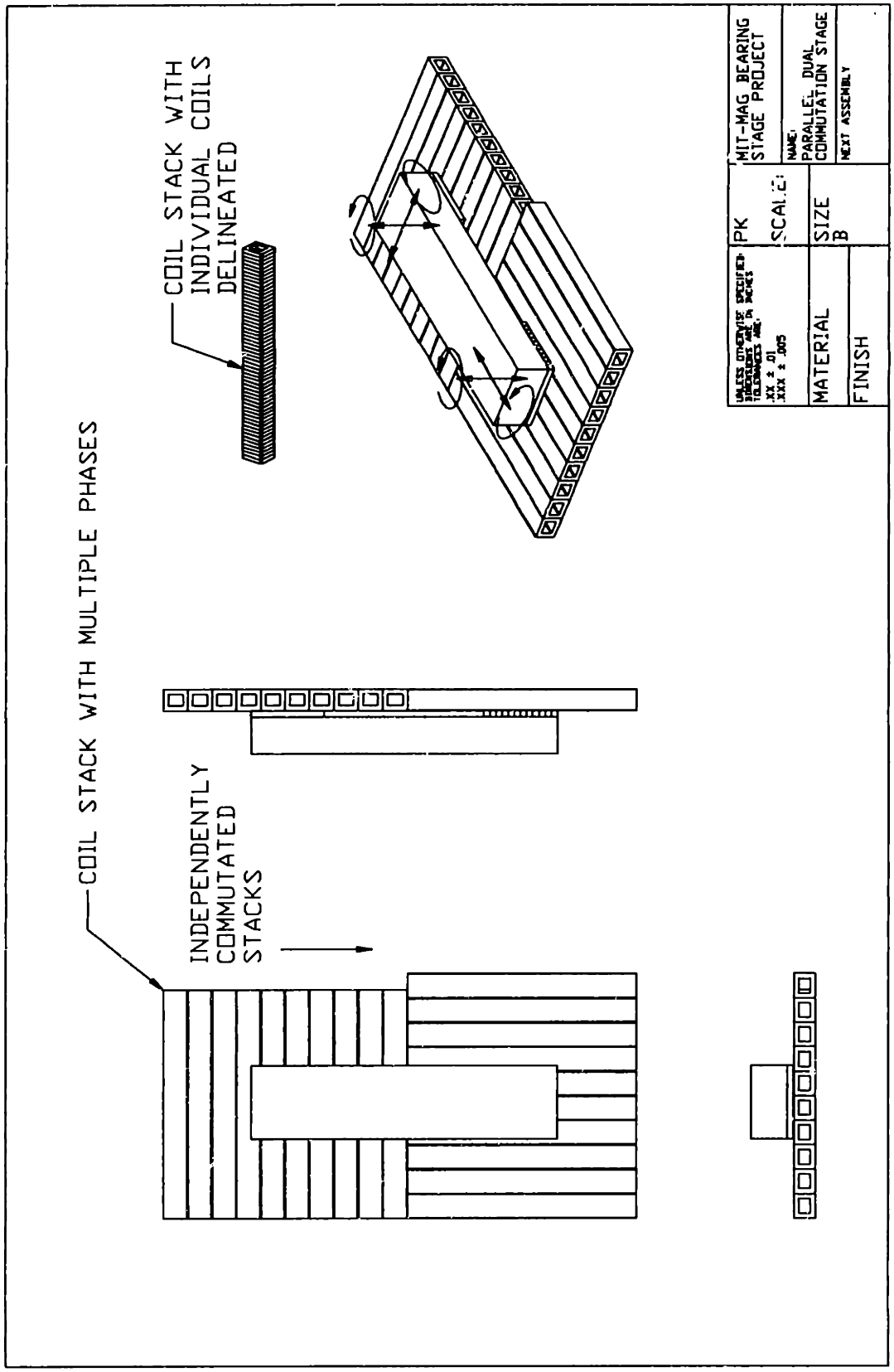

Figure 3-5: Stage with parallel coil stacks to achieve 6-axis control with only two magnet arrays.

produce suspension and x-directed translation force. The inner stator couples with the $y-z$ force arrays to produce suspension and y-directed translation force. Like in the previous design, coil stacks are independently commutatable. Arrows superposed over the magnet array locations show the direction and location of the available forces.

The inner stator operates through a large "air" gap, which happens to reduce this actuator's efficiency. However, the control effort in this direction is small if scanning is performed in the orthogonal direction and all the suspension is provided by the outer stator. I suggest using larger spatial period magnet and coil arrays for the large gap motor to increase the efficiency (as shown by the larger spatial period magnets in the figure).

The length of the coil stacks is a half integer multiple of the magnet spatial period and should be smaller than half the length of the smallest magnet arrays (i.e. the $x-z$ force arrays). That way the degrees of freedom can be easily decoupled because each magnet array will always be over atleast one coil stack that is not shared with its neighbor arrays nor overlapping its end. Alternatively, Figure 3-7 conceptually shows how the coil stacks can be independently commutated to achieve six degrees of freedom. In the outer stator, all the stacks beneath the stage are commutated synchronously to produce x-directed and z directed force. The inner stator is a single coil stack and commutates to produce y directed force and, if desired, suspension force. The $x-$directed forces associated with the small $x-z$ force arrays oppose the $x-$directed force of the large $x-z$ force array to produce yaw torque. Additionally, the $z-$directed forces of the small $x-z$ force arrays oppose the $z-$directed force of the large $x-z$ force array to produce roll torque. The $z-$directed forces of the small $x-z$ force arrays oppose each other for pitch torque.

It turns out that the inner and outer stators are slightly coupled unless the width of magnet arrays acting on the inner and outer stators are integer multiples of the orthogonal stator's spatial period. Thus, the design should incorporate this characteristic. The minimum footprint of the coils is the travel plus the sum of the magnet lengths for each side. Thus, the minimum desired footprint for a platen with length equal to the travel is likely to be achieved. A drawback of this design is extra elec-

tronics are required to commutate the many independently controllable coil stacks.

The three stages that I have presented illustrate different ways that the magnetic bearings could be combined for six degree of freedom actuation. Certainly, other topologies could be formulated that combine concepts from these stages in different kinematic variations. I only presented examples that I feel are representative of attractive possibilities in stage design.

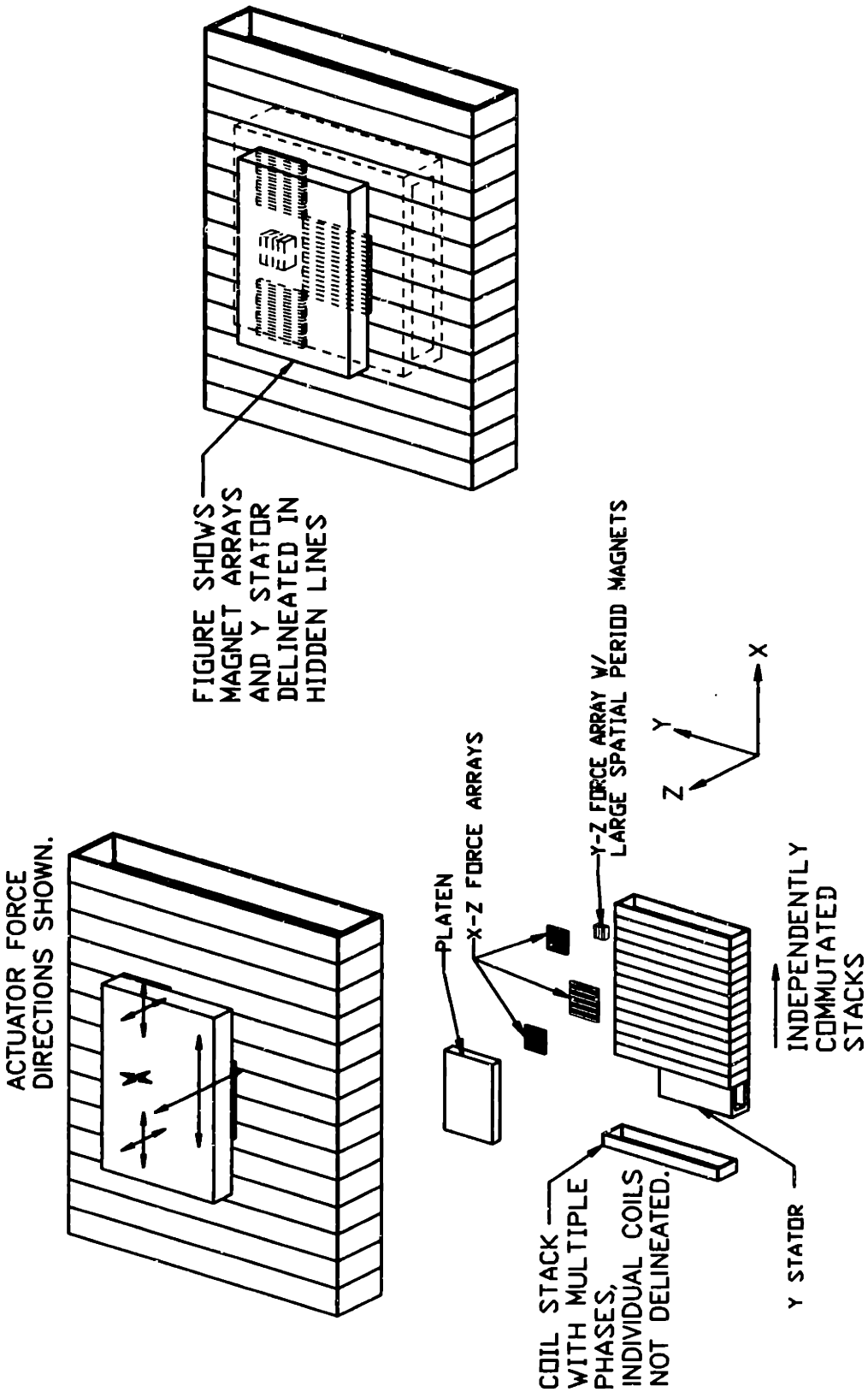

Figure 3-6: Stage with inner and outer stators.

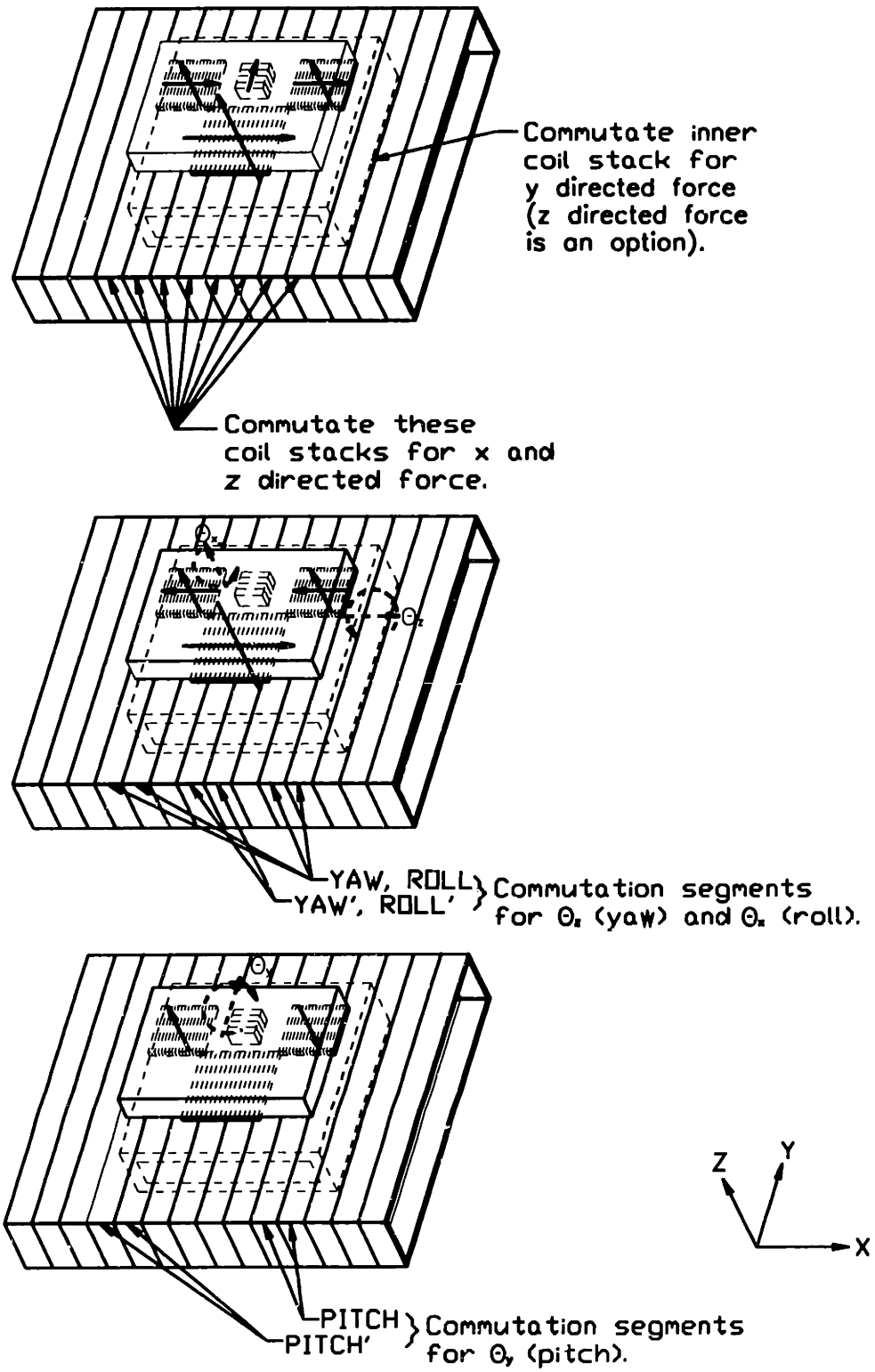

Figure 3-7: Independent commutation of coil stacks to achieve six degrees of freedom in the stage with inner and outer stators.

Chapter 4

Low fringing field magnetic bearing design

The fringing fields from magnetic media are governed by fundamental laws of physics. In this chapter, I first review Maxwell's equations, which are the governing equations of electromagnetic fields. I also review useful relations common to electromagnetic analysis. Then I derive expressions for the fringing fields of multipoles. This multipole analysis leads to low fringing field designs based on field cancellation. The designs allow the fields to be strong near the magnetic media but very weak a reasonable distance away. In practice, this design allows magnetic fields to be strong near a magnet array and in stator windings for high density force production but very weak in the ebeam trajectory in order not to induce ebeam writing errors. The analysis covers two dimensional multipoles formed from line-current dipoles and three dimensional multipoles formed from magnetic dipoles. For the three dimensional case, I first consider the family of solutions that are independent of ϕ in spherical coordinates. Then I consider the more complex case that is dependent on ϕ. After that, I present a general technique for solving for the scalar potential of multipoles built from parallel opposing submultipoles. Next, I analyze the field interactions between multipoles and spherical shields. The field requirements for ebeam lithography are derived and a technique for finding field solutions by magnetic charge integration are covered in the last sections of the chapter.

4.1 A brief review of electromagnetic field theory

In this section, I include the building blocks of electromagnetic field theory. For a more complete review, one can refer to [15, 25, 42].

In integral form, the fundamental laws of electromagnetic fields are given by Maxwell's equations as

$$\oint_C \mathbf{E} \cdot \mathbf{dl} = -\frac{d}{dt}\int_S \mathbf{B} \cdot \mathbf{dS} \qquad \text{(Faraday's law)}, \tag{4.1}$$

$$\oint_C \mathbf{H} \cdot \mathbf{dl} = \int_S \mathbf{J_f} \cdot \mathbf{dS} + \frac{d}{dt}\int_S \mathbf{D} \cdot \mathbf{dS} \qquad \text{(Ampere's Law with Maxwell's displacement current correction)}, \tag{4.2}$$

$$\oint_S \mathbf{D} \cdot \mathbf{dS} = \int_V \rho_f \, dV \qquad \text{(Gauss's Law), and} \tag{4.3}$$

$$\oint_S \mathbf{B} \cdot \mathbf{dS} = 0 \qquad \text{(Gauss's Law)}. \tag{4.4}$$

Here $\mathbf{E}$ is the electric field intensity, $\mathbf{D}$ is the electric displacement, $\mathbf{B}$ is the magnetic flux density, $\mathbf{H}$ is the magnetic field intensity, $\mathbf{J_f}$ is the free current density, ρ_f is the free electrical charge density, C is a contour of integration, and S is a surface associated with either C or V. The corresponding differential forms for these laws are

$$\nabla \times \mathbf{E} = -\frac{\partial \mathbf{B}}{\partial t}, \tag{4.5}$$

$$\nabla \times \mathbf{H} = \mathbf{J_f} + \frac{\partial \mathbf{D}}{\partial t}, \tag{4.6}$$

$$\nabla \cdot \mathbf{D} = \rho_f, \text{ and} \tag{4.7}$$

$$\nabla \cdot \mathbf{B} = 0. \tag{4.8}$$

The associated boundary conditions across a surface are given by

$$\hat{\mathbf{n}} \times (\mathbf{E_2} - \mathbf{E_1}) = \mathbf{0}, \tag{4.9}$$

$$\hat{\mathbf{n}} \times (\mathbf{H_2} - \mathbf{H_1}) = \mathbf{K_f}, \tag{4.10}$$

$$\hat{\mathbf{n}} \cdot (\mathbf{D_2} - \mathbf{D_1}) = \sigma_f, \text{ and} \tag{4.11}$$

$$\hat{\mathbf{n}} \cdot (\mathbf{B_2} - \mathbf{B_1}) = 0. \tag{4.12}$$

Here $\mathbf{K_f}$ is a free surface current density and σ_f is a free surface charge density. The constitutive relationship between the magnetic flux density and the magnetic field intensity is

$$\mathbf{B} = \mu_0(\mathbf{H} + \mathbf{M}) \tag{4.13}$$

where $\mathbf{M}$ is the magnetization density.

For the electric machines of interest, we can make the magnetoquasistatic (MQS) approximation [15] because light travels a very long distance during time periods of interest compared to the longest characteristic length of our systems ($\tau \times c >> L$). Thus, by the MQS approximation we neglect electromagnetic waves and Equation (4.6) reduces to

$$\nabla \times \mathbf{H} = \mathbf{J_f}. \tag{4.14}$$

For field analysis exterior to current flows, we have $\mathbf{J}_f$=0, and the magnetic field can be written as the gradient of the scalar potential

$$\mathbf{H} = -\nabla\Phi. \tag{4.15}$$

In spherical coordinates, as shown in Figure 4-1, $\nabla\Phi$ is given by

$$\nabla\Phi = \frac{\partial\Phi}{\partial r}\hat{\mathbf{i}}_r + \frac{1}{r}\frac{\partial\Phi}{\partial\theta}\hat{\mathbf{i}}_\theta + \frac{1}{r\sin(\theta)}\frac{\partial\Phi}{\partial\phi}\hat{\mathbf{i}}_\phi. \tag{4.16}$$

By combining Equation (4.8) and Equation (4.15), the magnetic fields in any linear magnetic material must obey Laplace's equation

$$\nabla^2\Phi = 0. \tag{4.17}$$

Laplace's equation in spherical coordinates is given by

$$\nabla^2\Phi = \frac{1}{r^2}\frac{\partial}{\partial r}\left(r^2\frac{\partial\Phi}{\partial r}\right) + \frac{1}{r^2\sin(\theta)}\frac{\partial}{\partial\theta}\left(\sin(\theta)\frac{\partial\Phi}{\partial\theta}\right) + \frac{1}{r^2\sin^2(\theta)}\frac{\partial^2\Phi}{\partial^2\phi}. \tag{4.18}$$

By employing any orthogonal coordinate system, Laplace's equation can be solved by separation of variables. The general solution in spherical coordinates [26] is given by

$$\Phi = R(r)\,\Theta(\theta)\,\Phi(\phi) \quad \text{where} \tag{4.19}$$

$$R(r) = C_1 r^p + C_2 r^{-(p+1)}, \tag{4.20}$$

$$\Theta(\theta) = C_3 \mathcal{P}_p^q(\cos(\theta)) + C_4 \mathcal{Q}_p^q(\cos(\theta)), \text{ and} \tag{4.21}$$

$$\Phi(\phi) = C_5 \sin(q\phi) + C_6 \cos(q\phi). \tag{4.22}$$

Note that $R(r)$, $\Theta(\theta)$, and $\Phi(\phi)$ are the separated functions that are dependent on only one coordinate. Here C_i refers to constants derived from boundary conditions, $\mathcal{P}_p^q$ is the generalized Legendre function of the first kind, $\mathcal{Q}_p^q$ is the generalized Legendre function of the second kind, and q and p are integer separation constants. The function $\mathcal{P}_p^q(\cos(\theta))$ is an odd function while $\mathcal{Q}_p^q(\cos(\theta))$ is an even function with respect to $\cos(\theta)$. The *generalized* Legendre functions $\mathcal{P}_p^q$ and $\mathcal{Q}_p^q$ do not reduce directly to *ordinary* Legendre functions, thus one must be careful to distinguish the two sets of functions. It is not necessary to understand the details of ordinary Legendre functions for the following analysis, thus, I will not delve into them. For those readers wishing further discussion, page 205 of [26] gives a description of the constants and other changes that distinguish the ordinary Legendre functions P_n and Q_n from the generalized Legendre functions. I will present the generalized Legendre functions that pertain to $\Theta(\theta)$ later in this chapter.

Laplacian solutions are simplified in the analysis of ironless motors because of the approximation $\mu \approx \mu_0$. This approximation is almost exact for copper, which has μ_r=.99990 [3], and very close for the rare earth magnet NeFeB, which has μ_r=1.05 [23]. Because of this approximation, it is valid to linearly superpose the fields produced by currents and permanent magnets in any solution process.

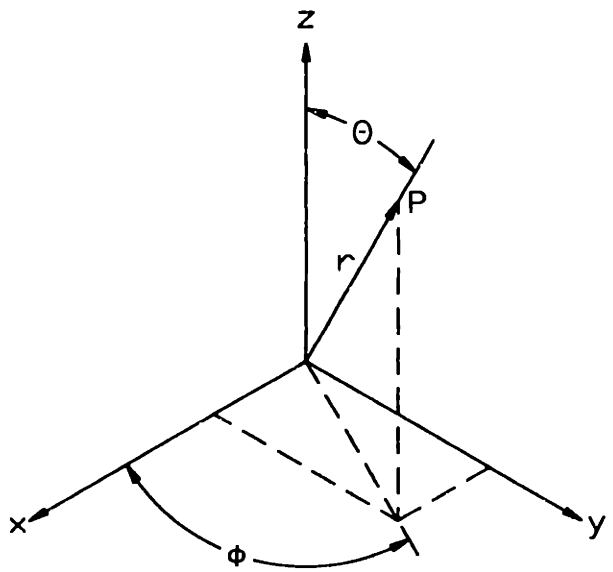

Figure 4-1: Definition of spherical coordinate system. The location of point P is defined by r, θ, and ϕ.

4.2 The general far-field solutions for two dimensional multipoles

In this section, I consider the two dimensional far field solutions resulting from combinations of current dipoles. This two dimensional analysis builds intuition on field cancellation and prepares the reader for the three dimensional analysis in the following sections.

An example of a current dipole is depicted in Figure 4-2. The far field[1] two dimensional magnetic vector potential of the current dipole is given by Equation (4.23)

$$\mathbf{A_z} = -\frac{\mu_0 I d}{2\pi}\left(\frac{\cos(\phi)}{r}\right). \tag{4.23}$$

This result is derived in Section 8.2 of [15] by taking the far field limit of two opposing line currents. The magnetic flux density given the vector potential is

$$\mathbf{B} = \nabla \times \mathbf{A}. \tag{4.24}$$

[1]Far field approximations are valid for points in space $r >> d$. As a rule of thumb, the approximations are very accurate for $\frac{r}{d} > 10$.

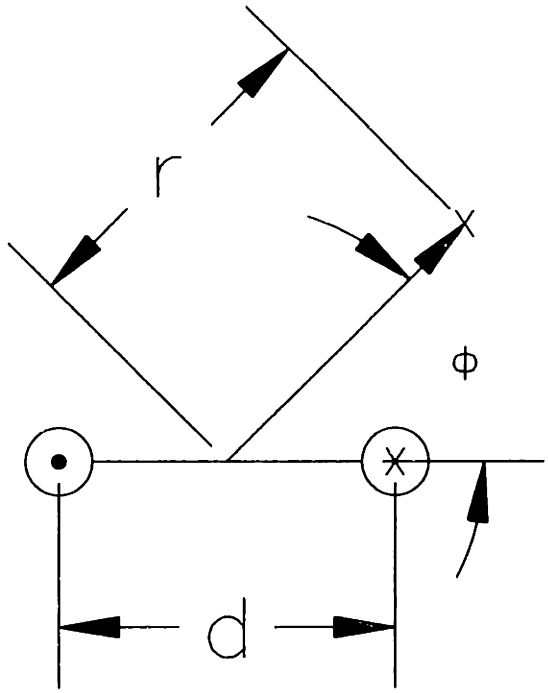

Figure 4-2: Current dipole (2-d)

In cylindrical coordinates $\nabla \times \mathbf{A}$ is given by

$$\nabla \times \mathbf{A} = \left(\frac{1}{r}\frac{\partial A_z}{\partial \phi} - \frac{\partial A_\phi}{\partial z}\right)\mathbf{i}_r + \left(\frac{\partial A_r}{\partial z} - \frac{\partial A_z}{\partial r}\right)\mathbf{i}_\phi + \left(\frac{1}{r}\frac{\partial (rA_\phi)}{\partial r} - \frac{1}{r}\frac{\partial A_r}{\partial \phi}\right)\mathbf{i}_z. \quad (4.25)$$

Far field cancellation is achieved with the addition of a parallel opposing dipole such as in the configuration shown in Figure 4-3. Here we assume that a pair of dipoles is arranged with anti-symmetry about the origin, and with separation between centers of X and Y in the horizontal and vertical directions respectively.

The vector potential for this anti-symmetric pair is derived by superposing Equation (4.23) according to the geometry shown. Moreover, the r and $\cos(\phi)$ terms of Equation (4.23) are written to account for the position offset from the origin of each of the opposing multipoles. For the dipole in quadrant I,

$$r_I = \sqrt{\left(r\cos(\phi) - \frac{X}{2}\right)^2 + \left(r\sin(\phi) - \frac{Y}{2}\right)^2} \quad \text{and} \quad (4.26)$$

$$\cos(\phi_I) = \frac{r\cos(\phi) - \frac{X}{2}}{r_I}. \quad (4.27)$$

For the dipole in quadrant III,

$$r_{III} = \sqrt{\left(r\cos(\phi) + \frac{X}{2}\right)^2 + \left(r\sin(\phi) + \frac{Y}{2}\right)^2} \quad \text{and} \tag{4.28}$$

$$\cos(\phi_{III}) = \frac{r\cos(\phi) + \frac{X}{2}}{r_{III}}. \tag{4.29}$$

The vector potential becomes

$$\mathbf{A_z} = -\frac{\mu_0 I d}{2\pi}\hat{\mathbf{i}}_z \times \left(\frac{r\cos(\phi) - \frac{X}{2}}{\left(r\cos(\phi) - \frac{X}{2}\right)^2 + \left(r\sin(\phi) - \frac{Y}{2}\right)^2} - \frac{r\cos(\phi) + \frac{X}{2}}{\left(r\cos(\phi) + \frac{X}{2}\right)^2 + \left(r\sin(\phi) + \frac{Y}{2}\right)^2}\right). \tag{4.30}$$

After manipulating the terms to be over a common denominator this equation becomes

$$\begin{aligned}\mathbf{A_z} = -\frac{\mu_0 I d}{2\pi} \times & \left(\left[r\cos(\phi) - \frac{X}{2}\right]\left[r^2 + r\left(X\cos(\phi) + Y\sin(\phi)\right) + \frac{X^2}{4} + \frac{Y^2}{4}\right]\right. \\ & \left. - \left[r\cos(\phi) + \frac{X}{2}\right]\left[r^2 - r\left(X\cos(\phi) + Y\sin(\phi)\right) + \frac{X^2}{4} + \frac{Y^2}{4}\right]\right)\hat{\mathbf{i}}_z \times \\ & \left(\left[r^2 + \frac{X^2}{4} + \frac{Y^2}{4}\right]^2 - r^2\left[X^2 + Y^2 + 2XY\cos(\phi)\sin(\phi)\right]\right)^{-1}. \end{aligned} \tag{4.31}$$

For $r >> \sqrt{X^2 + Y^2}$ the far field limit becomes

$$\mathbf{A_z} = -\frac{\mu_0 I d}{2\pi}\left(\frac{2X\cos^2(\phi) - X + 2Y\sin(\phi)cos(\phi)}{r^2}\right). \tag{4.32}$$

The vector potential is further simplified using trigonometric identities to yield

$$\mathbf{A_z} = -\frac{\mu_0 I d\sqrt{X^2 + Y^2}}{2\pi}\frac{\cos(2\phi - \arctan\frac{Y}{X})}{r^2}. \tag{4.33}$$

Generalizing even further, if Figure 4-3 described the superposition of two oppos-

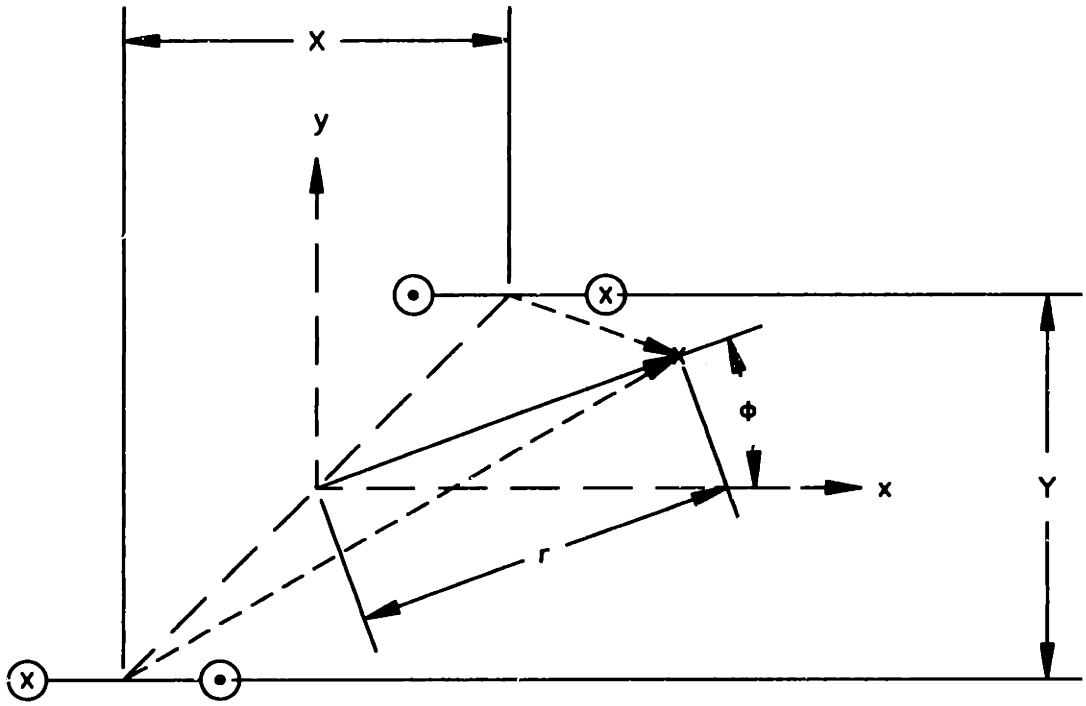

Figure 4-3: Parallel opposing dipoles

ing multipoles with the upper multipole being described in the far field by

$$\mathbf{A_z} = -C\frac{\cos(p\phi)}{r^p}, \tag{4.34}$$

the vector potential can be simplified in a similar derivation as for Equation (4.33), although binomial expansion of the terms and writing the trigonometric terms as real parts of complex numbers is required. Note that Equation (4.34) is also a solution to Laplace's equation in polar coordinates, since $\nabla^2\Phi$ is identical to the vector Laplacian in polar coordinates when the Coulomb gage, $\nabla \cdot \mathbf{A} = 0$ is employed. The vector potential must obey the vector Laplacian because of the following derivation: $\nabla \times \nabla \times \mathbf{A} = 0$ in current free regions since $\nabla \times \mathbf{H} = 0$ and by the vector identity $\nabla \times \nabla \times \mathbf{A} = \nabla(\nabla \cdot \mathbf{A}) - \nabla^2\mathbf{A} = -\nabla^2\mathbf{A} = 0$. Therefore, this analysis closely parallels an equivalent derivation using scalar potentials in place of the vector potentials. The equivalent analysis would use $\Phi = C\sin(p\phi)r^{-p}/\mu_o$ as the scalar potential.

I begin simplifying Equation (4.34) by writing

$$\cos(p\phi) = Re\left[e^{ip\phi}\right] = Re\left[cos(\phi) + i\sin(\phi)\right]^p. \tag{4.35}$$

For the multipole in quadrant I,

$$\sin(\phi_I) = \frac{r\sin(\phi) - \frac{Y}{2}}{r_I}. \tag{4.36}$$

For the multipole in quadrant III,

$$\sin(\phi_{III}) = \frac{r\sin(\phi) + \frac{Y}{2}}{r_{III}}. \tag{4.37}$$

The relations for the cosine terms and radius terms are given in Equations (4.26) through (4.29). Using Equation 4.34, the vector potential for the pair of opposing multipoles becomes

$$\begin{aligned}\mathbf{A_z} = -C\Bigg(&\frac{Re\left[\left(r\cos(\phi) - \frac{X}{2}\right) + i\left(r\sin(\phi) - \frac{Y}{2}\right)\right]^p}{\left[\left(r\cos(\phi) - \frac{X}{2}\right)^2 + \left(r\sin(\phi) - \frac{Y}{2}\right)^2\right]^p} - \\ &\frac{Re\left[\left(r\cos(\phi) + \frac{X}{2}\right) + i\left(r\sin(\phi) + \frac{Y}{2}\right)\right]^p}{\left[\left(r\cos(\phi) + \frac{X}{2}\right)^2 + \left(r\sin(\phi) + \frac{Y}{2}\right)^2\right]^p}\Bigg)\hat{\mathbf{i}}_z.\end{aligned} \tag{4.38}$$

After manipulating the terms to be over a common denominator, this equation becomes

$$\begin{aligned}\mathbf{A_z} = -C\Bigg(&Re\left[\left(r\cos(\phi) - \frac{X}{2}\right) + i\left(r\sin(\phi) - \frac{Y}{2}\right)\right]^p \\ &\left[r^2 + r\left(X\cos(\phi) + Y\sin(\phi)\right) + \frac{X^2}{4} + \frac{Y^2}{4}\right]^p \\ &-Re\left[\left(r\cos(\phi) + \frac{X}{2}\right) + i\left(r\sin(\phi) + \frac{Y}{2}\right)\right]^p \\ &\left[r^2 - r\left(X\cos(\phi) + Y\sin(\phi)\right) + \frac{X^2}{4} + \frac{Y^2}{4}\right]^p\Bigg)\hat{\mathbf{i}}_z \times\end{aligned}$$

$$\left(\left[r^2+\frac{X^2}{4}+\frac{Y^2}{4}\right]^2-r^2\left[X^2+Y^2+2XY\cos(\phi)\sin(\phi)\right]\right)^{-p}. \tag{4.39}$$

After binomial expansion and taking the far field limit, the vector potential reduces to

$$\mathbf{A_z}=-CpRe\left[\frac{2\left(\cos(\phi)+i\sin(\phi)\right)^{p-1}\left[\left(\cos(\phi)+i\sin(\phi)\right)\left(X\cos(\phi)+Y\sin(\phi)\right)-(X+Y)\right]}{r^{p+1}}\right]. \tag{4.40}$$

This relation can be nicely simplified after putting it in the form

$$\mathbf{A_z}=-CpRe\left[\left(\cos(\phi)+i\sin(\phi)\right)^{p-1}\left(\left[X\cos^2(\phi)+Y\sin(\phi)\cos(\phi)\right]+i\left[X\sin(\phi)\cos(\phi)+Y\sin^2(\phi)\right]\right)\right]r^{-(p+1)} \tag{4.41}$$

and then rewriting as

$$\mathbf{A_z}=-Cp\frac{Re\left[e^{i(p-1)\phi}(Xe^{i2\phi}-Ye^{i(2\phi-\pi/2)})\right]}{r^{p+1}}. \tag{4.42}$$

Finally, the far field solution is reduced to

$$\mathbf{A_z}=-Cp\frac{\sqrt{X^2+Y^2}\cos((p+1)\phi-\arctan\frac{Y}{X})}{r^{p+1}}. \tag{4.43}$$

By successive superposition of parallel opposing multipoles of higher and higher order, one can design a multipole with fields that fall arbitrarily fast in the far field. In fact, if we start with a dipole such as in Figure 4-2, the magnetic vector potential for the two-dimensional field cancellation with s successive superpositions can be shown to be

$$\mathbf{A_z}=-\frac{\mu_0 Id}{2\pi}\left(\prod_{m=1}^{s}m\sqrt{X_m^2+Y_m^2}\right)\frac{\cos((s+1)\phi-(\sum_{m=1}^{s}\arctan\frac{Y_m}{X_m}))}{r^{s+1}} \tag{4.44}$$

This result comes directly from successively applying Equation (4.43).

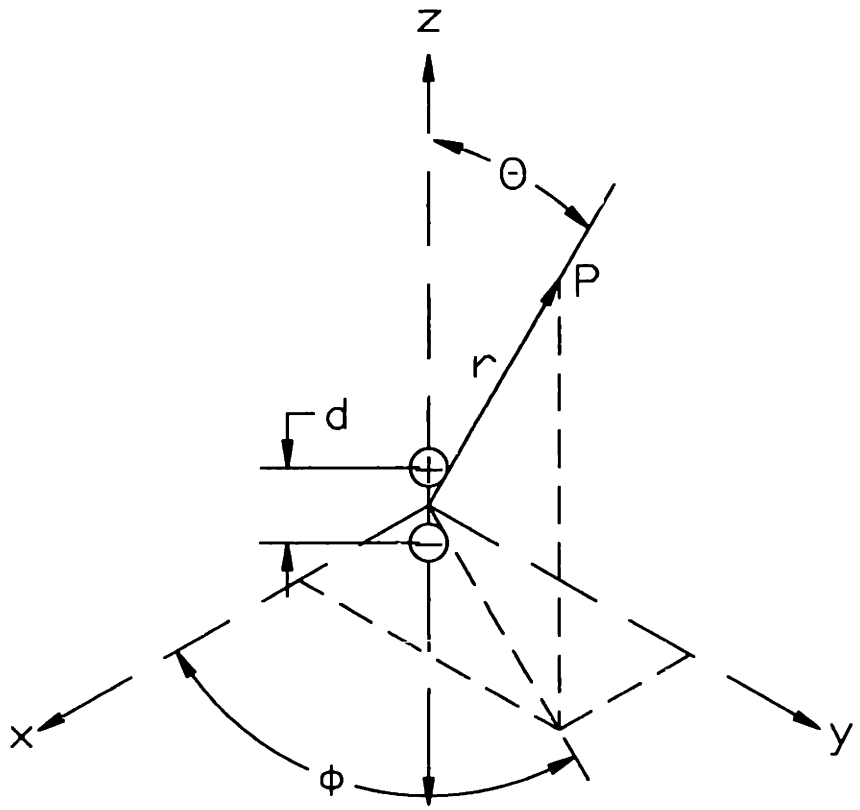

Figure 4-4: Dipole with dipole moment qd (3d)

4.3 Far field solutions for three dimensional multipoles with ϕ independence

In this section, I consider the three dimensional solution for multipoles with ϕ independence. The fundamental building block for any multipole is the dipole shown in Figure 4-4. The scalar potential of a three-dimensional dipole is given by

$$\Phi = C\frac{\cos(\theta)}{r^2} \tag{4.45}$$

Note that I switch from vector potential representation to scalar potentials for the three-dimensional solutions because the analysis is easier. The three dimensional dipoles cannot be represented by equivalent sheet currents flowing in one dimension and therefore the vector potential would require at least two nonzero vector components. Meanwhile, the scalar potential is a single function and not a multidimensional

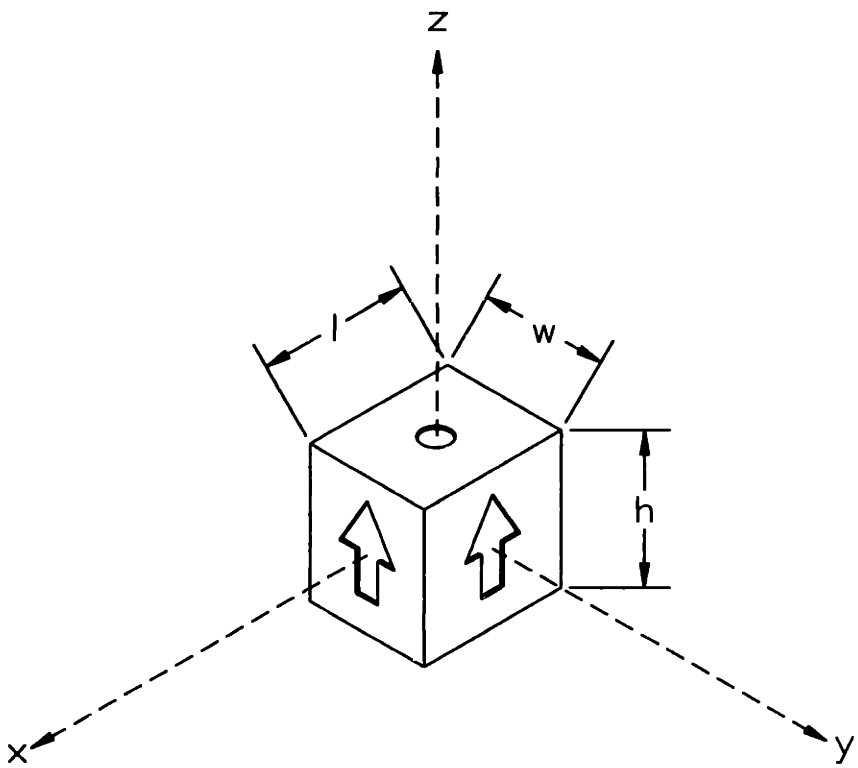

Figure 4-5: Magnet

vector.

For a parallelepiped magnet such as depicted in Figure 4-5 with magnetization density M, its centroid at the origin, height=h, pole faces with areas $l \times w$, and its north pole directed along the $+z$ axis, C is given by

$$C = \frac{Mlwh}{4\pi}. \tag{4.46}$$

Here C is derived from magnetic charge integration, which I discuss later in this chapter. Because this derivation takes a far field limit, one should note that a magnet only behaves as a dipole in the far field, where the fields of interest are at a distance much greater than any of the magnet dimensions. For a current loop of area A and carrying current I, C is

$$C = \frac{IA}{4\pi}. \tag{4.47}$$

This result can be derived by replacing M in Equation (4.46) by $K_f = I/h$. Here the sheet current is the current in the loop divided by the height of the wire. We can

show an equivalence between magnetization density and sheet current by considering a differential element with magnetic charge on its pole faces and free surface current flowing around the sides. For a permanent magnet with the constitutive relationship given by Equation (4.13), the field will be discontinuous across the pole faces and $\hat{\mathbf{n}} \cdot (\mathbf{H_2} - \mathbf{H_1}) = \mathbf{M_1}$. Here $\mathbf{H_1}$ is the field inside the differential element and $\mathbf{H_2}$ is outside, across the magnetic charge boundary. For a surface current, the field will be discontinuous across the sides and the differential element must satisfy the jump condition $\hat{\mathbf{n}} \times (\mathbf{H_3} - \mathbf{H_1}) = \mathbf{K_f}$ given by Equation (4.10). Here $\mathbf{H_3}$ is the field outside the differential element and across the surface current boundary. When $\mathbf{H_3} = 0$ and $H_2 = K_f - M_1 = 0$, the relation must satisfy $K_f = M_1$. For this condition, the fields external to a differential element exactly cancel. From this superposition, we can also conclude the surface charge on a magnet's pole faces can be substituted for an equivalent surface current circling its sides with the requirement $M_1 = -K_f$. By convention, north points opposite to the magnetization density and I indicate north by the direction of arrows in the figures that include magnets. The field solutions external to a magnet are identical to the fields external to a coil with the equivalent surface current.

For a coil of rectangular cross section and uniform current density such as shown in Figure 4-6, C is calculated by integrating the dipole moment of sheet current loops across the coil thickness. For the rectangular coil with dipoles of area $A(s)$ and sheet current I/t the dipole moment becomes

$$C = \frac{I}{4\pi t}\int_0^t A(s)ds = \frac{I}{4\pi t}\int_0^t (L+2s)(W+2s)\,ds. \tag{4.48}$$

The result is given by

$$C = I\,\frac{(t+L)(t+w)+t^2/3}{4\pi} = I\,\frac{l_{\text{effective}} \times w_{\text{effective}}}{4\pi}. \tag{4.49}$$

This expression shows that under the assumption of thin coils a current loop can be approximated by the average of the coil dimensions.

Cancellation of the far field is achieved by superposition of parallel opposing mul-

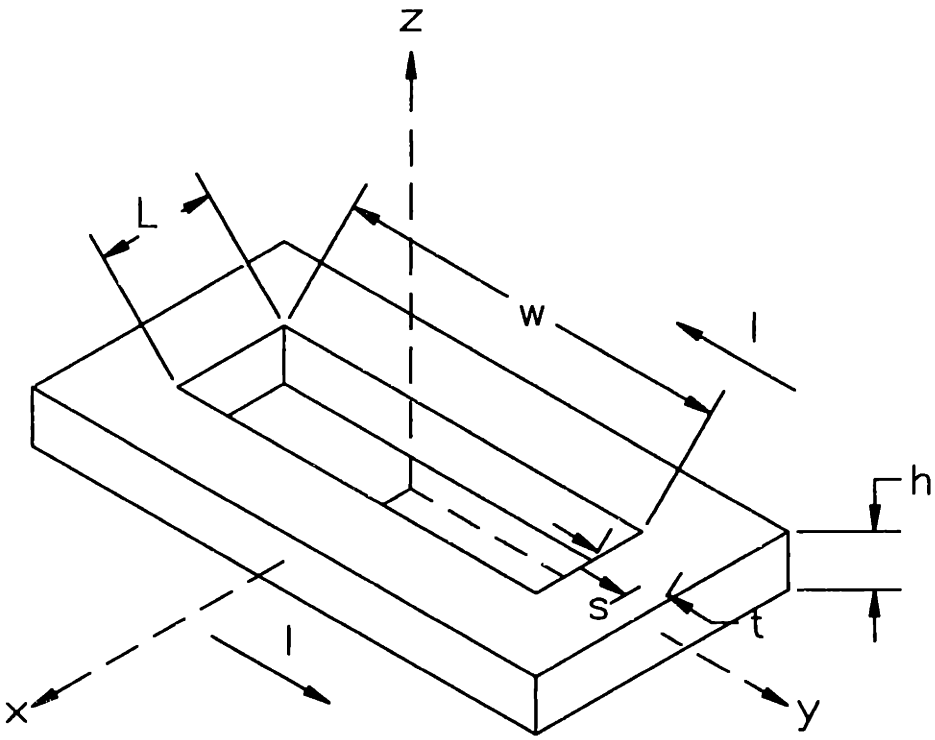

Figure 4-6: Coil of rectangular cross section and uniform current density $J = \frac{I}{th}$

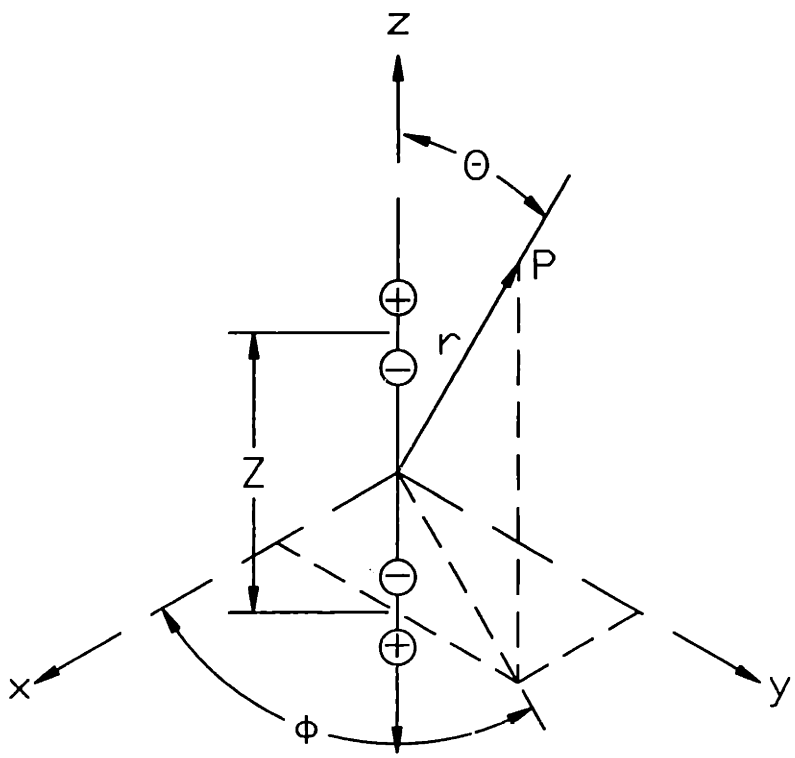

Figure 4-7: A multipole with Φ independent of ϕ

tipoles, which for this section follows the geometry shown in Figure 4-7. If Φ is known to be independent of ϕ, I will assume that the field solution must obey a harmonic function of the form

$$\Phi = \sum C_i r^{p_i} \cos^{m_i}(\theta). \tag{4.50}$$

Here m_i and p_i are integer separation constants and C_i is a constant. This expression is an educated "guess" based on the required form of Laplacian solutions in spherical coordinates as given by Equation (4.19). The limits of the summation are taken from the expressions for the multipoles that are superposed.

The superposition requires writing the scalar potentials for the geometric requirements. For the upper multipole in Figure 4-7 the multipole moment is shown as positive and the geometric requirements are

$$r_{(+)} = \left(r^2 + \left(\frac{Z}{2}\right)^2 - rZ\cos(\theta)\right)^{\frac{1}{2}}, \quad \text{and} \tag{4.51}$$

$$cos(\theta_{(+)}) = \frac{r\cos(\theta) - \frac{Z}{2}}{r_{(+)}}. \tag{4.52}$$

For the lower multipole in Figure 4-7 the dipole moment is negative and the geometric requirements are

$$r_{(-)} = \left(r^2 + \left(\frac{Z}{2}\right)^2 + rZ\cos(\theta)\right)^{\frac{1}{2}}, \quad \text{and} \tag{4.53}$$

$$cos(\theta_{(-)}) = \frac{r\cos(\theta) + \frac{Z}{2}}{r_{(-)}}. \tag{4.54}$$

Now I apply these geometric requirements to the superposition of two opposing multipoles of the form of Equation (4.50). The exact superposition equation is given by

$$\Phi = \sum C_i \left[\left(r^2 + \left(\frac{Z}{2}\right)^2 - rZ\cos(\theta)\right)^{\frac{p_i - m_i}{2}} \left(r\cos(\theta) - \frac{Z}{2}\right)^{m_i} - \left(r^2 + \left(\frac{Z}{2}\right)^2 + rZ\cos(\theta)\right)^{\frac{p_i - m_i}{2}} \left(r\cos(\theta) + \frac{Z}{2}\right)^{m_i}\right]. \tag{4.55}$$

Since p_i is negative for any multipole in an open cavity (i.e. we cannot have a singularity at infinity) and m_i is assumed to be positive, I first bring the terms for the upper and lower multipoles over a common denominator. After binomial expansion and elimination of the high order terms for the assumption $r >> Z$, the far field solution reduces to

$$\Phi = \sum C_i r^{p_i - 1} Z \left((m_i - p_i) \cos^{m_i+1}(\theta) - m_i \cos^{m_i-1}(\theta) \right). \tag{4.56}$$

The solution for additional levels of cancellation may be calculated by applying Equation (4.56) recursively. A graphical representation of a multipole with three sub-multipoles is shown in Figure 4-8. The reader will understand that the charges in the multipoles may themselves contain sub-multipoles. The higher order multipoles are built by superposing parallel sub-multipoles that have opposite signs. The new moment arms are drawn from the center of the moment arms of the sub-multipoles. The coordinate system origin used to describe a multipole becomes the middle of the moment arm associated with the last superposition. For example, the origin is shown to be the middle of the moment arm Z_{i+2} in Figure 4-8.

In most cases, a magnetic field designer will be starting with dipoles as the building blocks. Therefore, it is convenient to tabulate the far field solution for multipoles that are built from dipoles. The solutions for up to eight superpositions[2] are shown in Equations (4.57) through (4.65). The separated $\Theta(\theta)$ from these equations are special cases of the generalized Legendre series. These terms are the Legendre functions $\mathcal{P}_p^q(\cos(\theta))$ and $\mathcal{Q}_p^q(\cos(\theta))$ with $q = 0$ that terminate as polynomials.

$$\Phi = C\frac{\cos(\theta)}{r^2} \quad \text{s=0} \tag{4.57}$$

$$\Phi = -CZ_1\frac{1}{r^3}\left(1 - 3\cos^2(\theta)\right) \quad \text{s=1} \tag{4.58}$$

$$\Phi = -9CZ_1Z_2\frac{1}{r^4}\left(\cos(\theta) - \frac{5}{3}\cos^3(\theta)\right) \quad \text{s=2} \tag{4.59}$$

[2]designated s

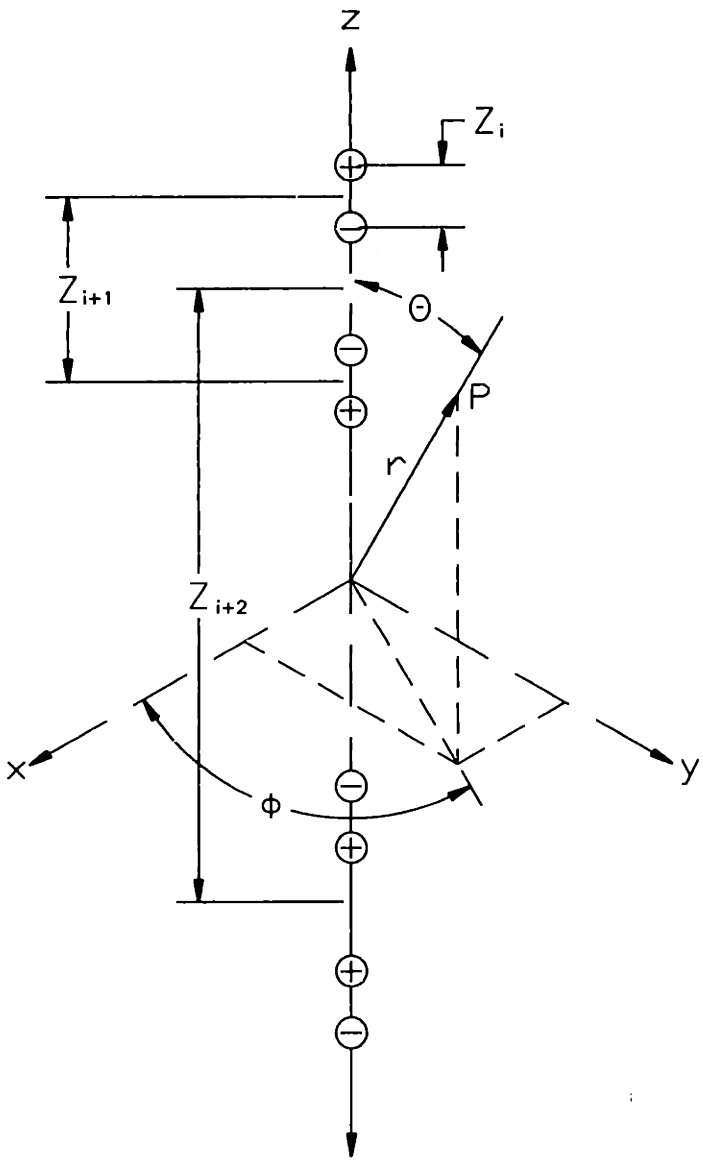

Figure 4-8: A multipole with three sub-multipoles depicted

$$\Phi = 9C\left(\prod_{i=1}^{3} Z_i\right)\frac{1}{r^5}\left(1 - 10\cos^2(\theta) + \frac{35}{3}\cos^4(\theta)\right) \quad \text{s=3} \quad (4.60)$$

$$\Phi = 225C\left(\prod_{i=1}^{4} Z_i\right)\frac{1}{r^6}\left(\cos(\theta) - \frac{14}{3}\cos^3(\theta) + \frac{21}{5}\cos^5(\theta)\right) \quad \text{s=4} \quad (4.61)$$

$$\Phi = -225C\left(\prod_{i=1}^{5} Z_i\right)\frac{1}{r^7}\left(1 - 21\cos^2(\theta) + 63\cos^4(\theta) - \frac{231}{5}\cos^6(\theta)\right) \quad \text{s=5} \quad (4.62)$$

$$\Phi = -11025C\left(\prod_{i=1}^{6} Z_i\right)\frac{1}{r^8}$$

$$\left(\cos(\theta) - 9\cos^3(\theta) + \frac{99}{5}\cos^5(\theta) - \frac{429}{35}\cos^7(\theta)\right) \quad \text{s=6} \quad (4.63)$$

$$\Phi = 11025C\left(\prod_{i=1}^{7} Z_i\right)\frac{1}{r^9}$$

$$\left(1 - 36\cos^2(\theta) + 198\cos^4(\theta) - \frac{1716}{5}\cos^6(\theta) + \frac{1287}{7}\cos^8(\theta)\right) \quad \text{s=7} \quad (4.64)$$

$$\Phi = 893025C\left(\prod_{i=1}^{8} Z_i\right)\frac{1}{r^{10}}$$

$$\left(\cos(\theta) - \frac{132}{9}\cos^3(\theta) + \frac{286}{5}\cos^5(\theta) - \frac{572}{7}\cos^7(\theta) + \frac{2431}{63}\cos^9(\theta)\right) \quad \text{s=8} \quad (4.65)$$

An exciting quality of these equations is that with each successive superposition, -1 is added to the exponent of r. Furthermore, if we manage C and Z_i in clever ways we achieve even faster falling fringing fields with each superposition. There will be more details about the design process in Chapter 5.

I have included the plots of the generalized Legendre polynomials in Figure 4-9 that correspond to Equations (4.57) through (4.65). Applying Equation 4.16 to these scalar potentials, I obtain the ratio of B_θ to B_r. Since the ratio of B_θ to B_r has no dependence on r, comparing $d(\Theta(\theta))/d\theta$ to $\Theta(\theta)(-s-2)$ reveals the relative magnitudes of the radial and tangential fields as a function of θ. This data is shown in Figures 4-10 and 4-11. It is interesting to note that the relative maximum magnitudes of B_r and B_θ do not vary widely – with the former ranging from 2 to 1.8 times the latter over this range of multipoles. Also, the relatively smaller magnitudes of the generalized Legendre polynomials of the first kind compared to the second kind tend to dampen the jump in multipole magnitude associated with the integer constants in front of Equations (4.57) through (4.65).

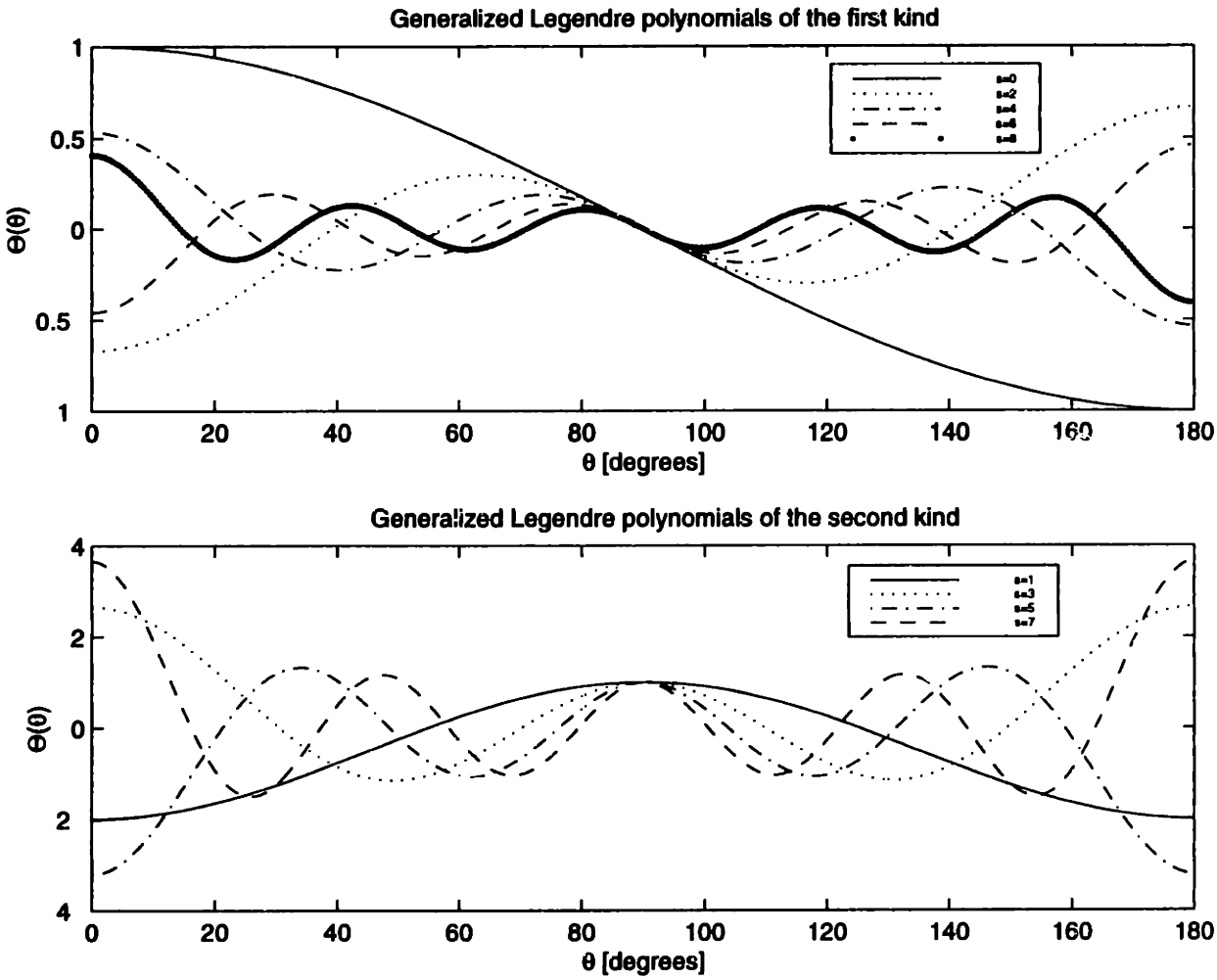

Figure 4-9: Generalized Legendre polynomials

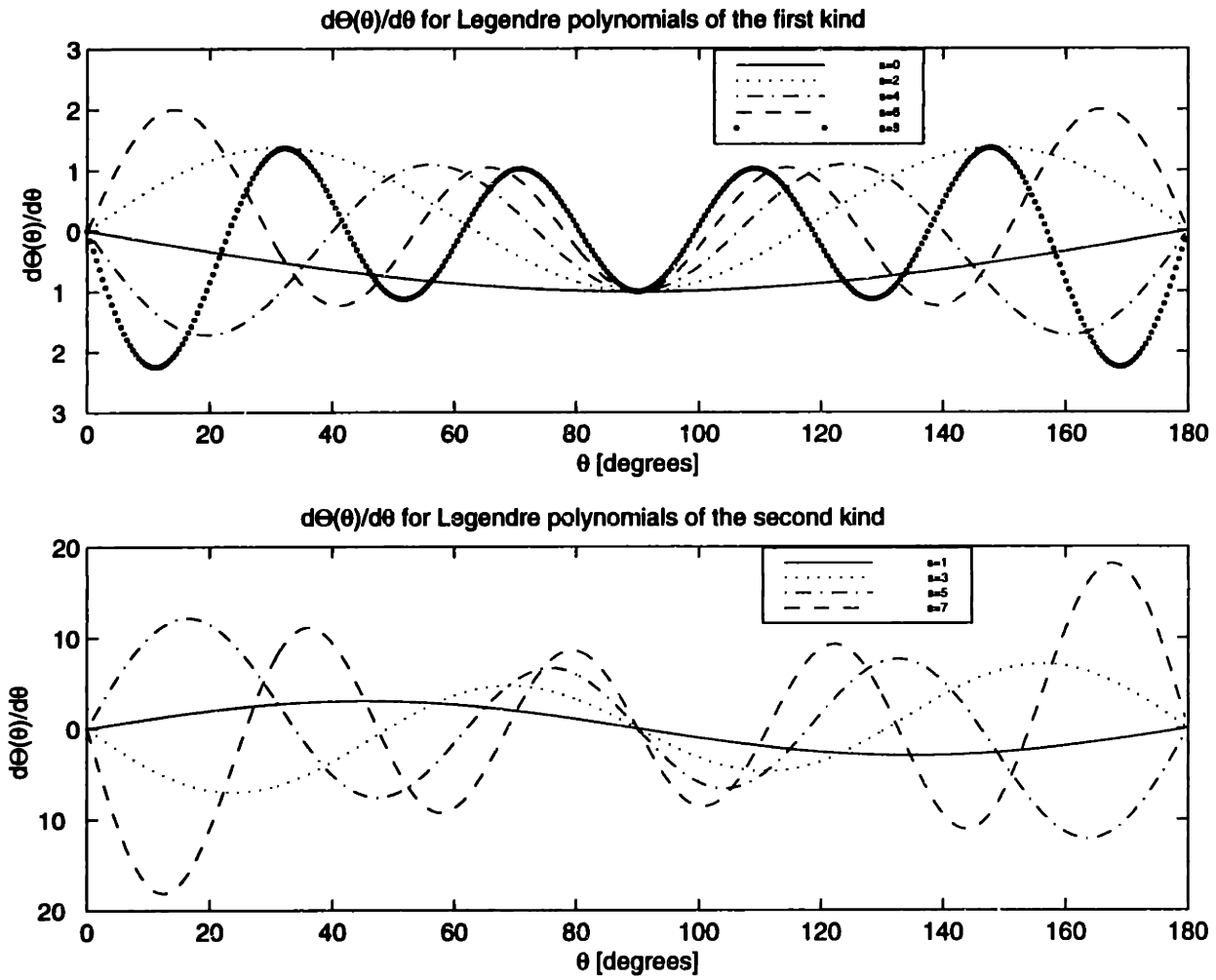

Figure 4-10: First derivative of the Legendre polynomials indicating relative B_θ magnitude

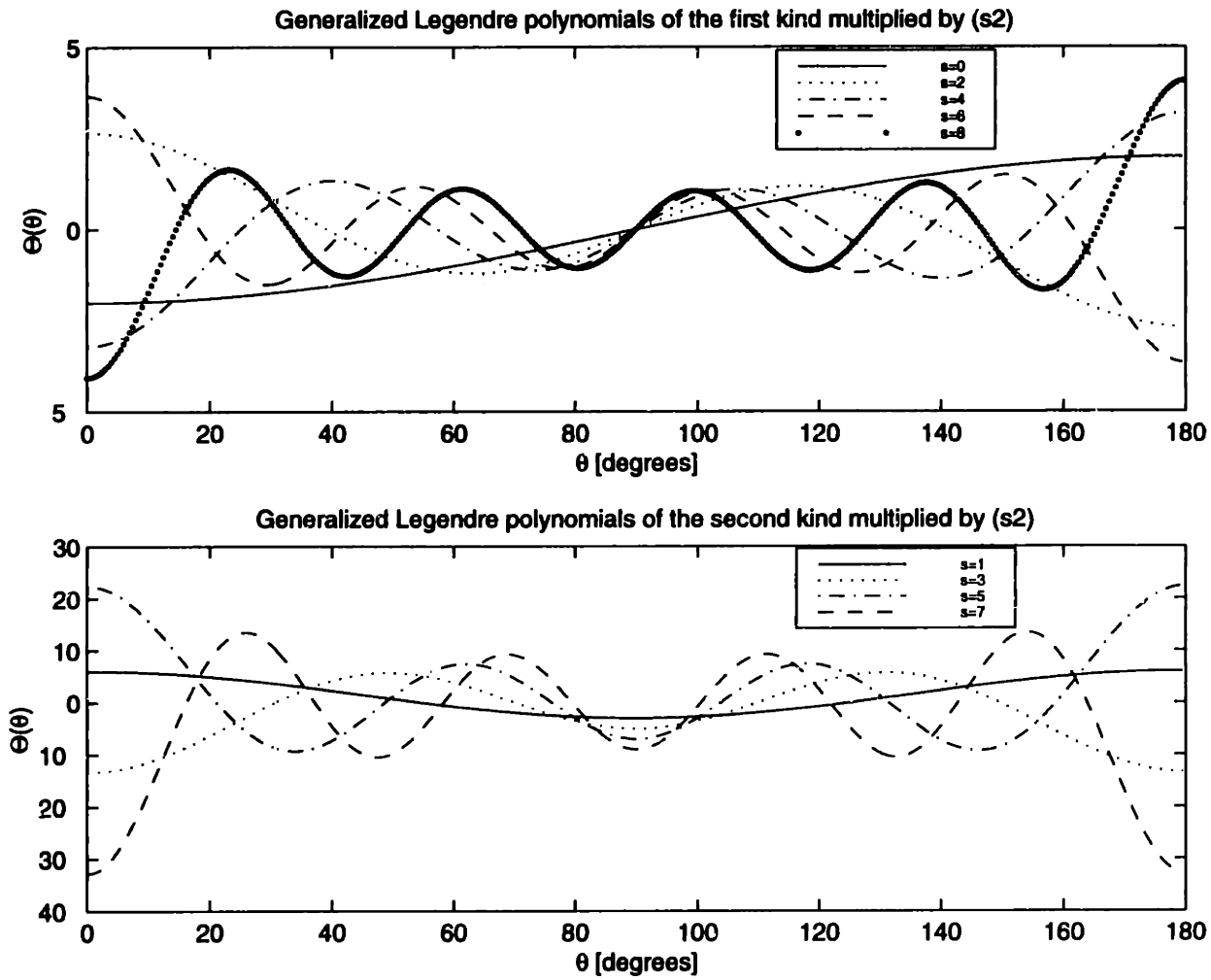

Figure 4-11: Generalized Legendre polynomials scaled by $(-s-2)$ to indicate the relative B_r magnitude

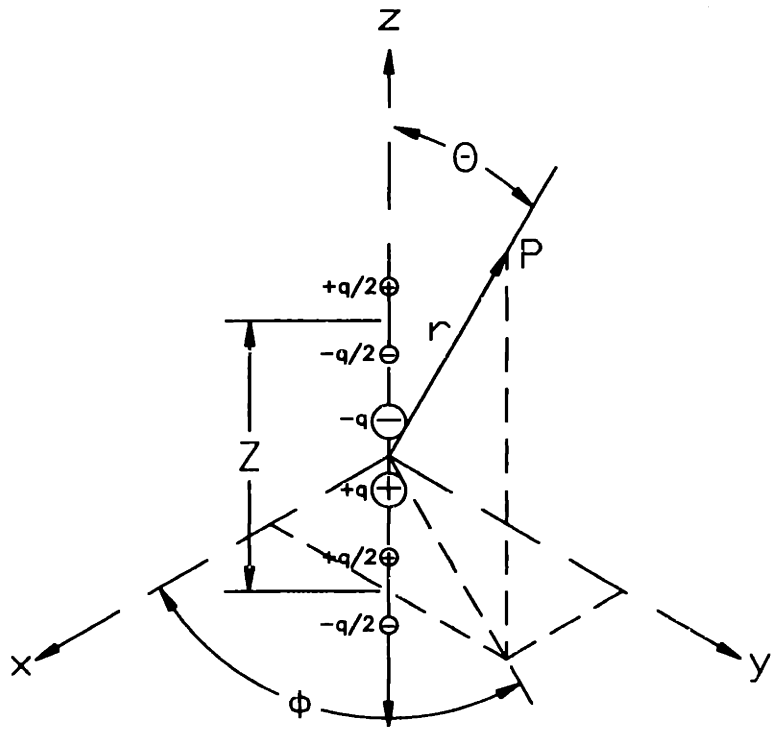

Figure 4-12: A multipole based on symmetric split placement. The scalar potential Φ is independent of the azimuthal coordinate ϕ.

In my effort to discover fast falling fringing fields, I will consider another field cancellation topology that takes advantage of symmetry. This topology is shown in Figure 4-12. In this technique, I exploit symmetry and place the centroid of the opposing multipoles on top of each other.

Again I assume that the field solution must obey a harmonic function of the form of Equation (4.50). If I superpose this solution according to the model in Figure 4-12, the far field solution reduces to

$$\Phi = \sum C_i r^{p_i-2} \frac{Z^2}{8} (m_i(m_i-1)\cos^{m_i-2}(\theta) + \cdots$$
$$(p_i - m_i)(1+2m_i)\cos^{m_i}(\theta) + (p_i - m_i)(p_i - m_i - 2)\cos^{m_i+2}(\theta)). \qquad (4.66)$$

This result can be derived by expanding the exact superposition equation and taking the far field limit. Or the easier way is to apply Equation (4.56) into itself. The $\frac{1}{8}$ factor arises because the underlying dipole moment contains a dipole charge of $\frac{q}{2}$ with a dipole moment arm of $\frac{Z}{2}$. Multiplying the charge and the square of the dipole

moment arm results in the $\frac{1}{8}$ factor. I include the first four superpositions, beginning with a dipole, in Equations (4.67) through (4.71). The first three superpositions, beginning with a quadrupole, are shown in Equations (4.72) through (4.75).

Because the symmetry provides higher order cancellation in this topology, a factor of -2 is added to exponent of r with each superposition. An obvious question comes to mind. Are there other cancellation topologies that can provide even higher order cancellation? Yes! In fact, perfect far-field cancellation occurs for two spherical shells of equal but opposite dipole moments but with coincident centroids. In practical situations, such as in planar stage design, this closed cavity topology is not an option. Nevertheless, the field designer can exploit symmetry to a great extent. For example, a topology that adds -3 to the exponent of r is shown in Figure 4-13. In this example, the multipoles are spaced evenly apart with the outer multipoles having 1/3 the magnitude of multipole moments of the inner multipoles. The building blocks are shown in the encircled groups on the right side of the figure. The multipole is created by three superpositions of submultipoles, which requires 2^3 of these submultipoles as shown in the figure. When the building blocks are aligned along an axis, as shown, and the submultipoles are dipoles then Equation (4.60), with three dipole superpositions, describes the multipole. The dipole moment C is given by $q/3 \times d$. The multipole moment arms Z_1, Z_2, and Z_3 are all equal.

$$\Phi = -C\frac{\cos(\theta)}{r^2} \quad \text{s=0} \quad (4.67)$$

$$\Phi = -\frac{9}{8}CZ_1^2\frac{1}{r^4}\left(\cos(\theta) - \frac{5}{3}\cos^3(\theta)\right) \quad \text{s=1} \quad (4.68)$$

$$\Phi = \frac{225}{64}C\left(\prod_{i=1}^{2} Z_i^2\right)\frac{1}{r^6}\left(\cos(\theta) - \frac{14}{3}\cos^3(\theta) + \frac{21}{5}\cos^5(\theta)\right) \quad \text{s=2} \quad (4.69)$$

$$\Phi = -\frac{11025}{512}C\left(\prod_{i=1}^{3} Z_i^2\right)\frac{1}{r^8}\cdots$$

$$\left(\cos(\theta) - 9\cos^3(\theta) + \frac{99}{5}\cos^5(\theta) - \frac{429}{35}\cos^7(\theta)\right) \quad \text{s=3} \quad (4.70)$$

$$\Phi = \frac{893025}{4096}C\left(\prod_{i=1}^{4} Z_i^2\right)\frac{1}{r^{10}}\cdots$$

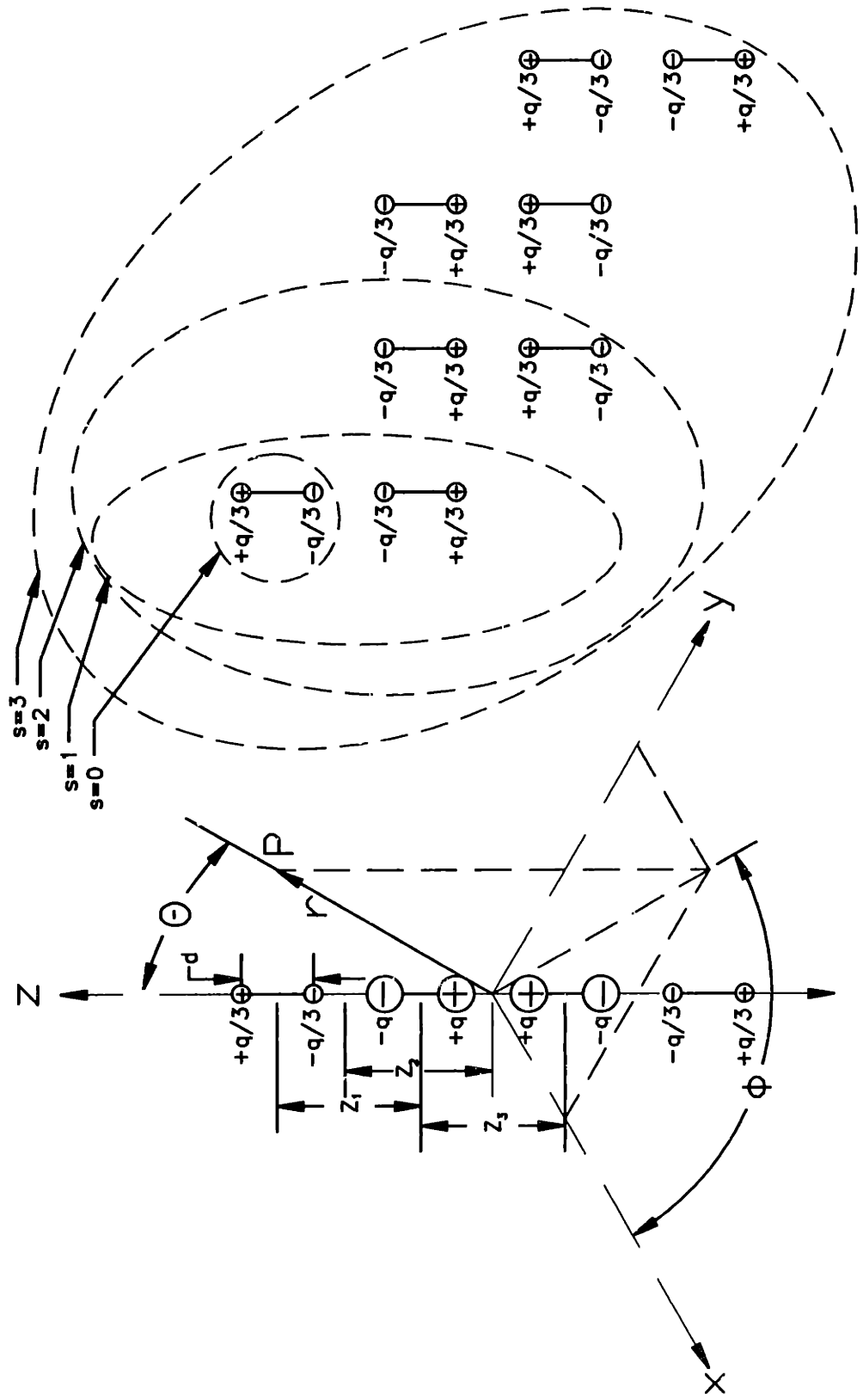

Figure 4-13: A multipole exploiting symmetry for higher order cancellation. Building blocks encircled on the right.

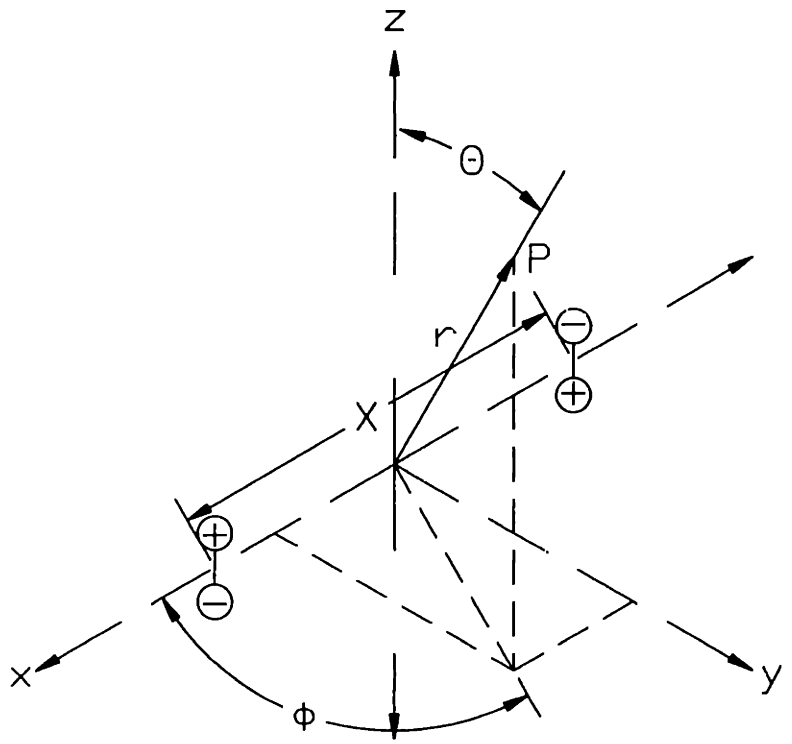

Figure 4-14: A multipole with Φ dependent on ϕ, submultipoles lying on x-axis.

$$\left(\cos(\theta) - \frac{132}{9}\cos^3(\theta) + \frac{286}{5}\cos^5(\theta) - \frac{572}{7}\cos^7(\theta) + \frac{2431}{63}\cos^9(\theta)\right) \quad \text{s=4} \quad (4.71)$$

$$\Phi = -C\frac{1}{r^3}\left(1 - 3\cos^2(\theta)\right) \quad \text{s=0} \quad (4.72)$$

$$\Phi = \frac{9}{8}CZ_1^2\frac{1}{r^5}\left(1 - 10\cos^2(\theta) + \frac{35}{3}\cos^4(\theta)\right) \quad \text{s=1} \quad (4.73)$$

$$\Phi = -\frac{225}{64}C\left(\prod_{i=1}^{2} Z_i^2\right)\frac{1}{r^7}\left(1 - 21\cos^2(\theta) + 63\cos^4(\theta) - \frac{231}{5}\cos^6(\theta)\right) \quad \text{s=2} \quad (4.74)$$

$$\Phi = \frac{11025}{512}C\left(\prod_{i=1}^{3} Z_i^2\right)\frac{1}{r^9}\cdots$$

$$\left(1 - 36\cos^2(\theta) + 198\cos^4(\theta) - \frac{1716}{5}\cos^6(\theta) + \frac{1287}{7}\cos^8(\theta)\right) \quad \text{s=3} \quad (4.75)$$

4.4 Far field solutions for three dimensional multipoles with ϕ dependence

In this section, I consider the three dimensional solution for multipoles with ϕ dependence. The basic topology is shown in Figure 4-14 where the submultipoles lie along the x-axis.

I will assume that the field solution must obey a harmonic function of the form

$$\Phi = \sum C_i r^{p_i} \cos^{m_i}(\theta) \sin^{n_i}(\theta) \cos^{q_i}(\phi). \tag{4.76}$$

Here p_i, m_i, n_i, and q_i are integer separation constants and C_i is a constant. This form is an educated "guess," that was motivated by the geometry and the requirement for analytic functions.

The superposition requires writing the scalar potentials for the specified geometry in Figure 4-14, where the submultipoles are assumed to lie along the x-axis. For the multipole on the positive side of the x-axis, the multipole moment is positive and the geometric requirements are

$$r_{(+)} = \left(r^2 + \left(\frac{X}{2}\right)^2 - rX\sin(\theta)\cos(\phi)\right)^{\frac{1}{2}}, \tag{4.77}$$

$$\cos(\theta_{(+)}) = \frac{r\cos(\theta)}{r_{(+)}}, \tag{4.78}$$

$$\sin(\theta_{(+)}) = \frac{\left(r^2\sin^2(\theta) + \left(\frac{X}{2}\right)^2 - rX\sin(\theta)\cos(\phi)\right)^{\frac{1}{2}}}{r_{(+)}}, \quad \text{and} \tag{4.79}$$

$$\cos(\phi_{(+)}) = \frac{r\sin(\theta)\cos(\phi) - \frac{X}{2}}{r_{(+)}\sin(\theta_{(+)})}. \tag{4.80}$$

For the multipole on the negative side of the x-axis, the multipole moment is negative and the geometric requirements are

$$r_{(-)} = \left(r^2 + \left(\frac{X}{2}\right)^2 + rX\sin(\theta)\cos(\phi)\right)^{\frac{1}{2}}, \tag{4.81}$$

$$\cos(\theta_{(-)}) = \frac{r\cos(\theta)}{r_{(-)}}, \tag{4.82}$$

$$\sin(\theta_{(-)}) = \frac{\left(r^2\sin^2(\theta) + \left(\frac{X}{2}\right)^2 + Xr\sin(\theta)\cos(\phi)\right)^{\frac{1}{2}}}{r_{(-)}}, \quad \text{and} \tag{4.83}$$

$$\cos(\phi_{(-)}) = \frac{r\sin(\theta)\cos(\phi) + \frac{X}{2}}{r_{(-)}\sin(\theta_{(-)})}. \tag{4.84}$$

The exact superposition equation is obtained by applying these geometric requirements to Equation 4.76 and is given by

$$\Phi = \sum C_i \left[\left(r^2 + \left(\frac{X}{2}\right)^2 - rX\sin(\theta)\cos(\phi)\right)^{\frac{p_i-n_i}{2}} (r\cos(\theta))^{m_i}\right.$$
$$\left(r^2\sin^2(\theta) + \left(\frac{X}{2}\right)^2 - Xr\sin(\theta)\cos(\phi)\right)^{\frac{n_i-q_i}{2}} \left(r\sin(\theta)\cos(\phi) - \frac{X}{2}\right)^{q_i} -$$
$$\left(r^2 + \left(\frac{X}{2}\right)^2 + rX\sin(\theta)\cos(\phi)\right)^{\frac{p_i-n_i}{2}} (r\cos(\theta))^{m_i}$$
$$\left.\left(r^2\sin^2(\theta) + \left(\frac{X}{2}\right)^2 + Xr\sin(\theta)\cos(\phi)\right)^{\frac{n_i-q_i}{2}} \left(r\sin(\theta)\cos(\phi) + \frac{X}{2}\right)^{q_i}\right]. \tag{4.85}$$

After manipulating the terms to be over a common denominator, I perform binomial expansion. Then the far field limit reduces to

$$\Phi = -\sum C_i r^{p_i-1} X_i \cos^{m_i}(\theta) \left[q\sin^{n_i-1}(\theta)\cos^{q_i-1}(\phi) + \right.$$
$$\left.(p_i - m_i - n_i)\sin^{n_i+1}(\theta)\cos^{q_i+1}(\phi) + (n_i - q_i)\sin^{n_i-1}(\theta)\cos^{q_i+1}(\phi)\right]. \tag{4.86}$$

The solutions for up to eight superpositions are shown in Equations (4.87) through (4.95). I begin with dipole building blocks and recursively apply Equation (4.86).

$$\Phi = C\frac{\cos(\theta)}{r^2} \quad \text{s=0} \tag{4.87}$$

$$\Phi = 3CX_1\frac{1}{r^3}\cos(\theta)\sin(\theta)\cos(\phi) \quad \text{s=1} \tag{4.88}$$

$$\Phi = -3C\left(\prod_{i=1}^{2} X_i\right)\frac{1}{r^4}\left(\cos(\theta) - 5\cos(\theta)\sin^2(\theta)\cos^2(\phi)\right) \quad \text{s=2} \tag{4.89}$$

$$\Phi = -45C\left(\prod_{i=1}^{3} X_i\right)\frac{1}{r^5}$$
$$\left(\cos(\theta)\sin(\theta)\cos(\phi) - 7/3\,\cos(\theta)\sin^3(\theta)\cos^3(\phi)\right) \quad \text{s=3} \tag{4.90}$$
$$\Phi = 45C\left(\prod_{i=1}^{4} X_i\right)\frac{1}{r^6}$$
$$\left(\cos(\theta) - 14\,\cos(\theta)\sin^2(\theta)\cos^2(\phi) + 21\,\cos(\theta)\sin^4(\theta)\cos^4(\phi)\right) \quad \text{s=4} \tag{4.91}$$
$$\Phi = 1575C\left(\prod_{i=1}^{5} X_i\right)\frac{1}{r^7}$$
$$\left(\cos(\theta)\sin(\theta)\cos(\phi) - 6\,\cos(\theta)\sin^3(\theta)\cos^3(\phi) + \frac{33}{5}\,\cos(\theta)\sin^5(\theta)\cos^5(\phi)\right) \quad \text{s=5} \tag{4.92}$$
$$\Phi = -1575C\left(\prod_{i=1}^{6} X_i\right)\frac{1}{r^8}$$
$$\left(\cos(\theta) - 27\,\cos(\theta)\sin^2(\theta)\cos^2(\phi) + 99\,\cos(\theta)\sin^4(\theta)\cos^4(\phi) - \frac{429}{5}\,\cos(\theta)\sin^6(\theta)\cos^6(\phi)\right) \quad \text{s=6} \tag{4.93}$$
$$\Phi = -99225C\left(\prod_{i=1}^{7} X_i\right)\frac{1}{r^9}$$
$$\left(\cos(\theta)\sin(\theta)\cos(\phi) - 11\,\cos(\theta)\sin^3(\theta)\cos^3(\phi) + \frac{143}{5}\,\cos(\theta)\sin^5(\theta)\cos^5(\phi) - \frac{143}{7}\,\cos(\theta)\sin^7(\theta)\cos^7(\phi)\right) \quad \text{s=7} \tag{4.94}$$
$$\Phi = 99225C\left(\prod_{i=1}^{8} X_i\right)\frac{1}{r^{10}}$$
$$\left(\cos(\theta) - 44\,\cos(\theta)\sin^2(\theta)\cos^2(\phi) + 286\,\cos(\theta)\sin^4(\theta)\cos^4(\phi) - 572\,\cos(\theta)\sin^6(\theta)\cos^6(\phi) + \frac{2431}{7}\,\cos(\theta)\sin^8(\theta)\cos^8(\phi)\right) \quad \text{s=8} \tag{4.95}$$

Note that I have introduced $\sin(\theta)$ into the solution, although the traditional form of the generalized Legendre functions, $\mathcal{P}_p^q$ and $\mathcal{Q}_p^q$, are functions of $\cos(\theta)$. The traditional form is derived from the Legendre wave equation (page 201 of [26]), which is given by

$$(z^2-1)\frac{d^2Z}{dz^2} + 2z\frac{dZ}{dz} + \left(\chi^2 a^2(z^2-1) - p(p+1) - \frac{q^2}{z^2-1}\right)Z = 0. \tag{4.96}$$

Here $Z(z)$ is the solution to the Legendre wave equation and χ, a, p, and q are

separation constants. Meanwhile the differential equation for $\Theta(\theta)$ obtained from solving Laplace's equation by separation of variables in spherical coordinates is given by

$$\frac{d^2\Theta}{d\theta^2} + cot(\theta)\frac{d\Theta}{d\theta} + \left(p(p+1) - \frac{q^2}{sin^2(\theta)}\right)\Theta = 0. \tag{4.97}$$

Equation (4.97) is the form of the Legendre wave equation where χa=0 and $z = \cos(\theta)$. Since the traditional solutions to the Legendre wave equation that one might find in a field theory handbook such as [26] are in terms of the variable z, the traditional solutions of Equation (4.97) will be in terms of $\cos(\theta)$. In my solutions, if $\sin(\theta)$ is written as the binomial expansion of $\sqrt{1-\cos^2(\theta)}$ and $\Phi(\phi)$ is separated, the solutions become the traditional form. By introducing $\sin(\theta)$, however, I am able to write the solutions as polynomials instead of infinite series. Another motivation for introducing $\sin(\theta)$ is the derivation of my solutions by the far field limit method was less laborious.

For the sake of comparison, the results found in [26] on pages 201-202 for the generalized Legendre functions where χa=0 are given by

$$\mathcal{P}_p^q(z) = z\sum_{m=0}^{\infty}\frac{(-1)^m\Delta_m'(1)z^{2m}}{(2m+1)!} \quad \text{and} \tag{4.98}$$

$$\mathcal{Q}_p^q(z) = \sum_{m=0}^{\infty}\frac{(-1)^m\Delta_m'(0)z^{2m}}{(2m)!} \tag{4.99}$$

where $\Delta_m'(1)$ and $\Delta_m'(0)$ are given by the determinants

$$\Delta_m'(1) = \begin{vmatrix} B_2-2 & 2\cdot 3 & 0 & 0 & \cdots & 0 \\ B_4-2 & B_2-6 & 4\cdot 5 & 0 & \cdots & 0 \\ B_6-2 & B_4-6 & B_2-10 & 6\cdot 7 & \cdots & 0 \\ \cdots & \cdots & \cdots & \cdots & \cdots & \cdots \\ B_{2m-2}-2 & B_{2m-4}-6 & B_{2m-6}-10 & \cdots & \cdots & (2m-2)(2m-1) \\ B_{2m}-2 & B_{2m-2}-6 & B_{2m-4}-10 & \cdots & \cdots & B_2-4m+2 \end{vmatrix} \tag{4.100}$$

and

$$\Delta_m'(0) = \begin{vmatrix} B_2 & 1\cdot 2 & 0 & 0 & \cdots & 0 \\ B_4 & B_2-4 & 3\cdot 4 & 0 & \cdots & 0 \\ B_6 & B_4-4 & B_2-8 & 5\cdot 6 & \cdots & 0 \\ \cdots & \cdots & \cdots & \cdots & \cdots & \cdots \\ B_{2m-2} & B_{2m-4}-4 & B_{2m-6}-8 & \cdots & \cdots & (2m-3)(2m-2) \\ B_{2m} & B_{2m-2}-4 & B_{2m-4}-8 & \cdots & \cdots & B_2-4m+4 \end{vmatrix} \quad (4.101)$$

where

$$B_{2l} = p(p+1) - lq^2. \quad (4.102)$$

For $z = \cos(\theta)$ and Φ independent of ϕ (or we could identically say $q = 0$) these expressions for the generalized Legendre functions are identical to $\Theta(\theta)$ found in Equations (4.57) through (4.65). The series expansion of the generalized Legendre functions where $q = 0$ takes the form

$$\mathcal{P}_p^0(z) = z\left\{1 - \frac{z^2}{3!}[p(p+1) - 1\cdot 2] + \frac{z^4}{5!}[p(p+1) - 1\cdot 2][p(p+1) - 3\cdot 4]\right.$$
$$\left. -\frac{z^6}{7!}[p(p+1) - 1\cdot 2][p(p+1) - 3\cdot 4][p(p+1) - 5\cdot 6] + \cdots\right\} \quad \text{and} \quad (4.103)$$

$$\mathcal{Q}_p^0(z) = \left\{1 - \frac{z^2}{2!}p(p+1) + \frac{z^4}{4!}p(p+1)[p(p+1) - 2\cdot 3]\right.$$
$$\left. -\frac{z^6}{6!}p(p+1)[p(p+1) - 2\cdot 3][p(p+1) - 4\cdot 5] + \cdots\right\}. \quad (4.104)$$

When q does not equal zero, the scalar potentials are dependent on ϕ and the series expansion of the generalized Legendre functions take the form

$$\mathcal{P}_p^q(z) = z\left\{1 - \frac{z^2}{3!}[p(p+1) - q^2 - 2]\right.$$
$$\left. +\frac{z^4}{5!}[p(p+1)[p(p+1) - 2q^2 - 14] + q^4 + 20q^2 + 24] - \cdots\right\} \quad \text{and} \quad (4.105)$$

$$\mathcal{Q}_p^q(z) = \left\{1 - \frac{z^2}{2!}[p(p+1) - q^2]\right.$$

$$+\frac{z^4}{4!}[p(p+1)[p(p+1)-2q^2-6]+q^4+8q^2]-\cdots\Big\}. \qquad (4.106)$$

Though it is more difficult to prove, the expressions for the generalized Legendre functions also describe the $\Theta(\theta)$ given in Equations (4.87) through (4.95). The proof is more difficult because the equations must be rewritten as infinite series of separated functions $R(r)$, $\Phi(\phi)$, and $\Theta(\theta)$. More importantly, the general solution to Laplace's equation corresponds to my solutions achieved through superposition of homogeneous solutions and taking the far field limit. My solutions go a step further by also correctly specifying the magnitude of the constants C_i associated with Equations (4.20) through (4.22) when given the dipole moment of the underlying dipoles. Also, my solution technique explicitly describes field cancellation by superposition of multipoles, which is not obvious from purely mathematical approaches for solving the differential equations obtained from separation of variables.

The plots of the functions that I designate $\Phi(\theta,\phi)$ are shown in Figures 4-15 through 4-23. Here $\Phi(\theta,\phi)$ are defined as the unitless functions of θ and ϕ taken from Equations (4.87) through (4.95) but exclude C, the integer constant in front of the equations, the product of the multipole moment arms, and the term r. The contour plot that is shown in the plane of the upper three dimensional figure is repeated in the lower plot for clarity. Although the functions are plotted for only the first quadrant of the $\theta-\phi$ surface, this data is representative of the entire surface. For even s, the $\Phi(\theta,\phi)$ dependence on θ and ϕ is even, with the ϕ dependence also being π periodic. For odd s, the dependence on θ is odd and the dependence on ϕ is even.

It is interesting to compare the field magnitudes of multipoles that are dependent and independent of ϕ. The normalized field magnitudes are obtained by solving for the fields derived from the scalar potentials and Equation (4.16). The fields are normalized with respect to C, the r dependence, and the product of the multipole moment arms. Similarly, the normalized functions are obtained by setting C, r, and the product of the multipole moment arms equal to one. Explicitly, the normalized

field magnitude for multipoles independent of ϕ is given by

$$\text{Normalized } H = -\nabla\Phi \frac{r^{s+3}}{C\left(\prod_{i=1}^{s} Z_i\right)}. \tag{4.107}$$

For multipoles dependent on ϕ, the normalized field magnitudes are calculated in the same way but, for consistency with my prior nomenclature, X substitutes for Z.

Figure 4-24 shows interesting relationships between the maximum magnitude of the radial and tangential components for the multipoles. Here Normalized $H_{tangential} = \sqrt{(\text{Normalized } H_\theta)^2 + (\text{Normalized } H_\phi)^2}$. I found the maximum magnitudes by calculating the normalized fields over the same surface grid used to calculate the scalar potentials shown in Figures 4-15 through 4-23. After taking the absolute value, I took the maximum value in the array.

The upper plot in Figure 4-24 shows that the normalized fields rise with respect to the number of superpositions. For the higher order multipoles in this range, the rise is approximately a decade per superposition. The fact that the normalized fields rise with each superposition does not necessarily mean that the actual fields will rise at the far field distance of interest. These normalized fields do not reflect the possible reduction in magnitude of the underlying dipole moment nor the typically small ratio of the underlying multipole moment arm in comparison to the radial distance of interest. Similarly, field cancellation schemes that lead to attenuation reduce the magnitude of the underlying dipole moment and include multipole moment arms that are small compared to the distance to the far field region of interest. Field cancellation techniques are further developed in Chapter 5. The lower plot highlights some important relationships. For multipoles independent of ϕ, the maximum radial fields range from 2 to 1.8 times the maximum tangential fields, whereas for multipoles dependent on ϕ, the ratio of radial to tangential fields ranges from 2 to 1.3. The radial and tangential fields are slightly larger for multipoles independent of ϕ. The maximum radial fields are up to 1.6 times larger and the tangential fields are up to 1.2 times larger for the multipoles independent of ϕ. As a designer, it is important to recognize that the difference between the maximum field magnitudes for multipoles independent

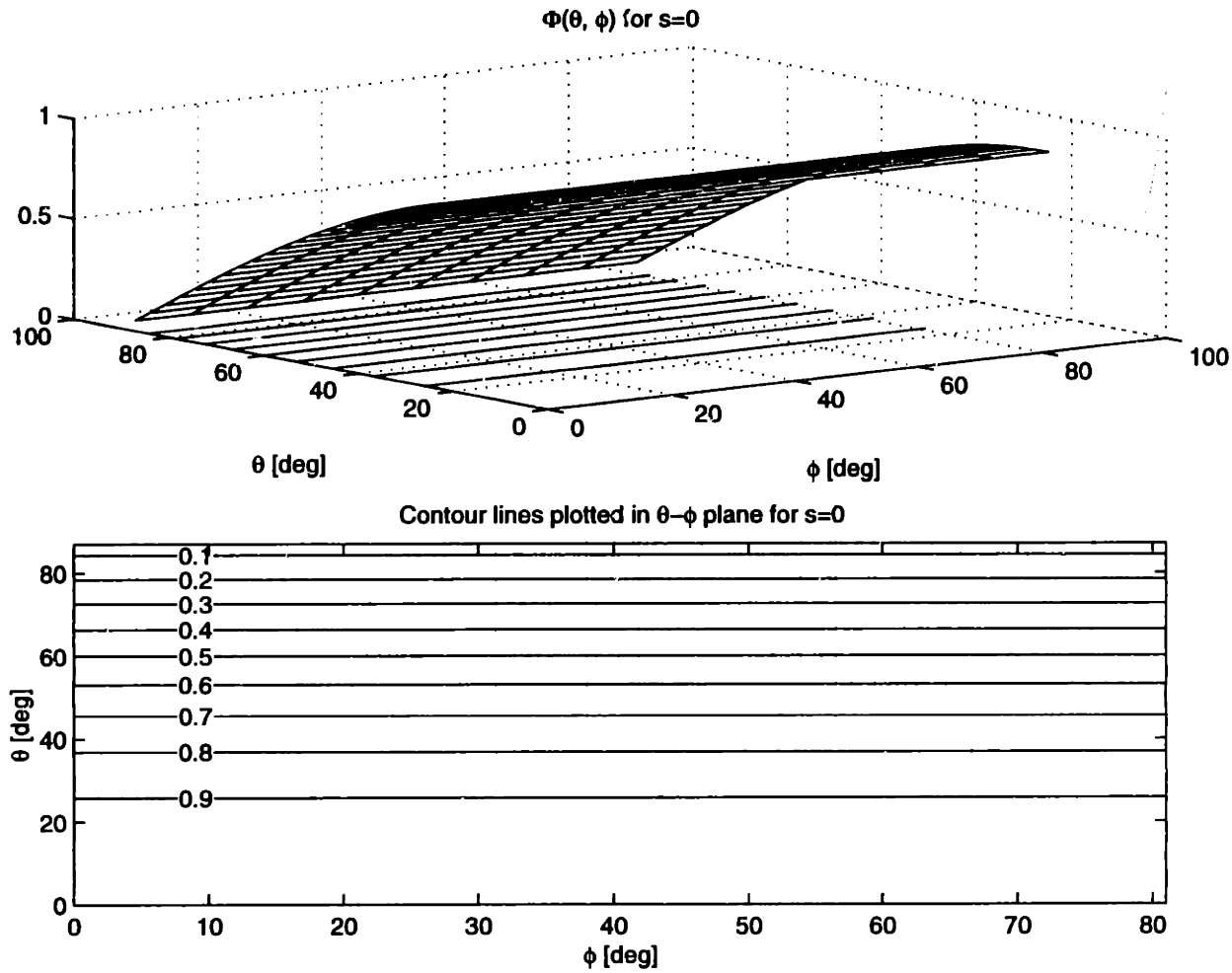

Figure 4-15: Dependence of Laplacian solution on θ and ϕ for s=0

and dependent of ϕ is not appreciable. When the design calls for large attenuation, efforts should concentrate on reducing C and the product of the multipole moment arms rather than weighing the performance trade-off of ϕ dependence.

Just as in the previous section, symmetry conditions can be exploited. The basic topology is shown in Figure 4-25. Again I will assume that the field solution must obey a harmonic function of the form of Equation (4.76). This time, however, I simplify the superposition by recognizing that for the solutions of interest $n_i = q_i$ and drop the terms with coefficients $n_i - q_i$. This turns out to be a requirement of the field solutions built from superposed dipoles and can be seen by examining Equation (4.86). If I superpose this solution according to the model in Figure 4-25, the far field solution is found by applying Equation (4.86) into itself. The far field solution

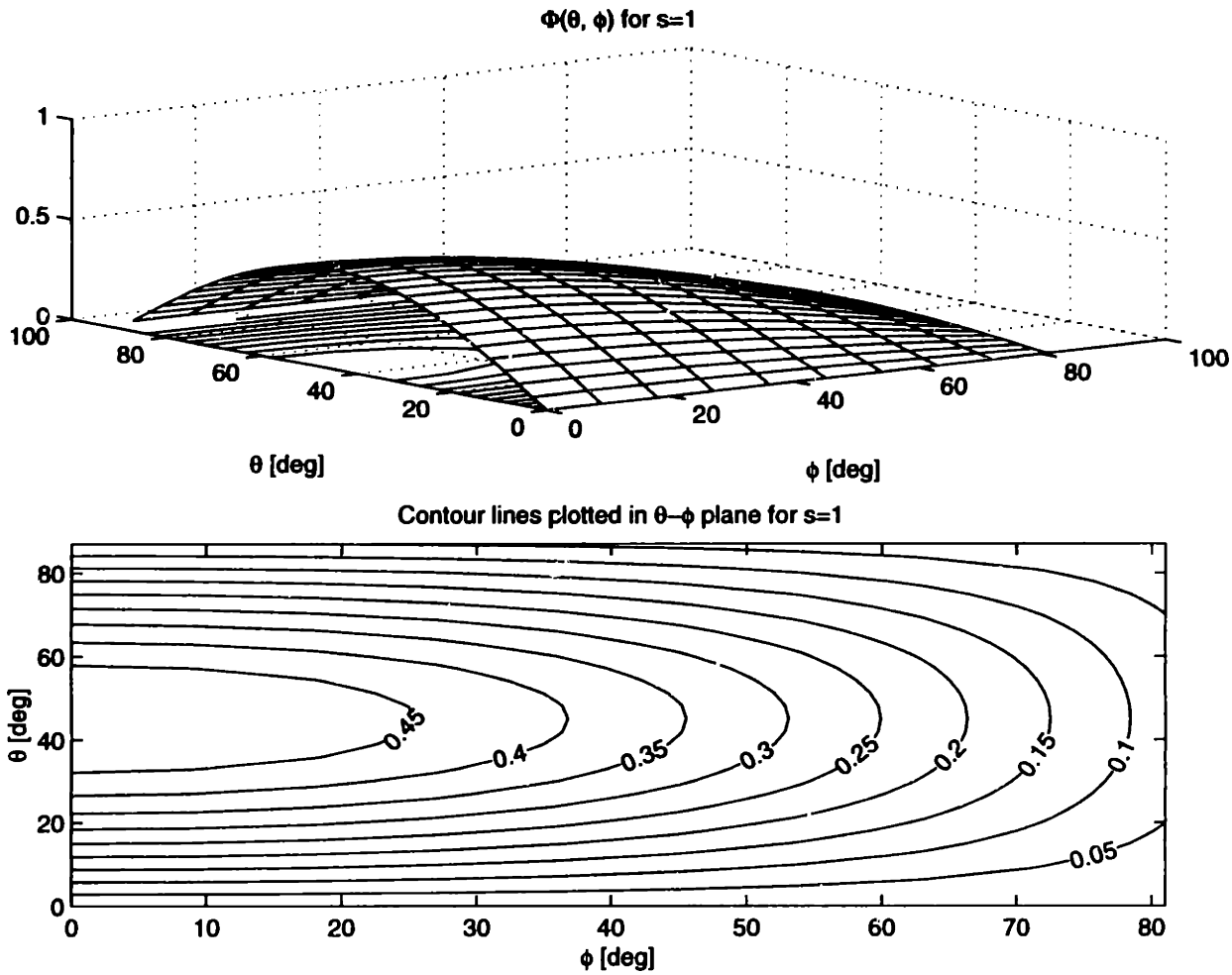

Figure 4-16: Dependence of Laplacian solution on θ and ϕ for s=1

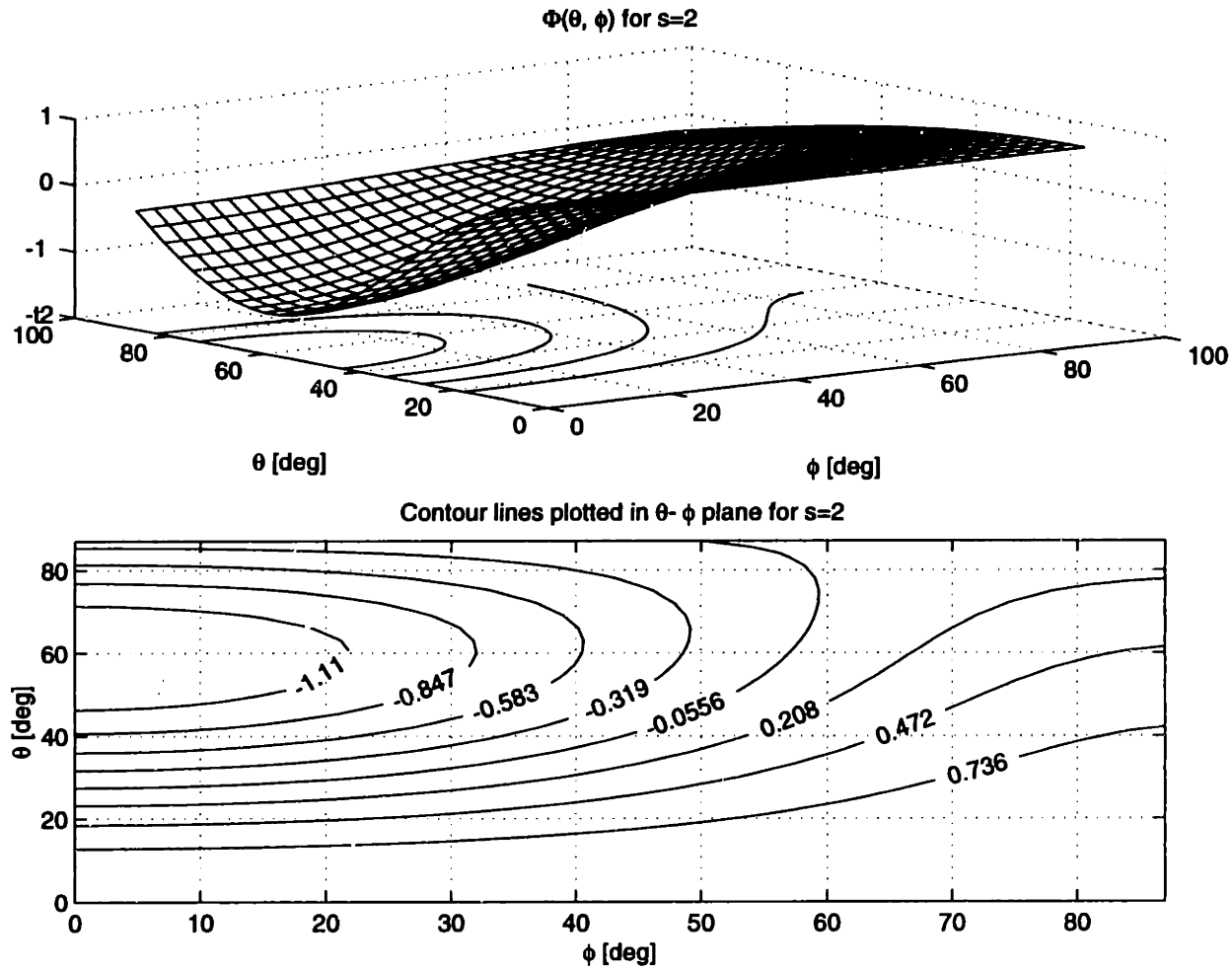

Figure 4-17: Dependence of Laplacian solution on θ and ϕ for s=2

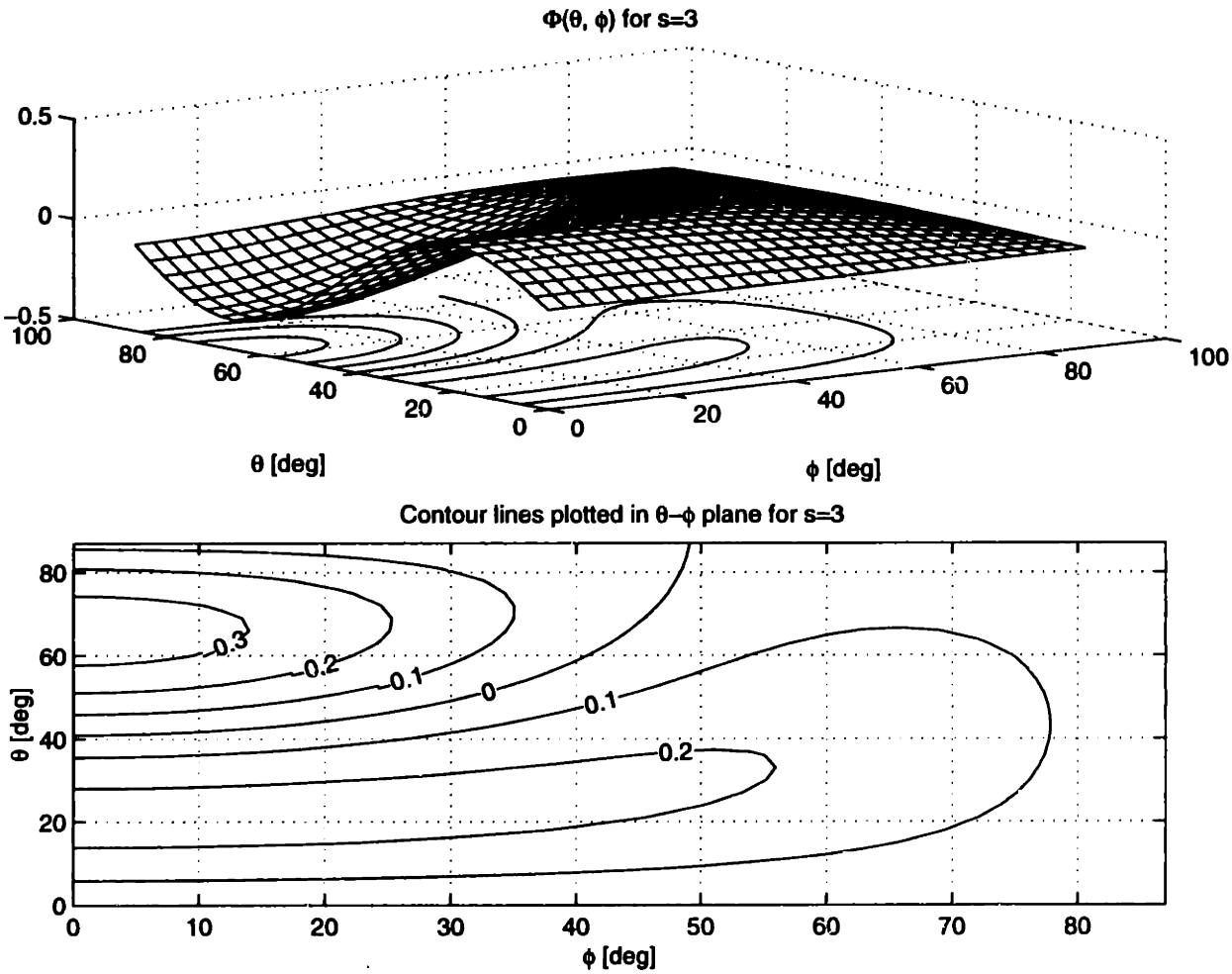

Figure 4-18: Dependence of Laplacian solution on θ and ϕ for s=3

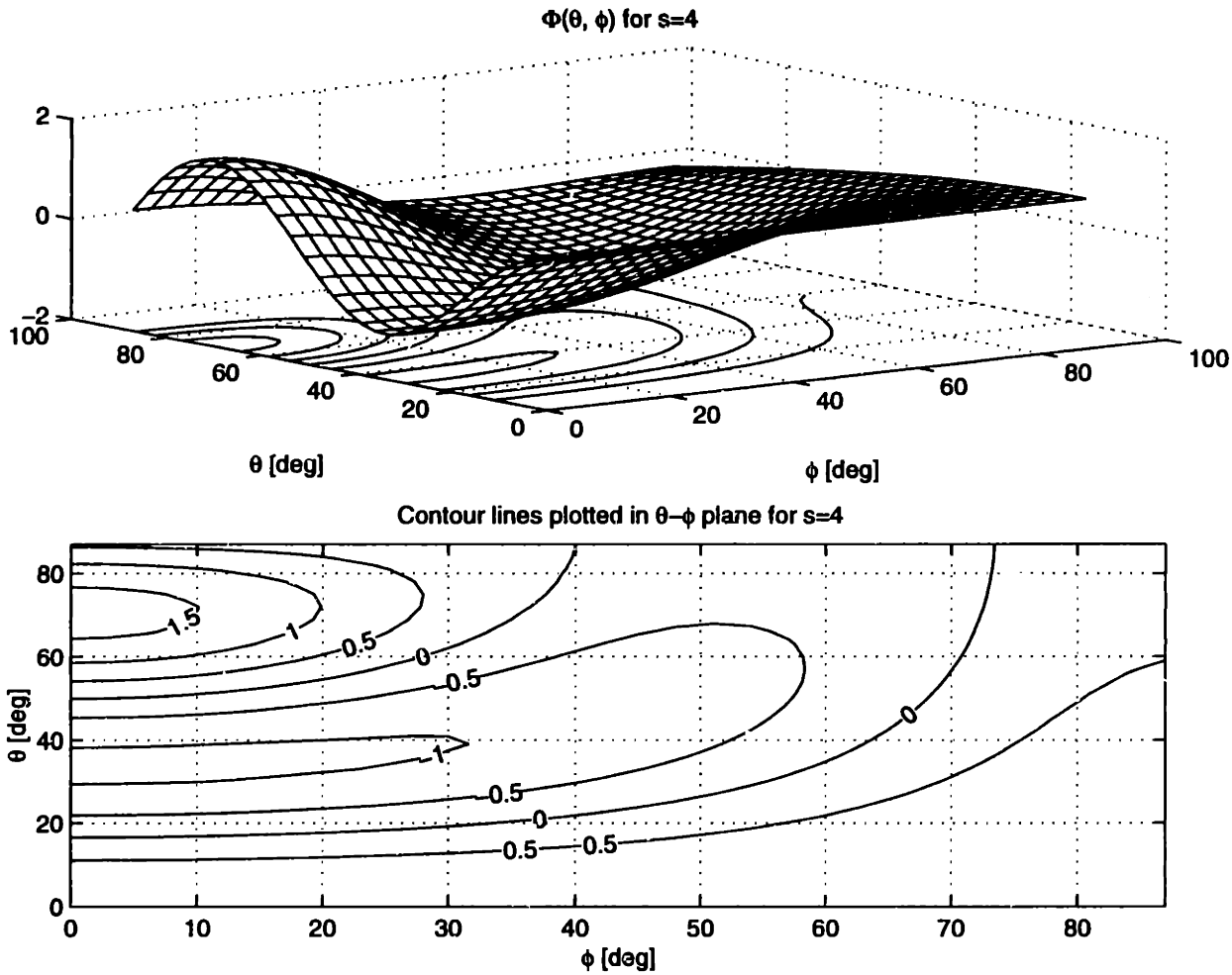

Figure 4-19: Dependence of Laplacian solution on θ and ϕ for s=4

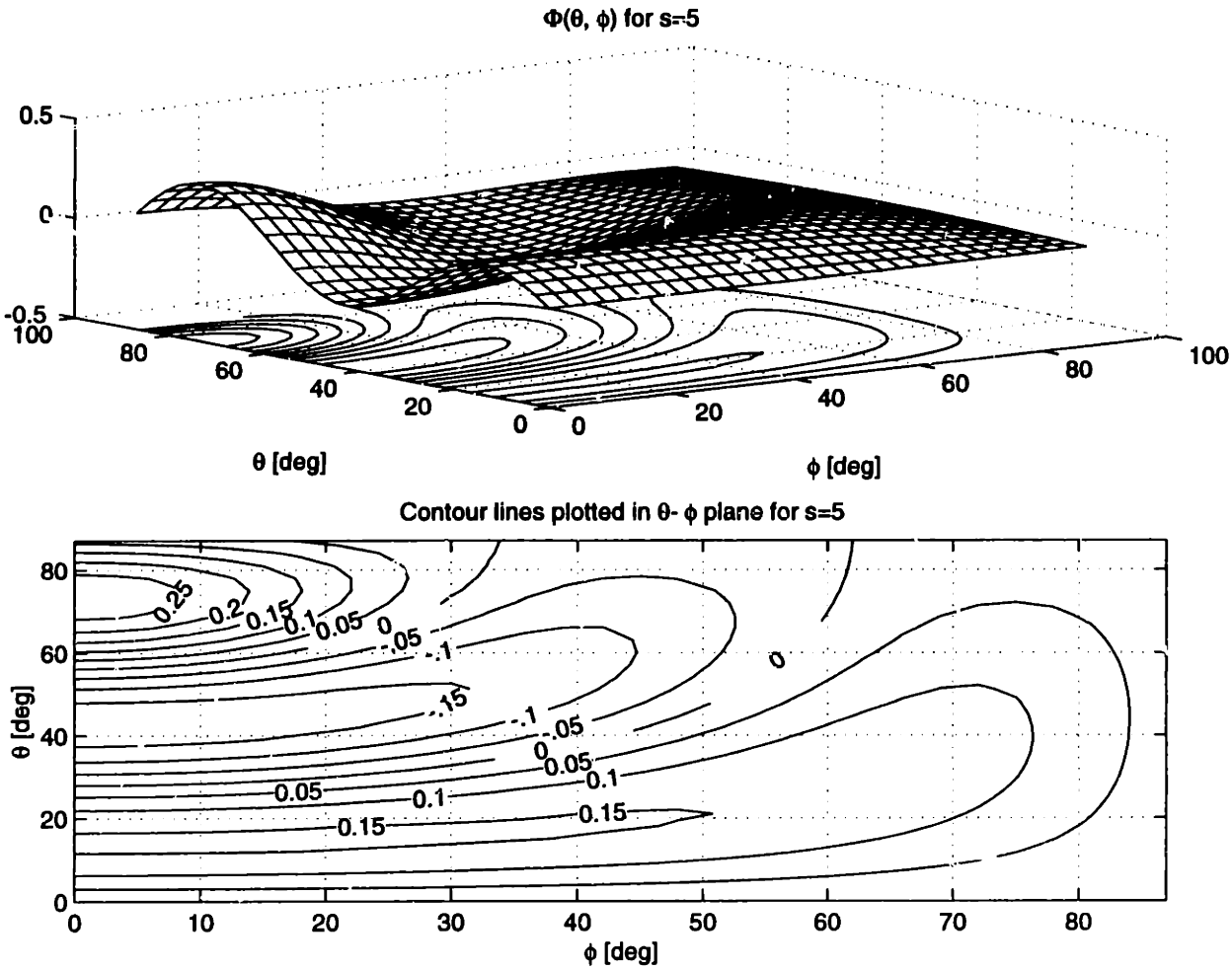

Figure 4-20: Dependence of Laplacian solution on θ and ϕ for s=5

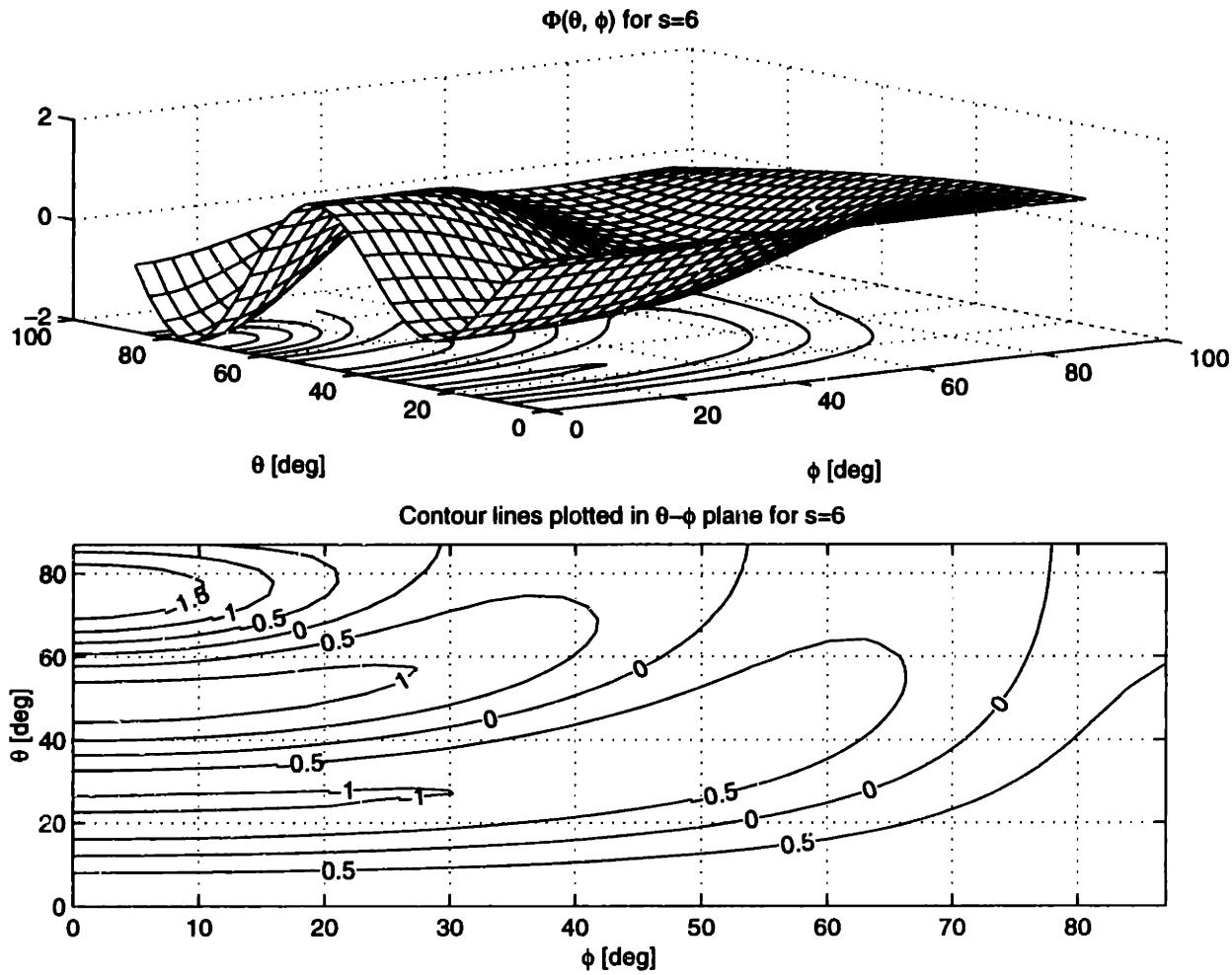

Figure 4-21: Dependence of Laplacian solution on θ and ϕ for s=6

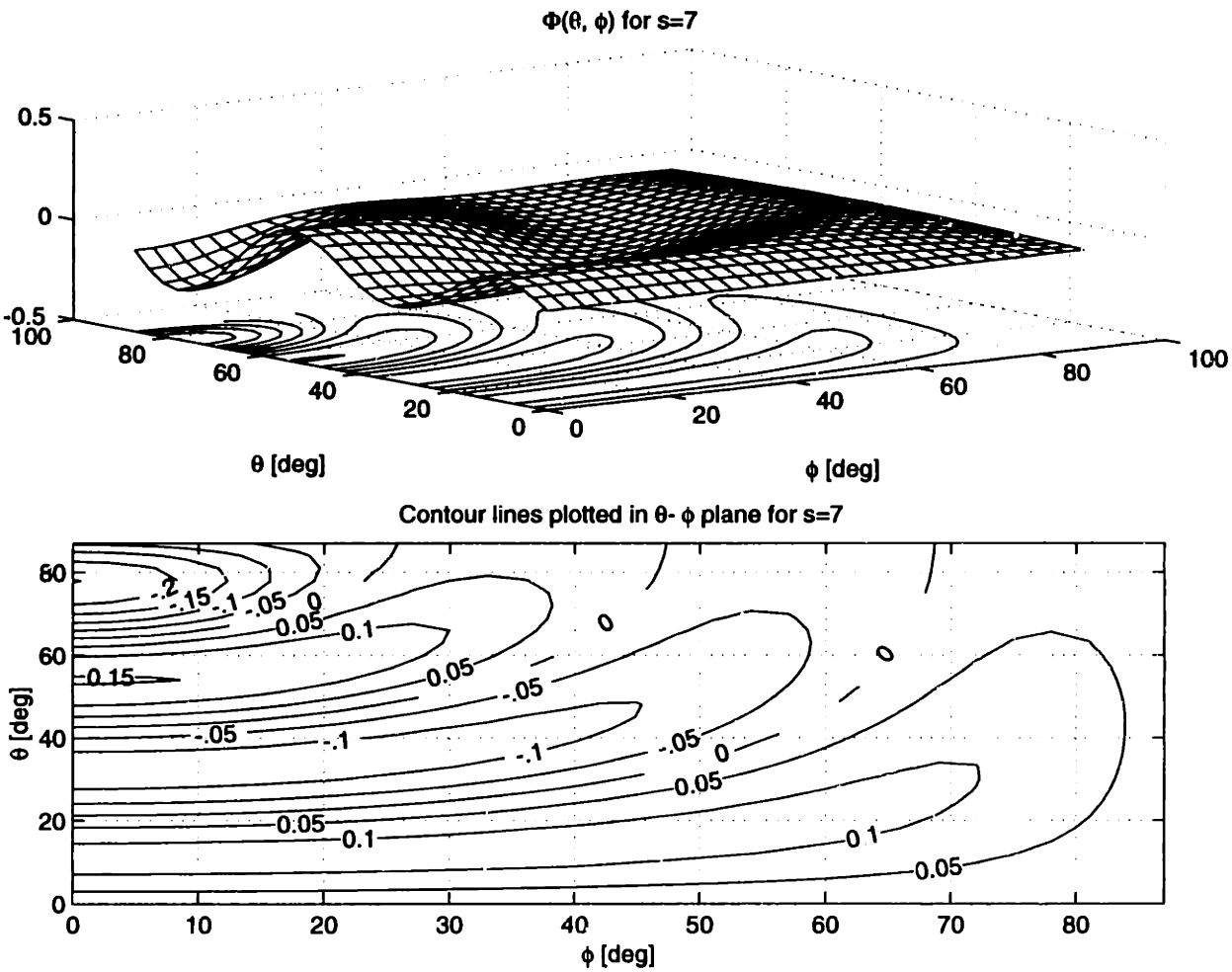

Figure 4-22: Dependence of Laplacian solution on θ and ϕ for s=7

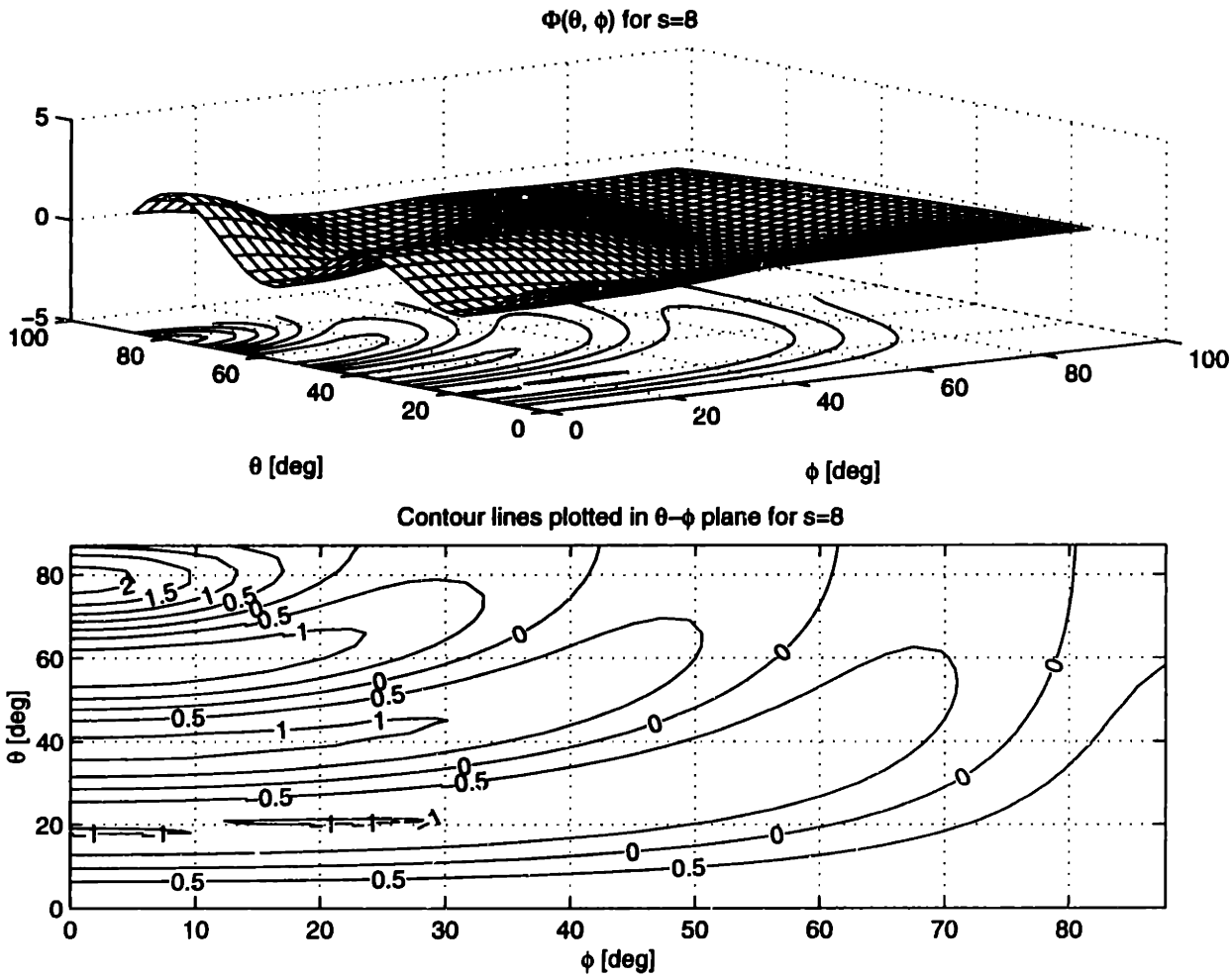

Figure 4-23: Dependence of Laplacian solution on θ and ϕ for s=8

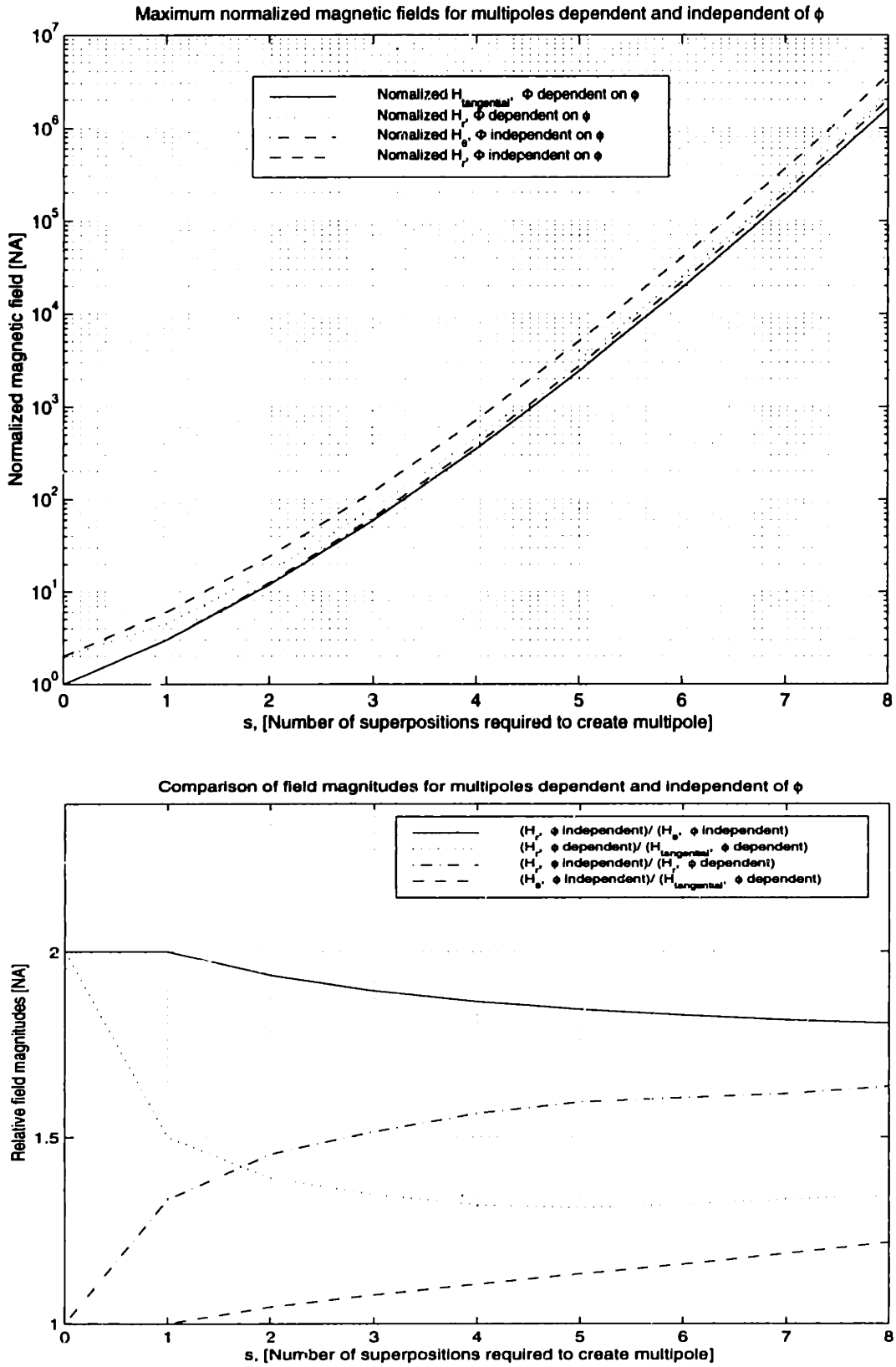

Figure 4-24: Comparison of magnetic fields for multipoles independent and dependent on ϕ

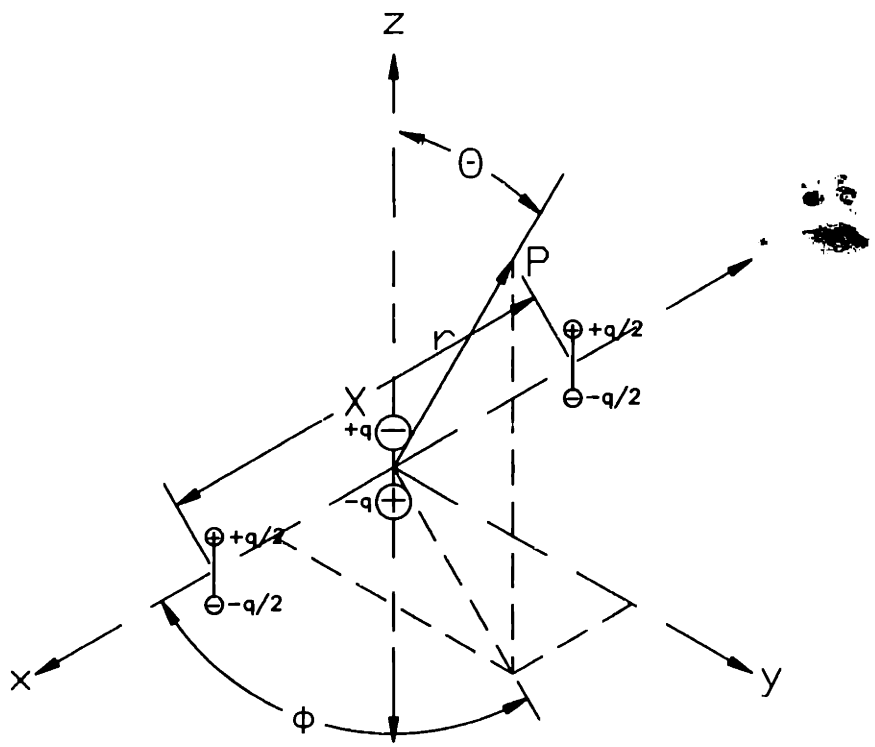

Figure 4-25: A multipole based on symmetric split multipole placement. Φ is dependent of ϕ

.

reduces to

$$\Phi = \sum C_i r^{p_i-2} \frac{X^2}{8} cos^{m_i}(\theta)\,(q_i(q_i-1)\sin^{n_i-2}(\theta)\cos^{q_i-2}(\phi) + \cdots$$
$$(p_i - m_i - n_i)(1+2q_i)\sin^{n_i}(\theta)\cos^{q_i}(\phi) + \cdots$$
$$(p_i - m_i - n_i)(p_i - m_i - n_i - 2)\sin^{n_i+2}(\theta)\cos^{q_i+2}(\phi)). \qquad (4.108)$$

This time, I won't display the solutions for the first few superpositions because they are easily derived by applying the appropriate boundary conditions to Equations (4.87) through (4.95).

4.5 The general far field solution for multipoles

A multipole does not necessarily need to be constructed of parallel opposing sub-multipoles that lie on the z-axis as in Figure 4-7 or on the x-axis as in Figure 4-14.

Instead, the parallel opposing submultipoles may lie at arbitrary locations in a plane. For this class of solutions, I begin with transformations for a coordinate system rotated in a plane. The transformations can then be used to rewrite scalar potentials such that the submultipoles are colinear on an axis of a new coordinate system . The new coordinate system readily allows the calculation of the scalar potentials in the far field limit using the superposition calculations that I have already covered.

The transformation definition is depicted in Figure 4-26. Note that I have found a transformation similar to Euler angles [7] a convenient choice for describing the new coordinate system. Here, the transformed coordinate system, designated by x_2, y_2, z_2, is rotated about the y axis in the $x-z$ plane by the angle γ. The angles θ_2 and ϕ_2 along with r describe the location of the point P in the transformed coordinate system. The useful relations for transforming scalar potentials are given by

$$\cos(\theta) = \cos(\theta_2)\cos(\gamma) - \sin(\theta_2)\cos(\phi_2)\sin(\gamma), \quad \text{and} \tag{4.109}$$

$$\sin(\theta)\cos(\phi) = \cos(\theta_2)\sin(\gamma) + \sin(\theta_2)\cos(\phi_2)\cos(\gamma). \tag{4.110}$$

As an example, the potential of a dipole given by Equation (4.45) when $\gamma = \pi/2$ is given by

$$\Phi = C\frac{-\sin(\theta_2)\cos(\phi_2)}{r^2}. \tag{4.111}$$

The general representation for multipoles is shown in Figure 4-27. The scalar potential can be solved by transforming the coordinate system as shown in Figure 4-28. The coordinate transformation for this case becomes

$$\cos(\theta) = \frac{1}{\sqrt{X^2+Z^2}}\left(X\cos(\theta_2) + Z\sin(\theta_2)\cos(\phi_2)\right), \quad \text{and} \tag{4.112}$$

$$\sin(\theta)\cos(\phi) = \frac{1}{\sqrt{X^2+Z^2}}\left(-Z\cos(\theta_2) + X\sin(\theta_2)\cos(\phi_2)\right). \tag{4.113}$$

After transforming the submultipoles, the resulting multipole of the system is obtained by applying Equation (4.86).

There is another analytical case that is useful. This case arises when multipoles

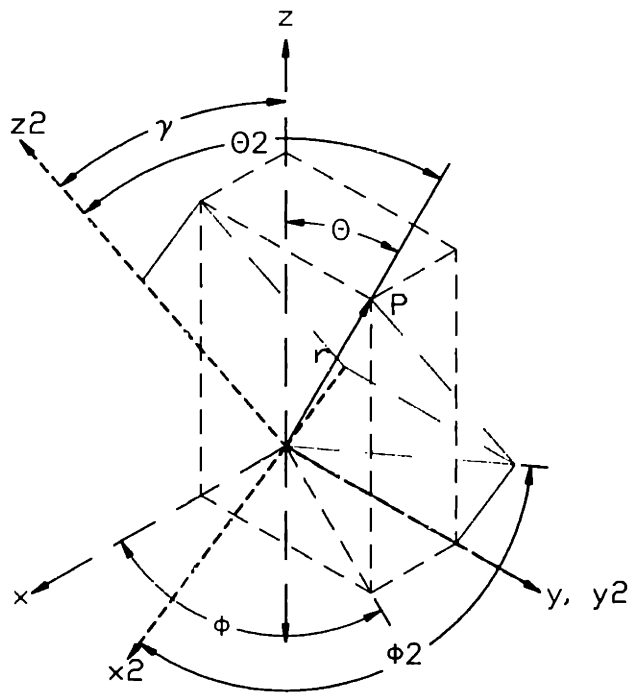

Figure 4-26: Coordinate transformation

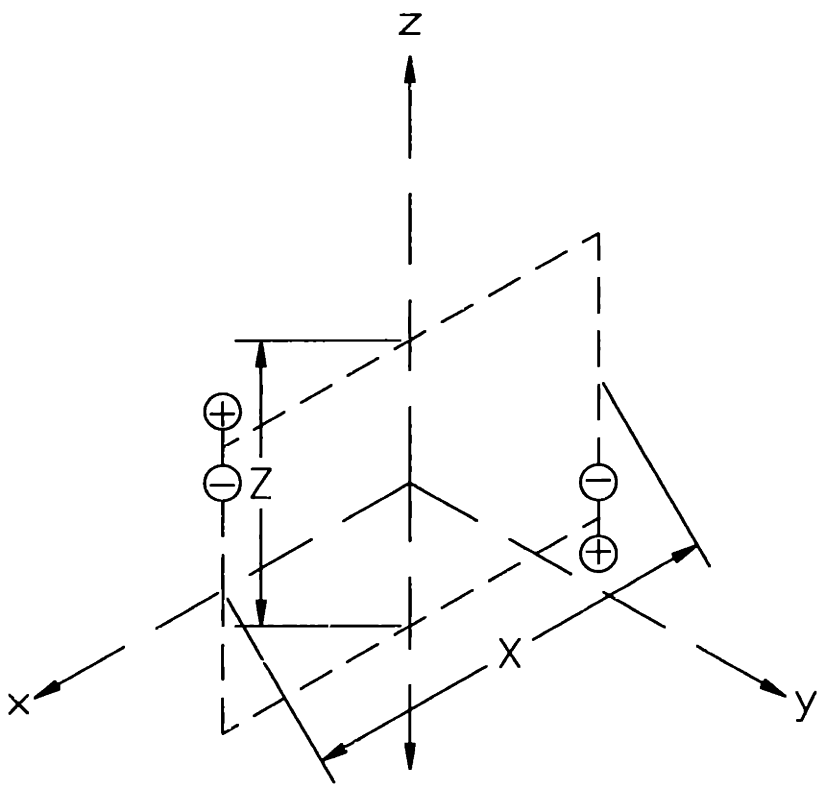

Figure 4-27: The general topology for multipoles

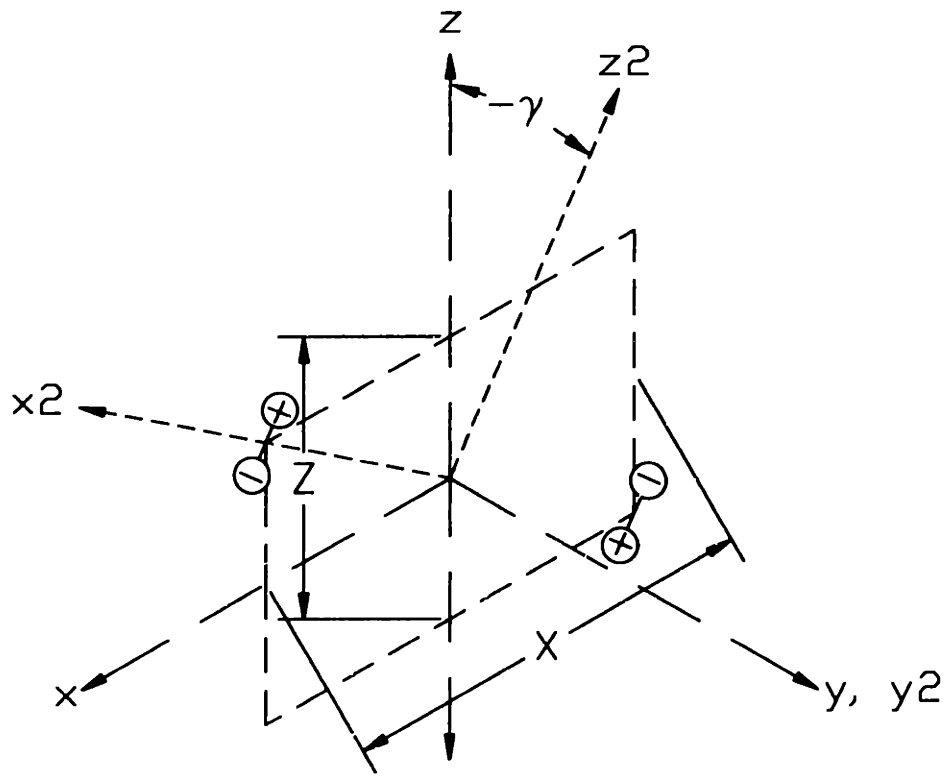

Figure 4-28: The general topology with a coordinate transformation

with ϕ dependence are superposed with orientations as shown in Figure 4-7. After superposing potentials represented by Equation (4.76), the far field solution reduces to

$$\Phi = \sum C_i r^{p_i-1} Z \sin^{n_i}(\theta) \cos^{q_i}(\phi) \left((m_i + n_i - p_i) \cos^{m_i+1}(\theta) - m_i \cos^{m_i-1}(\theta) \right) \quad (4.114)$$

Now that this solution is available, it is possible to consider an alternative transformation. The transformation shown in Figure 4-29 is defined by

$$\cos(\theta) = \frac{1}{\sqrt{X^2 + Z^2}} \left(Z \cos(\theta_2) - X \sin(\theta_2) \cos(\phi_2) \right), \quad \text{and} \quad (4.115)$$

$$\sin(\theta)\cos(\phi) = \frac{1}{\sqrt{X^2 + Z^2}} \left(X \cos(\theta_2) + Z \sin(\theta_2) \cos(\phi_2) \right). \quad (4.116)$$

Regardless of which transformation is used, the field solutions will be equivalent. However, the solutions will be less laborious for the coordinate system that minimizes the number of transformations. For systems that require transformation of many

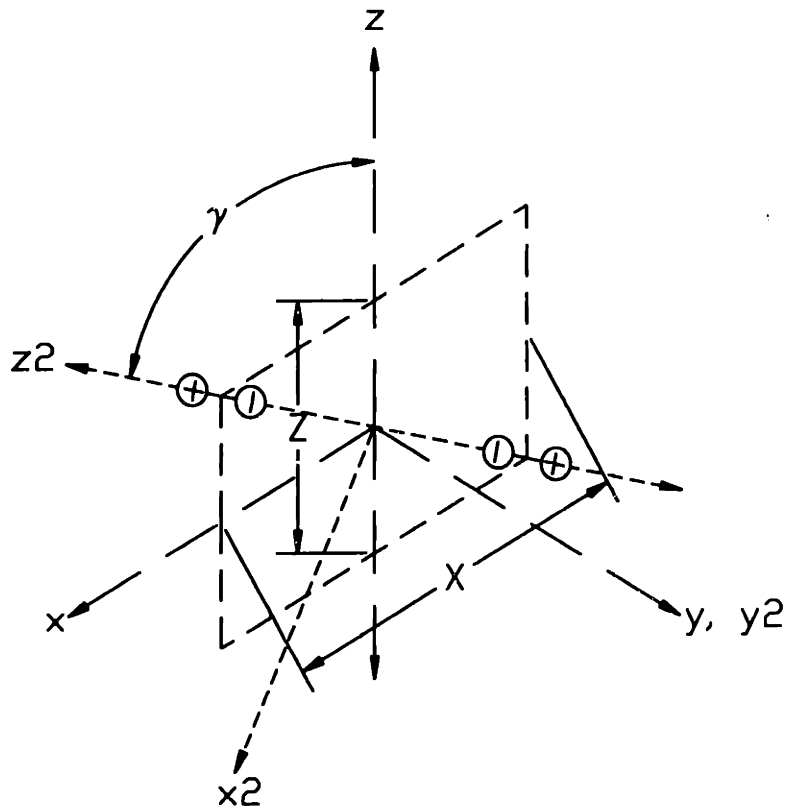

Figure 4-29: The general topology with an alternative coordinate transformation

different coordinate systems, a computer is a practical necessity for computing the transformations. The readers now have the tools to solve for the fields of their own multipole topologies.

4.6 Shielding of multipoles

Since the vacuum chamber in an ebeam lithography machine is likely to be very highly shielded from the environmental fields, it is of interest to consider the interaction between multipoles in the chamber and the shielding. The model that I use for this analysis is shown in Figure 4-30. If the general representation of a multipole is given by

$$\Phi = C_1 r^{-(p+1)} \Theta(\theta) \Phi(\phi), \tag{4.117}$$

the scalar potential in each region will have the form

$$\text{for} \quad r < R_1 \qquad \Phi_I = \left(C_1 r^{-(p+1)} + C_2 r^p\right) \Theta(\theta)\,\Phi(\phi), \tag{4.118}$$

$$\text{for} \quad R_1 < r < R_2 \qquad \Phi_{II} = \left(C_3 r^{-(p+1)} + C_4 r^p\right) \Theta(\theta)\,\Phi(\phi), \quad \text{and} \tag{4.119}$$

$$\text{for} \quad R_2 < r \qquad \Phi_{III} = C_5 r^{-(p+1)}\,\Theta(\theta)\,\Phi(\phi). \tag{4.120}$$

The solution requires this form to meet the jump conditions from Equations (4.10) and (4.12). These jump conditions are now applied at the boundaries r=R_1 and r=R_2 after finding the field components from Equation (4.16). Four independent equations in four unknowns result. I used Maple[3] symbolic mathematical software to solve these algebraic equations. The remaining constant necessary to describe the fields inside the sphere drops out as

$$\frac{C_2}{C_1} = \frac{(p+1)(\frac{\mu}{\mu_0}-1)(p\frac{\mu}{\mu_0}+(p+1))(\left(\frac{R_1}{R_2}\right)^{2p+1}-1)}{R_1^{2p+1}\left([p\frac{\mu}{\mu_0}+(p+1)][(p+1)\frac{\mu}{\mu_0}+p]-\left(\frac{R_1}{R_2}\right)^{2p+1}p(p+1)(\frac{\mu}{\mu_0}-1)^2\right)}. \tag{4.121}$$

If $\mu >> \mu_0$ and $R_1/R_2 \approx 1$ as is the case in most shield designs, this equation can be approximated by

$$\frac{C_2}{C_1} \approx -\frac{1}{R_1^{2p+1}}. \tag{4.122}$$

Since the base of the ebeam column is at R_1, it is useful to consider what happens at R_1. First I consider the radial field component. After applying Equation (4.122) to Equation (4.119) and solving for the radial flux density, B_r inside the shell becomes

$$B_r = \mu_o\left(C_1(p+1)r^{-(p+2)} + \frac{C_1 p}{R_1^{2p+1}}r^{(p-1)}\right)\Theta(\theta)\,\Phi(\phi). \tag{4.123}$$

The radial flux density at R_1 is amplified by (2p+1)/(p+1) times the case where no chamber shield is present. Meanwhile, B_θ and B_ϕ are completely nulled. Note that the nulling of the tangential components is expected, since an infinitely permeable

[3]Maple V, Release 4 available from Waterloo Maple Incorporated

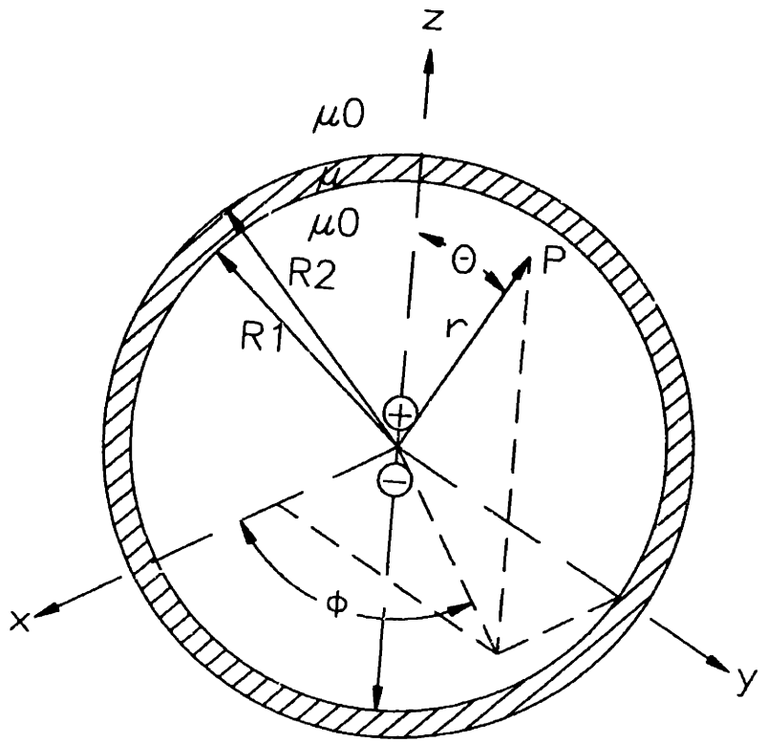

Figure 4-30: A multipole inside a spherical shield

material can only have fields entering perpendicular to its surface.

This result indicates that chamber shielding is beneficial for attenuation of the transverse fields. The shielding is likely to "pull" the fields along the axis of the ebeam trajectory and null the perpendicular components. Thus, the field that would have contributed to ebeam deflection is attenuated. In a real system, the actual effects of the chamber shielding are complicated by the geometry of the aperture through which the ebeam passes into the chamber, the distance the ebeam travels beyond the base of the column, and the finite permeability of the column base. However, the model's assumptions are not likely to be grossly incorrect and I would expect that the chamber shielding would decrease the transverse multipole field components. To argue this explicitly, I consider the case where $r = R_1(1 - \Delta)$ and $0 < \Delta << 1$. The ratios of the field components with the spherical shield to the field components

without it are given by

$$\frac{B_{r,withshielding}}{B_{r,withoutshielding}} \approx \frac{2p+1}{p+1} - \frac{(2p+1)\,p\Delta}{(p+1)}, \tag{4.124}$$

$$\frac{B_{\theta,withshielding}}{B_{\theta,withoutshielding}} \approx (2p+1)\Delta, \quad \text{and} \tag{4.125}$$

$$\frac{B_{\phi,withshielding}}{B_{\phi,withoutshielding}} \approx (2p+1)\Delta. \tag{4.126}$$

B_θ and B_ϕ are the field components that we are interested in because they cross the ebeam trajectory. One can also see that better attenuation ratios are achieved for small Δ. Unfortunately, a finite Δ is an inevitable requirement that prevents the stage from crashing into chamber cover, accounts for assembly and part tolerances, and allows the packaging of height sensors and imaging electronics. Another interesting conclusion is that better attenuation ratios are achieved for lower order multipoles. To put this in perspective, let's say that $\Delta = 1/48$. For a dipole the maximum attenuation ratio is 1/16; for a multipole with p = 8 the maximum attenuation ratio is 17/48 or about 1/3.

It is also of interest to consider the shielding of the fields outside the sphere. The attenuation ratio of the fields for $r > R_2$ is given by

$$\frac{C_5}{C_1} = \frac{\frac{\mu}{\mu_0}(2p+1)^2}{[p\frac{\mu}{\mu_0}+(p+1)][(p+1)\frac{\mu}{\mu_0}+p] - \left(\frac{R_1}{R_2}\right)^{2p+1} p(p+1)(\frac{\mu}{\mu_0}-1)^2}. \tag{4.127}$$

If $\mu >> \mu_0$, $R_1 = R_2 - t$, and $t << R_2$ where t is the shielding thickness, this equation can be approximated by

$$\frac{C_5}{C_1} \approx \frac{\mu_0}{\mu}\frac{(2p+1)}{p(p+1)}\frac{R_2}{t}. \tag{4.128}$$

This relation shows that shielding is more efficient for higher order multipoles, higher relative permeability, and smaller radius to wall thickness ratios. For the case when $p = 1$, Equation (4.127) is the solution for a dipole, which is consistent with the results given in [16].

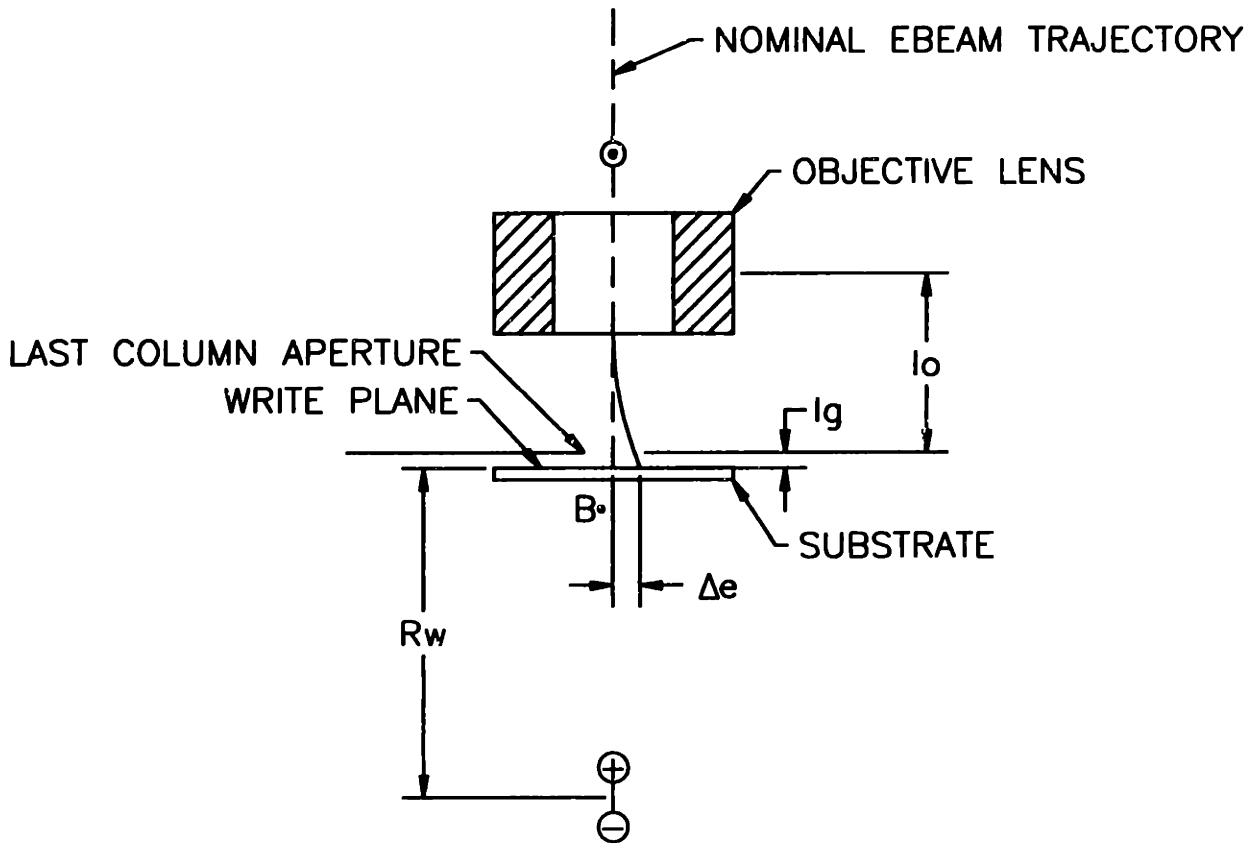

Figure 4-31: Ebeam deflection

4.7 Field requirements for an ebeam stage

In this section, I estimate the deflection of the ebeam due to the fringing field of the stage. The model that I consider is shown in Figure 4-31 where the multipole has a field component crossing the ebeam axis described by

$$B = \frac{B_w R_w^{p+2}}{r^{p+2}}. \tag{4.129}$$

Here B_w is the transverse flux density at the write plane. I am interested in the deflections in two regions: the path between the last column aperture and the write plane, l_g, and the path between the nominal objective lens position and the last column aperture, l_o. The reason for separating these regions is that l_o is very well shielded from the chamber thus it should be valid to apply an attenuation ratio inside the column. Also, I do not consider the path beyond the objective lens because this

region is much less sensitive to ebeam deflections. Moreover, because the objective lens demagnifies the ebeam greatly, the deflections prior to the objective lens are also demagnified greatly.

Assuming small deflections of the ebeam relative to the curvature of deflection, the allowable B_w for the required Δ_e is derived from integration along l_g.

The Lorentz force law, given by

$$\mathbf{F} = q(\mathbf{E} + \mathbf{v} \times \mathbf{B}), \tag{4.130}$$

governs the motion of the electrons. The velocity of the electrons along the column axis is calculated from the voltage of the electron gun by energy balance and is given by

$$v = \sqrt{\frac{2V_e q_e}{m_e}} \tag{4.131}$$

Here v is the electron velocity, V_e is the gun voltage, m_e is the mass of an electron, and q_e is the charge of an electron. The acceleration required by the Lorentz force law is now integrated twice with respect to the time. The time is integrated for $t = 0$ to $t = -\frac{l_g}{v}$. to give the displacement

$$\Delta_e = \int_0^{-\frac{l_g}{v}} \int_0^t \frac{qv}{m_e} \frac{B_w R_w^{p+2}}{(R_w - vs)^{p+2}} \, ds \, dt. \tag{4.132}$$

After integration, the allowable field at the write plane simplifies to

$$B_w = \Delta_e \frac{p(p+1)}{R_w^2} \sqrt{\frac{m_e V_e 2}{q_e}} \frac{1}{\left(1 - \left(1 + \frac{l_g}{R_w}\right)^{-(p+1)} \left(\frac{l_g(p+1)}{R_w} + 1\right)\right)}. \tag{4.133}$$

As an example, I have computed the allowable B_w when Δ_e=1nm, l_g=1/8″, R_w=6″, and V_e=50kV for various multipoles in Table 4.1. The multipoles range from $p = -2$ for a uniform field, to $p = 8$. The allowable B_w does not change much for the various multipoles because we are far from the source and the fields attenuate very little over the distance of interest. The allowable B at the last aperture

p	Allowable B_w at R_w(T)	Unshielded B at the last column aperture (T)	Allowable B at the last column aperture (T)	Required 1/(attenuation factor) inside column
-2	1.50E-07	1.50E-07	1.04E-09	144
1	1.56E-07	1.47E-07	1.61E-09	91
2	1.58E-07	1.46E-07	1.85E-09	79
3	1.60E-07	1.45E-07	2.13E-09	68
4	1.63E-07	1.44E-07	2.44E-09	59
5	1.65E-07	1.43E-07	2.78E-09	51
6	1.67E-07	1.42E-07	3.16E-09	45
7	1.69E-07	1.41E-07	3.58E-09	39
8	1.72E-07	1.40E-07	4.05E-09	34

Table 4.1: Field requirement for various multipoles

is computed by reapplying Equation (4.133) with Δ_e=1nm but with R_w accounting for the increased R due to l_g and l_o becoming l_o=3/2". The required 1/(attenuation factor) inside column is computed by taking the ratio of the unshielded B at the last column aperture to the allowable B. Since I would expect a well designed column shield to provide attenuation of at least 1/500 for a dipole field– easily exceeding the 1nm deflection requirements, the ebeam deflection can be estimated by the result for the integration along l_g.

If we also account for the attenuation of the multipole's fields that cross the ebeam trajectory because of the interaction with the shielded chamber cover, the allowable B_w becomes even larger. To be conservative, $B_w = \pm 2 \times 10^{-7}$ Tesla is a good rule of thumb for design purposes.

I should also mention that stray fields affect ebeam lithography in more ways than just placement accuracy. A high performance ebeam lithography column will shape an ebeam with distinct "optical" properties. However, if the deflections of the ebeam due to stray fields are small compared to the cross section of the ebeam, we can neglect the small optical aberrations that may be introduced.

4.8 Field Solutions by Magnetic Charge Integration

In the previous sections I developed solutions from a boundary value perspective, i.e. by seeking solutions that solve Laplace's equation in the selected coordinates. As an alternative approach, we can calculate the potential and thereby the associated fields with the superposition integral. A general relation representing the potential produced by magnetized material [1] is given by

$$\Phi(\mathbf{P}) = -\frac{1}{4\pi}\int_V \frac{\nabla\cdot\mathbf{M}}{r}dV + \frac{1}{4\pi}\int_S \frac{\mathbf{M}\cdot\hat{\mathbf{n}}}{r}dS. \tag{4.134}$$

Here the potential is given at a point $\mathbf{P}$, i.e. with coordinates x, y, z for the Cartesian case. For a uniformly magnetized block, $\nabla\cdot\mathbf{M} = 0$ and thus the magnetic field solution can be reduced to the integral of the surface charges $\mathbf{M}\cdot\hat{\mathbf{n}}$ on the North face and the South face of the block.

The solution for the magnetic flux density produced by a magnetic charge sheet located on surface S_q is given by

$$\mathbf{B}(\mathbf{P}) = -\frac{\mu_o\mathbf{M}\cdot\hat{\mathbf{n}}}{4\pi}\int_{S_q}\frac{\mathbf{r}-\mathbf{r_q}}{|\mathbf{r}-\mathbf{r_q}|^3}dS_q. \tag{4.135}$$

Here $\mathbf{r}$ is the location of the point $\mathbf{P}$, and $\mathbf{r_q}$ is the location of the magnetic charge that is integrated. For the charge sheet located at the origin as in Figure 4-32 the flux density is explicitly given by

$$\mathbf{B}(\mathbf{P}) = -\frac{\mu_o\mathbf{M}\cdot\hat{\mathbf{i}}_z}{4\pi}\int_{-\frac{W}{2}}^{\frac{W}{2}}\int_{-\frac{L}{2}}^{\frac{L}{2}}\frac{(x-x_q)\hat{\mathbf{i}}_x + (y-y_q)\hat{\mathbf{i}}_y + z\hat{\mathbf{i}}_z}{((x-x_q)^2+(y-y_q)^2+z^2)^{\frac{3}{2}}}\,dx_q\,dy_q. \tag{4.136}$$

There are essentially two integral types. One where the field component is parallel to the surface and the second where the field component is perpendicular to the

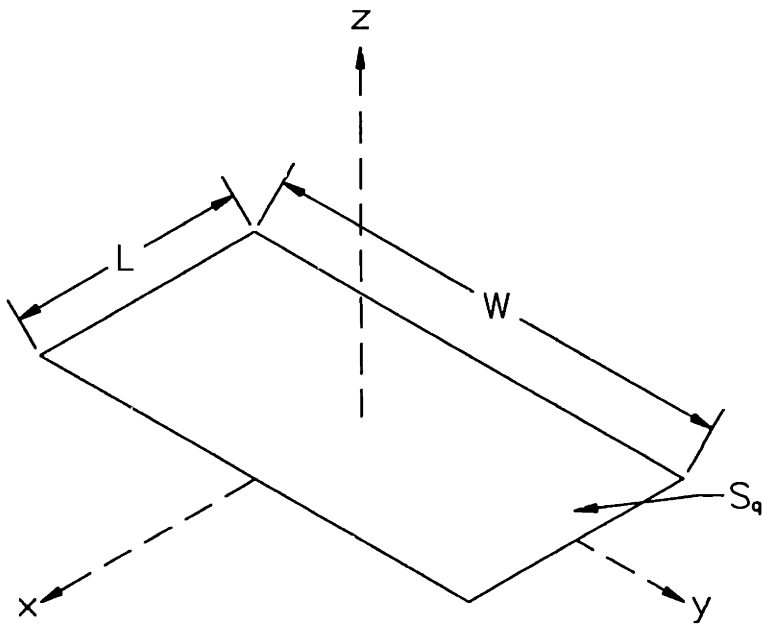

Figure 4-32: Sheet of surface charge for integration

surface. The first type, results in nice closed form expressions where

$$B_x(\mathbf{P}) = -\frac{\mu_o \mathbf{M}\cdot\hat{\mathbf{i}}_z}{4\pi}\ln\left(\frac{\left[W-2y+\sqrt{(2x+L)^2+(2y-W)^2+(2z)^2}\right]}{\left[W-2y+\sqrt{(2x-L)^2+(2y-W)^2+(2z)^2}\right]}\right.$$
$$\left.\frac{\left[-W-2y+\sqrt{(2x-L)^2+(2y+W)^2+(2z)^2}\right]}{\left[-W-2y+\sqrt{(2x+L)^2+(2y+W)^2+(2z)^2}\right]}\right), \quad \text{and} \quad (4.137)$$

$$B_y(\mathbf{P}) = -\frac{\mu_o \mathbf{M}\cdot\hat{\mathbf{i}}_z}{4\pi}\ln\left(\frac{\left[L-2x+\sqrt{(2x-L)^2+(2y+W)^2+(2z)^2}\right]}{\left[L-2x+\sqrt{(2x-L)^2+(2y-W)^2+(2z)^2}\right]}\right.$$
$$\left.\frac{\left[-L-2x+\sqrt{(2x+L)^2+(2y-W)^2+(2z)^2}\right]}{\left[-L-2x+\sqrt{(2x+L)^2+(2y+W)^2+(2z)^2}\right]}\right). \quad (4.138)$$

The second integral type is more difficult, although [32] manages to solve it in closed form. Unfortunately, the closed form expression is computationally intensive. For the field component perpendicular to charge surfaces, I opt for numerical integration when I use the superposition integral in this thesis. I integrated the surface charge in one dimension analytically and numerically in the other dimension. The analytical integration leaves the expression for B_z given by

$$B_z = -\frac{\mu_o \mathbf{M} \cdot \hat{\mathbf{i}}_z}{4\pi} \int_{-\frac{W}{2}}^{\frac{W}{2}} \left(\frac{z(2x-L)}{[(y-y_q)^2+z^2]\sqrt{(2x-L)^2+(2y-2y_q)^2+(2z)^2}} - \frac{z(2x+L)}{[(y-y_q)^2+z^2]\sqrt{(2x+L)^2+(2y-2y_q)^2+(2z)^2}} \right) dy_q \quad (4.139)$$

A computer is ideal for numerically integrating this expression. One should note that these expressions are completely general for charge sheets. The fields for a charge sheet located at any orientation and at any location can be computed by coordinate transformation of the field components and the coordinate systems.

I developed code in Matlab's [4] .m file format that uses the closed form and numerical integration solutions that I just described. This code is very general and accurate. It is restricted to charge sheets, and therefore soft iron materials are not easily represented other than by matching boundary conditions with the associated charges. I used the code extensively to analyze my magnetic bearing prototype. A listing of the code that I used is given in Appendix A. Results of calculations are reported in Chapter 5.

[4]Matlab Version 5.1.0.421 available from the Mathworks Incorporated

Chapter 5

Experiment

I designed and implemented a prototype synchronous motor magnetic bearing with low fringing fields. The design is based on seven levels of field cancellation, which yields a multipole with field components that fall as r^{-10}. In this chapter, I describe the

- verification of the analytical models
- detailed design of a low fringing field magnetic bearing
- formulation and assessment of manufacturing techniques
- experimental measurement of the fringing fields
- assessment of electromechanical performance for the low fringing field bearing
- mechanical design of the test setup
- electronics architecture for data acquisition and motion control

It is important to verify the electromagnetic field theory in light of the complexities of a real system. This chapter solidifies the useful concepts that drive a designer toward a practical low fringing field magnetic bearing. For a real system, we learn that magnet and coil tolerances are important concerns in high performance field cancellation schemes. Methods for simulating tolerance effects lead to an understanding

of the limitations imposed by the imperfect real world manufacturing. Exploration of tolerance compensation methods indicates that cancellation approaching the performance of the theoretical array is possible.

I also illuminate the design options for placing opposing multipoles for field cancellation. The analysis of the prototype serves as a good benchmark for many of these concepts. A real system must also be manufacturable, therefore I discuss the procedures that I employed for fabricating the prototype. Details of the experimental setup are covered in the next section.

5.1 Experimental Setup

The experimental setup is shown in Figures 5-1 and 5-2 [1]. The major subassemblies include a magnet array, stator, laser interferometry system, force sensor system, air bearing, and support structure. The magnet array and stator form a synchronous motor that can produce forces in suspension and translation. I have included two photographs of the actual setup in Figures 5-3 and 5-4.

The magnet array and stator are low fringing field designs that implement the field cancellation techniques that I developed in Chapter 4. The laser interferometry system and the force sensor system is used to assess the electromechanical performance of the synchronous motor bearing. Also, the setup is a test bed for precision motion control experiments, which are discussed in Chapter 6. Although the air bearing constrains the motion to a single translation degree of freedom, the full electromechanical performance of the synchronous motor can be assessed because the force sensors transduce the suspension force. Three piezo force sensors support the air bearing rod and the sum of the forces is insensitive to the location of the air bearing carriage on the rod. The sum of the charge output from the piezo sensors is the measure of suspension force. Also, for field measurements a flux gate magnetometer is employed. The experiments lead to the characterization of the fields and

[1] The scales shown in the drawings in this thesis are valid when the drawing border is stretched to the paper size listed in the drawing template

the electromechanical performance of the magnetic bearing. The electromechanical analysis, field analysis, field measurements, and mechanical design and manufacture are further described in the rest of this chapter.

5.2 Magnetic bearing electromechanical design and analysis

Other researchers [19, 38, 39, 40] from the Precision Motion Control Laboratory at MIT have developed an effective design and analysis framework for synchronous machines. The force and electrical terminal relations for design purposes can be derived from this framework. While this analysis neglects edge effects by modeling the stator and the magnet array as extending infinitely in space, the model is sufficiently accurate for design purposes.

The magnet and coil topology is shown in Figure 5-5. This configuration of rotating magnetization is known as the Halbach array after Klaus Halbach who applied them to linear undulators [13]. The detailed force calculations for synchronous motors are found in [40]. Here, the vertical and horizontal magnetization along with the current density are represented as Fourier series. The jump conditions of Equations (4.10) and (4.12) are applied at the upper and lower boundaries of the magnet array to find the scalar potential solutions and the associated fields. The stator fields can be found by solution of the magnetic vector potential as in [19]. With the superposed field solutions for the stator and magnet array, integration of the stress tensor about either the stator or the magnet array then yields the horizontal and vertical force components.

For a block Halbach magnet array and under the approximation of a sinusoidal current distribution in the stator, the translational force, $F_{x\lambda}$, and suspension force, $F_{z\lambda}$, per spatial period λ are given by

$$\begin{bmatrix} F_{x\lambda} \\ F_{z\lambda} \end{bmatrix} = \mu_0 M G e^{-\gamma z_0} \begin{bmatrix} \cos(\gamma x) & \sin(\gamma x) \\ -\sin(\gamma x) & \cos(\gamma x) \end{bmatrix} \begin{bmatrix} J_a \\ J_b \end{bmatrix} \tag{5.1}$$

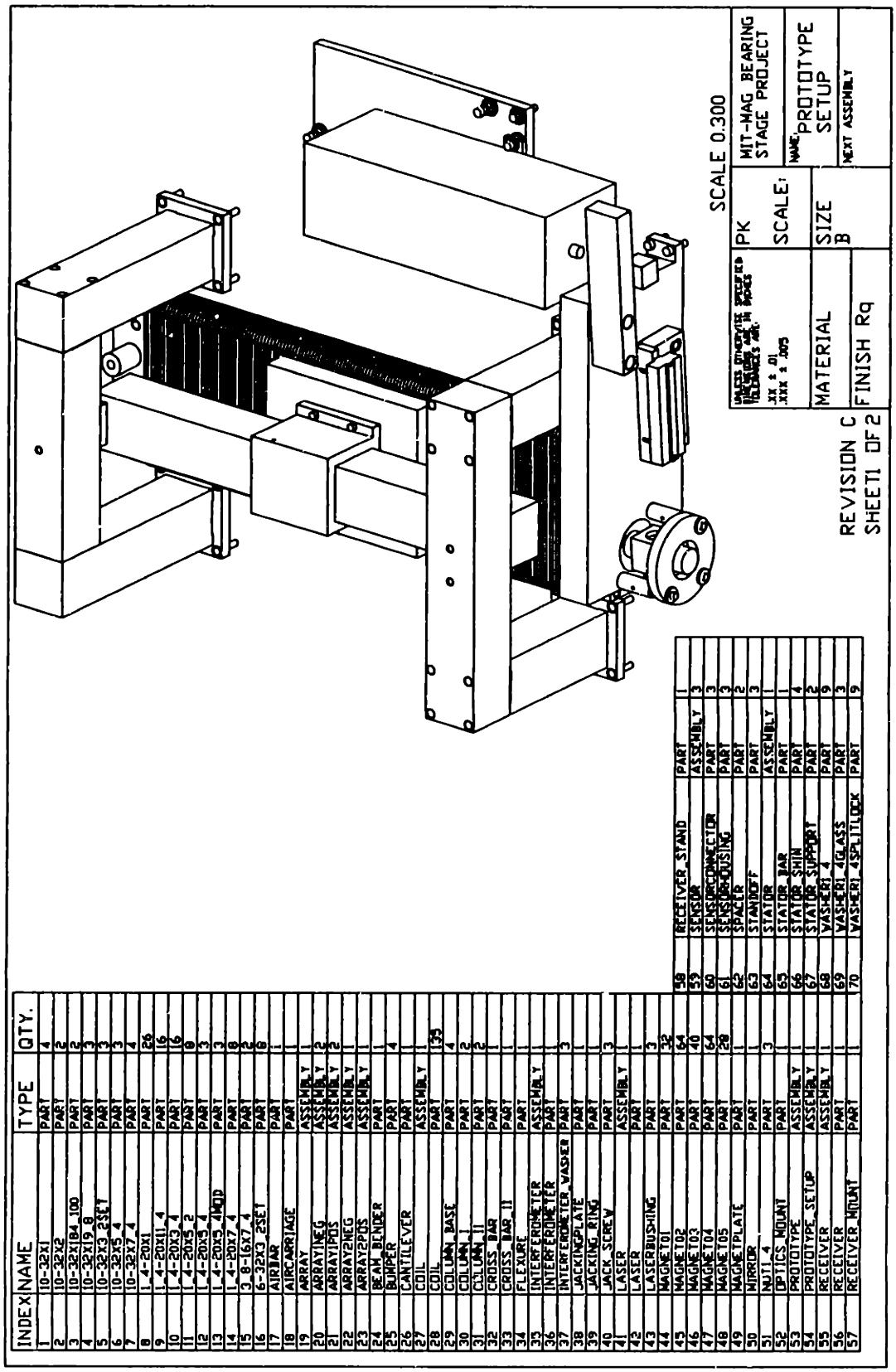

Figure 5-1: Experimental setup

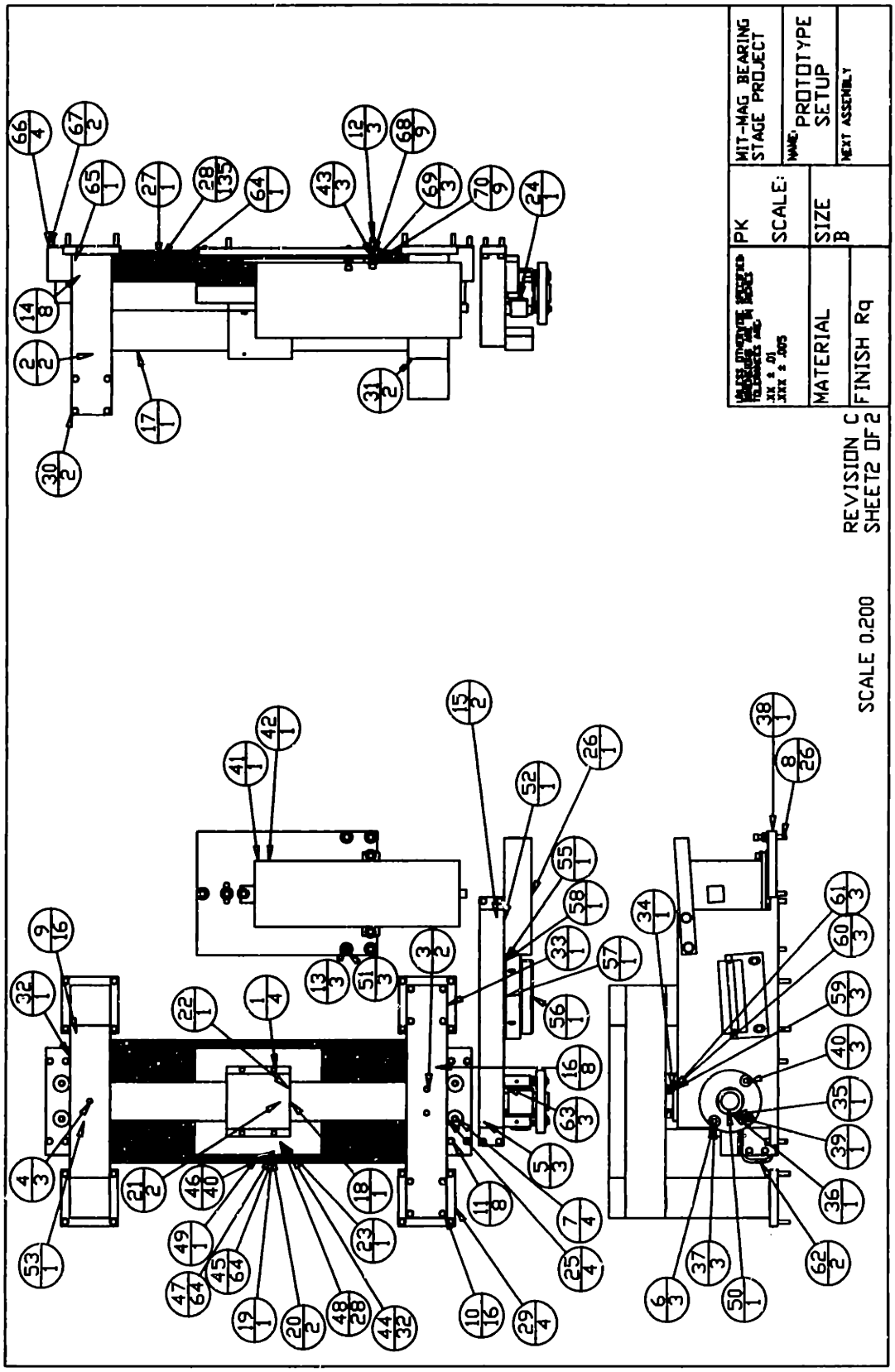

Figure 5-2: Experimental setup continued

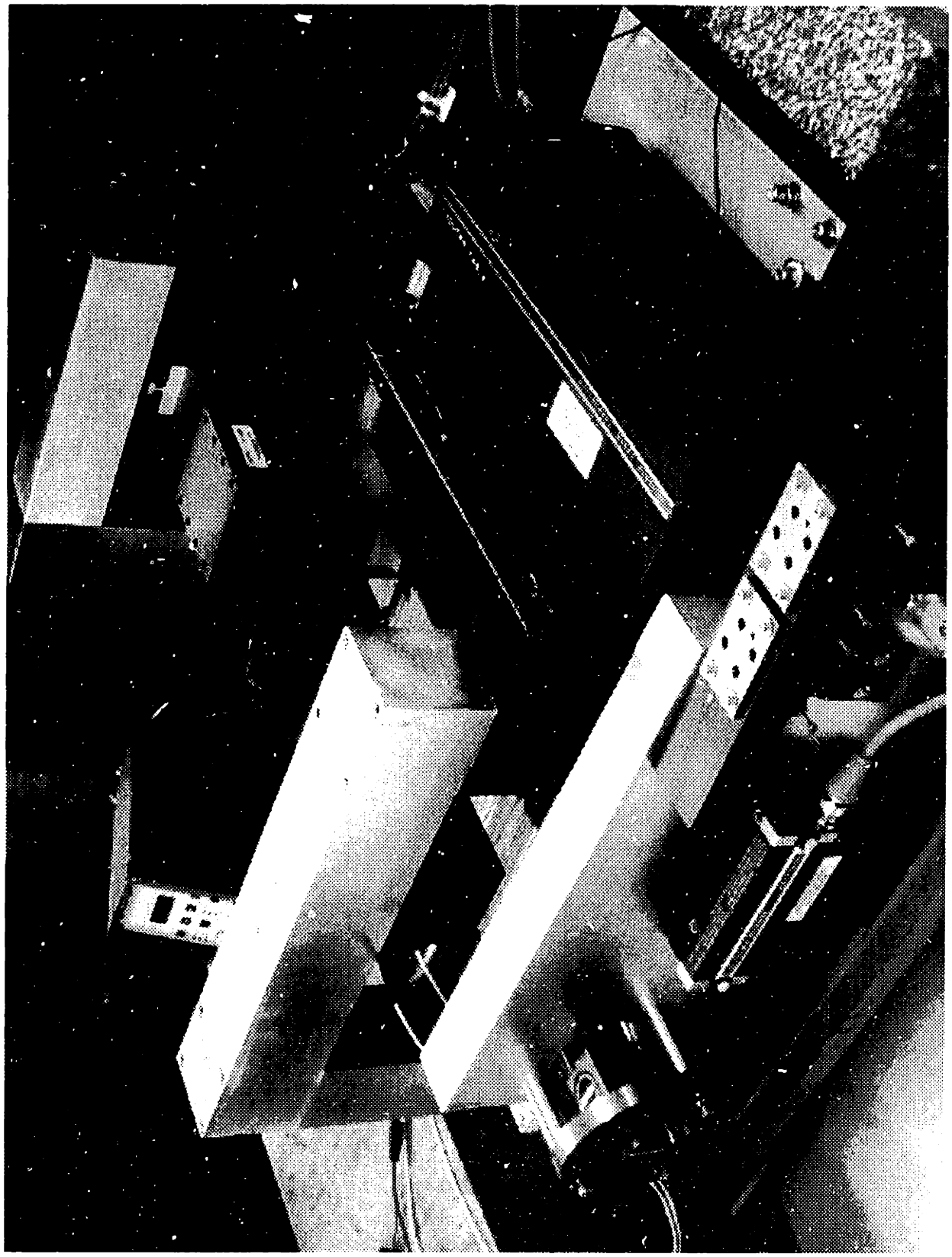

Figure 5-3: Photograph of experimental setup

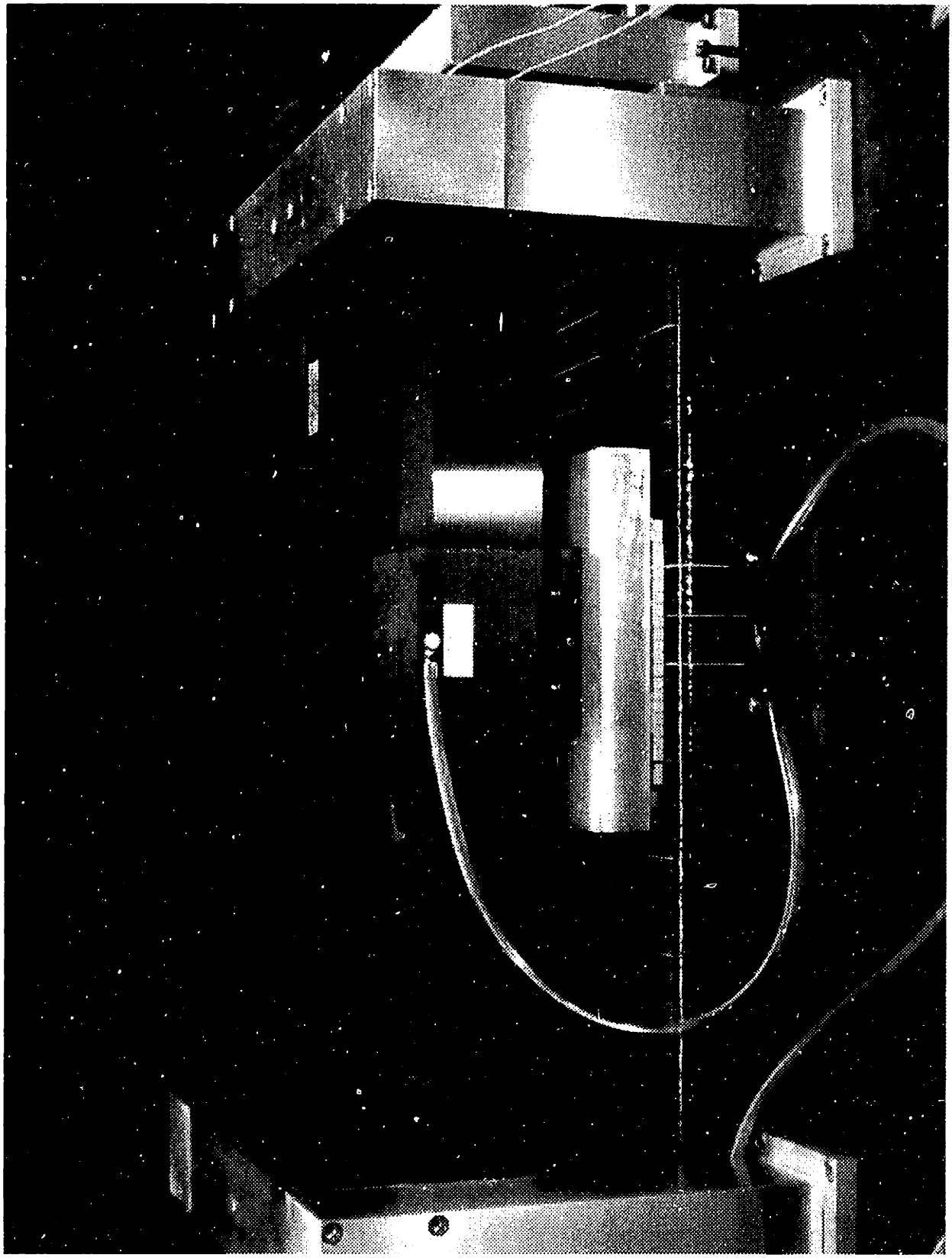

Figure 5-4: Photograph of experimental setup, side view

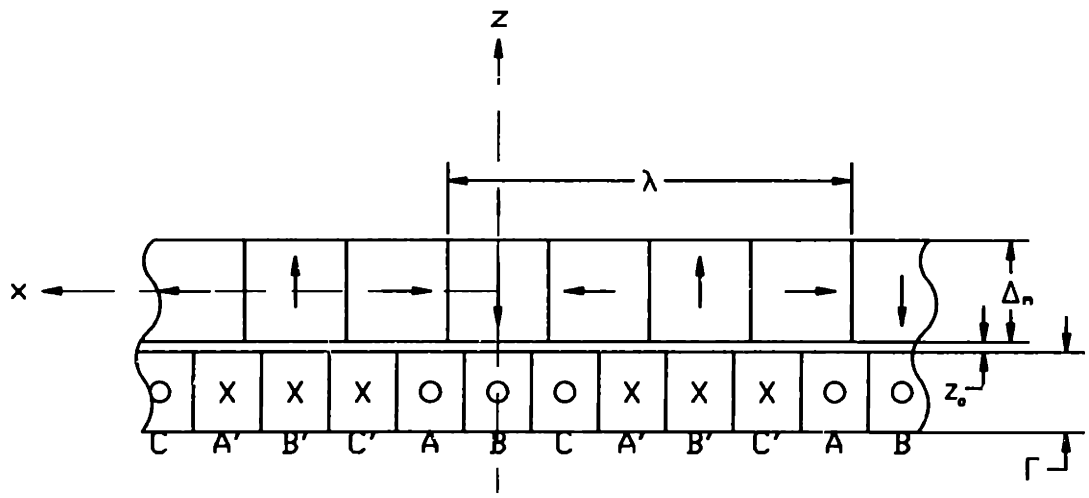

Figure 5-5: Synchronous motor with three phase currents

where

$$\gamma = \frac{2\pi}{\lambda} \tag{5.2}$$

$$G = \frac{\sqrt{2} w_m \lambda^2}{\pi^2}(1 - e^{-\gamma\Gamma})(1 - e^{-\gamma\Delta_m}). \tag{5.3}$$

Here λ is the magnet and coil spatial period, Γ is the stator thickness, Δ_m is the magnet thickness, and J_a and J_b are half the peak current density components associated with the commutation law and must be correlated to the phase currents. I choose to design a stator with three phases as depicted in Figure 5-5. As in [19], I invert Equation (5.1) and apply the inverse Blondel Park transformation , to yield the phase currents I_A, I_B, and I_C in amps as

$$\begin{bmatrix} I_A \\ I_B \\ I_c \end{bmatrix} = \frac{2e^{\gamma z_0}}{\mu_0 \eta M G N_m} \begin{bmatrix} -1 & 0 \\ -\frac{1}{2} & \frac{\sqrt{3}}{2} \\ \frac{1}{2} & \frac{\sqrt{3}}{2} \end{bmatrix} \begin{bmatrix} \cos(\gamma x) & -\sin(\gamma x) \\ \sin(\gamma x) & \cos(\gamma x) \end{bmatrix} \begin{bmatrix} F_x \\ F_z \end{bmatrix}. \tag{5.4}$$

Here N_m is the number of magnet spatial periods interacting with the stator and η is the turns density of the stator coils. To simplify the initial current estimation for the purpose of design, it is reasonable to just consider the suspension force requirements, $F_z = mg$ and $F_x = 0$, and then calculate the current requirement from Equation (5.4).

The validity of this approximation is kinematically dependent on the stage topology but since the lateral acceleration requirements are typically about 1/10 the vertical suspension requirement in an ebeam lithography stage, this assumption will in most cases be close enough to use as a design rule. Furthermore, if the amplifier is sized for 2× to 3× this nominal force, the margin is sufficient to accommodate the actual force requirements. Using this simplification, the phase currents become

$$\begin{bmatrix} I_A \\ I_B \\ I_c \end{bmatrix} = \frac{2e^{\gamma z_0}}{\mu_0 \eta M G N_m} \begin{bmatrix} \sin(\gamma x) \\ \frac{1}{2}\sin(\gamma x) + \frac{\sqrt{3}}{2}\cos(\gamma x) \\ -\frac{1}{2}\sin(\gamma x) + \frac{\sqrt{3}}{2}\cos(\gamma x) \end{bmatrix} \begin{bmatrix} F_z \end{bmatrix}, \tag{5.5}$$

which reduces to

$$\begin{bmatrix} I_A \\ I_B \\ I_c \end{bmatrix} = \frac{2e^{\gamma z_0}}{\mu_0 \eta M G N_m} \begin{bmatrix} \sin(\gamma x) \\ \sin(\gamma x + \frac{\pi}{3}) \\ \sin(\gamma x + \frac{2\pi}{3}) \end{bmatrix} \begin{bmatrix} F_z \end{bmatrix}. \tag{5.6}$$

Because the range of the trigonometric function sin is from -1 to 1, the maximum force output of the synchronous motor with three phase currents, where no phase current can exceed the current limit I_{max}, is given by

$$F_z = \frac{\mu_0 M G N_m \eta I_{max}}{2e^{\gamma z_0}}. \tag{5.7}$$

The geometric parameters can now be reduced systematically. The magnet heights are selected to achieve fields of about 80% of those achieved for infinitely high magnets and are thus set to $\Delta_m = \lambda/4$. The block Halbach array (4 blocks per period λ) is selected because it very closely approximates the fields of a continuous rotation Halbach array but magnet blocks are easily fabricated. The fields are expected to be $2\sqrt{2}/\pi$ of the ideal case or about 90% [40]. The stator thickness is set to $\Gamma = \lambda/5$ which is derived in [40] as the power optimal case. For a three phase stator, each coil has width $\lambda/6$. The cross sectional area of each coil is now defined and I set $\eta I_{max} = J_{max}\lambda^2/30$, where η is the turns density.

Since a small stage footprint and thus a small magnet footprint is highly desired, it is useful to calculate the area of the magnet array from Equation (5.7) as

$$N_m \lambda w_m = \frac{30\sqrt{2}\pi^2 F_{z,max} e^{\gamma z_0}}{\mu_0 M \lambda^3 J_{max}(1-e^{-\frac{2\pi}{5}})(1-e^{-\frac{2\pi}{4}})}. \tag{5.8}$$

Note that I have eliminated G with Equation (5.3). Equation (5.8) indicates that λ should be driven large for the area to be driven small. However, in the case of a low fringing field design, the underlying dipole moment and the moment arms of the multipoles must also be considered as these become worse as the wavelength is increased.

The underlying dipole moment of each set of magnets with the same orientation in a block Halbach array is due to 1/4 of the magnet volume because there are four magnets per spatial period. The number of magnets in each set is $\frac{\lambda}{4} N_m$ with the corresponding magnet volume given by $\frac{\lambda}{4} N_m w_m \Delta_m$. After combining this volume with Equation (4.46), and Equation (5.8), C is given by

$$C = \frac{M}{4\pi}\frac{\lambda}{4} N_m w_m \Delta_m = \frac{15\sqrt{2}\pi F_{z,max} e^{\gamma z_0}}{32\mu_0 \lambda^2 J_{max}(1-e^{-\frac{2\pi}{5}})(1-e^{-\frac{2\pi}{4}})}. \tag{5.9}$$

This relation indicates that to drive C small, λ must be driven large. However, we must consider some other factors. First of all, the multipole moment arm inherent in the complete rotation Halbach array is proportional to λ. Secondly, when I consider the thermal effects in Section 7.2, J_{max} turns out to be inversely proportional to Γ. Thus, J_{max} is inversely proportional to λ because Γ is set proportional to λ. The product of the underlying dipole moment and the first multipole moment arm of the complete rotation Halbach array therefore is independent of λ if we are designing a motor based on the thermal current limit. In the arrays that I consider in this thesis, even higher levels of cancellation are achieved in topologies with additional multipole moment arms that have a component that is also proportional to λ. Since the product of the multipole moment arms and the underlying dipole moment is proportional to the magnitude of a multipole's fringing field, a low fringing field design would dictate

that λ be driven small in the case of higher levels of cancellation.

The spatial period cannot be driven arbitrarily small, however. Sufficient forces must be available in the entire focusing range of the stage. Therefore the ratio of the air gap z_o and the spatial period cannot be excessively large lest the motor becomes very power inefficient. That is, the field decays in a characteristic distance $z = 1/\gamma$, as given in Equation (5.1). Also, it is reasonable to assemble only a finite number of magnets and coils.

I chose to build a magnetic bearing based on the focusing constraint where I designed for a gap of 500$\pm$250μm. The lower limit is based on an allowance for the magnet array and stator flatness specifications. The upper limit is dictated by photomask tolerances and expected assembly tolerances of an ebeam system. The spatial period is chosen nominally to be 2.54×10^{-2} m (1″) because I chose the force output of the magnetic bearing to decrease by no more than 20% from the zero gap condition.

The prototype magnet array is shown in Figure 5-6. It is a variation of a block Halbach array that takes advantage of field cancellation produced by parallel opposing dipoles. The details of the fringing field performance and multipole design are discussed later in this chapter. The array is built from magnets as shown in Figure 5-7. Although the magnets are .25″ on each side, the epoxy and the magnet tolerances yielded 2.4 mils thickness per interface. Thus, the actual λ is 2.565 cm (1.0098″). However, using the nominal λ=2.54 cm and W_m = 16.91 cm the analysis is close enough for engineering purposes. The properties of this magnet array are shown in Table 5.1. The experimental force output of the motor was obtained using the experimental setup's force sensors. The Kistler Model 9212 force cells were used in conjunction with a Kistler Type 5010 Dual Mode Amplifier and a HP3478A Multimeter. The sensor output was calibrated with weights that were placed on the air bearing rod. Since the sensitivity of all three Kistler cells do not vary by more than $\pm$.2%[2], it was valid, for the accuracy of interest, to sum the charge output from the sensors regardless of where the weights were placed on the air bearing rod. This

[2]Data taken from Kistler data sheets supplied with the sensors

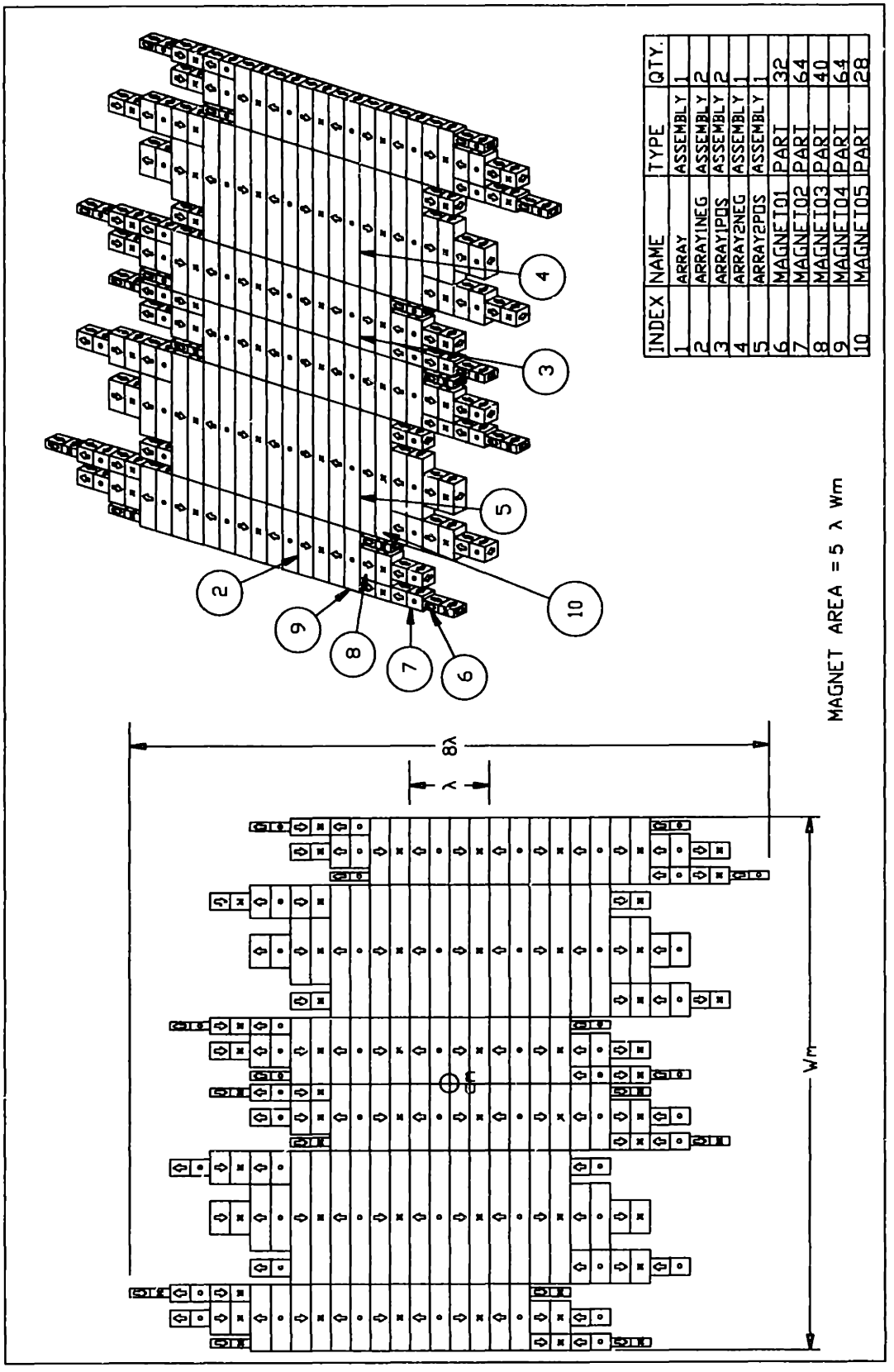

Figure 5-6: Prototype magnet array

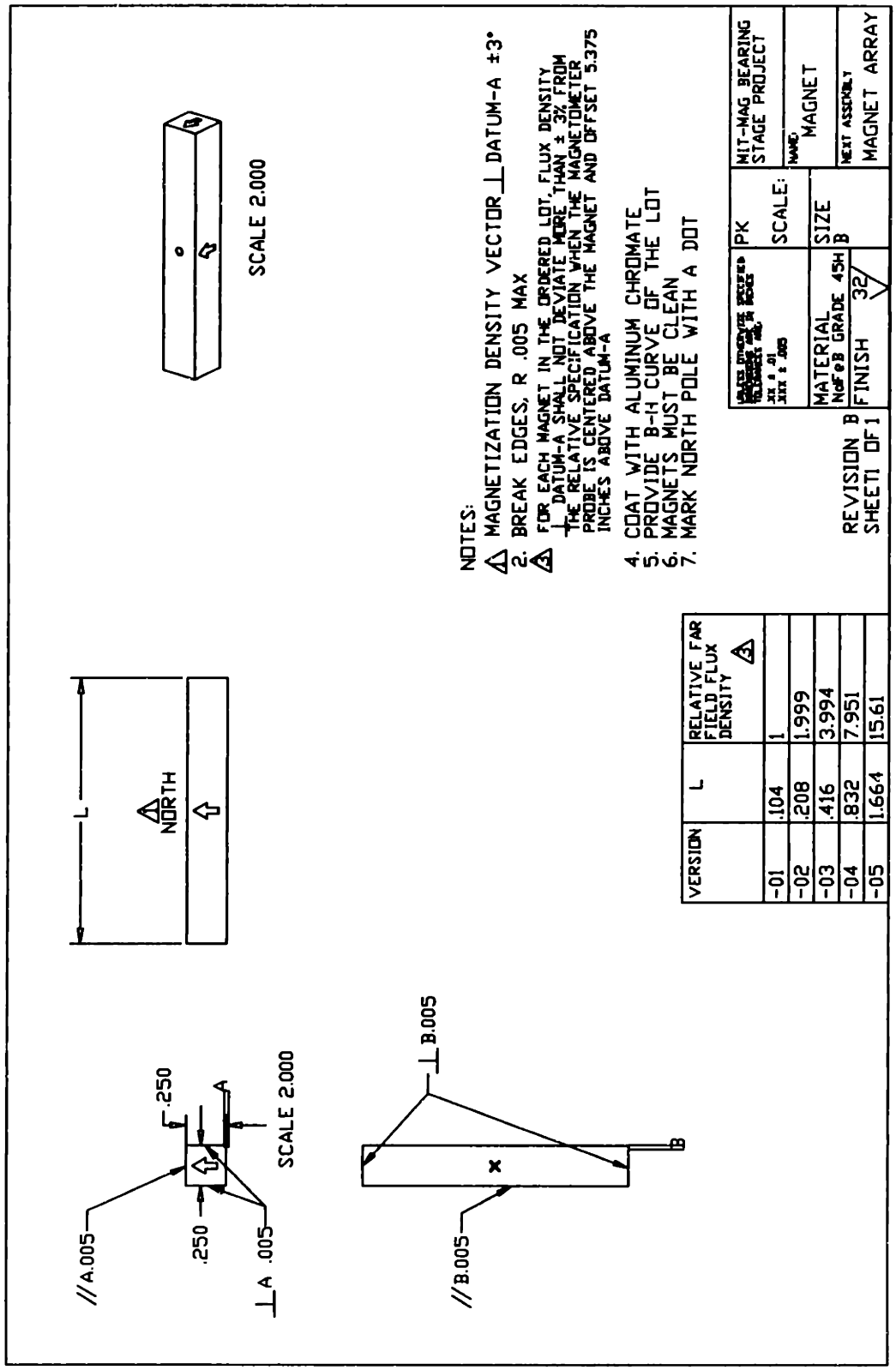

Figure 5-7: Magnets used to build the prototype array

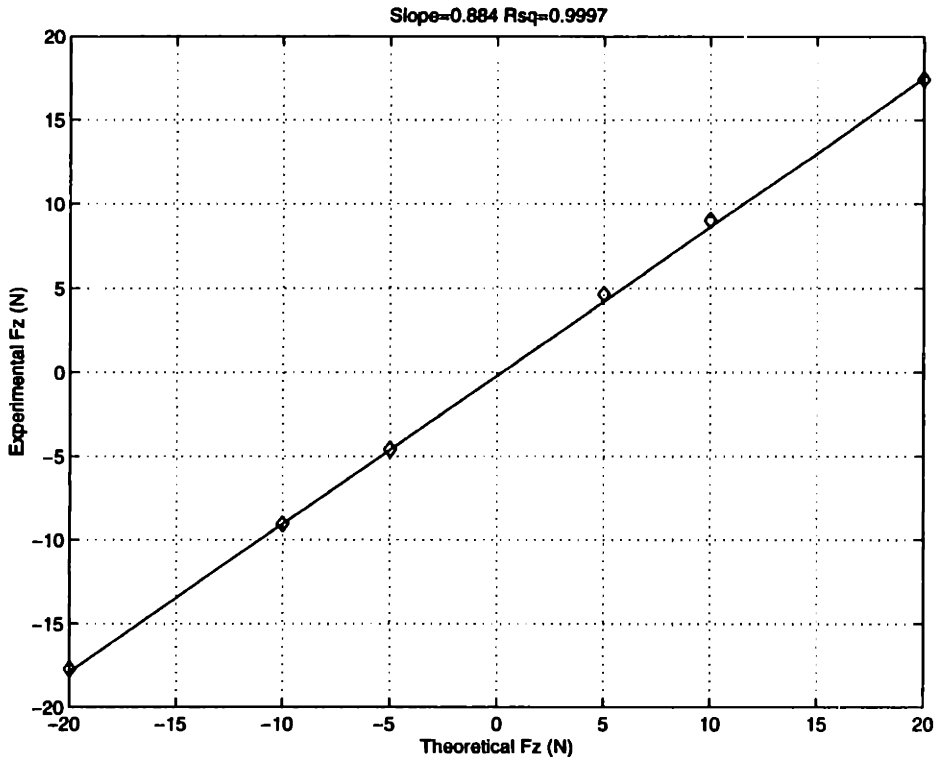

Figure 5-8: Experimental force versus theoretical force with least squares straight line fit

property was confirmed experimentally.

The results of the experiment are shown in Figure 5-8. The experimental force output is 88% of the theoretical prediction. This is very good corroboration of the theory considering that the model neglects the significant edge effects of the magnet array.

The moving mass was designed to represent approximately one fourth the mass of a production ebeam system that would require $13'' \times 13''$ of travel. Using back of the envelope calculations, the mass of a Zerodur interferometer mirror, $9'' \times 9'' \times 1/2''$ reticle, reticle carrier, NeFeB magnets, support for a $6''$ high structure, and margin for other hardware, the platen should weigh in at under 21kg. For the prototype, the magnetic bearing is oversized for the mass it moves. This is because I was conservative about the power dissipation in the stator. The stator, which has a resistance of 72.5Ω, supports the full weight of the prototype platen with only 58 watts of power [3].

[3] ΣI^2 flowing through the stator is $1.5 \times I_{max}^2$ according to the three phase commutation scheme.

Description	Units	Value
Array Pitch	m	0.0254
Array Width	m	0.1691
Magnet Remanence	T	1.35
Number of Pitches	NA	5
Maximum Gap	μm	750
stator thickness	m	5.08E-3
Magnet thickness	m	6.35E-3
Turns Density	turns/m^2	2.51E+6
G	m^3	1.12E-5
I_{max}, thermal current limit	A	5.88
$F_{z,max}$ at maximum gap	N	462.69
F_z /amp	N/A	78.69
Experimental Fz/amp	N/A	69.60
% of theoretical force	%	88%
Prototype Maximum Suspended Mass	kg	41.72
Actual Prototype Moving Mass	kg	5.19

Table 5.1: Magnetic Bearing Properties

5.3 Stator field analysis

The stator and the coils used in the prototype are shown in Figure 5-9 and Figures 5-10 and 5-11 respectively. The stator consists of 129 full current-density coils and 3 half current-density coils on each end. This stator can be modeled as a multipole of the form of Equation (4.59). Figure 5-12 shows how the stator is constructed to form a multipole with two levels of field cancellation. The first level of cancellation is due to the opposing dipoles inherent in a conventional synchronous motor stator with an integer number of spatial periods. For the three phase stator, one spatial period consists of 6 coils. I designate the $s = 1$ arrays with positive and minus signs on the ends, indicating that the currents in the three coils on the end of the 6 coil stack flow in the opposite direction the currents in the three coils on the other end. When these opposing $s = 1$ arrays are superposed with a $\lambda/2$ offset, the currents will have the correct phase relationship for a synchronous motor. For field cancellation purposes, the superposed arrays become an $s = 2$ array with $\lambda/2$ as the associated multipole moment arm.

The prototype stator is really a colinear superposition of 22 multipoles, each represented by the $s = 2$ building block. The multipoles are spaced colinearly apart by λ. As an initial approximation, the far fields of the 22 multipole will add. The dipole moment C from Equation (4.58) is derived by multiplying Equation (4.49) by 22 (the number of multipoles) and by 54 (the number of turns in each coil). Note that a factor of $1/2$ needs to be applied to C because the underlying dipoles are half current density coils. For the prototype stator C is calculated to be $.384 \times I$ (Amps m^2) from

$$C = \frac{22 \times 54 I \, l_{effective} \, w_{effective}}{2 \times 4\pi}. \tag{5.10}$$

The current I by the far field approximation is the sum of three currents flowing in the same direction. This approximates the sinusoidally distributed currents in the stator by one "lumped" phase. The scalar potential is completed by applying C and the multipole moment arm product given by $\lambda^2/4$ into Equation (4.59).

Fields emitted from coils can be calculated by the same algorithms as for magnets

Figure 5-9: Stator

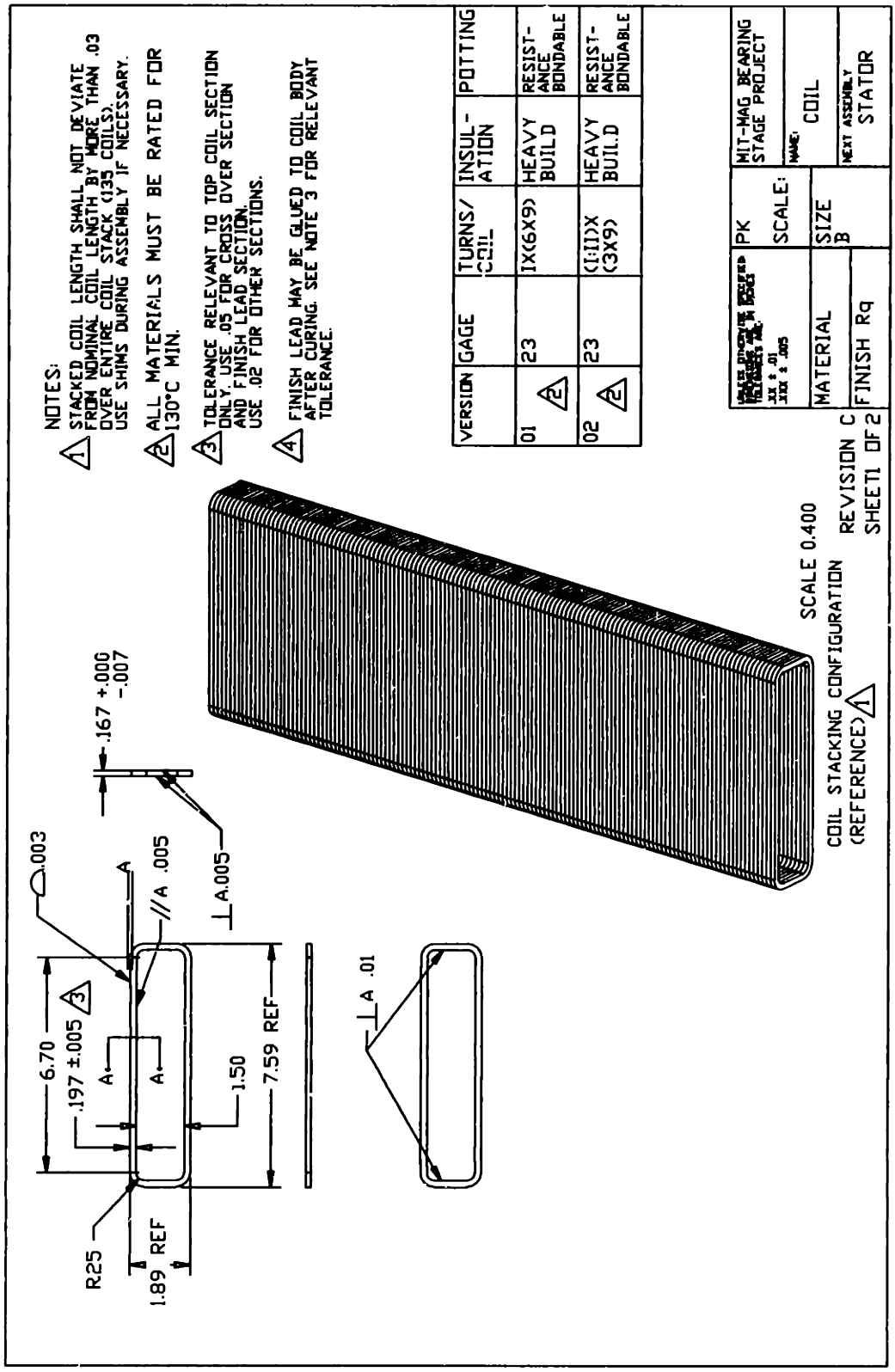

Figure 5-10: Coil used in the prototype stator

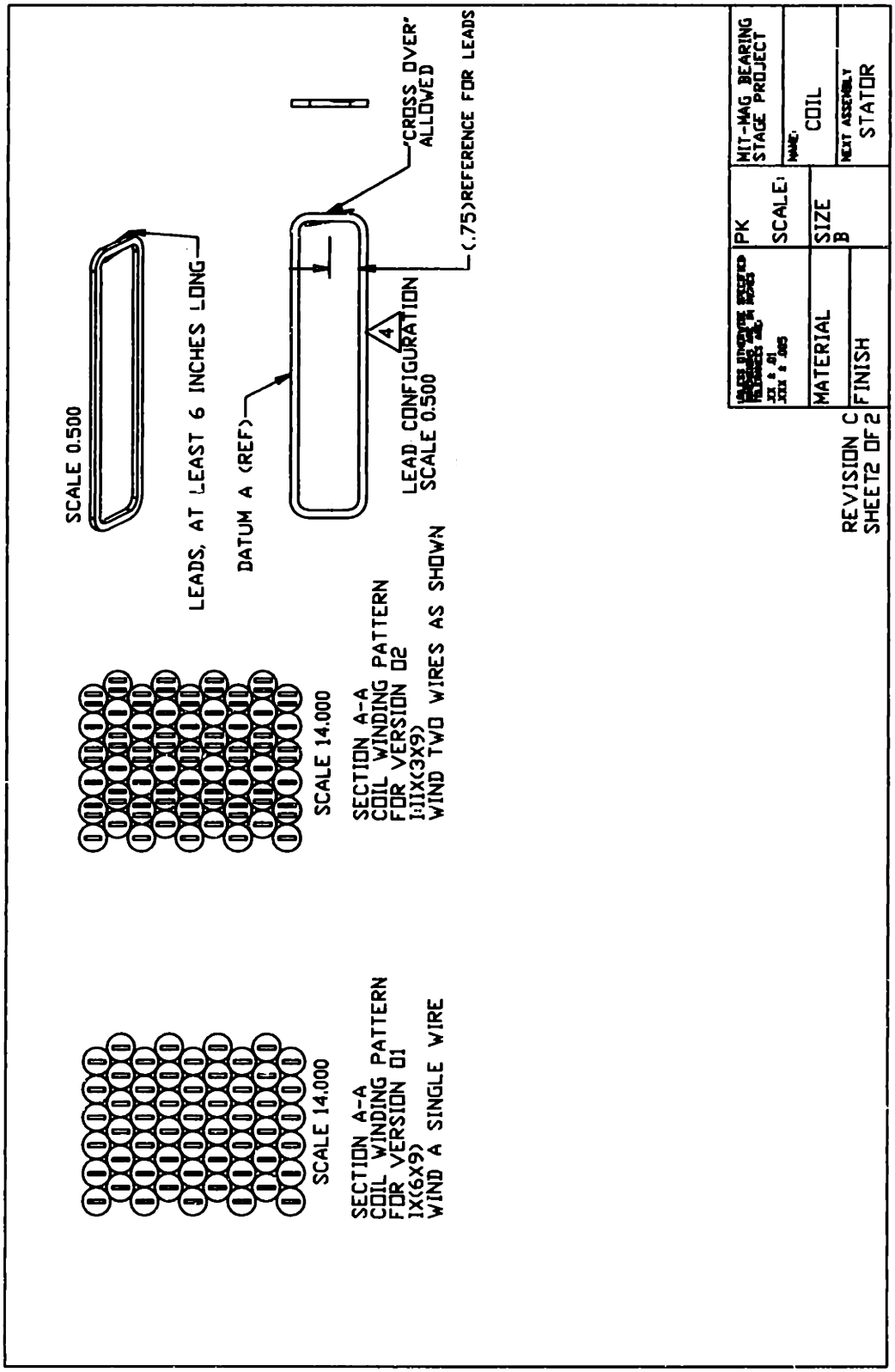

Figure 5-11: Coil used in the prototype stator continued

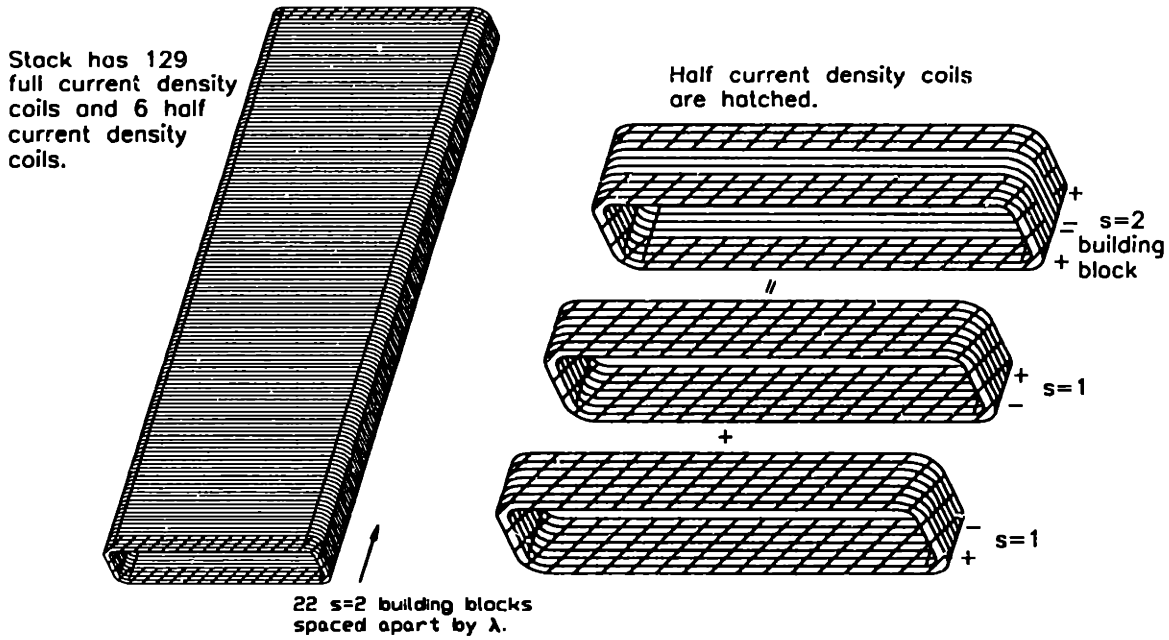

Figure 5-12: Multipole represenation of the prototype stator

by making an analogy between surface currents and magnetic charge. The plot of the fields computed with the charge integration method five inches above the stator is shown in Figure 5-13. A current of .4 amps or equivalently J_{max} of 1×10^6 A/m^2 in one phase is used in the calculation. The maximum flux density that would contribute to deflection of the electron beam is given by B_{xz}, which is defined as

$$B_{xz} = \sqrt{B_x^2 + B_z^2}. \tag{5.11}$$

The reference frame is shown in Figure 5-9, where z is along the long dimension of the coil stack and x is along the short dimension of the coil stack. The maximum magnitude of B_{xz} in this plane is 7.76×10^{-8}T. To help put the performance of the cancellation in perspective, it is interesting to compare the same field map to that of the conventional array (without the half current density end coils) shown in Figure 5-14. In this case, the maximum B_{xz} magnitude is $6.59 \times 10^{-7}T$ or 8.5× higher. For a valid comparison, both coil arrays are assigned the same travel capacity and surface currents. Bear in mind that this conventional array with an integer number of periods naturally consists of pairs of opposing coils and thus includes one level of

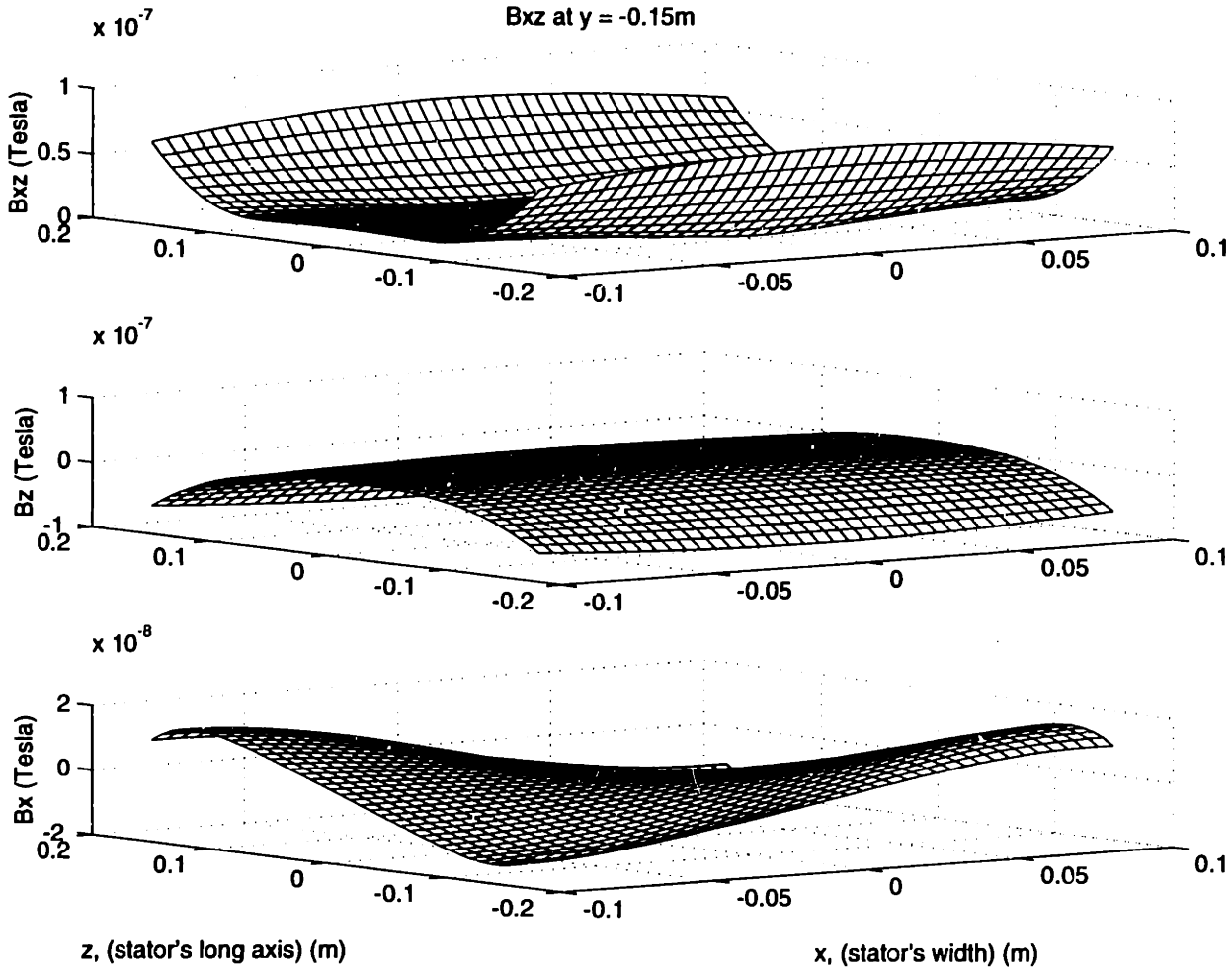

Figure 5-13: Flux density in the plane 5 inches above the top surface of the prototype stator with half current density end turns

dipole cancellation already.

Figure 5-15 shows the flux density as a function of height y above the stator's center using three different calculation methods. The multipole theory calculation is based on Equation (4.59). If the multipole theory is applied with the stator modeled as a single multipole centered at the origin, there is significant deviation from the charge integration solution when the distance from the multipole is not much greater than the largest characteristic length of the model. The largest characteristic length in this case is essentially the length of the stator. However, when I sum the solutions of the 22 underlying multipoles taking into account that they are distributed along the length of the stator the multipole theory is very accurate in the entire region of interest. The

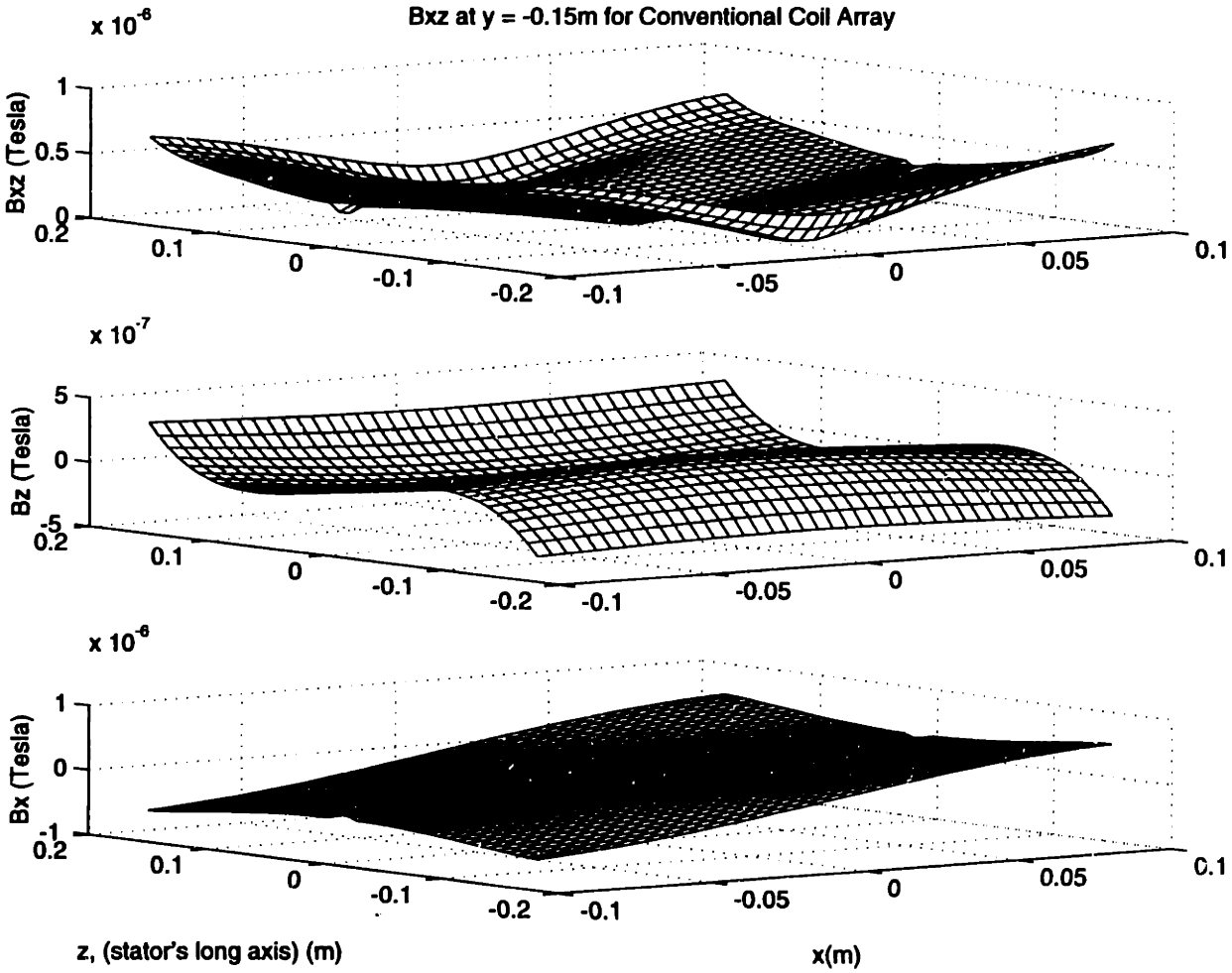

Figure 5-14: Flux density in the plane 5 inches above the top surface of a conventional stator

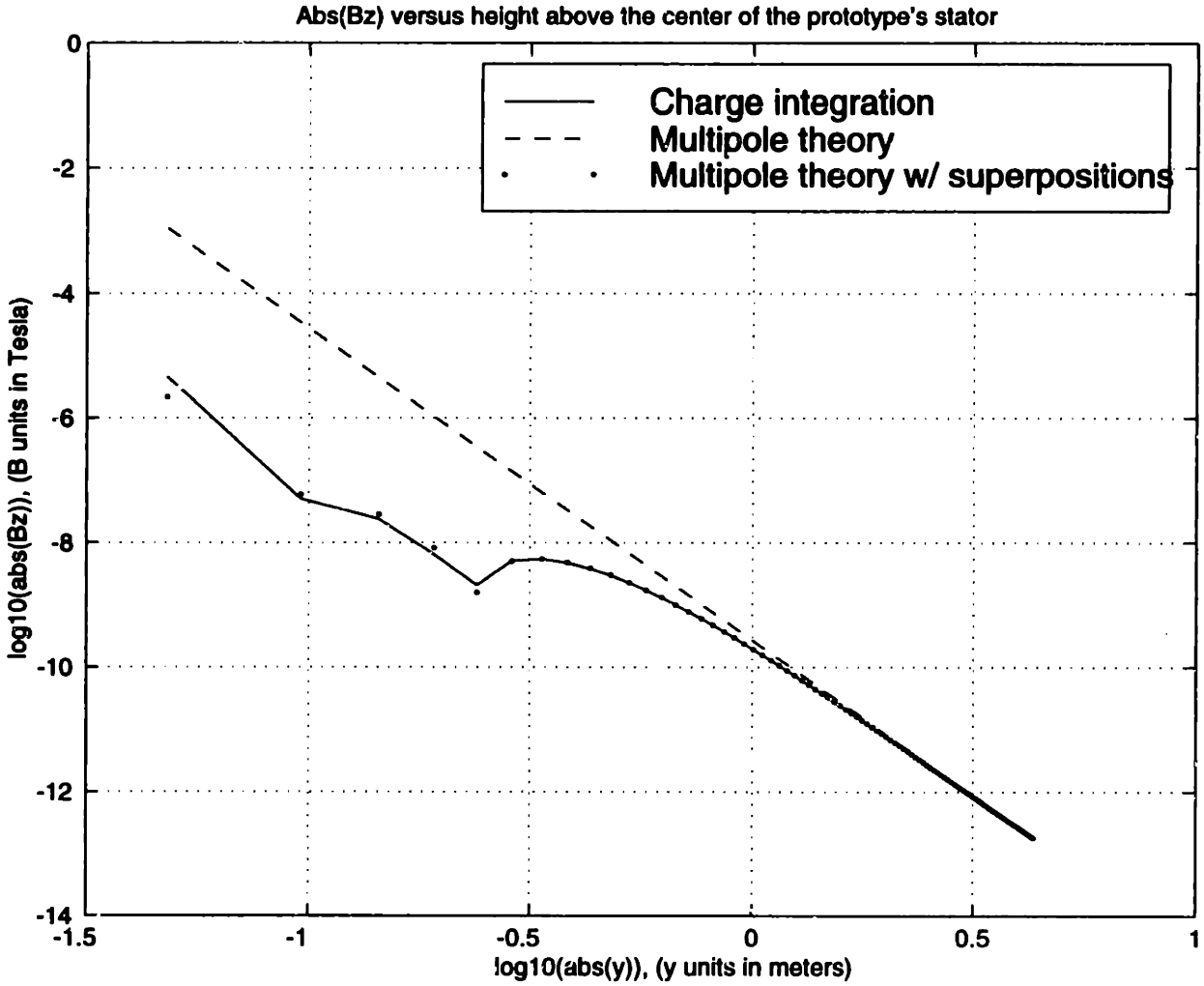

Figure 5-15: Flux density above stator calculated using three different methods

intersting dip in the curve is due to the changing orientation of the magnetic field vector. At the dip the calculated component (in the z direction, above the center of the stator) of the field is nulled as the field changes orientation with respect to the height above the stator. Furthermore, the angle θ calculated for the individual multipoles changes as y changes. When the fields for the 22 multipoles distributed along a line are superposed, we see the null in the calculated field component as the dip.

The fields in this section thus far have been computed with J_{max} of $1 \times 10^6 A/m^2$ in one phase. For a valid performance evaluation, the fields need to be scaled to account for the J_{max} that would support the full weight of the platen and to account for the

current in the other phases. Although the currents in the phases are sinusoidally distributed, the far field solution is essentially the same as if the sum of the currents in each phase is used in a single coil. This is valid because the centers of the phases are separated at most by 1/3 of a spatial period or 1/3 of an inch for the prototype. This characteristic length is very much shorter than the distances of interest for field calculations.

The maximum scale factor that accounts for suspension of the prototype mass and the commutation is 3.66. To account for the mass of the prototype, I use the values from Table 5.1 where the moving mass is 5.19kg and the force per amp is 69.60 N/A. This gives the maximum current required in a single phase. I then use of the fact that a current density of 1×10^6 A/m^2 in a prototype coil corresponds to a terminal current of .4 amps. To account for the fact that there are three phases, I sum the phase currents from Equation 5.5 and find that the maximum sum is two times the maximum current in a single phase. The scale factor then is $2 \times 5.19\text{kg} \times (9.81\text{m/s}^2)/(.4\text{A})/(69.60\text{N/A}) = 3.66$. In this case, the maximum expected B in the plane five inches above the stator is $2.85\times10^{-7}T$. However, if we consider that the coil may be nominally centered under the ebeam as in the stacked coil stage of Figure 3-6, it is valid to just consider the inner area of the coil. If just the inner 2″ by 2″ square above the coil is included in the calculation, then the maximum flux density shown in Figure 5-16 is 7.62×10^{-8}. This square sufficiently accounts for the entire range of field magnitudes that the ebeam would experience for the entire range of commutation if the stator is nominally centered under the column (with an allowance for up to 1.5″ offset for whatever architecture reason). The calculation uses the effective 1g current density of $3.67\times10^6 A/m^2$. It is interesting to note from the figure that B_{xz} does not increase as the area of interest enlarges for this centered location. If the stator is offset from the ebeam axis as in some of the proposed designs, a similar calculation could be performed in the area of interest.

Again, it is interesting to compare the performance to that of a conventional stator. The results of the same calculation but for a conventional stator are shown in Figure 5-17. The maximum flux density in this case is 4.83×10^{-7}T or 6.34 times

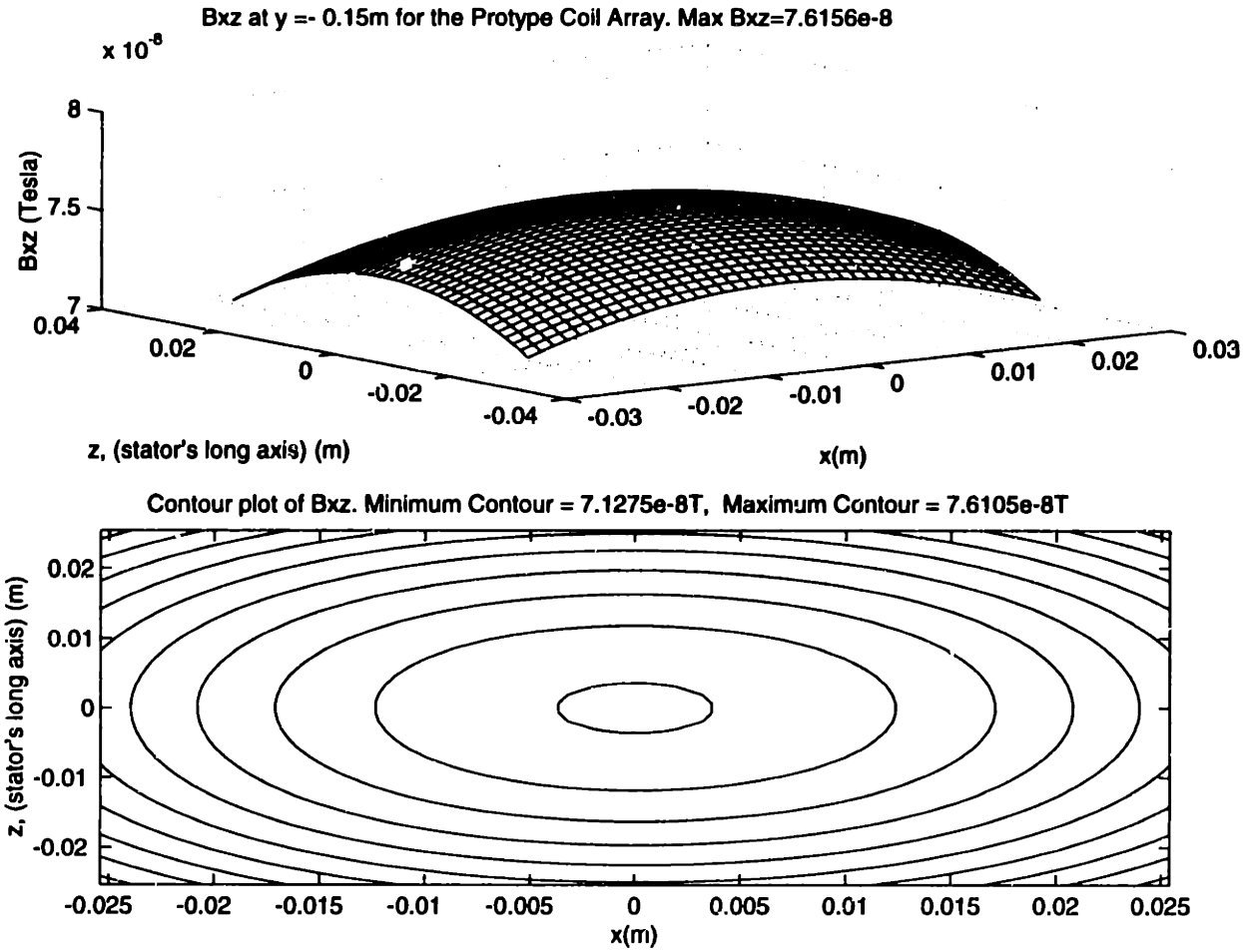

Figure 5-16: Flux density in the plane 5 inches above the top surface of the prototype stator when the current is scaled to suspend the prototype mass (F_y=-51N).

higher than the prototype's result. Furthermore, B_{xz} increases as the area of interest enlarges, making the performance sensitive to stator placement.

There are several inconsistencies with the prototype stator and a system that would be suitable for ebeam lithography. In order to test whether the stator topology that was tested for the prototype would scale to meet real system requirements, I calculated the necessary height to meet the 2mG flux density if the stator had the appropriate modifications. For instance, if the magnets were allowed to occupy a footprint of $14'' \times 14''$ the required stator top surface width would be $27''$ long for $13'' \times 13''$ of travel. If in this footprint the magnets occupied 5/16 of the footprint area, the magnet area would be 1.84 times that of the prototype. The effective current density must support 21 kg (204N) in this configuration and J_{max} becomes

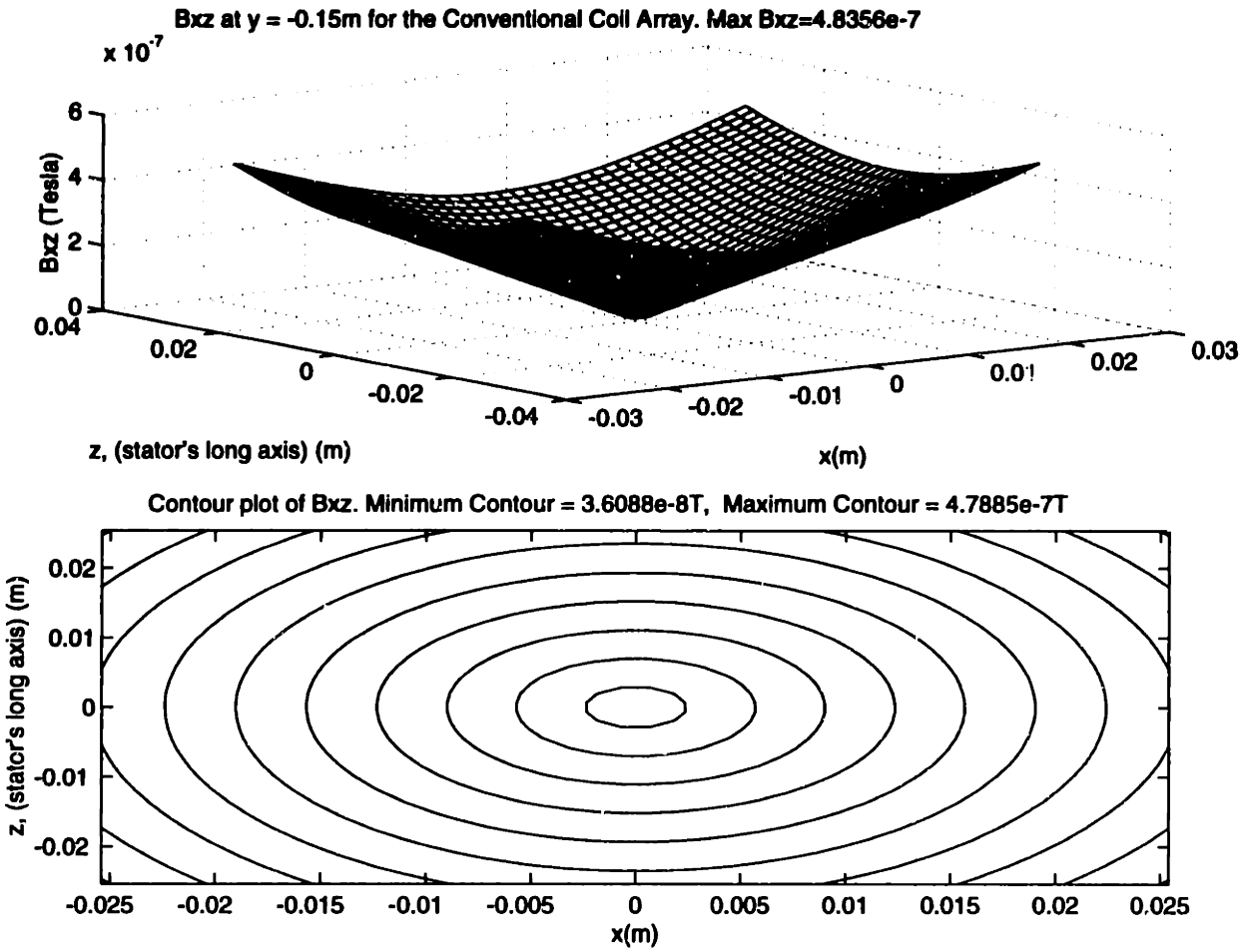

Figure 5-17: Flux density in the plane 5 inches above the top surface of a conventional stator when the current is scaled to suspend the prototype mass (F_y=-51N).

$8\times10^6 A/m^2$ for field calculation purposes. The stator would also need to be 8″ longer than the prototype, but I do not add the 8 extra periods of coil for this calculation because the result will be close enough for estimation purposes. After applying these parameters, a 2mG flux density is attained at 5.7″ above the stator's center plane. Thus, the write surface of the reticle would be allowed to be placed 4.75″ above the stator's top surface , as the top surface is .95″ above the center plane (if the magnetic bearing fringing field was limited by the stator). The plot of the flux density versus position above the stator is shown in Figure 5-18. Note that this time the multipole theory with superpositions is not as successful as for the prototype stator. This is because this stator has a very long characteristic length associated with its 27″ width. The multipole theory could readily shorten this characteristic length by breaking up the multipoles into smaller multipoles and then applying the superpositions. For instance, if we wanted very accurate solutions at 5″ above the stator, in calculation I would break the stator into strips about 1/10 this length or .5″ wide. The superposition of the field solutions for the 54 strips would yield the very accurate solutions desired.

This field analysis serves as a good feasibility study. The scaled model of a stator that would be suited for real system requirements shows that the top of the low fringing field stator would require a spacing of approximately 5″ from the write surface of the reticle. Certainly, field cancellation could be extended to achieve faster falling fringing fields but a 5″ spacing is very reasonable considering that sufficient space is required for a high natural frequency structure.

5.4 Magnet and coil tolerances

Effective field cancellation schemes must account for magnet and coil tolerances in addition to the prediction from ideal theory. In this section I lay the necessary groundwork that leads to simulations considering the effects of tolerances.

This analysis must consider variations in remanence, magnetization orientation, height, width, length, squareness, parallelism, and magnet/coil placement. Unfortu-

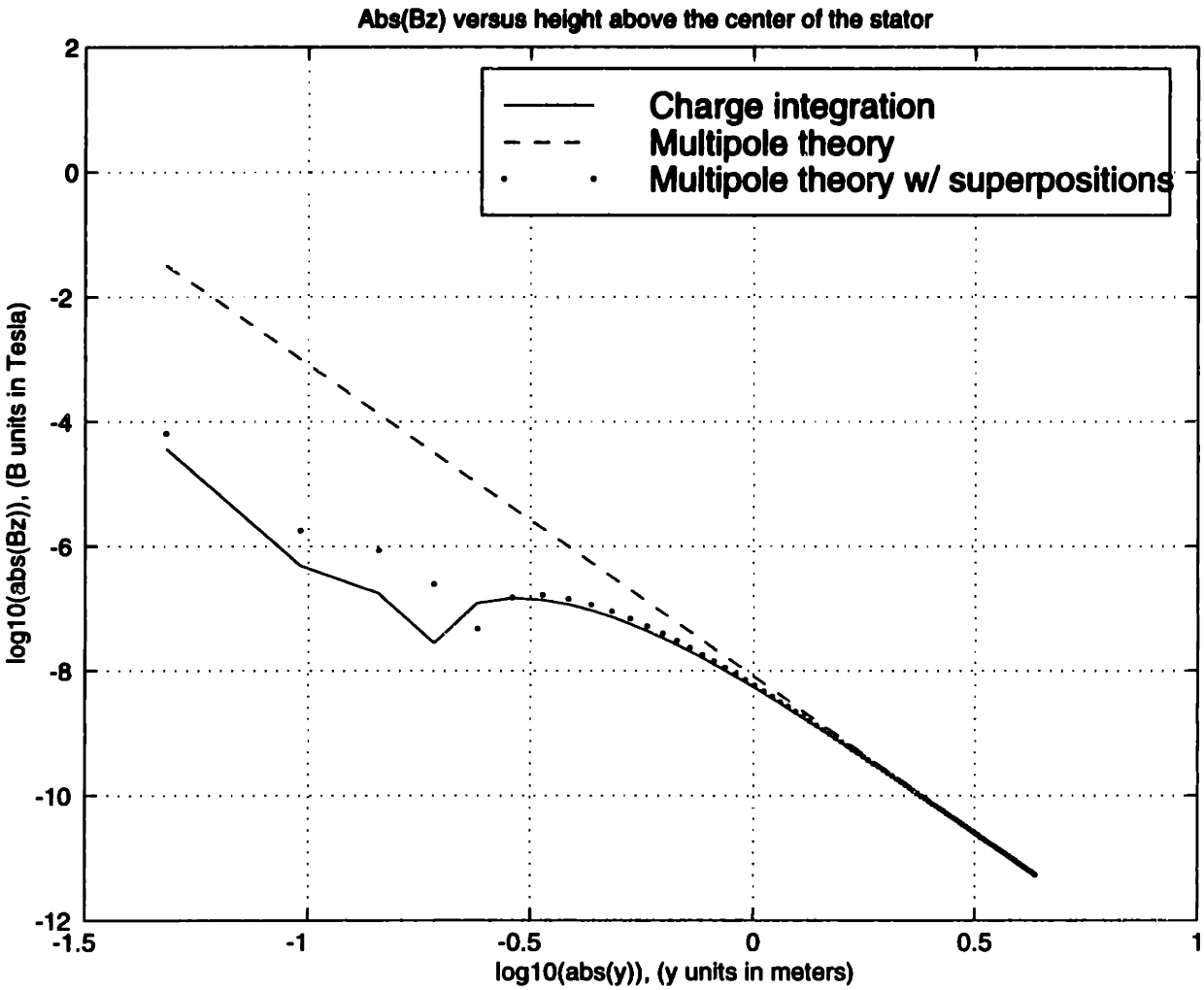

Figure 5-18: Flux above a stator scaled to system requirements

nately, it is likely that the tolerance requirements will exceed standard specifications in high performance cancellation schemes. This is going to be especially true for magnet arrays, which in most cases will have higher equivalent surface currents than the coils and worse manufacturing tolerances.

One way to deal with this tolerance limitation is specification of a "lumped remanence," which is derived from specification of a magnet's flux density at a far field point in space. Thus, tolerances including the remanence, height, width, length, squareness, parallelism are lumped together. Moreover, one can specify the flux density at a point (or points) in space whereby the magnet vendor must attenuate a magnet's remanence toward a nominal lumped remanence value. This allows tighter magnetic flux density specifications in the far field than would be possible by specifying all the terms in the lumped remanence separately. However, there is a limit to how tightly the lumped remanence term can be held and this method alone is not likely to be sufficient to achieve the rapidly falling fringing fields desired.

The lumped remanence for magnets which I term ΔC is defined as

$$\frac{\Delta C}{C} = \sqrt{(\frac{\Delta_M}{M})^2 + (\frac{\Delta_l}{l})^2 + (\frac{\Delta_w}{w})^2 + (\frac{\Delta_h}{h})^2} \tag{5.12}$$

where C, M, l, w, and h are the nominal values defined for Equation (4.46) and the Δ terms are their respective variations. In my experience, magnet vendors routinely machine magnet blocks to better than $\pm.005''$. Thus, for a magnet block .25"x.25"x.25" the expected lumped remanence contribution due to machining alone will be over 3%. On top of that, if the vendor's magnetizing process induces remanence with variations of 3%, the lumped remanence climbs to over 4%. By the way, 3% remanence variations are much better than I would expect unless 3% was specified to the vendor. Stock magnets from vendors can have remanence variations of up to 20%. In my experience, a good vendor can readily fabricate dipoles with a $\pm 3\%$ lumped remanence on a custom order. I did not locate any vendor who would do better without significant cost increases.

The lumped remanence for coils, assuming that the coils are wound with the

correct number of turns, is defined as

$$\frac{\Delta C}{C} = \sqrt{(\frac{\Delta_l}{l})^2 + (\frac{\Delta_w}{w})^2}. \tag{5.13}$$

Here l and w are the effective length and width given by Equation (4.49). In the case of a magnetic bearing stage for electron beam lithography the smallest of these dimensions is expected to be greater than an inch. Furthermore, in my experience, coils can be wound consistently to the dimensions of the tooling within $\pm.003''$. Thus, the lumped remanence for coils is expected to be less than .3%.

Another critical parameter is the magnetization orientation. For magnets, orientation can be held to $\pm 3^o$ with respect to a block's side. I could not locate a magnet vendor who would guarantee better. It should be noted that die pressed grades of magnets are the magnets of choice for high performance cancellation schemes because they generally have better orientation tolerances than isostatically pressed materials. Furthermore, assembly tolerances play a role in the magnetization orientation. For instance, for a magnet with .25″x.25″ cross section and .005″ geometrical tolerances, the best tolerance for assembly orientation is expected to be $\pm 1^o$. For coils, the orientation tolerance is expected to be considerably better, less than half a degree.

The final tolerance consideration is the magnet/coil placement. In general, an assembly process can locate the components to $\pm.01''$ of the nominal. In the far field, this tolerance generally has negligible influence if all the other characteristic lengths are much bigger.

The sensitivity of an array's fringing field to the tolerances is largely dependent on the degree of attenuation desired. In my later analysis, Monte Carlo simulations characterize these sensitivities for a protyped array. This analysis strategy can readily be extended to other arrays.

5.4.1 Tolerance compensation schemes

The fringing field contribution due to tolerances can be reduced by exploiting statistical averaging. In this method, many small magnet blocks are assembled, resulting

in reduction of fringing fields because of the averaging effect. The expected relation of the fringing field due to tolerances, where N is the number of assembled magnets, and under the assumption that the errors are uncorrelated in each block is

$$B \cong \frac{1}{\sqrt{N}}. \tag{5.14}$$

This method is an expensive option because generally many machined magnets would be required and assembly would be very tedious. However, it should be noted that statistical averaging is inherent in every magnet array.

Another way to achieve field attenuation is with shielding. Unfortunately, as I already discussed in Chapter 3, a planar stage is difficult to shield without compromising its structural performance. Thus, I do not consider shielding effects other than those due to the permeable material expected to be surrounding the vacuum chamber.

Another possibility includes sorting magnets. Because fields can be measured to better than a part per million using a flux gate magnetometer, it is possible to measure the magnitude and orientation of magnet dipoles to better accuracy than the vendor is willing to provide. A magnet lot could then be measured and sorted to "match" magnet properties for better cancellation. This technique has major drawbacks in that it is labor intensive and it still cannot compensate for assembly tolerances.

Yet another way to attenuate the fringing fields due to tolerances is to include a another layer of field cancellation beyond the levels inherent in the magnetic array. This method holds great promise as a low cost solution because it requires relatively little additional magnetic material and it would allow the overall tolerances to be relaxed. Also, it is expected to be very effective because it can accommodate assembly tolerances. In this method, the fields are mapped and then analyzed to decompose the multipole contributions. Trimming magnets are then designed, constructed, and placed to achieve field cancellation approaching that of the perfect theoretical array. The implementation of this procedure is a promising area for further work beyond the boundaries of this thesis.

5.5 Stator tolerance analysis

Field cancellation schemes are likely to be limited by the tolerances of the magnetic components. In the case of the stator, I simulated its sensitivity to tolerances in lumped remanence, coil orientation, and position through monte carlo simulation. Moreover, I assigned a 3σ tolerance to the coils and then used a normally distributed random number generator in Matlab to assign new properties to each coil in the array.

The simulations calculated the distance to achieve a nominal B_{zz} at the corner of the stator. As you can see from Figure 5-13, B_{zz} in the plane above the stator is nearly the maximum at the corner. The results of these simulations are shown in Figure 5-19. The nominal location h_{ref}, is 5.35″ above the top surface of the array. Each of the graphs examine the independent effects of coil orientation, position, and lumped remanence. While the data does not provide the complete picture statistically, it does provide some indication as to the sensitivity of the fringing field to the tolerances. The fringing field shows strong sensitivity to the coil orientation tolerance, Θ_z, when its 3σ envelope is only 1.2 degrees. Here Θ_z corresponds to 3σ pitch of individual coils about the x-axis shown in Figure 5-9. Meanwhile the position tolerance is not very sensitive, whereby only a small increase in height to the nominal B_{zz} occurs for .04″ of random displacement. The data for the positional tolerance is peculiar, where no effect is seen up to .03″, and then nearly a 15% increase for the .04″ tolerance. Because of the limited amount of data, it is impossible to make firm conclusions. More importantly, the coil positional tolerance did not show any significant effect over a very generous range of tolerances. The lumped remanence begins to show sensitivity when it has $3\sigma B_r$ of 2%. Note that the data shows that the field is reduced for the $3\sigma B_r$ of 2%. This is statistically possible, but the fields associated with the tolerances could just as easily been additive as subtractive. Again it is impossible to make any firm conclusions with the limited amount of data. A complete field map and more data would provide better insight, but it turns out that good tolerances on the coil array are relatively easy to achieve. For practical purposes, I did not pursue further data.

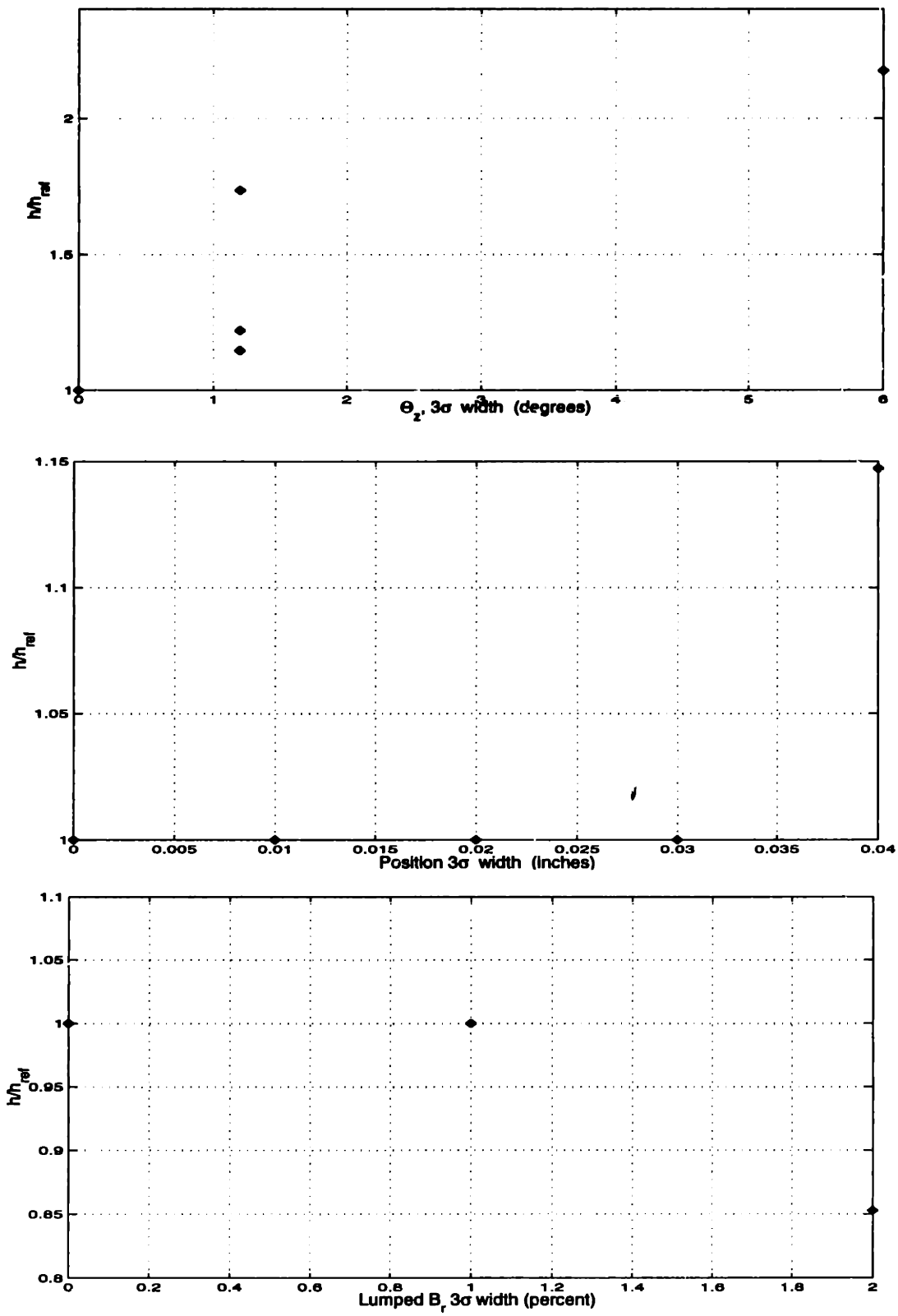

Figure 5-19: Results from coil array tolerance simulations

The expected tolerances are readily calculated from the drawing specifications and the analysis in Section 5.4. The lumped remanence for a coil, which is given per Equation (5.13), yields .8%. However, the consistency of the coil fabrication was much better than the drawing specifications. In my experience, the coils were dimensionally consistent to .003″. Thus, the expected lumped remanence is calculated as .3%. The angular tolerance can be estimated from the perpendicularity specification and the minimum characteristic length of the coil cross section since the coils are pressed together firmly during assembly. The angular tolerance becomes .2 degrees. While the positional tolerances were allowed to be .03″, when the array was constructed the position of the coils were calibrated during the shimming process to .01″. Given these estimates, the tolerances were not expected to appreciably diminish the performance of the stator.

5.6 Coil array manufacture

The coils were manufactured with the tooling shown in Figures 5-20 and 5-21. Wire Winders[4] wound the coils, while MIT's Central Machine Shop fabricated the tooling. The winding begins by inserting the start lead into the groove machined into the tooling. Because it turned out to be difficult to start the winding on the center of the long section, another groove was placed on the end of the inner plate such that the winding could start on a corner. This resulted in the winding cross over on the short length of the coil as reflected in Figure 5-11. After winding the wire, additional plates are clamped to the tops of long sections of coil. During the curing process, the coils form to the shape of the tooling. In order to meet the relatively tight height specification for one of the coil cross sections, the tops of the inner and outer plates were machined by Wire Winders. After the curing, the coil was removed from the tooling by separating the plates. The pins assured that the tooling could be reassembled precisely for the next coil winding.

A modification to the tooling that I would suggest for future designs would in-

[4]Wire Winders, Inc., 151 Mount Vernon Road, Milford, NH 02055

clude either thicker inner and outer plates or additional fasteners placed to prevent the bowing of the inner and outer plates. Moreover, because of unexpectedly high clamping forces, the bowing of the tooling prevented the initial coils from meeting the width specification. This problem was solved by curing the coils with C clamps that forced the ends of the plates together. However, it would be desirable to avoid the use of the clamps by preventing significant bowing in the first place.

5.7 Measured stator fields

As previously discussed, in order to not deflect the ebeam the fringing field contribution from the stage should be kept below 2mGauss. Thus, the minimum resolution of the measurement instrument should be better than .2mGauss. For research purposes, it helps to have even better resolution if subarrays and field aberrations due to tolerances are to be characterized. For my measurements, I used a Bartington Mag-03MC100 Three Axis flux gate magnetometer with a Bartington Mag-03PSU Power Supply Unit[5]. This instrument has a measurement range of $\pm$1G, calibration accuracy of$\pm$.5%, and noise rating of $< 25\text{pTrms}/\sqrt{\text{Hz}}$ at 1Hz. A third order low pass filter with 1Hz bandwidth was employed to attenuate environmental noise. I designed this filter to attenuate 60Hz noise to 50ppm. Since the ambient 60Hz noise was measured to range between 10mG and 20mG, these field components contribute less than 1μG to the field measurements. Finally, the data was read with an HP3478A Multimeter.

For the measurement of weak, fast falling fringing fields, this instrument has several important limitations. First of all, because of the finite size of the flux gate needles, care must be taken to avoid measurement errors due to the changing orientation of the field components across the needle[6]. Moreover, the flux gate needles average the field along its cores and, in the worst case, a 180 degree rotation along its cores yields a null reading. These errors are reduced as measurements are taken

[5]Manufactured by Bartington Instruments Ltd., 10 Thorney Leys Business Park, Witney, Oxford OX8 7GE, England

[6]the needle length is 20mm

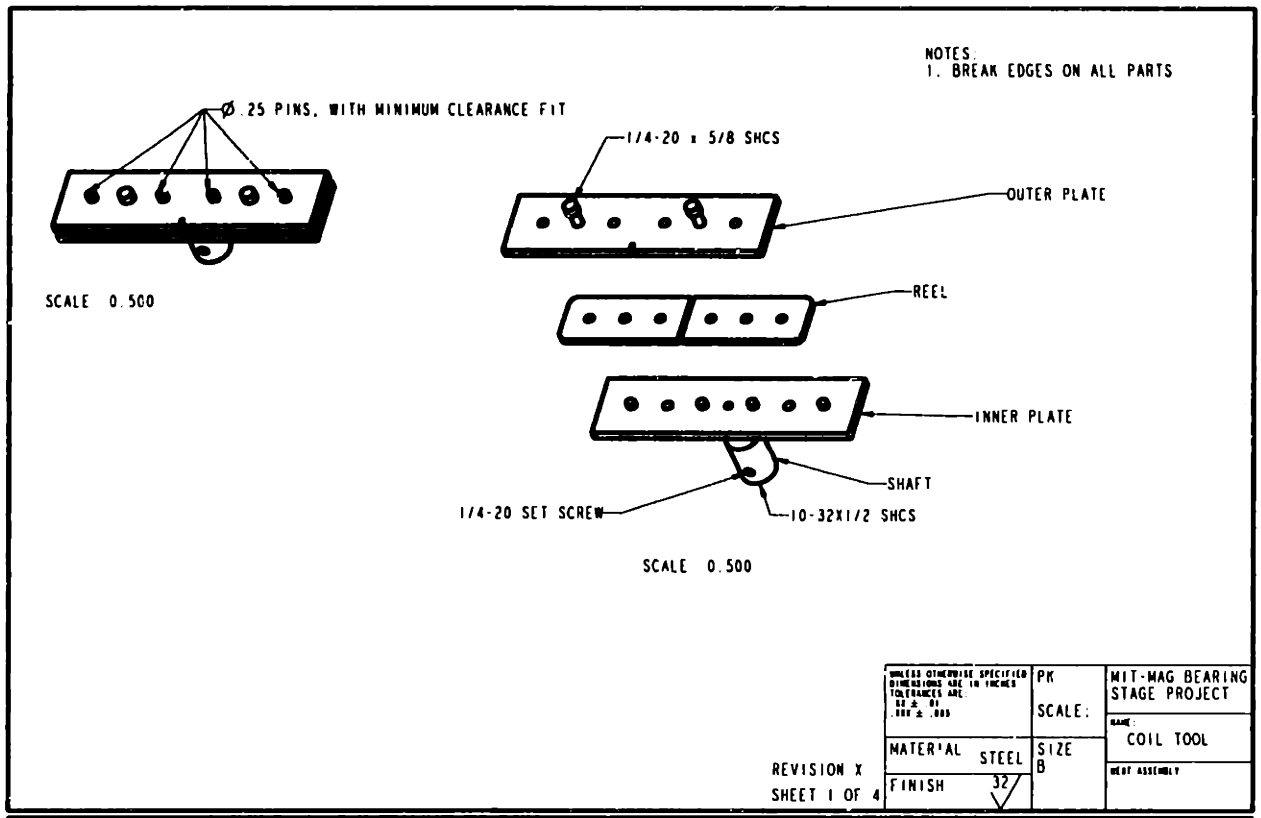

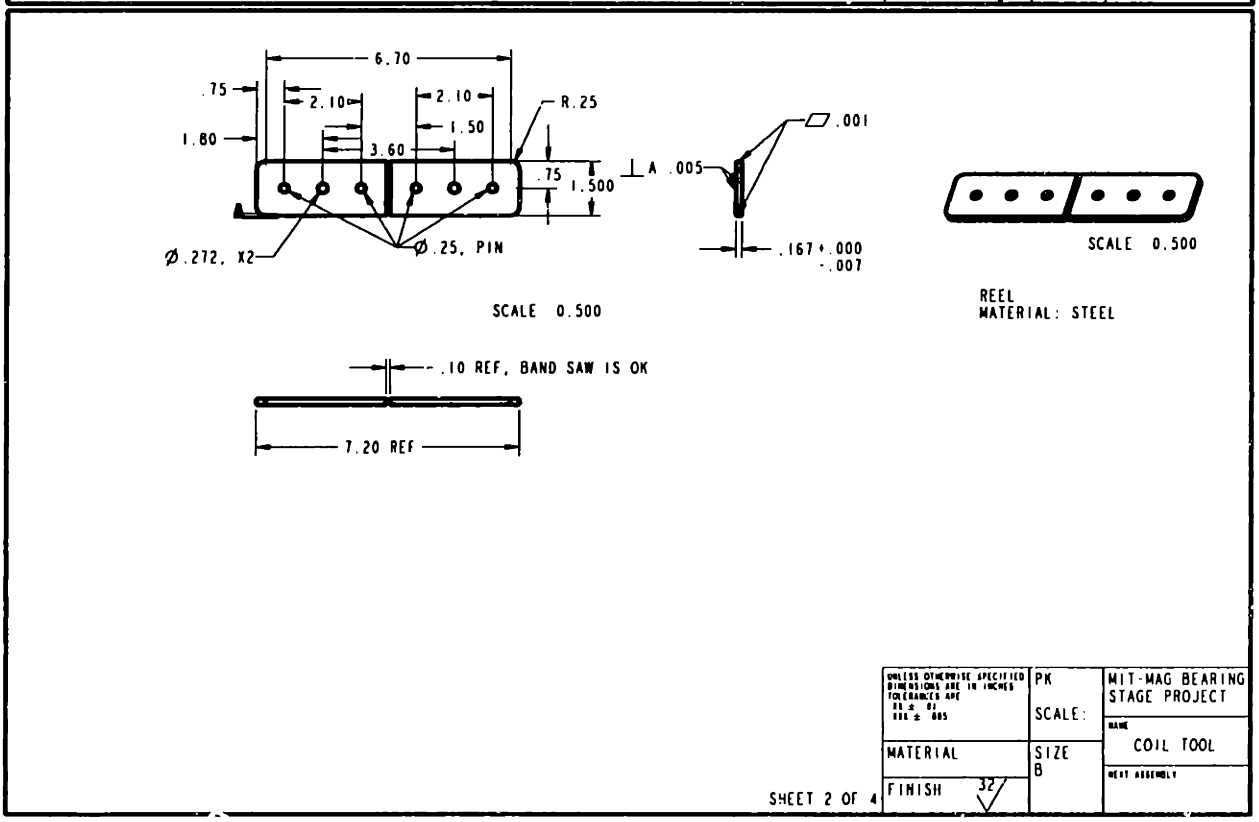

Figure 5-20: Coil tooling

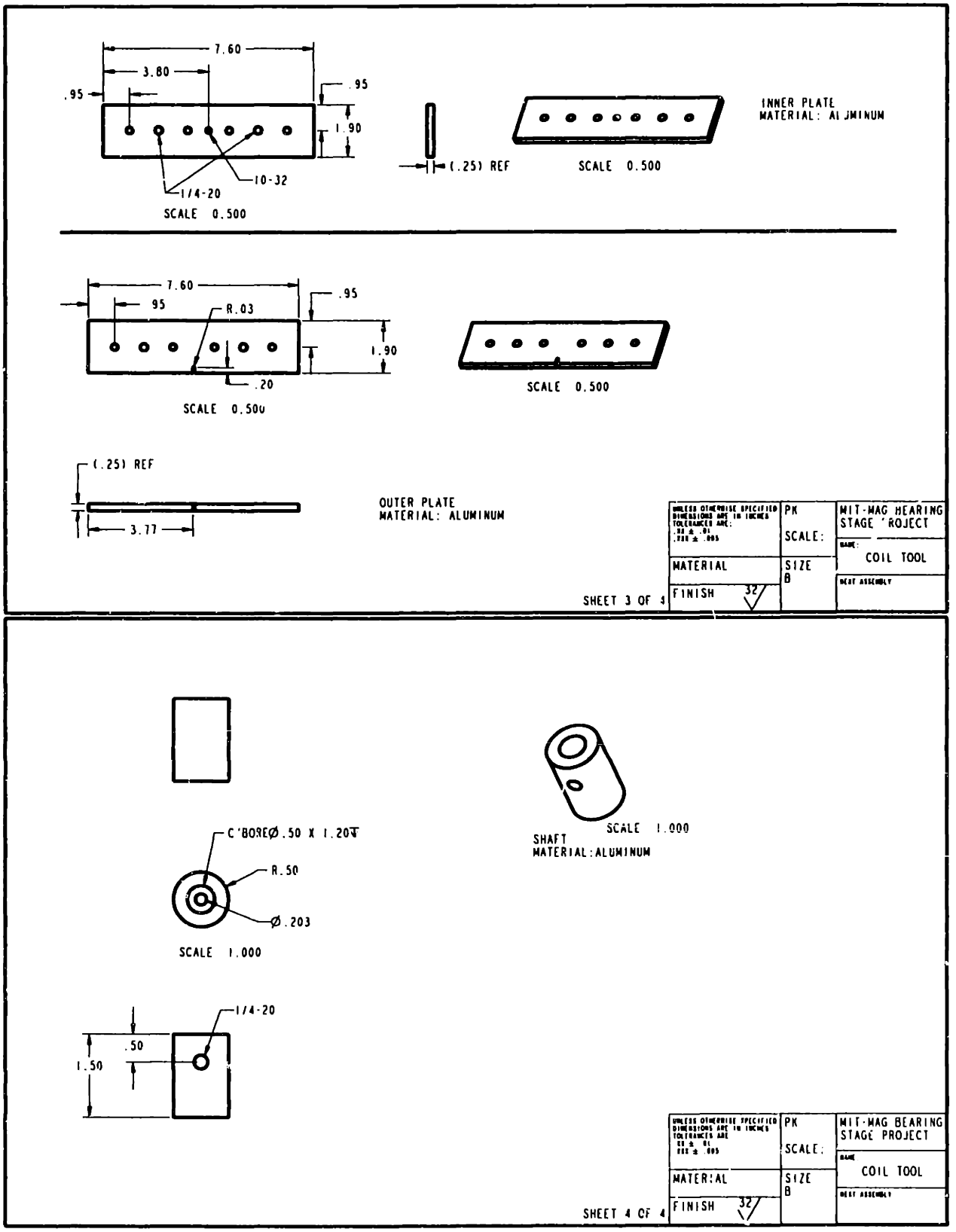

Figure 5-21: Coil tooling continued

at greater distances from the multipoles. However, at large distances the signal to noise ratio of the sensor renders the measurement meaningless. It is a good idea to reduce the characteristic length of the slender needle by orienting the needle radially with respect to the multipole's origin. However, this is not always possible. Another limitation of the sensor is that practical mounting schemes can align the magnetometer to no better than ± 1 degree. Furthermore, the location of the flux gate cores is known to only about ± 2mm.

With any low field measurements, the earth's field must be subtracted from the measurement. For stator measurements, this is easily accomplished by subtracting the field reading when the stator is off from when the stator has current flowing through it. For magnet array measurements, the magnetometer cannot be moved after measuring the earth's field and therefore the array must be free to be positioned.

Experimental field data from the stator is shown in Figure 5-22, where the distance $abs(y)$ is in the negative y direction as per the coordinate system shown in Figure 5-9. This data was taken with the magnetometer probe directly over the phase A in the middle of the coil stack. The nominal current is .4 amps. The magnetometer was fastened to a granite bar and its height was adjusted by propping the bar with blocks as shown in Figure 5-23. I do not expect that the position of the magnetometer with respect to the stator was known to better than $\pm .1''$ in this setup.

The data shows good corroboration of the theory for B_x. From the plot in Figure 5-13 one can see that B_z is predicted to be null at the nominal sensor location. I attribute the experimental results for B_z primarily to the leads. For the theoretical prediction of B_z in Figure 5-22, I took into account the dipole formed by the stator's leads that I neglected in previous calculations. The leads form a dipole the length of the stator. I assume a 2-d dipole with $.5''$ width. The width estimate comes from the coils having a thickness of about $.2''$ and the measured lead overhang of $.15''$ on each side. The current associated with the dipole is equal to the current in the stator. To calculate the dipole's fringing field I use Equation (4.23), which is the 2-d vector potential for a current dipole. For the calculation I assume the dipole is centered on the side of the stator. The leads that daisy chain the phases are located on the

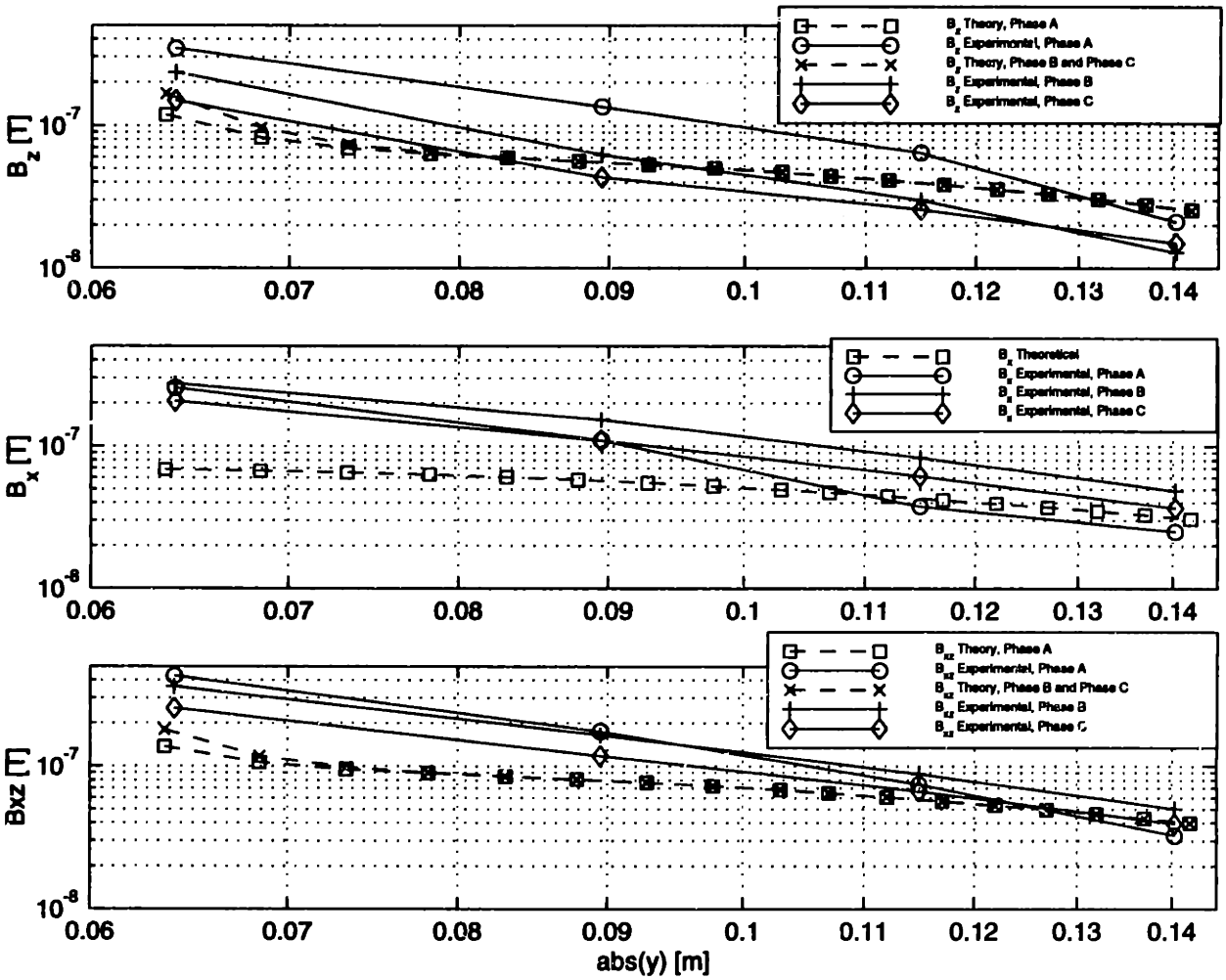

Figure 5-22: Experimental and theoretical data for stator

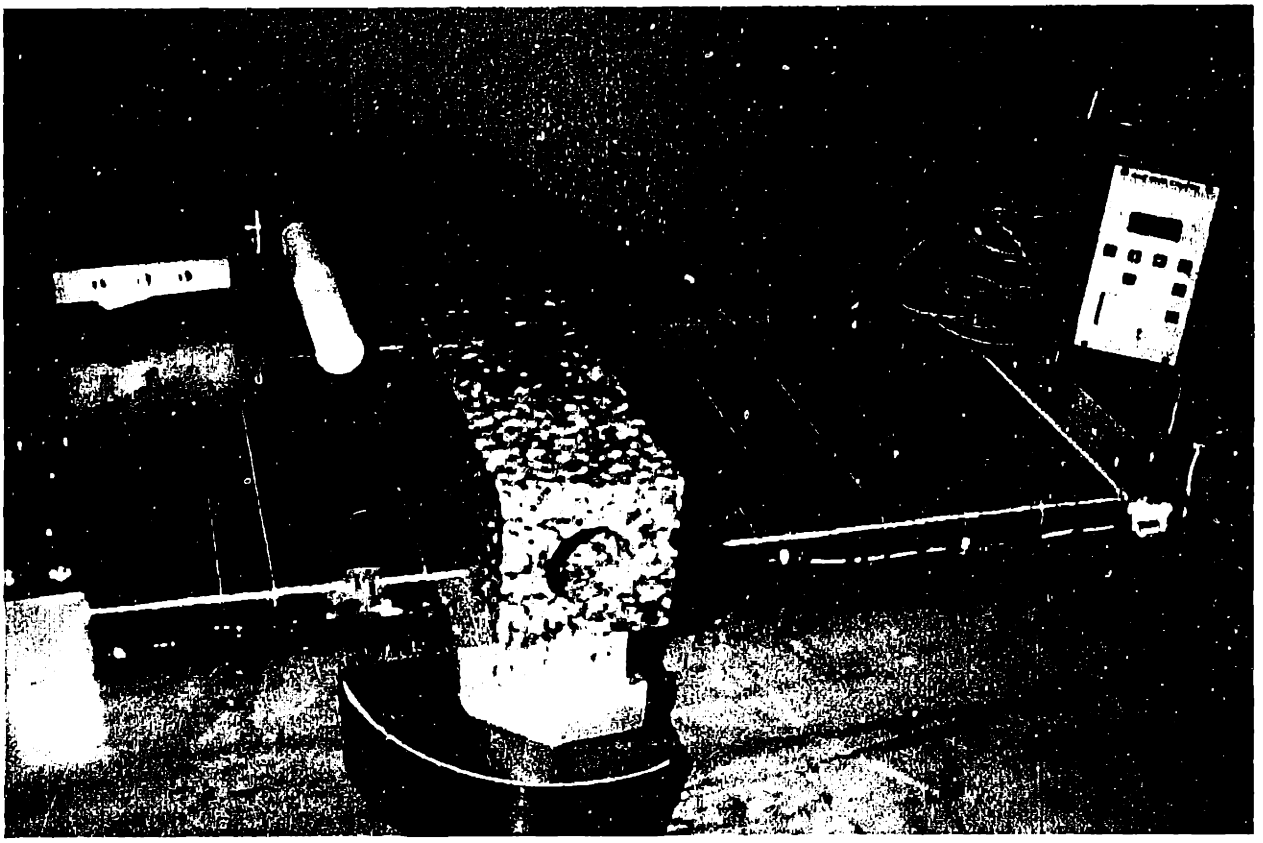

Figure 5-23: Magnetometer configuration for stator field measurements

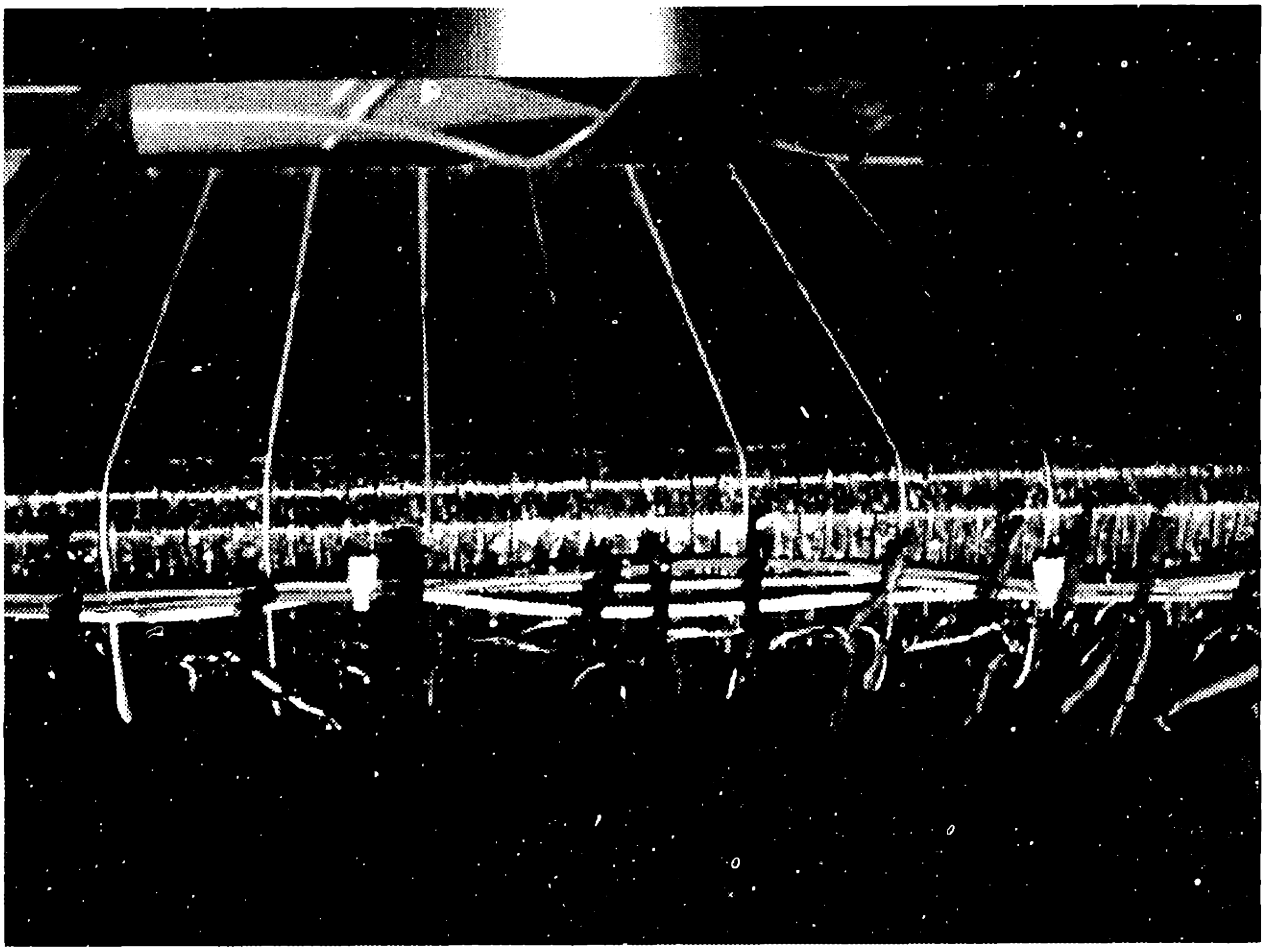

Figure 5-24: Leads on the outside of the stator

inside and the outside of the stator while the return leads to the amplifiers travel on the outside. The leads along the outside of the stator can be seen in Figure 5-24. After accounting for the fields from the leads, the stator measurements corroborate the theory very well.

5.8 Electrical terminal relations

The electrical terminal relations are derived from Faraday's law. Taking a result from [19]. Equation (4.1) can be expanded to yield

$$-V_s + \oint_L \frac{\mathbf{J}_f}{\sigma} \cdot d\mathbf{l} + \oint_L \left(-v_x B_z^M + v_z B_x^M\right) \mathbf{i}_y \cdot d\mathbf{l} = -\frac{d}{dt} \int_S \mathbf{B} \cdot \mathbf{dS}. \tag{5.15}$$

Here V_s is the driving voltage at the winding terminals. I use the coordinate system shown in Figure 5-5 to describe the vector components. The second term is the ohmic voltage drop and can be replaced by IR_s. The third term is the back EMF (electromotive force) where B^M is the flux density of the magnet array. The term on the right side of the equation is the voltage due to self and mutual inductance of the stator coil.

R_s is calculated as

$$R_s = \frac{l_{wire}}{A_{wire}\sigma}. \tag{5.16}$$

Although the theoretical relation for the back EMF is derived in [19], I ignore this term because it is relatively small considering the slow velocity requirements. Furthermore, the current amplifier removes this term from the controller. Reference [19] also derives the relation for the self inductance, while ignoring the winding end turns. I found it more convenient and more accurate to use the relation for inductance derived for a long coil. The inductance in this case is given by

$$L = \frac{\mu_o N_h^2 N_{coils} N_t \left((t+l)(t+w) + t^2/3\right)}{h}. \tag{5.17}$$

N_{coils} is the number of coils per phase. N_t and N_h are the number of turns wound along the thickness and height dimensions shown in Figure 4-6. Note that the geometric terms in the numerator designate the cross sectional area used to calculate the dipole moment of a thick coil from Equation (4.49). For the prototype, I calculated the stator inductance as .0343 mH while the measured value was .0357 mH. This is about a 3% error – about 10 times less error than the calculation that ignores the winding end turns in [19].

5.9 Magnet array field analysis

The prototype magnet array shown in Figure 5-6 is constructed from parallel opposing dipoles and can be described by multipole theory. The dipoles are arranged such that seven levels of cancellation superpositions are achieved. The design methodology

starts by calculating the required magnet area, given the required force and the magnet array properties, i.e. spatial period, magnet height, remanence, air gap, thermal current limit, etc. Based on a scheme for arranging the magnet arrays in parallel opposing configurations, arrays are superposed to create higher order multipoles. Superposition of arrays continues until the far field achieves the desired attenuation at the specified distance. Each superposition is based on dividing the previous multipole array into smaller, opposing multipoles. For instance, given a magnet array, a higher order multipole with the same magnet area is created by attaching an array with half the product of the dipole moment and the multipole moment arms to an identical array but with magnetization of the reverse sign. For a synchronous motor, the arrays need to be attached such that the magnetization of the arrays maintains constant rotation of the magnetization. Therefore, the opposing arrays are offset by half a spatial period. For the prototype, the scheme for arranging the magnet arrays above the second superposition also results in a multipole moment arm with a sideways offset. This concept is best described by the prototype example.

The first two levels of cancellation are shown in Figure 5-25. The quadrupole arrays are constructed from five pairs of dipoles. The five underlying dipoles in the quadrupole arrays contribute a far field dipole moment given by

$$C = \frac{5MW_m\lambda^2}{4096\pi}. \tag{5.18}$$

For the prototype, C = 0.0455 Amps m^2.

The subassembly that I used for the prototype differs from the combined quadrupole arrays. I make this change because I recognize that the end magnets have half the far field dipole moment of those in the center section. Furthermore, in the far field distances of interest these relatively narrow end magnets so closely resemble dipoles that the prototype subassembly has essentially the same far field as if the end magnets were the same size as the inner magnets but half the magnetization density. By centering the end magnets, I also eliminate the sideways multipole moment arm component. For the higher cancellation levels, the characteristic lengths associated with

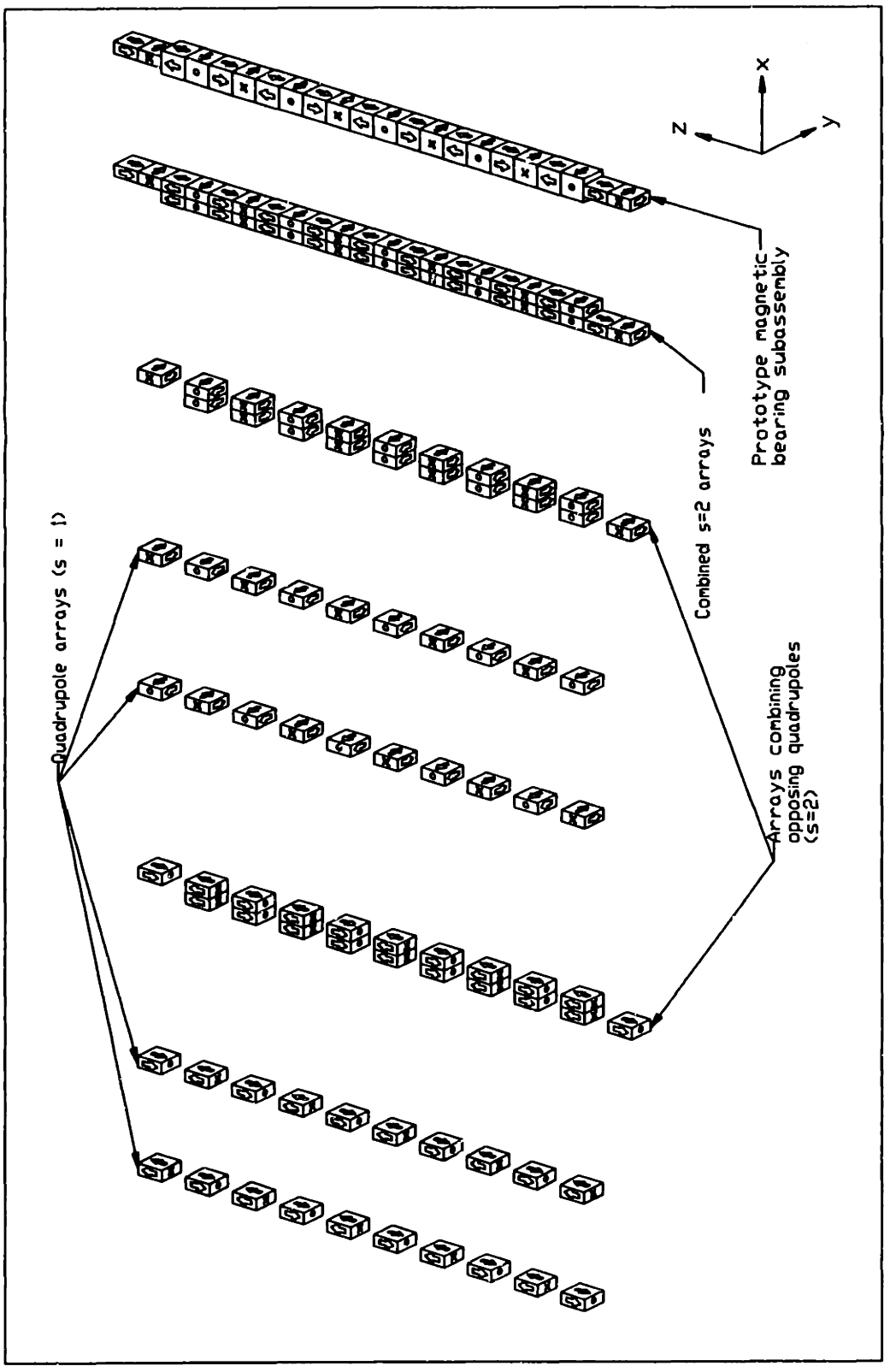

Figure 5-25: Construction of a magnet array subassembly

the end magnets are larger and at the far field distances of interest[7], approximating long sections of magnets as dipoles is not accurate. Therefore, the end magnets cannot be centered about the array width for the higher cancellation levels. The prototype array's design reflects this characteristic and results in the pattern of magnet "fingers" on the end of the array.

The scalar potential for the quadrupole array with poles aligned along the suspension axis (y axis) is given by

$$\Phi_{s1} = -3C\frac{\lambda}{2}\frac{1}{r^3}\left(cos(\phi + \pi/2)sin(\theta)\cos(\theta)\right). \tag{5.19}$$

The scalar potential for the quadrupole array with poles aligned along the translation axis (z axis) is given by

$$\Phi_{t1} = C\frac{\lambda}{2}\frac{1}{r^3}\left(1 - 3\cos^2(\theta)\right). \tag{5.20}$$

The next assembly represented by the prototype magnetic bearing subassembly shown in Figure 5-25 yields scalar potentials

$$\Phi_{s2} = 3C\left(\frac{\lambda}{2}\right)^2\frac{1}{r^4}cos(\phi + \pi/2)sin(\theta)\left(1 - 5\cos^2(\theta)\right) \tag{5.21}$$

$$\Phi_{t2} = 9C\left(\frac{\lambda}{2}\right)^2\frac{1}{r^4}\left(\cos(\theta) - \frac{5}{3}\cos^3(\theta)\right). \tag{5.22}$$

The next two levels of cancellation are in the subassembly shown in Figure 5-26. This subassembly can be thought of as the symmetric superposition of an inner array and two outer arrays, the outer arrays each with half the opposing multipole moment of the inner array. The scalar potentials for this subassembly can be derived by transforming the coordinate system as shown with $\gamma = \arctan(\frac{3W_m}{128\lambda})$. Note that this assembly is built with a sideways offset of the submultipoles. Therefore, the multipole moment arm is now the vector magnitude of $\lambda/2$ and the sideways offset. The scalar potentials are revealed after applying Equation (4.114). However, the expressions become very lengthy in the transformed coordinates and I choose, for con-

[7]I set 6″ above the base of the array as the design goal for a maximum of ± 2mG fields

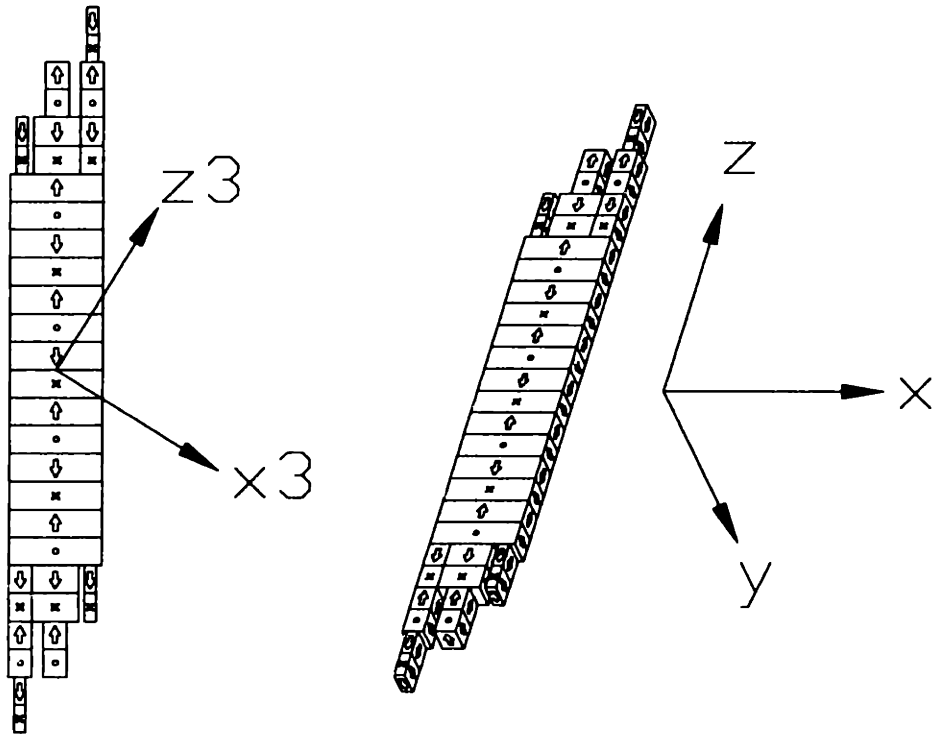

Figure 5-26: Magnet array subassembly

venience, to rely on the magnetic charge integration method to convey the theoretical results. The next two levels of cancellation are based on symmetric superposition of ARRAY_{1neg} with ARRAY_{2pos}. These arrays are designated in the bill of materials in Figure 5-6. Also, for clarity I show the subassembly arrays distinguished in Figure 5-27. ARRAY_{1neg} was intended to have half the opposing multipole moment of ARRAY_{2pos}. However, there is a flaw in the prototypes's design. When I divided the width of ARRAY_{2pos}, I also divided the width of the submultipole arms associated with the array width. Thus, the multipole moments are not balanced as I intended. Fortunately, the performance of these cancellation levels was not drastically reduced. This is because the multipole moment arms are misbalanced by significantly smaller lengths than the multipole moment arms associated with λ. I proceeded with the last level of cancellation by superposing this array with an opposing array composed of ARRAY_{1pos}–ARRAY_{2neg}–ARRAY_{1pos}. In total there are seven levels of cancellation, which yields a multipole with sixteen poles. The majority of the far field components decay as r^{-10}. But there also are components that decay as r^{-8} because of the

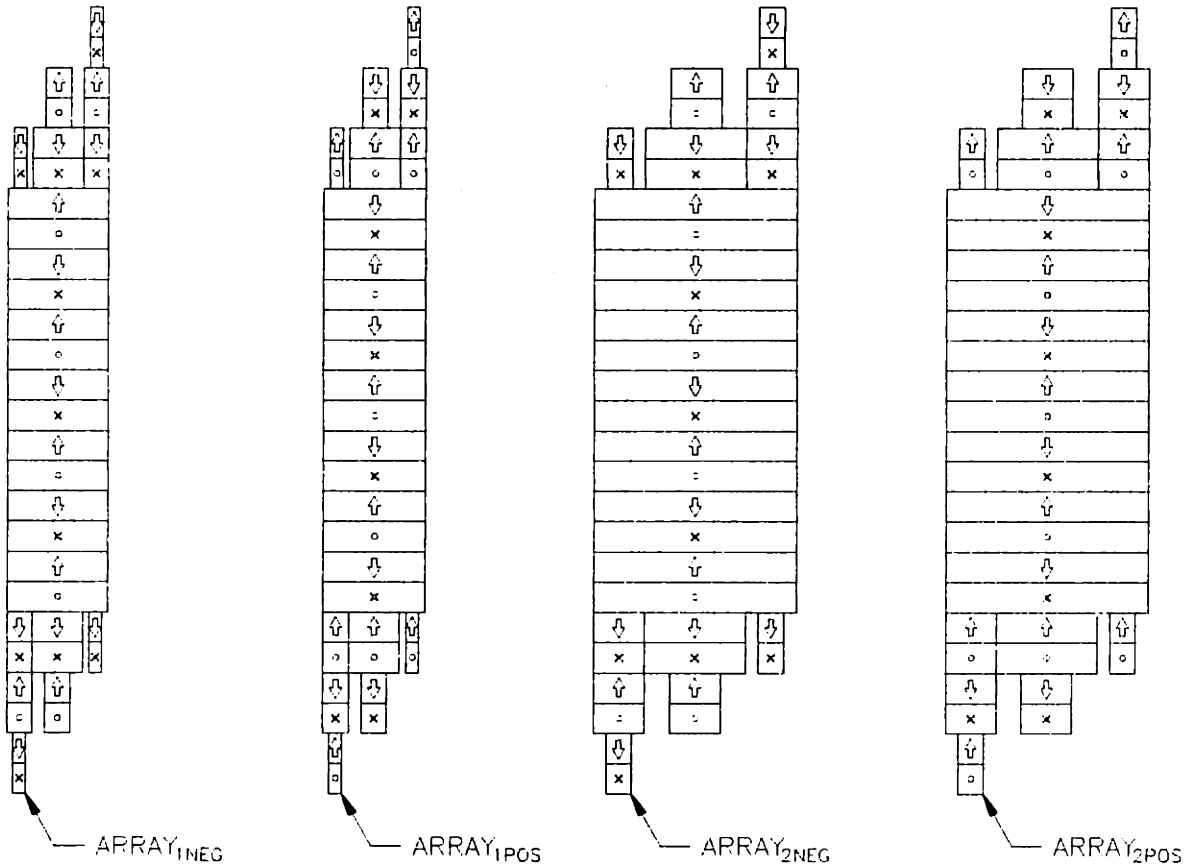

Figure 5-27: Magnet array subassemblies

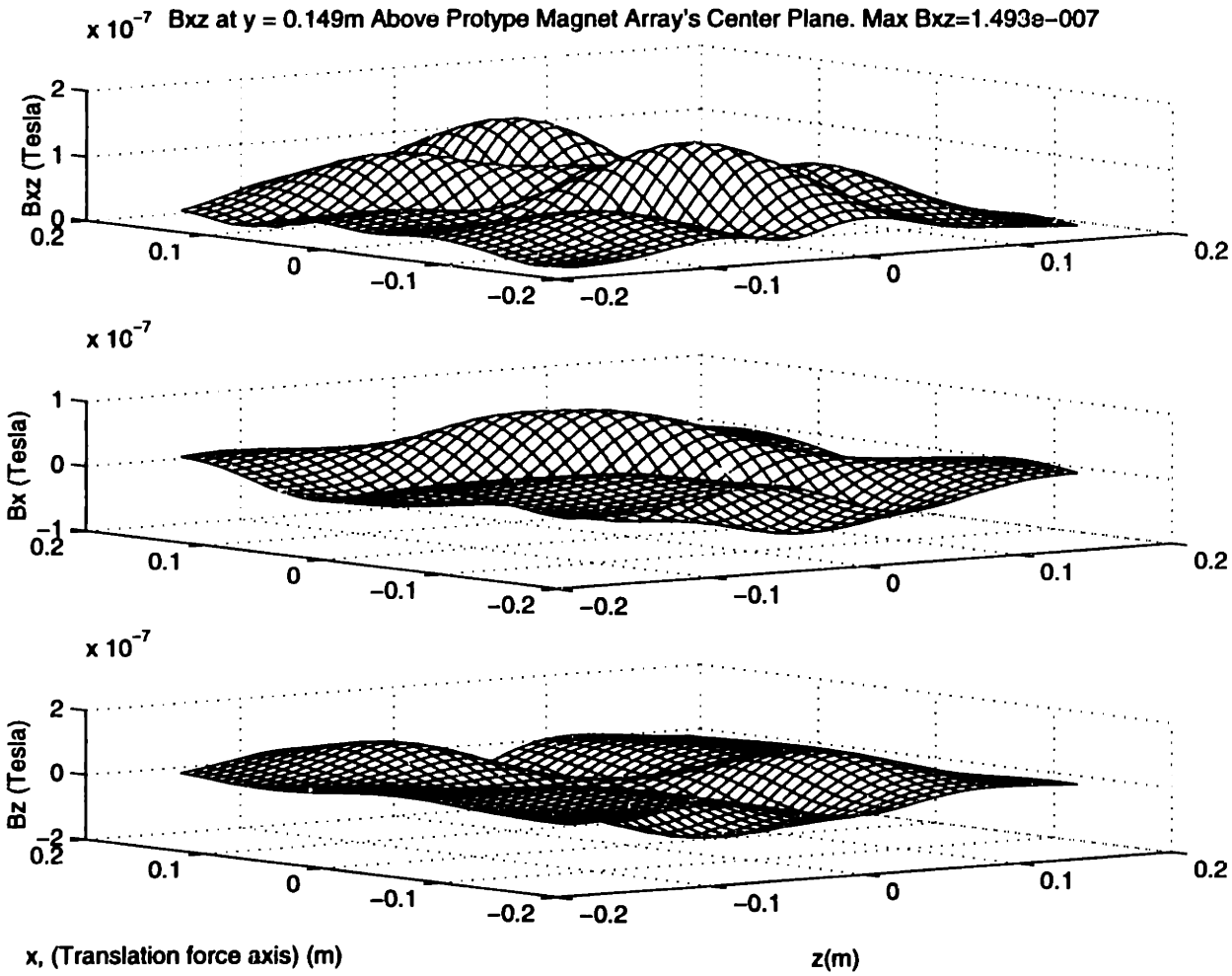

Figure 5-28: Fields at nominal write plane for the prototype array

misbalanced cancellation on two superpositions.

The simulated flux density of the array is shown at six inches above the base of the array in Figure 5-28. The design goal of flux densities less than ± 2mGauss above the base of the array is achieved. Figure 5-29 shows the same data but with a contour plot. Figure 5-30 shows the vector plot of the same data with eight of the sixteen poles noted. Figure 5-31 helps put the position of the magnet array in perspective by overlaying the vector plot on top of the magnet array.

To put the performance of the prototype array in perspective, I perform an identical calculation but with a conventional block Halbach array. This array, with five complete periods, should have nearly the same force rating of the prototype array. The data shown in Figure 5-32 reveals that the maximum B_{xz} is 1.85×10^{-4}T or about

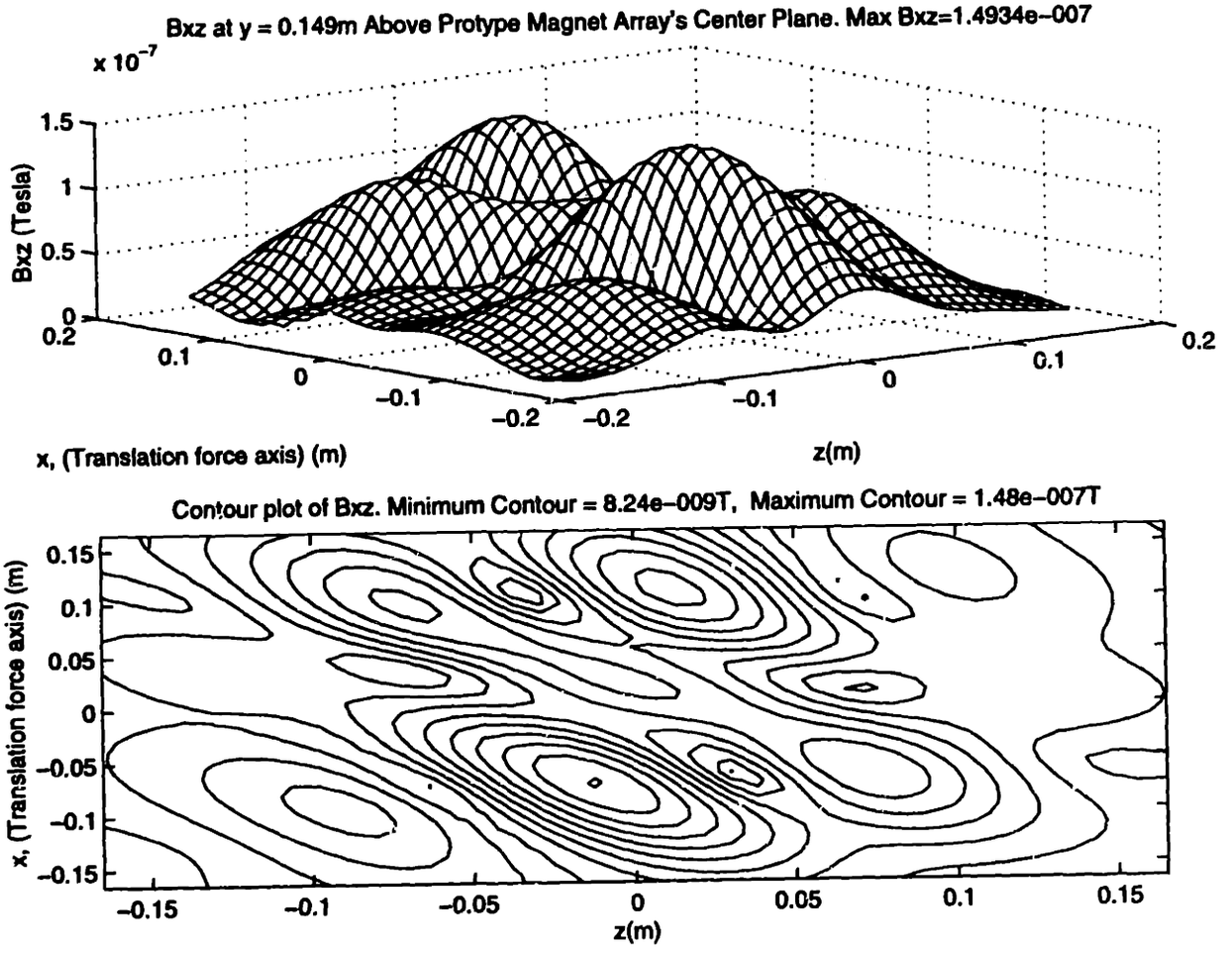

Figure 5-29: Fields at nominal write plane, 0.149 m above magnet array center plane, including contour plot

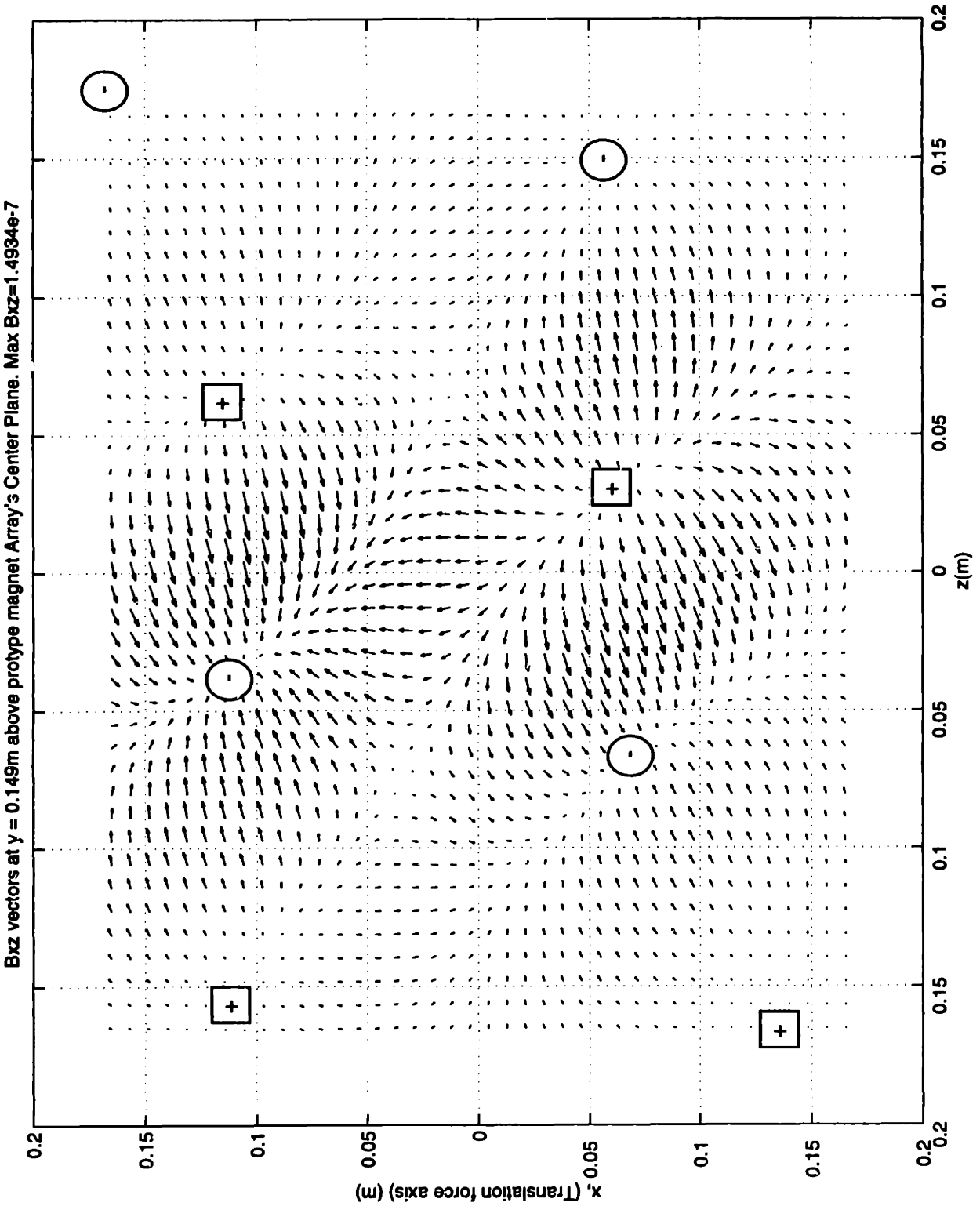

Figure 5-30: Fields at nominal write plane, vector plot

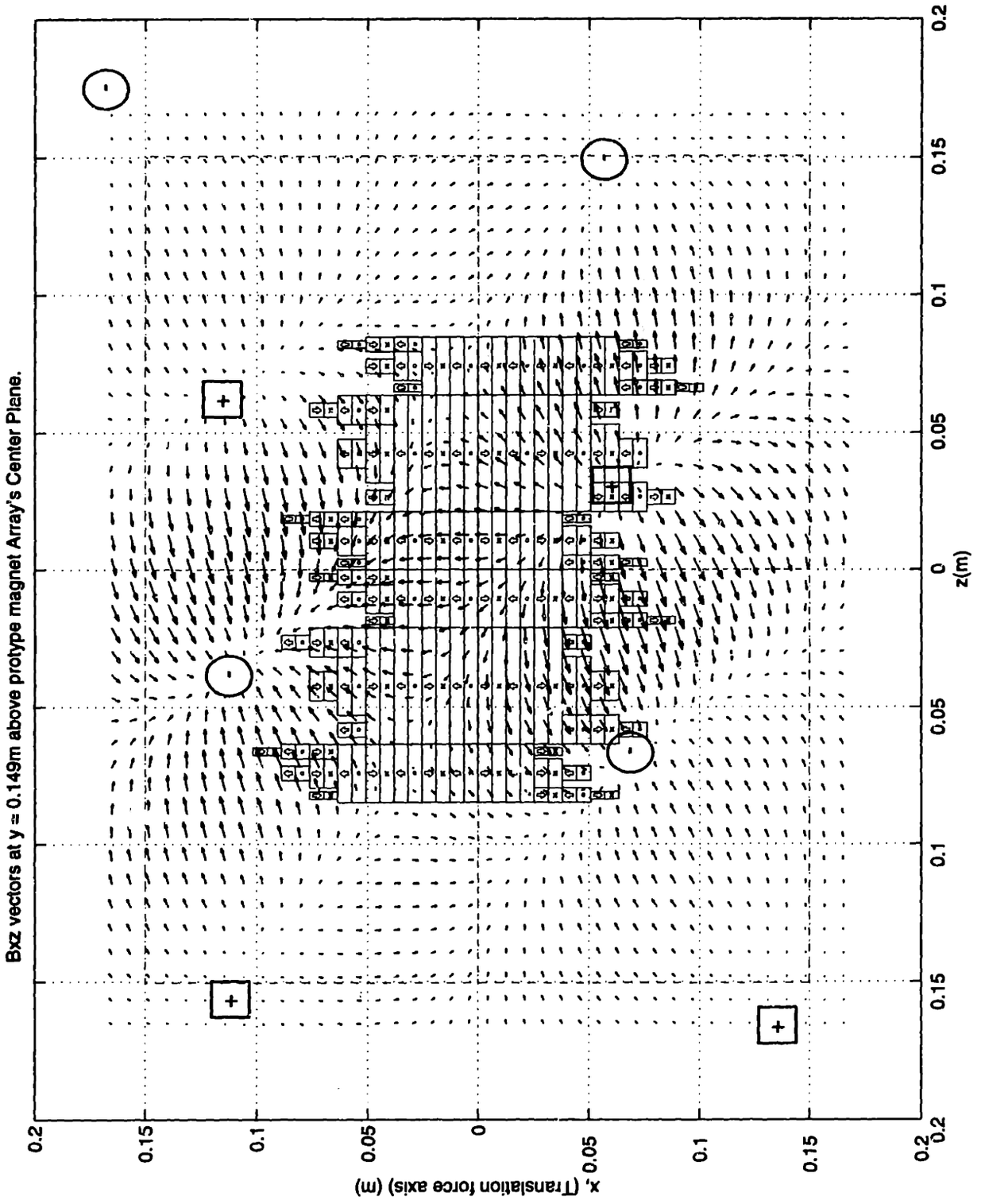

Figure 5-31: Fields at nominal write plane, vector plot overlayed on magnet array.

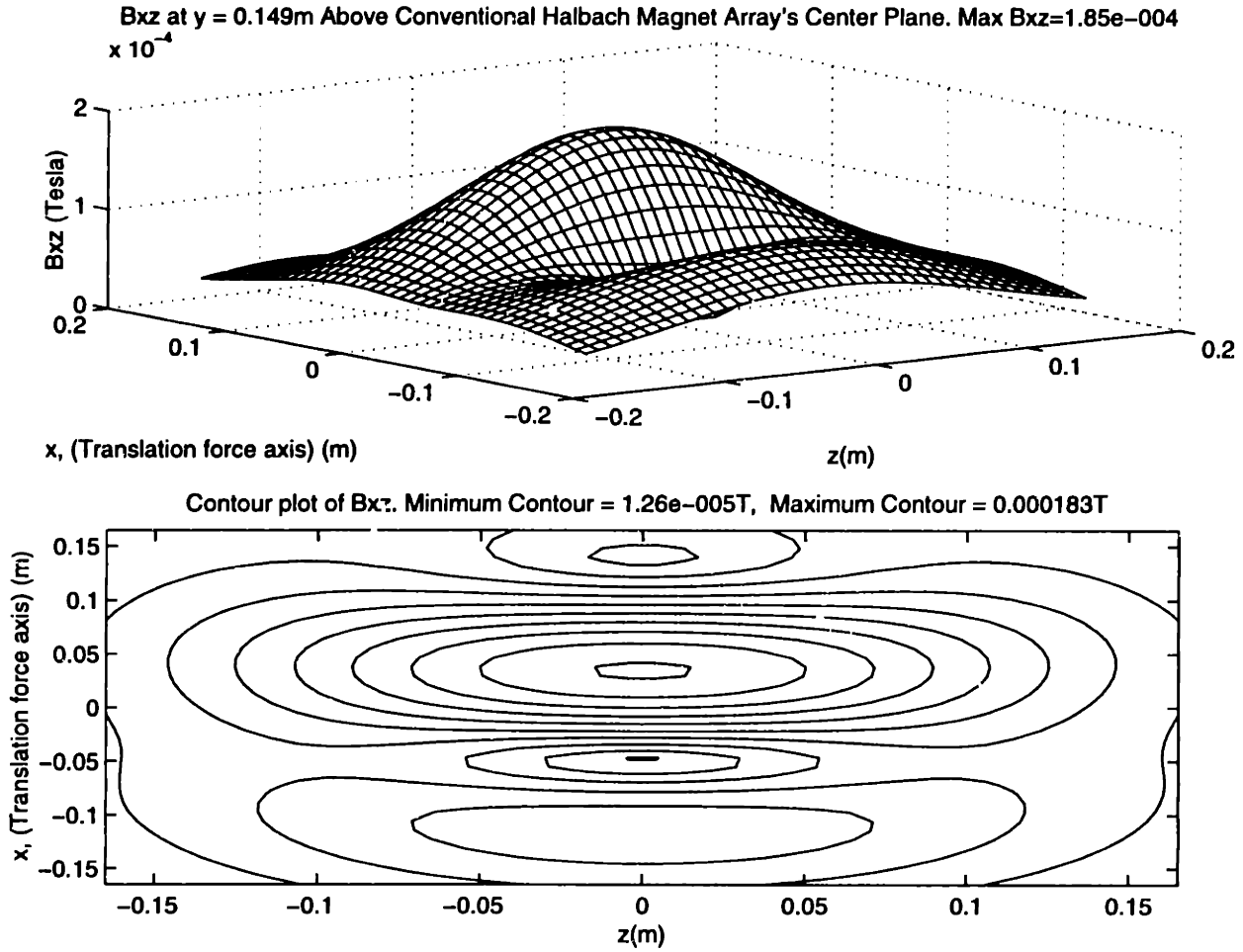

Figure 5-32: Fields at nominal write plane for conventional array, including contour plot

1200 times higher than the prototype array. The fields from the conventional array also fall much slower (as r^{-4}) and the required height calculated by magnetic charge integration for $\pm$ 2mGauss fields is 36 inches (.914 m). In the course of my investigation, I discovered a relatively simple way to predict the field magnitudes of candidate designs. In this method, I recognize that the multipoles that are functions of ϕ do not have significantly different field magnitudes compared to the multipoles that are independent of ϕ. This property is corroborated by my analysis in Figure 4-24. Therefore, I could predict the field magnitudes with the dipole constant and the product of the multipole moment arms applied to Equations (4.57) through (4.65). These multipoles are relatively simple for calculations because they are ϕ independent. The data for a sample analysis using this technique is shown in Table 5.2.

s	X (m)	Z (m)	$\sqrt{X^2+Z^2}$ (m), reference	$\prod$ *multipole moment arms* (m^s)	C (Am^2)	Legendre Constant	$\frac{d(\Theta(\theta))}{d\theta}$ Constant	Distance to$\pm$ 2mG Fields (m)
0	NA	NA	NA	NA	5.8291	1	1.00	3.321
1	.0127	0.0	0.0127	1.27E-02	2.9146	-1	3.00	0.914
2	-.0127	0.0	0.0127	1.61E-04	1.4573	-9	1.38	0.449
3	-.0127	-.0053	0.0138	2.34E-06	0.7286	9	7.04	0.294
4	-.0127	-.0106	0.0165	1.03E-07	0.3643	225	1.72	0.228
5	.0127	-.0211	0.0247	1.50E-08	0.1822	-225	12.15	0.203
6	.0127	-.0423	0.0441	2.48E-10	0.0911	-11025	2.00	0.200
7	.0127	-.0846	0.0855	3.41E-12	0.0455	11025	18.13	0.213

Table 5.2: Sample calculations using simplified design procedure

The distance X and Z are taken from the prototype array. This analysis should use the moment arm designated by $\sqrt{X^2+Z^2}$ and I show this length as a reference. Note that the product of the multipole moment arms accounts for Z required to be larger for the lower order superpositions than the higher order superpositions. Moreover, with each successive superpositions all the Z lengths are halved and a new Z is introduced into the product that is equal to $W_m/2$. C reflects the requirement that it is halved with each successive superposition. The Legendre Constant is taken directly from the leading integers in Equations (4.57) through (4.65). $d(\Theta(\theta))/d\theta$ constant is the maximum value taken from Figure 4-10 for the respective multipole, which accounts for the magnitude of B_θ. Furthermore, I assume B_θ is a good representation of the flux that will be transverse to the ebeam. The distance to the desired flux density (2mG) is calculated by

$$Distance = \cdots \left| \frac{\mu_o(\prod \, moment\, arms)\, C\, (Legendre\, Constant) \left(\frac{d(\Theta(\theta))}{d\theta}\, Constant\right)}{B_{desired}} \right|^{\frac{1}{s+3}}. \quad (5.23)$$

The results are not too far from the actual values, especially for the cases where the distances are large compared to the largest characteristic length. For instance, for the s =1 array, the result is nearly exactly the value calculated by magnetic charge

integration. Where the distances are below .3 meters, however, the actual values are appreciably less than the predicted values. This is not surprising considering the long characteristic length associated with the width of the array. However, even below .3 meters, these figures are a good first guess.

I should mention that although the calculation predicts the s=7 array has worse properties than the s=6 array, in actuality it does not. The prediction does not account for the faster rotating magnetic field orientation that tends to null fields for multipoles arranged along a line. Moreover, there is an important contribution to field cancellation close to the array because 180° phase shifts are achieved with smaller angular increments with the higher harmonics that are associated with the higher order multipoles. This effect was seen as the dip in Figure 5-15

There certainly are other cancellation topologies that would exceed the performance of the prototype magnet array. The prototype used just one cancellation topology, which is ideal when it is practical to buy only a few magnet versions. However, the cancellation topology has a drawback in that it has a few multipole moment arms that limit the array's performance because they are large.

In the ideal case one could purchase magnets with arbitrary remanence and use these as the end magnets. In this way, all the multipole moment arms could be designed to be $\lambda/2$. The remanence of the end magnet sections would be assigned by superposing opposing arrays with $\lambda/2$ offset, which is the smallest moment arm allowable since the synchronous motor is intended to produce force.

As an example, Figure 4-13 uses this superposition arrangement. Figure 5-33 shows the general construction scheme with magnets of magnetization M_o superposed to form higher order multipoles. The $s = 1$ array is a Halbach array with an integer number of periods. If the array does not have an integer number of periods then its far field will be that of a dipole and not a quadrupole. Similarly, without the integer number of periods the Halbach array will have at least one magnet that is not paired with a parallel opposing magnet. We begin with the quadrupole because the dipole would limit far field attenuation. The break in the array idicates that any number of integer periods could be used. The encirclement designated $s = 2$ shows

how the $s = 1$ array is paired with a parallel array of opposite magnetization to form this higher order multipole. The opposing array is offset by $\lambda/2$ in the horizonatal direction because we want to align the magnetization. In the near field, the net array has strong flux densities, which makes it useful for a synchronous machine. The array to the right shows the result of combining these arrays. The end half periods have half the magnetization of the inner magnets. The $s = 3$ encirclement is formed from superposing the $s = 2$ array with a parallel array of opposite magnetization. Again, the opposing array is offset by $\lambda/2$. The superposed arrays form the array shown to the right. For the purpose of emphasizing the pattern, the arrays used to build the $s = 4$ array are also shown. The procedure can be continued for any number of superpositions.

Table 5.3 shows the predicted performance of an array with the same force capability as the prototype array but with all the subarrays superposed with multipole moment arms equal to $\lambda/2$. The data reveals that significantly better performance is attainable. For the prototype, I did not have the luxury to investigate the manufacturing implications associated with buying magnet grades that are not catalog items, thus for the prototype I ruled out this topology despite its superior performance. As an alternative, one could construct a magnet assembly of small magnets spaced to achieve an effective remanence. Its fields would be designed to closely match that of a continuous magnet with a specified remanence. However, I decided it would be too expensive and time consuming to assemble the many small magnets required in these assemblies. Instead, I chose an array topology that could use a limited number of magnet versions, all with the same remanence, at the expense of performance.

With further research of magnetization processes and magnet assembly, I believe construction of arrays with multipole moment arms equal to $\lambda/2$ will be possible. These arrays offer the most efficient far field cancellation for synchronous motor magnet and coil arrays because the length of the multipole moment arms are minimized. Table 5.4 shows the relative magnetization for the trimming magnets in these arrays. The trimming magnets describe the magnets on the ends of the array. Figure 5-33 depicts the relative magnetization for arrays up to $s = 4$. Each trim level consists of a

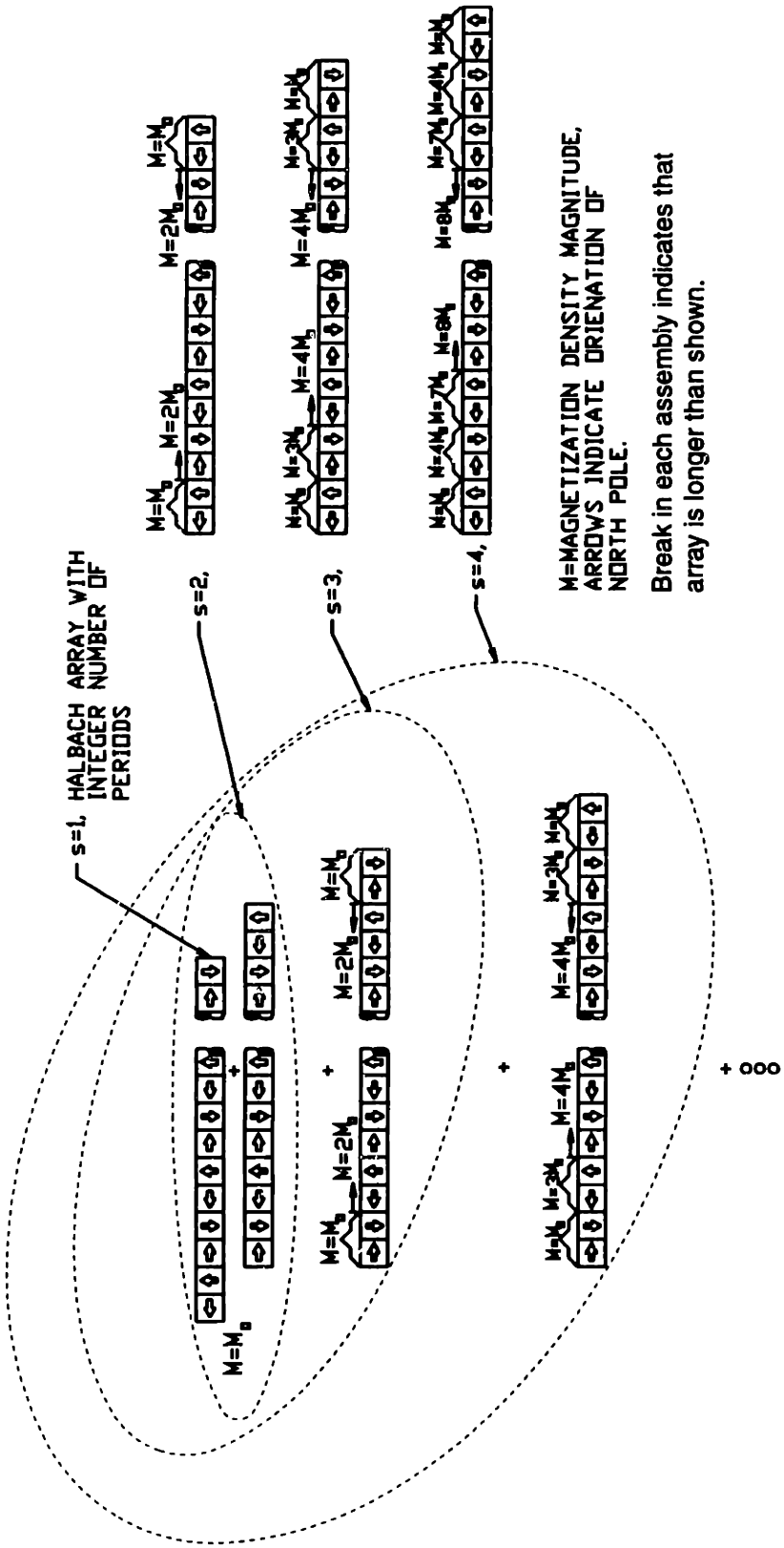

Figure 5-33: Construction of multipoles by superposition

s	X (m)	$\prod$ *multipole moment arms* (m^s)	C (Am^2)	Legendre Constant	$\frac{d(\Theta(\theta))}{d\theta}$ Constant	Distance to± 2mG Fields (m)
0	NA	NA	5.8291	1	1.00	3.321
1	.0127	1.27E-02	2.9146	-1	3.00	0.914
2	.0127	1.61E-04	1.4573	-9	1.38	0.449
3	.0127	2.05E-06	0.7286	9	7.04	0.290
4	.0127	2.60E-08	0.3643	225	1.72	0.218
5	.0127	3.30E-10	0.1822	-225	12.15	0.179
6	.0127	4.20E-12	0.0911	-11025	2.00	0.155
7	.0127	5.33E-14	0.0455	11025	18.13	0.141

Table 5.3: Calculations for magnet arrays constructed with $\lambda/2$ multipole moment arms

Trim level	s=	1	2	3	4	5	6	7	8
Trim 1		1	1	1	1	1	1	1	1
Trim 2			2	3	4	5	6	7	8
Trim 3				4	7	11	16	22	29
Trim 4					8	15	26	42	64
Trim 5						16	31	57	99
Trim 6							32	63	120
Trim 7								64	127
Trim 8									128

Table 5.4: Relative magnetization for trimming magnets. Required magnet periods for last trim level: $N\lambda$ for odd s and $(N + \frac{1}{2})\lambda$ for even s

half period of magnets. The lowest trim level corresponds to the magnets on the end of the array. The full remanence sections contain the number of periods of magnets designated in the last row where N is an integer greater or equal to zero. In practice, the magnetization for the trim levels are achieved by scaling the maximum magnetization to the relative values. The relative magnetization for the highest trim levels for s is calculated by multiplying two times the remanence of the highest trim level of $s - 1$. The lower trim levels are calculated by adding the relative magnetization for the same trim level and the lower trim level for $s - 1$.

5.10 Magnet array tolerance analysis

The high order of field cancellation in the magnet array is likely to be degraded by magnet and assembly tolerances. A monte carlo simulation was performed to characterize the array's sensitivity to the tolerances. Figure 5-34 shows the results.

The expected tolerances are derived from Figure 5-7 and the assembly tolerances. The lumped remanence is specified as ±3%. Note that the drawing reflects a relative far field flux density correction for the different magnet lengths. This would not be necessary if the magnetic fields could be measured arbitrarily far away. In fact, a spacing of ten times the longest characteristic length (1.664″) would be a good location for measurements. However, I assume that the magnet vendors use a hall effect gauss meter, which I assume to have a measurement accuracy of ± 1mG. Thus, for the vendor's measurements to be accurate to ±1% the fields should be in the range of 100mGauss at the least. I calculate the distance where the smallest magnet's fields (Magnet-01) equal 100mGauss, which is about 5.375″ above the datum shown. This distance is not sufficient to describe the long magnets with the far field approximation. Thus, I calculate the relative far field flux density to account for the magnet length and the spacing of the measurement. If this is not done, the longest magnet (Magnet-05) would be specified as 2.5% stronger than I really wanted. This error is unreasonable considering that I wanted to hold ±3% remanence tolerances.

The angular tolerances reflect the specified magnet tolerance of ±3° and the assembly tolerance of ±1.1°. The assembly tolerance is based on the .005″ parallelism and perpendicularity tolerances and the .25″ length. The root sum square angular tolerance is thus ±3.2°.

The positional tolerances are expected to be under ±.01″ based on the .005″ magnet geometrical tolerances and assembly tolerances. The assembly tolerances are estimates based on the limits of the tooling, which I discuss in Section 5.11.

I perform Monte Carlo simulations to determine the sensitivity of the prototype array to tolerances. I assign the nominal 3σ tolerances to magnets with length $W_m/16$, which is the same length as Magnet-03. Because the magnet array contains magnets

of different widths, each magnet is assigned a tolerance assuming the root sum of squares relation holds. This relation is

$$\sigma = \sigma_0 \sqrt{\frac{w}{W_0}} \tag{5.24}$$

where for my analysis σ_0 is the tolerance for the Magnet-03 and W_0 is its length. The symbols σ and w are the tolerance assigned to the individual magnet and the width of the magnet respectively. Just like in the stator tolerance simulations, I calculate the height above a corner where the fields fall to a nominal value. I chose h_{ref}= 4.85″ with a nominal field of 2mGauss. The simulations independently varied the angular, position, and remanence tolerances. The results of these simulations are shown in Figure 5-34. The data shows that the angular tolerance begins to have significant field contributions at only $\pm.3^o$. The performance degradation at the expected angular tolerance of $\approx \pm 3^o$ is large – the required height to the nominal field is tripled. Meanwhile the lumped remanence begins to make significant field contributions when $3\sigma B_r = .3\%$. At the expected $3\sigma B_r$ of $\pm 3\%$, the data shows that the required height nearly triples. The position 3σ shows relatively little contribution to the fields at the $\pm.01''$ tolerance of interest.

The data shows significant performance degradation for the expected magnet array tolerances. It would not be surprising to find the prototype array would achieve the desired ±2mGauss fields at 3 times the distance as for the perfect array. To put this in perspective, a single magnet dipole of the same grade as the prototype magnet would produce ±2mGauss flux density if it was a cube 3.1×10^{-3} inches on each side. This amounts to only .04% of the prototype array's magnet volume. Indeed, it is critical to cancel dipole fields.

5.11 Magnet array manufacture

The tooling used to assemble the magnet array is shown in Figures 5-35, 5-36, 5-37, and 5-38. The functional requirements of the tooling include bonding the magnets,

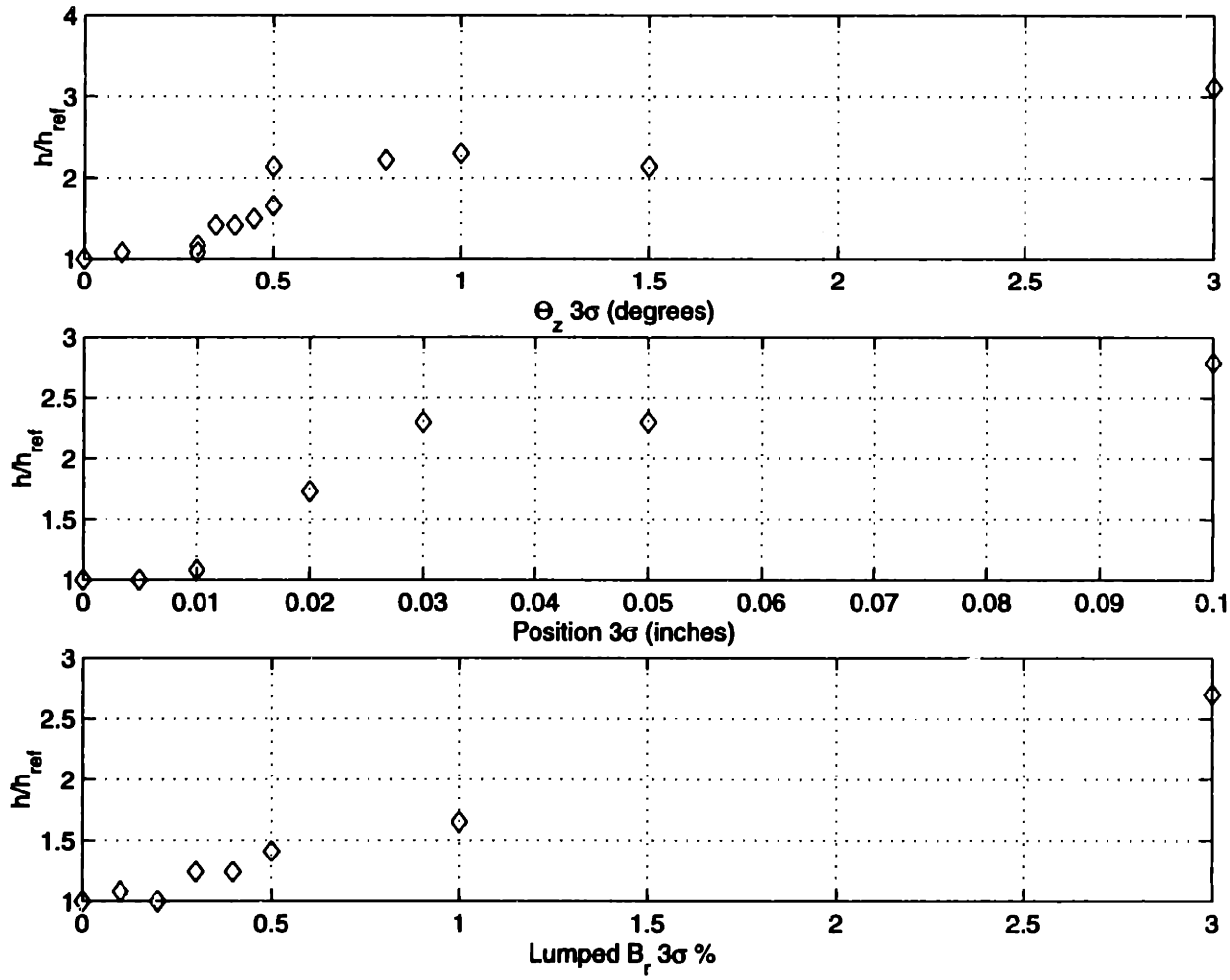

Figure 5-34: Results from magnet array tolerance simulations

ensuring that the side of the magnet array facing the stator is flat, and holding the assembly tolerances of the magnet array. I wanted to meet .005″ flatness and .01″ assembly tolerances. The process must be able to force the magnets together and against a planar reference surface. The planar reference surface should have grooves machined into it to allow excess epoxy to flow between the magnets. The excess epoxy is cleaned from the array after curing. I used E408 Stoner Dry Film Mold Release[8] to ensure I could remove the assemblies from the tooling. A photograph of the tooling is shown in Figure 5-40.

I used two methods to force the magnets against the planar reference surface. For small subassemblies I used the magnetic tooling plate that took advantage of steel to magnetically force the magnets against the reference surface. For large subassemblies, the forces became unwieldy and sliding the assembly along the surface scratched the high spots on the magnet array. It would be possible to reduce the attractive forces by designing the tooling plate to saturate at lower flux densities, but the lower forces are not sufficient to force the magnets flat against the plate. For this reason, I rely entirely on mechanical clamping for the larger arrays. The clamp bars contain many tapped holes that allow nylon tipped set screws to be forced against the magnet blocks.

The position of the edges of the magnets that are supposed to be aligned are set with a stiff brass straight edge when the set screws are snug but not tight. After alignment, the set screws are tightened. Because at least one edge of the magnets in the Halbach array is attracted to its neighbor magnet it is easy to press the magnets firmly together when tightening the set screws.

The spacing between the end magnets are set with aluminum spacers machined for this purpose. The end magnets are forced into place with the clamp bar's set screws, while a hand held probe ensured the magnet was forced against the neighboring magnet and the spacer.

The magnets are bonded with the epoxy materials that I discuss in Section 5.14. After the subassembly arrays that are designated as ARRAY_{1pos}, ARRAY_{1neg},

[8]Stoner,1070 Robert Fulton Highway, Quarryville, PA 17566

$ARRAY_{1pos}$, and $ARRAY_{2neg}$ in Figure 5-6 were assembled, they were adhered to an aluminum backing plates. Figure 5-39 shows this configuration for array2neg. The backing plate was necessary to provide ruggedness for these larger arrays. Moreover, without it, these arrays would fracture at the epoxy bonds during normal handling conditions. Needless to say it is good practice to wear safety glasses when handling insecure magnet arrays.

After these subassemblies were completed, they were bonded together by forcing one section of the assembly tightly into the magnet tooling plate, while the abutting assembly was forced into it with the clamp bar and against the tooling plate with the magnet clamp. The bolt pattern on the magnet tooling plate allows the magnet clamps to be positioned for this operation.

For the prototype assembly, many cure cycles were required, which made this process time consuming. However, I chose to design a relatively versatile tooling, in which I had high confidence, as opposed to taking a high risk with a more sophisticated tooling that might not work. For production, a combination of mechanical clamping and epoxy should be employed to provide the necessary clamping strength for long term reliability. Also, tooling should be designed to limit the curing to one or two cycles.

5.12 Measured fields of the magnet array

The magnet array field measurements were obtained using a Bartingtion Mag-03MC100 Three Axis flux gate magnetometer, Bartington Mag-03PSU Power Supply Unit, Tektronix AM502 differential amplifier, third order 1Hz bandwidth low pass filter, and CIO-DAS1402/16[9] 16 bit analog to digital converter board attached to a PC. The z axis position of the magnet array was measured with the interferometer system. Meanwhile, the y position was adjusted by propping the magnetometer with blocks, much like the procedure for the stator field measurements. A photograph of this configuration is shown in Figure 5-41. The position accuracy of the measurements is

[9]Available from Computer Boards Inc. 125 High Street. Mansfield, MA 02048

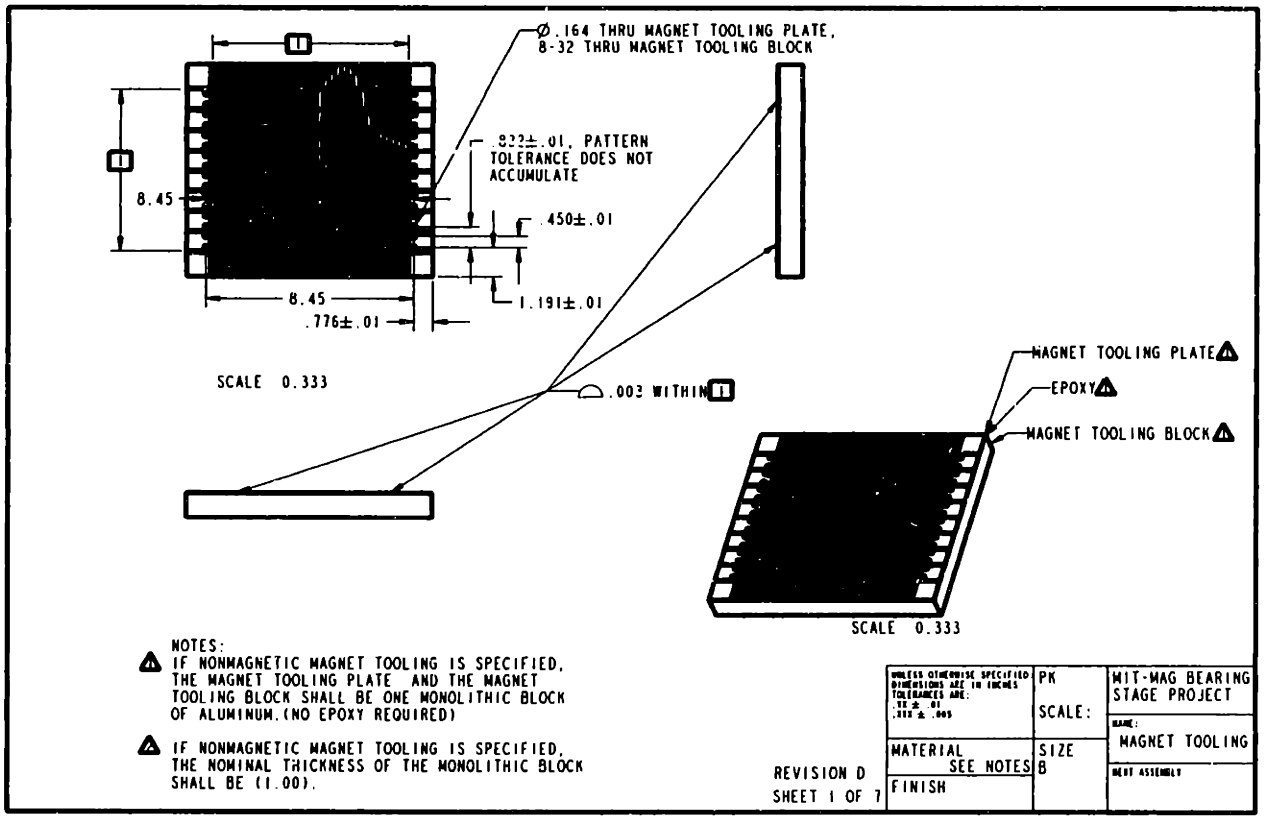

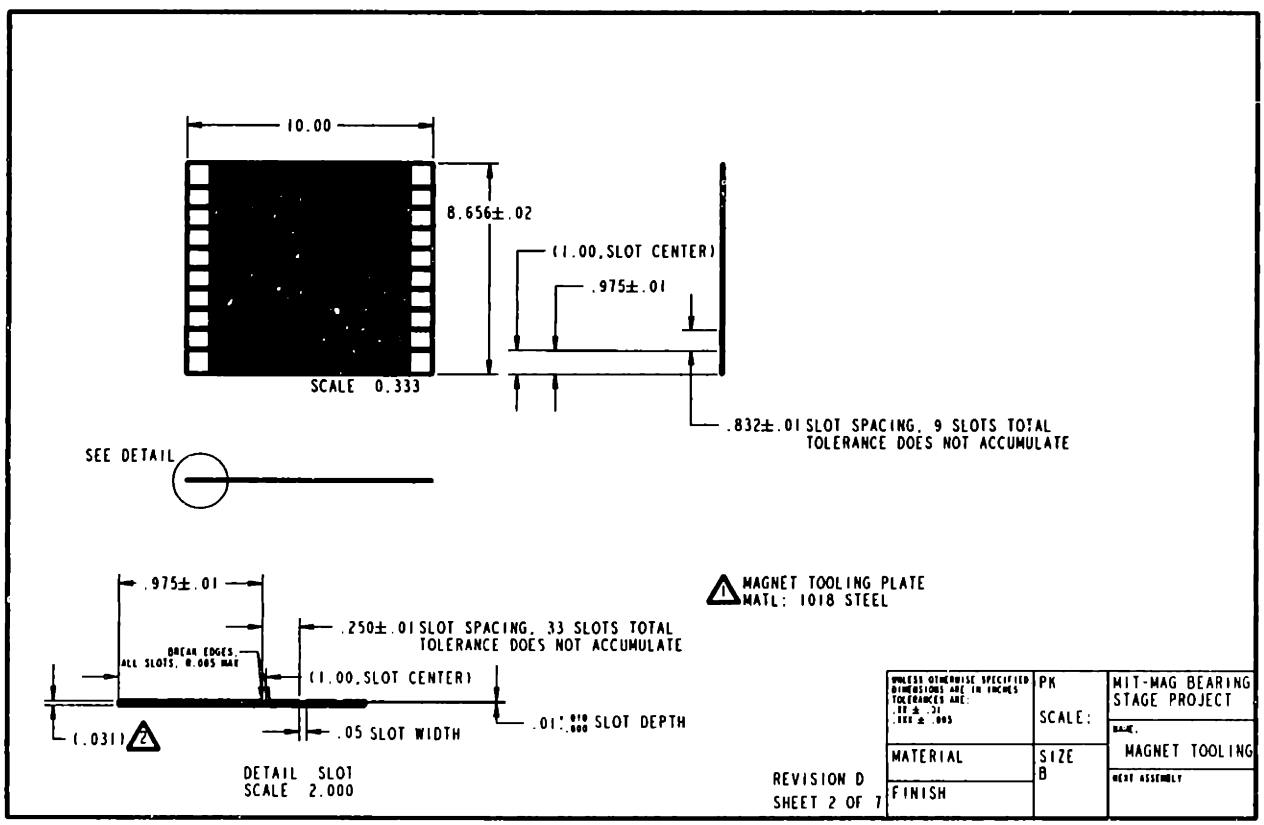

Figure 5-35: Tooling for assembling the prototype magnet array

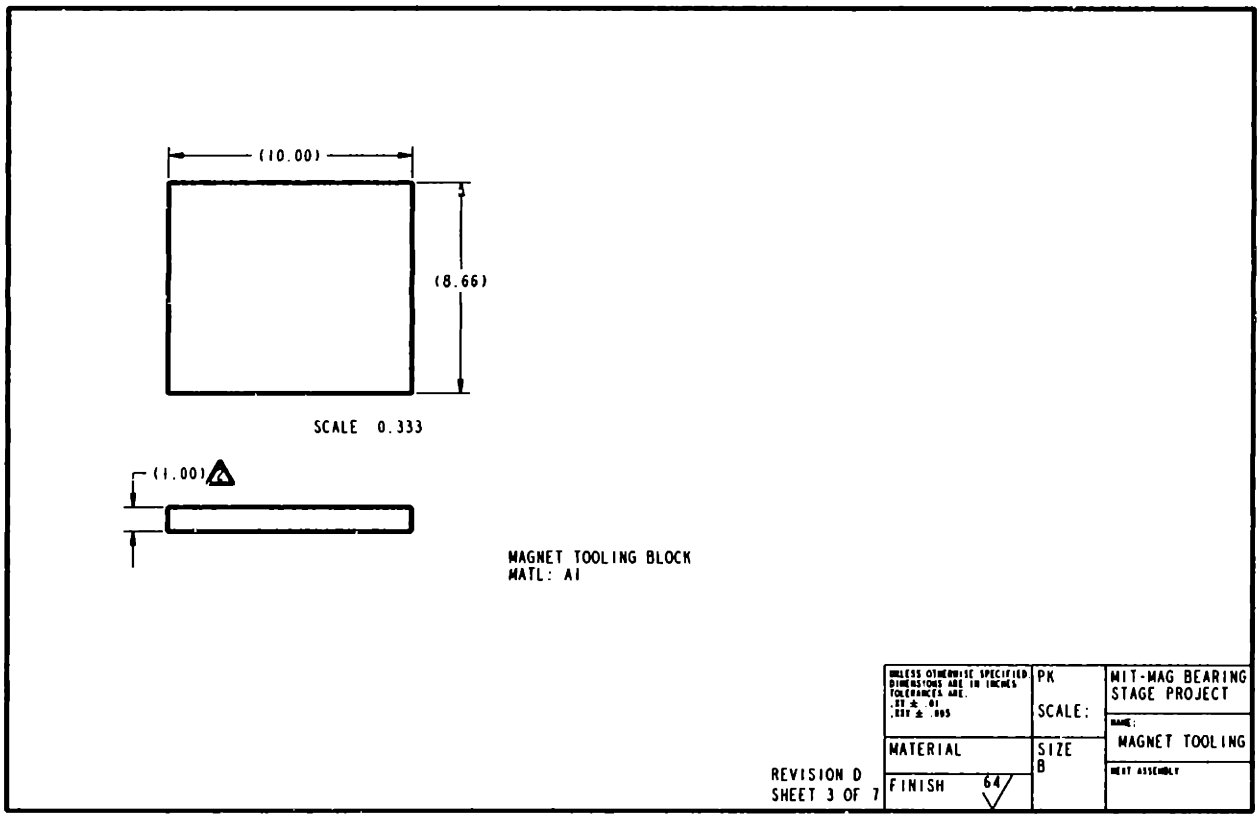

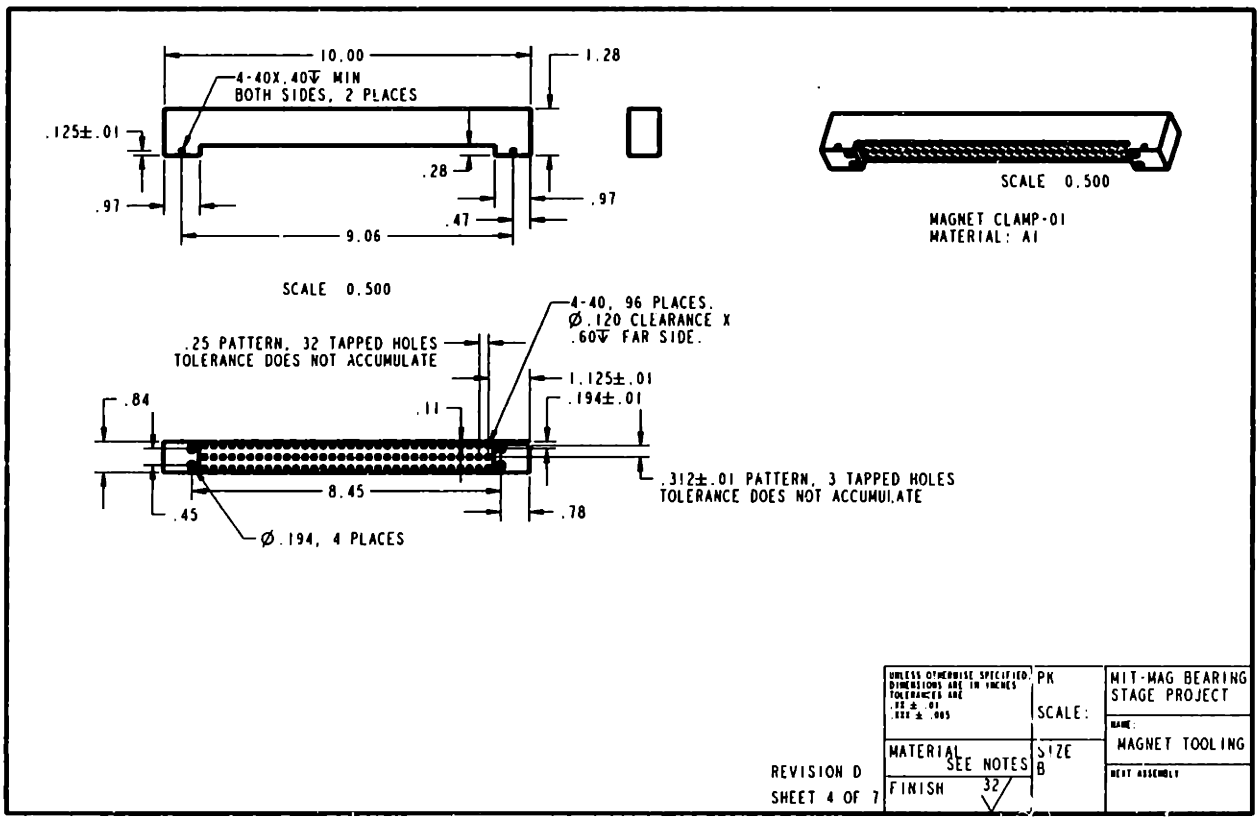

Figure 5-36: Tooling for assembling the prototype magnet array, continued I

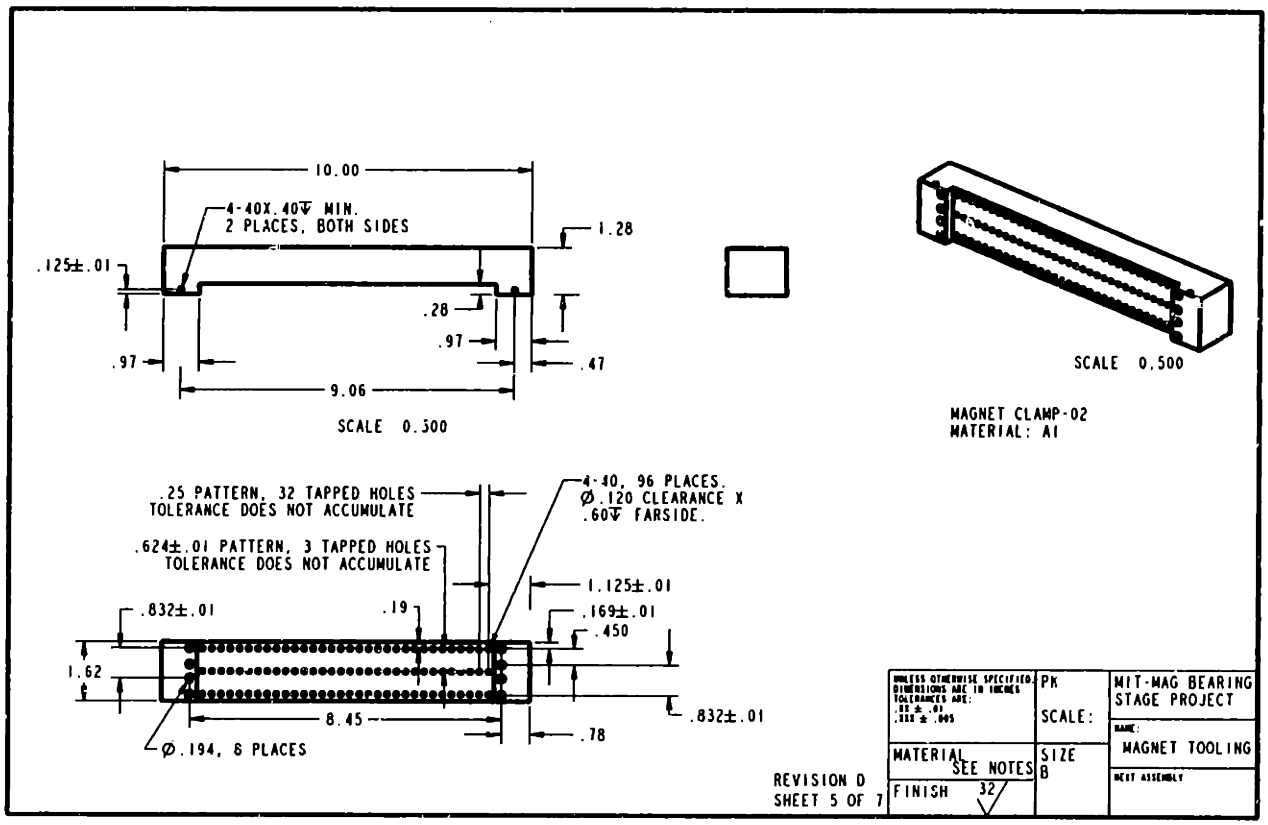

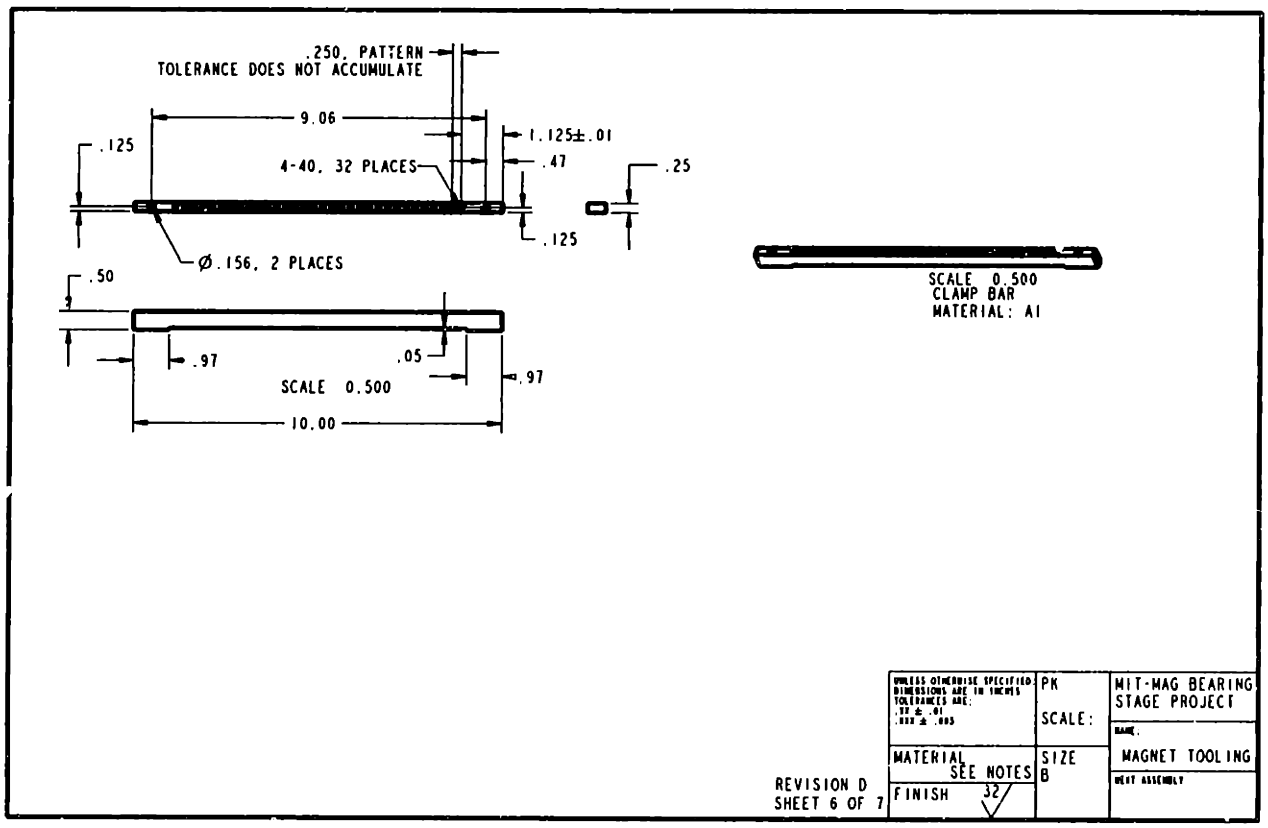

Figure 5-37: Tooling for assembling the prototype magnet array, continued II

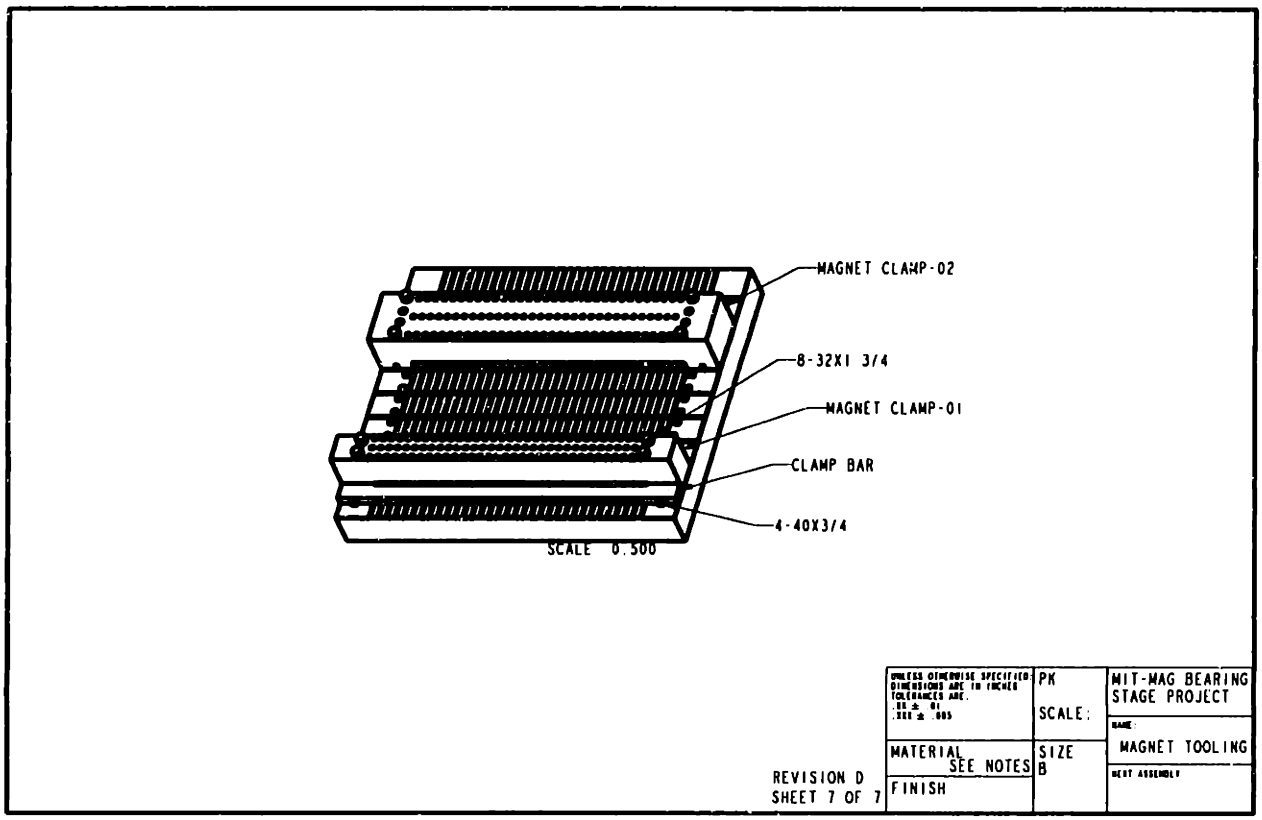

Figure 5-38: Tooling for assembling the prototype magnet array, continued III

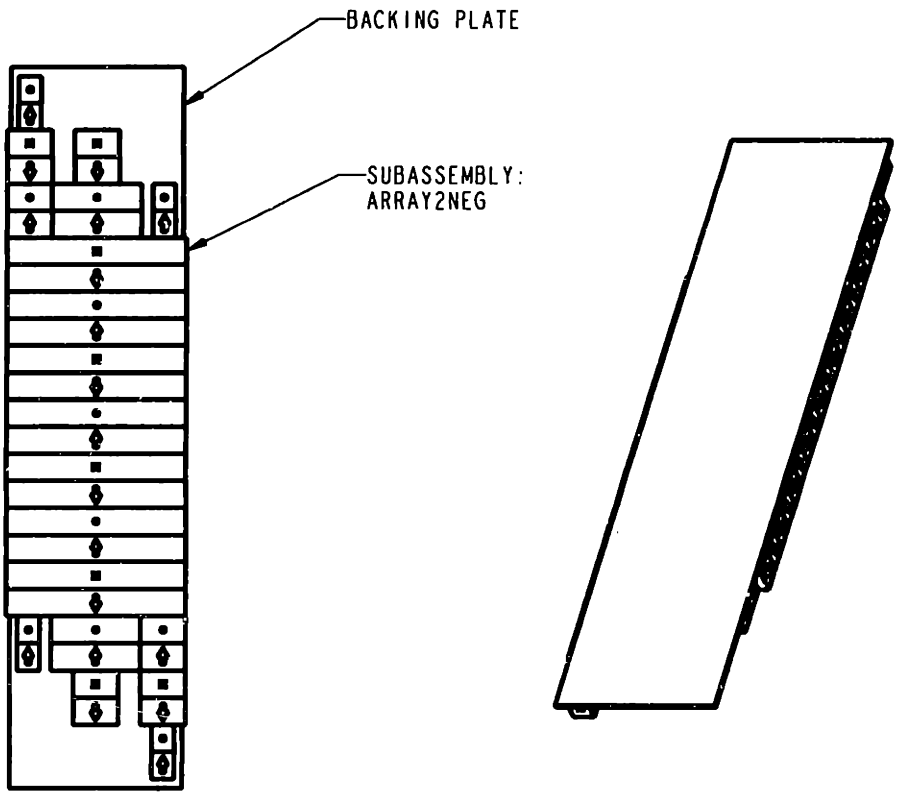

Figure 5-39: Magnet array subassembly with backing plate

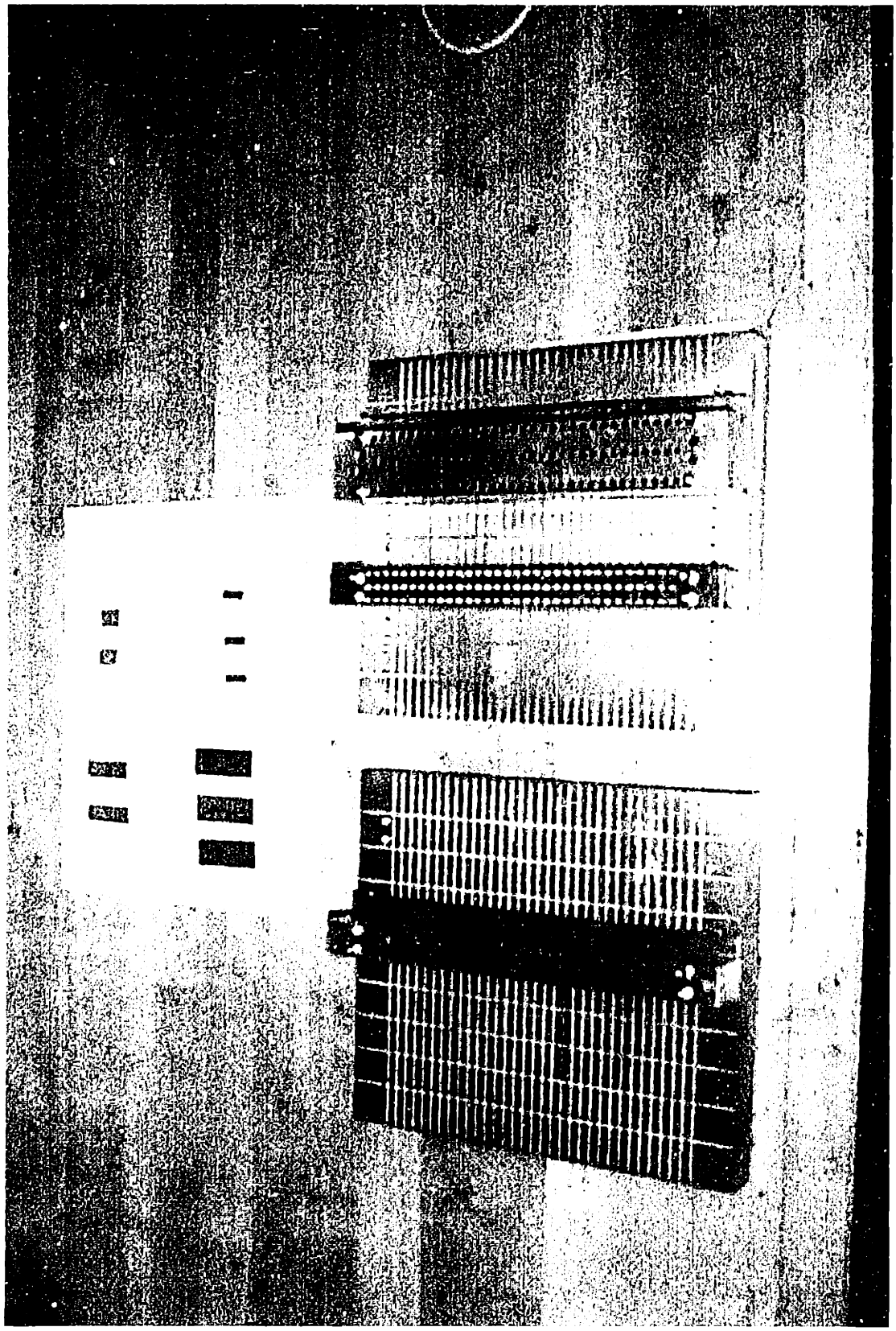

Figure 5-40: Magnet tooling

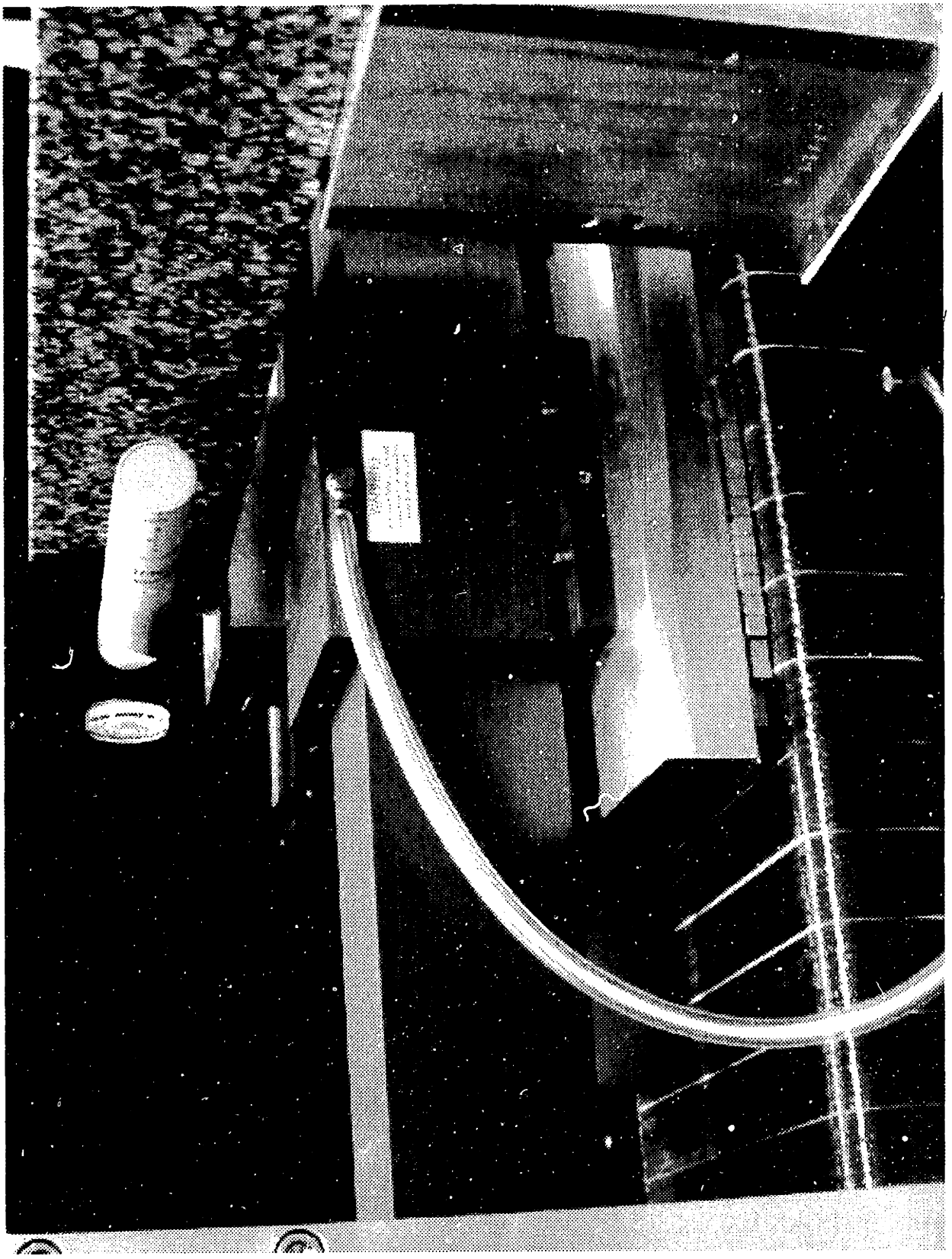

Figure 5-41: Configuration for magnet array measurements

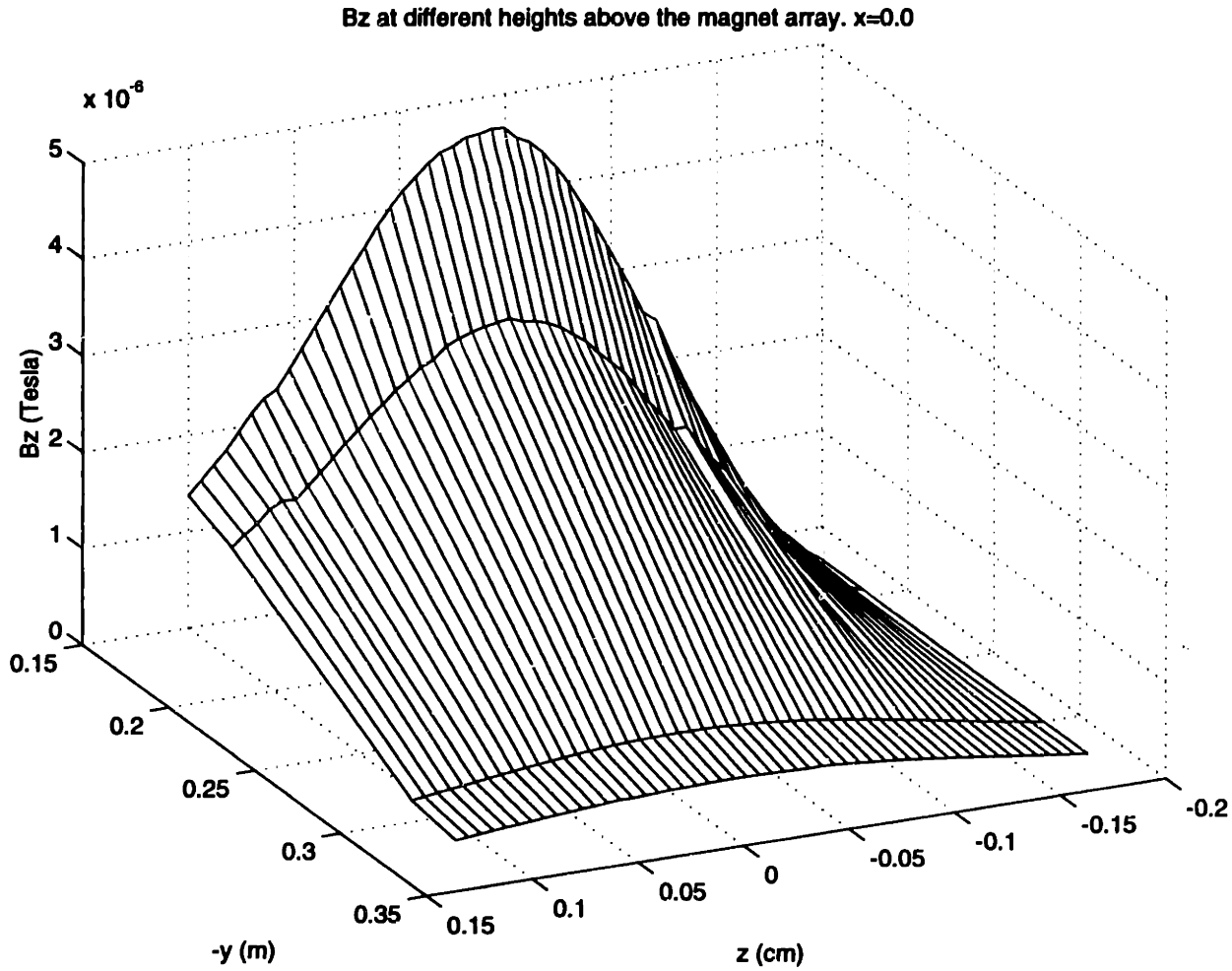

Figure 5-42: Measured flux density in $z - y$ plane

better than .02". The z axis data was scanned in $50\mu m$ intervals, with measurement resolutions of $\lambda/128$ (4.9 nm). The fields at the beginning of the scan were initialized to zero. This introduces error when comparing the scan data, so one must note that there is really an offset between the plots. One way to eliminate this error is to initialize the magnetometer reading very close to zero when the magnet array is placed farther from the probe. Because of the inconvenience of realigning the interferometer mirror, I avoided doing this. Thus the reader must recognize the relative error, especially at the smaller flux density values. At the stronger, flux density values the error is small enough to infer the field properties of interest. Figure 5-42 shows the flux density in the $z - y$ plane along the magnet array's centerline. In consistency with the coordinate system used in previous figures, the $-y$ direction is the height

above the array and the z direction is along the direction of translation. The fields appear to be predominantly those of a dipole, since a single pole dominates over the subtended angle. Figure 5-43 shows the flux density in the $x - z$ plane at $y = 12.8''$ above the array.The x direction is along the array's width. The data reveals that the peak to peak flux density varies by less than 4mG peak to peak. Since the tolerance analysis data calculated the heights where the absolute field magnitude reaches 2mG above the array and not the peak to peak field variations in the plane above the array, it is valid to apply a scaling law to the experimental data for comparison purposes. Assuming the fields decay as r^{-3} and the peak value of the 3.9mG then the fields are expected to decay to 2mG at 16″ from the array center plane. This is consistent with the tolerance simulations presented previously where the fields for the prototype array are expected to attain 2mG at about three times the distance of the theoretical array or about 18″. This is remarkable consistency with the Monte Carlo simulations. Since the actual performance was better than the predicted performance, I suspect the actual remanance and angular tolerances of the magnets were slightly better than expected. Furthermore, the correspondence between the simulations and the experimental results indicates that modelling the associated magnet tolerances as a 3σ gaussian distribution (where the 3σ value is equal to the specified tolerance) is an excellent (but slightly conservative) way to simulate the effects of tolerances.

5.13 Mechanical design

The functional requirements driving the mechanical design of the experimental setup included position control, structural resonance, and the limited gap between the magnet array and the stator. Since I wanted to implement precision motion control in a single degree of freedom, I chose an air bearing slide[10] such that stiction would not limit the position control performance. This air bearing, which has a vertical stiffness of 47.4×10^7N/m, has a natural frequency of 481 Hz with the prototype moving mass of 5.19kg. Incidentally, the rotational vibration modes are also esti-

[10]manufactured by Dover Instrument Corporation, 200 Flanders Road. Westboro, MA 01581

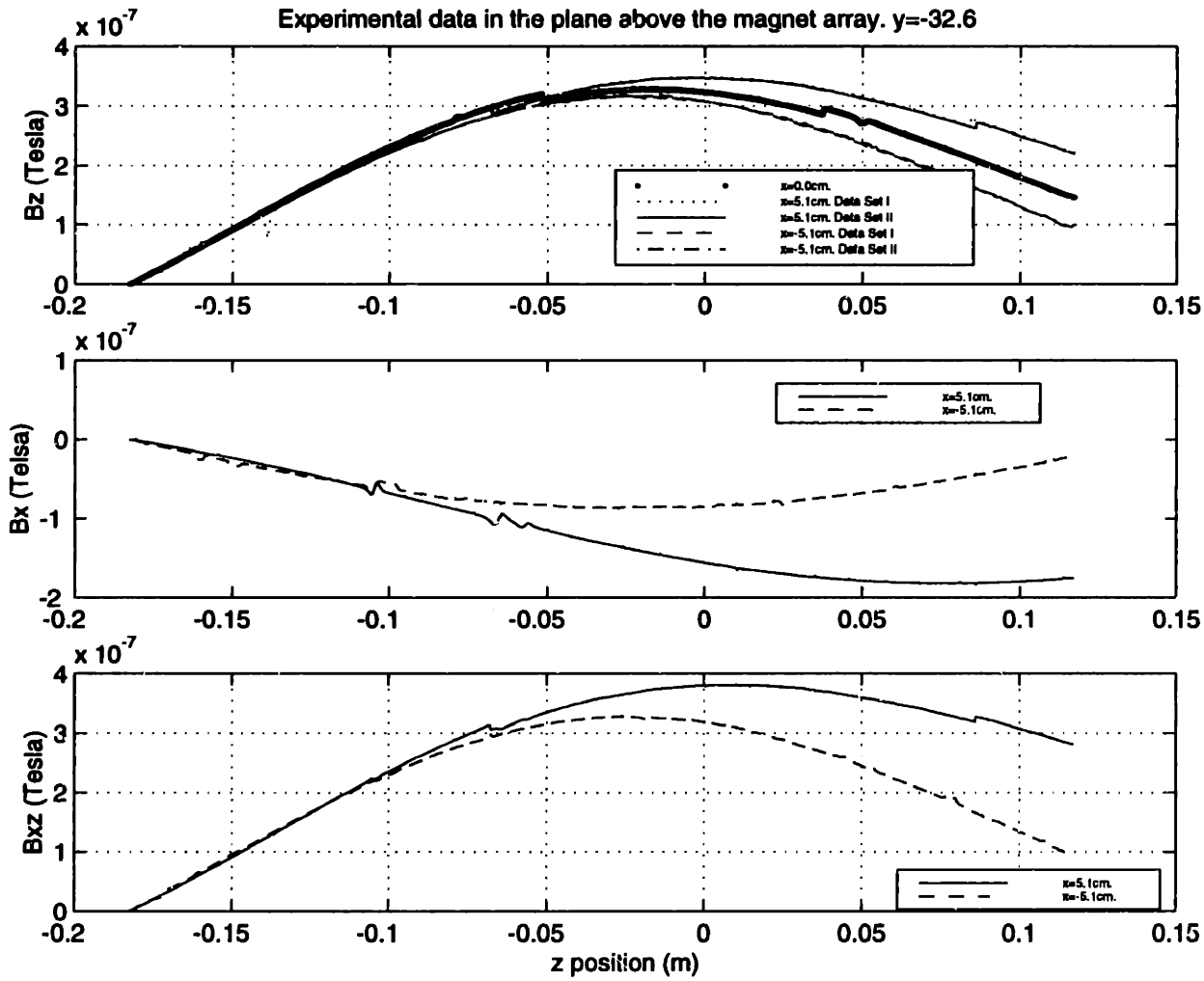

Figure 5-43: Meashured flux density in x-z plane

mated to be close to 500 Hz based on the rotational stiffness and moment of inertia of the moving mass on the air bearing. The rest of the mechanical support structure was designed for natural frequencies of 800 Hz and the stator was designed for 600 Hz. I used a combination of lumped parameter approximations and eigenvalue calculations in ANSYS Multiphysics software to design the components. The limiting component was expected to be the air bearing, with the first natural frequency of the system estimated at about 80% of the air bearing natural frequency or about 380 Hz. I believe the dynamics of the structure structure were compromised by the base since the first natural frequency was found to be 280 Hz. The base is a 1/2″ solid aluminum breadboard [11] supported on elastomer pads that cover about 40% of the base's area. Because the pad area was shimmed during leveling of the air bearing, it is likely that not all the pad area contacts the breadboard. This would account for lower base stiffness. The lower than expected first natural frequency was not the limiting factor in the controls, thus I made no effort to stiffen the base and I did not rigorously pursue whether my suspicions about the source of the structural properties were correct. The 280 Hz ringing of the platen after a force step response is shown in Figure 5-44. The force was produced by the stator with the translation position held constant with control.

Because the efficiency of the magnetic bearing is dependent on the air gap between the stator and the magnet array, I made special efforts to keep the gap small. It was reasonable to design for a nominal gap of .01″ given the expected flatness of the stator and magnet array. The surface of the magnet array was given an error budget of .005″ while the stator was given an error budget of about .008″. If a magnet array is assembled perfectly, its flatness should conform to the flatness of the tooling. The magnet tooling that I used was specified with a profile of surface of .003″. Thus, a small allowance for assembly errors and mold release thickness was acceptable. The stator flatness is limited by the consistency of the coil thickness and the flatness of the stator reference surface. The consistency of coil thickness was found to be ±.003″ and the stator bar reference was machined to .003″flatness. Sufficient margin was left

[11]Model #SA-30X30 manufactured by Newport Corporation

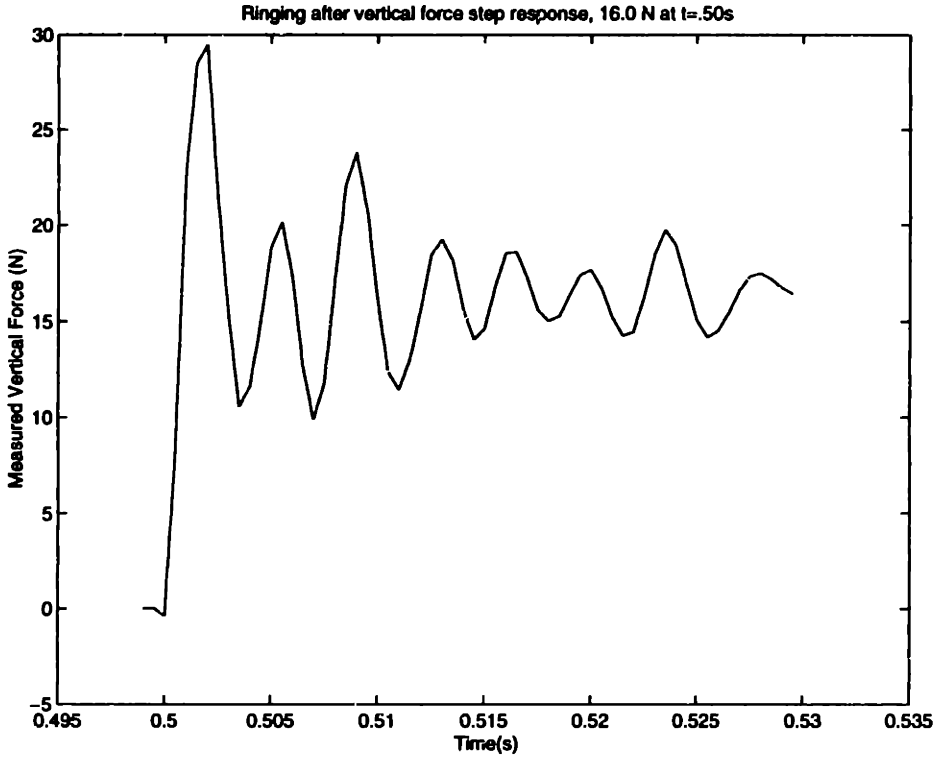

Figure 5-44: Ringing after a force step

for assembly tolerance. After assembling both the stator and the magnet array, the stator supports were shimmed to close the gap to a maximum of .01″.

5.14 Vacuum compatibility issues

Although for the prototype, the experiments were in atmosphere and did not require vacuum compatibility, a production stage must be designed for low outgassing. Because an ebeam system operates at high vacuum pressures of $< 10^{-6}$ Torr, any outgassing of the stage components must not excessively load the vacuum system. As a rule of thumb, all materials should meet or exceed NASA's total mass loss (TML) specification for <1% TML and collected volatile condensable materials (CVCM) specification for <.1% CVCM. These are experimental measures that indicate how much and how long a material will outgas. The details of the testing procedure that defines TML and CVCM can be found in ASTME595-93. Furthermore, NASA publishes a reference, which lists the materials that they have tested [4]. This document

conveniently categorizes the materials that are low outgassing. Since the magnet array uses epoxy and the stator contains potting, these polymers should be selected from this list. Needless to say, any other polymers exposed to vacuum should also meet the vacuum specifications.

While I made no special efforts to select a vacuum compatible coil potting material for the prototype, I did try using Eccobond 285 with 24 LV catalyst to bond the magnet array. I selected the epoxy for its vacuum properties, its high shear strength with aluminum (2100 psi, the coating on the magnets is aluminum with an aluminum chromate flash), and its low viscosity. This vacuum compatible epoxy presented major difficulties. Its long cure time (8-16 hours) and brittleness slowed successful assembly to unacceptable levels. I especially had problems once large assemblies were formed because micro-defects in the bonds would lead to fracture of the epoxy under normal handling conditions. Because of time constraints, I finished the magnet assembly with two hour epoxy, available at the local hardware store, which was much less brittle.

For a production ebeam machine, the combination of mechanical constraint of the magnets and a better epoxy would prevent the problems of bond failure. Constraining magnets certainly is not an insurmountable problem but further development is necessary.

Because NeFeB corrodes, the magnets should be coated with a vacuum compatible coating. Coatings such as aluminum chromate and cadmium chromate are routinely used by magnet vendors where vacuum compatibility is required. Polymer coatings such as non vacuum compatible epoxy should be avoided.

Further engineering is also warranted on coil potting. The potting process will require vacuum impregnation to prevent voids in the coils – a relatively expensive operation compared to resistance bonding. I did not experiment with vacuum impregnation because this problem was not considered a risk issue and because of time constraints. There is also an alternative to vacuum compatibility if materials present a problem. Components could be hermetically sealed to separate them from vacuum.

Besides material compatibility, a stage engineered for vacuum should be designed with good vacuum practice in mind. That is, the surface area should be minimized

because surface desorption can be the largest constraint in pump down time. Furthermore, the surfaces should not be permeable to water and other fluids. Lastly, joining and sealing operations must not allow virtual leaks.

5.15 Digital architecture and sensor layout

A block diagram of the digital architecture and the sensor layout is shown in Figure 5-45. The laser interferometer feedbacks position to the control computer for motion control in one degree of freedom. The force sensors detect the vertical forces produced by the magnetic bearing. This data is used for analysis of the vertical forces and for force control. The magnetometer interfaces to the computer with the analog output from the dual mode amplifier and the 16 bit A/D converter. The 16 bit D/A converter outputs to the three linear amplifiers to control the currents in the three phases of the magnetic bearing.

5.16 Amplifier Design

The amplifier architecture is shown in Figure 5-46. My design goal was a linear current amplifier that behaves like a low pass filter with about 1600 Hz bandwidth. Considering that the controls are expected to operate at about 100 Hz bandwidth, the dynamics of the amplifier can then be ignored for control purposes.

This amplifier can be analyzed in blocks by considering the power booster stage and the differential amplifier stage. I begin the design by canceling the zero in the booster stage with one of its poles by setting $\frac{R_m}{L_m} \approx \frac{1}{R'C'}$. The magnetic bearing was determined to have $R_m = 72.49\Omega$ with an HP3478A Multimeter and an inductance of $L_m = 35.7mH$ with a 35665A dynamic signal analyzer[12]. Thus, $\frac{1}{R'C'}$ was set to about 320Hz by setting R'=.47MΩ and $C' = 1000$ pF. C_3 is included in the design to add a high frequency pole, thereby causing higher order roll off at the higher frequencies

[12]The inductance was calculated after measuring the bandwidth and the resistance of a sensing resistor in the L-R circuit

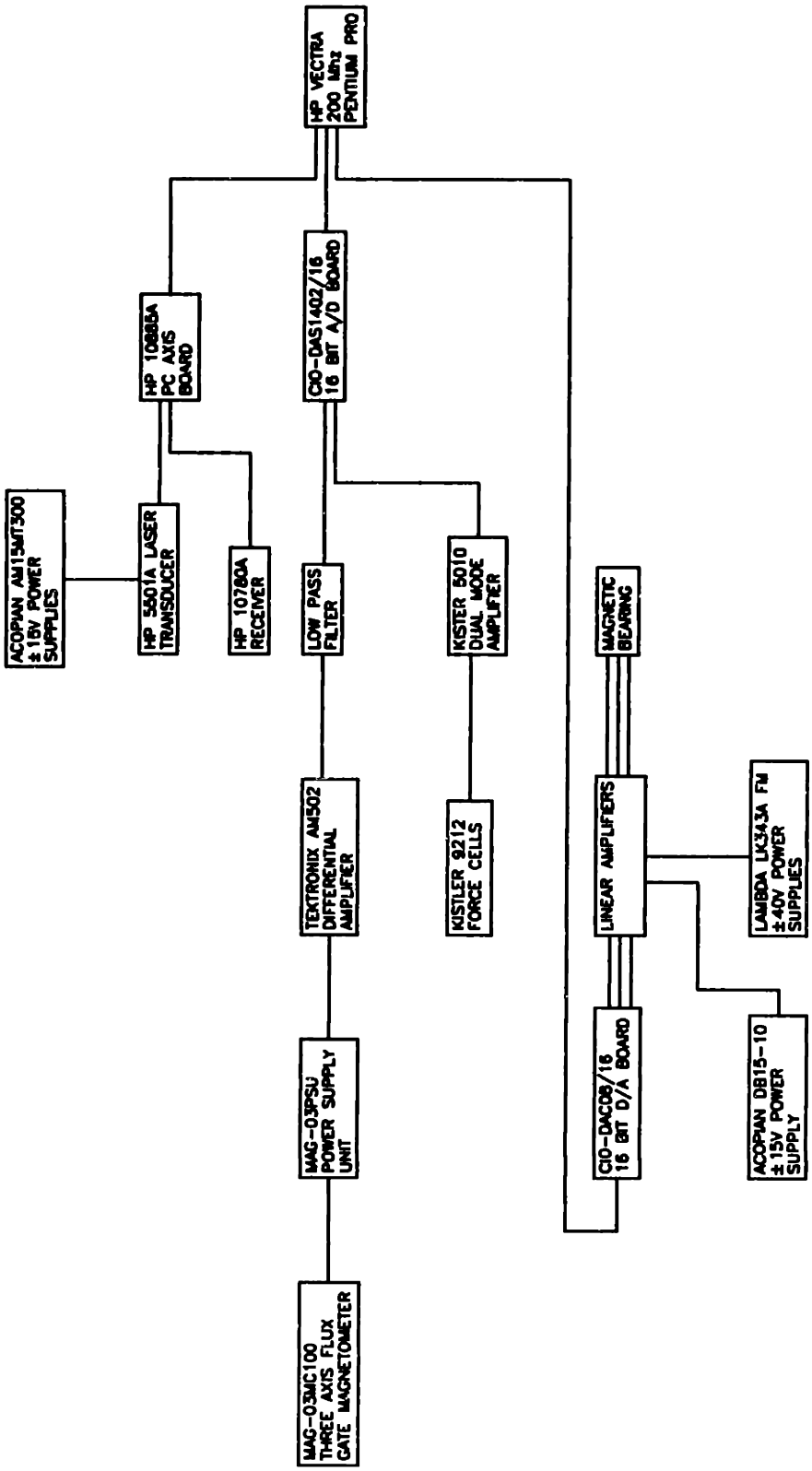

Figure 5-45: Digital architecture and sensor layout

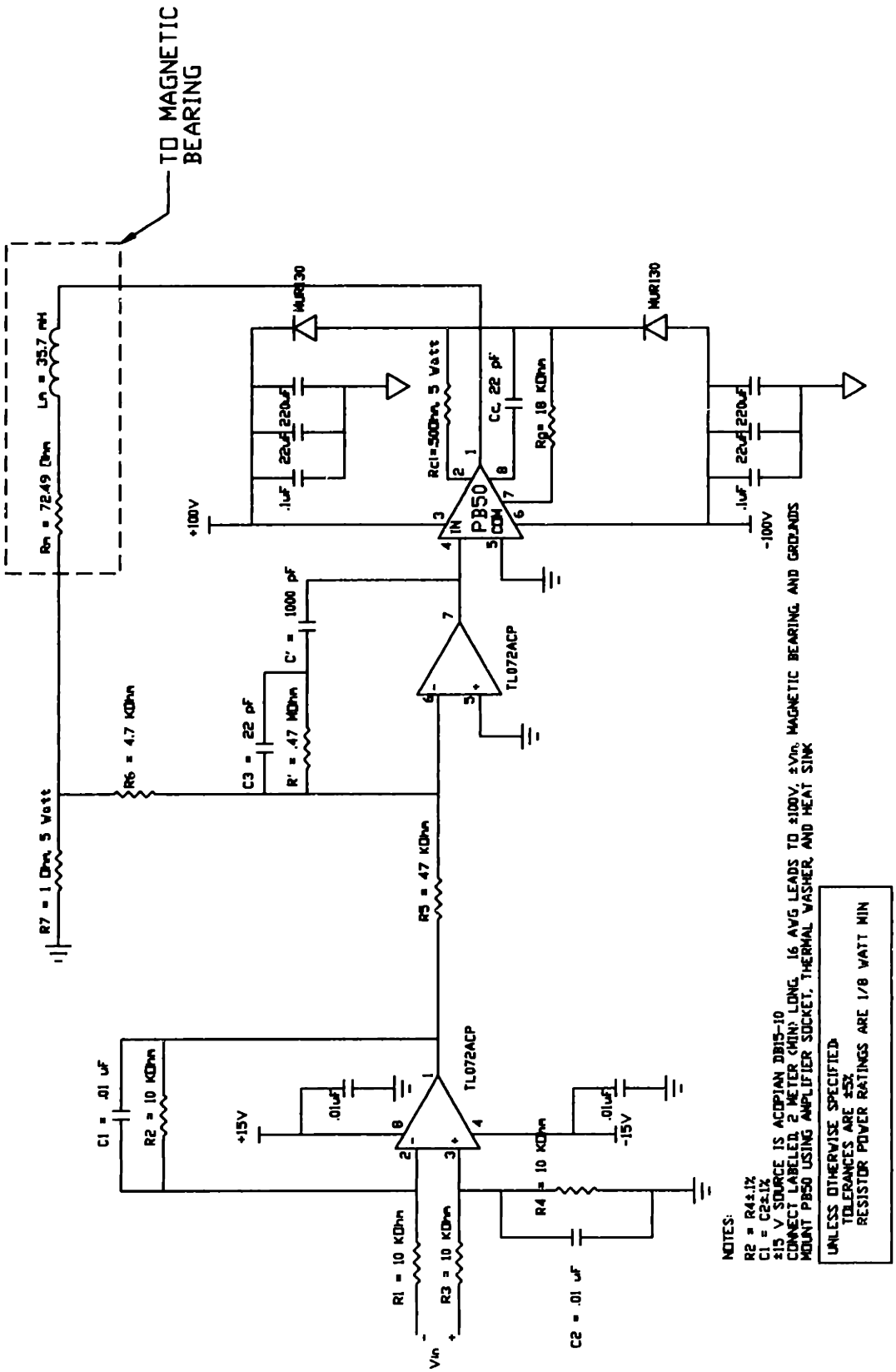

Figure 5-46: Amplifier architecture

without appreciably reducing the phase margin at the lower frequencies of interest. The higher frequency poles are at about 7000 Hz.

Next, I select the nominal power supply voltage to the power booster by calculating the voltage across the motor with the nominal current of 0.398 amps. The nominal voltage requirement is 28.9 volts (the inductance contribution is small in the range of driving frequency and input magnitude). The PB50[13] is chosen as the power booster and could be used in conjunction with ± 100 volt (max) sources to produce a voltage output of ± 90 volts (max). This margin of $3.1\times$ on the voltage requirement should be sufficient for control purposes.

The TL072ACP has a maximum voltage output of ± 12 volts with ± 15 volt supplies. The gains across these op amps are set to one, leaving an acceptable margin before saturation since the inputs from the D/A board in my computer ranges from ± 10 volts. The gain across the power booster is sized to 9 since the PB50 will provide a maximum output of ± 90 volts. The booster gain taken from the Apex catalog is given by

$$G_b = \frac{R_g + 6.2K\Omega}{3.1K\Omega} + 1. \tag{5.25}$$

In practice, a standard 18 $K\Omega$ resistor results in a booster gain of 8.81. Component selection proceeds by considering the amplifier's differential stage. The transfer function of the differential stage is given by

$$\frac{V_{out,differential}}{V_{in,differential}} = \frac{R_2R_4(C_1 + C_2)s + R_2 + R_4}{(R_1 + R_3)(R_2C_1s + 1)(R_4C_2s + 1)}. \tag{5.26}$$

Simplifying by setting $R_1 = R_2 = R_3 = R_4 = R_d$ (resulting in unity DC gain) and setting $C_1 = C_2 = C_d$ I eliminate the zero and the transfer function becomes:

$$\frac{V_{out,differential}}{V_{in,differential}} = \frac{1}{(R_dC_ds + 1)}. \tag{5.27}$$

In practice, R_2 and R_4 are held within .1% of each other. The capacitances C_1 and

[13]Manufactured by Apex Microtechnology Corporation, 5980 N. Shannon Road, Tucson, Arizona 85741-5230

C_2 are assigned the same tolerance.

The static gain of the booster stage is now set based on the limits of the maximum power supply voltage and the voltage range of the D/A converter ($\pm 10V$). Because the desired booster output is limited to 90V, the current gain is assigned by the approximation

$$I_{gain} = \frac{V_{source,max}}{V_{in,max}(R_m + R_7)}. \tag{5.28}$$

which, equals .122 resulting in a margin of 10*.122/.398 = 3.08 for the current.

The static booster current gain is given by

$$\frac{I_{winding}}{V_{out,differential}} = -\frac{R_6 + R_7}{R_5 R_7}. \tag{5.29}$$

The resistors are sized for the current gain of less than -.122. In practice, standard 4.7 $K\Omega$ and 47 $K\Omega$ resistors are used for R_6 and R_5 respectively. The gain is -.100, which now yields a current margin of 2.5×.

Now R_d and C_d are chosen as 10 $K\Omega$ and .01 μF to yield a nominal amplifier bandwidth of the approximately 1600 Hz. The bode plot for the amplifier is shown in Figure 5-47.

Lastly the current limiting resistors are set according catalog specifications for the PB50 given by

$$I_L = .65/R_{cl}. \tag{5.30}$$

I set I_L to 1.3 Amps by choosing a .50 Ω resistor.

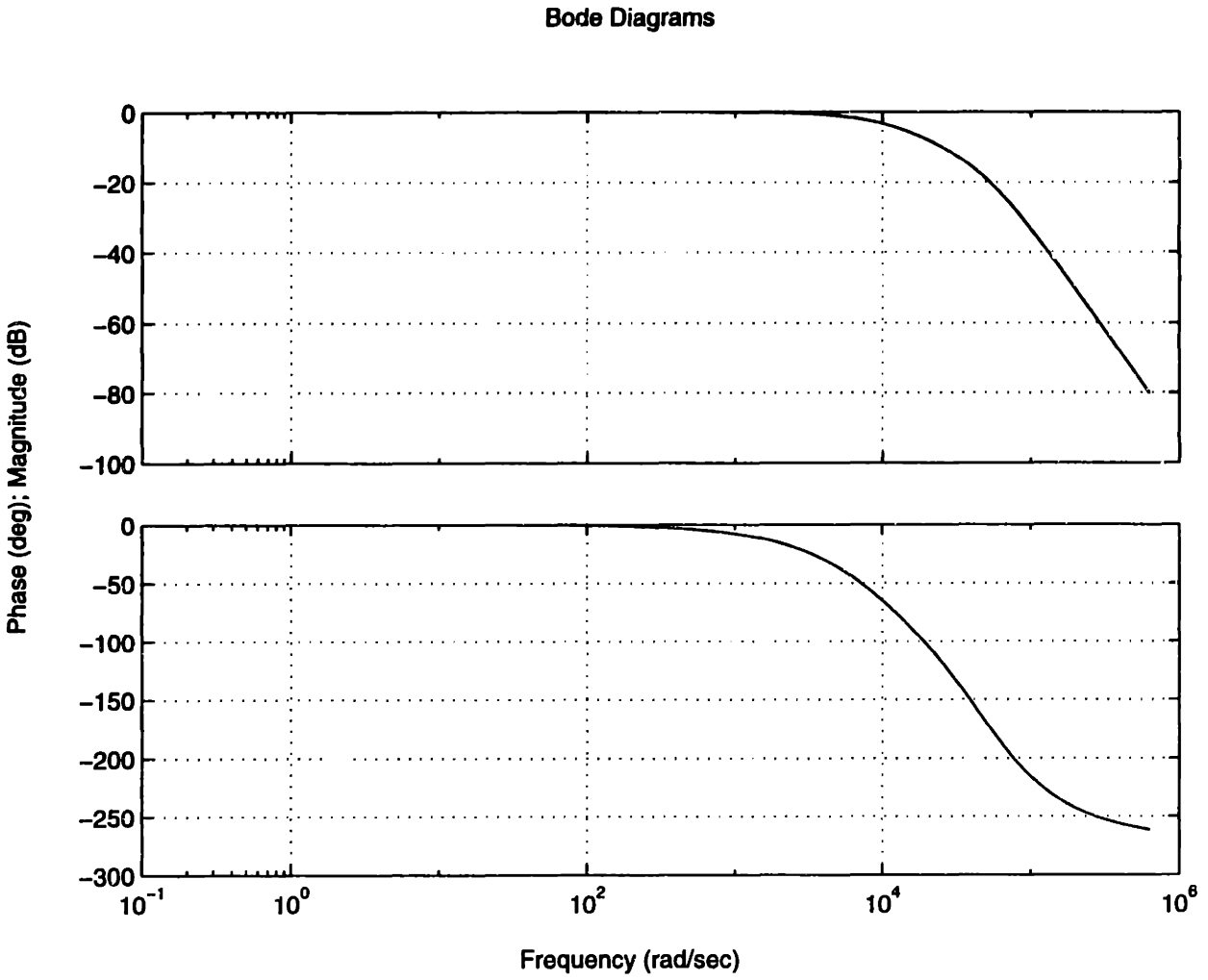

Figure 5-47: Bode plot for the linear current amplifier

Chapter 6

Controls

6.1 Controller performance requirements

The controller must drive the stage within positional accuracy and position noise requirements. The positional accuracy requirement is determined from the acceptable scan range of the ebeam and not the pattern accuracy requirement. Moreover, the ebeam can be scanned in real time to correct for the measured position error of the stage. The scan length for a commercial system can be hundreds of microns long and in the MEBES 4500 the maximum scan length is 1.1mm long [9]. Because of the ebeam's ability to deflect, the ebeam exposes a stripe, many small pixels wide, on each stage pass. This reduces the number of times the stage needs to raster to expose an entire pattern. Similarly, for the same throughput, the stage can travel at slower velocities, which generally translates to smaller platen disturbances.

However, long scan lengths tend to increase pattern errors because of limitations in metrology, ebeam aberrations, and scan nonlinearities. While certain techniques such as height correction [9] can be implemented to reduce these errors, for the best performance, the machine will operate at scan lengths below its maximum. If a maximum scan window that produces acceptable performance is specified, it is important that the address on the substrate at the time of writing not exceed this window. More specifically, the ebeam machine must write stripes that are narrower than the maximum scan length by an amount equal the platen positional accuracy. If the desired

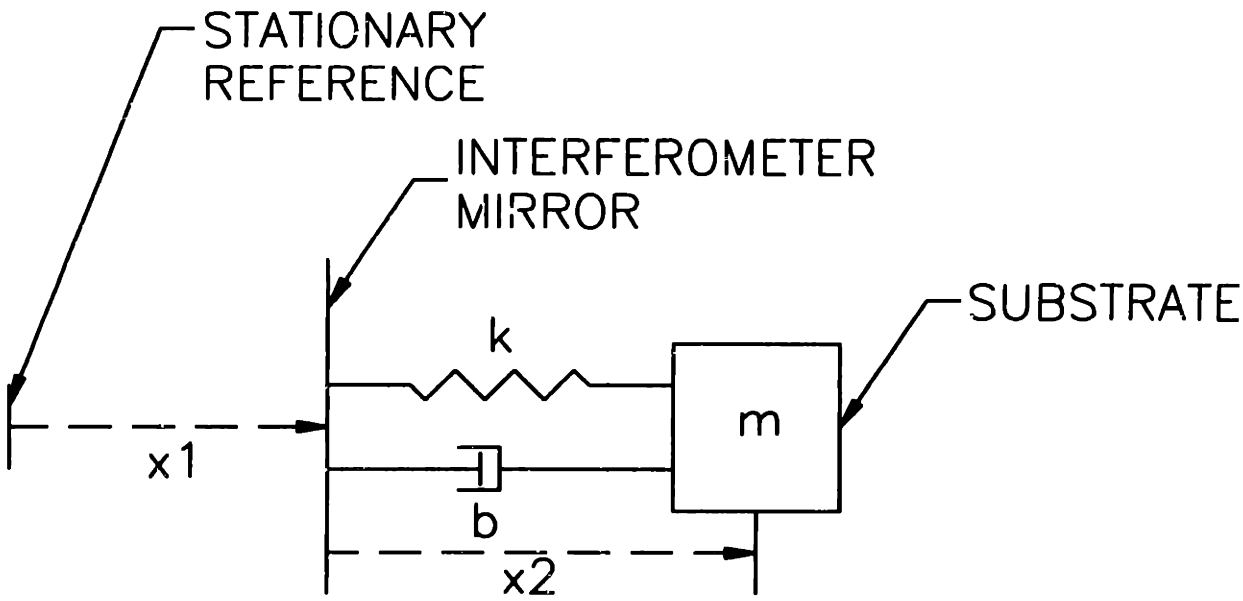

Figure 6-1: Model of platen resonant structure

positional accuracy is set to $\frac{1}{100}\times$ the scan length and a scan length of 100 μm is assumed, then the required stage accuracy is 1μm.

The position noise requirement of the stage is primarily limited by the structural resonance of the platen. For engineering purposes, I assume the substrate is attached to the interferometer mirror by means of a resonant structure [36] with natural frequency and damping factor designated ω_n and ζ. The schematic for this model is shown in Figure 6-1. The transfer function and its magnitude for this system is given by Equations (6.1) and (6.2) respectively.

$$G(s) = \frac{X_2(s)}{X_1(s)} = -\frac{s^2}{s^2 + 2\zeta\omega_n s + w_n^2}, \tag{6.1}$$

$$|G(j\omega)| = \frac{1}{\sqrt{\left(\frac{2\zeta\omega_n}{\omega}\right)^2 + \left(\left(\frac{\omega_n}{\omega}\right)^2 - 1\right)^2}} \tag{6.2}$$

where

$$\omega_n = \sqrt{\frac{k}{m}}, \quad \text{and} \tag{6.3}$$

$$\zeta = \frac{b}{2\sqrt{km}}. \tag{6.4}$$

The expected displacement of the substrate relative to the interferometer mirror due to controller position noise can be modeled stochastically. A review of the basic stochastics can be found in [22]. The controller position noise can be described by the autocorrelation function, which is given by

$$R_x(\tau) = \lim_{T\to\infty} \int_{-T}^{T} x(t)\, x(t-\tau) dt. \tag{6.5}$$

If τ=0, the autocorrelation function reduces to the mean squared of the waveform or the variance. The Fourier transform of the autocorrelation function is the spectral density of the waveform and is given by

$$S_x(\omega) = \int_{-\infty}^{\infty} R_x(\tau) e^{-j\omega\tau}\, d\tau. \tag{6.6}$$

If the controller position noise is modeled as a random waveform $x(t)$ with a spectral density $S_x(\omega)$, the spectral density of the output waveform y(t), assuming a linear plant, is given by

$$S_y(\omega) = |G(j\omega)|^2\, S_x(\omega). \tag{6.7}$$

Thus, the spectral density of the displacement of the substrate relative to the interferometer mirror can be modeled if the spectral density of the controller position noise is known. The variance of the relative substrate displacement is calculated by taking the inverse Fourier transform to obtain the autocorrelation function at τ=0. The variance is given by

$$\sigma_y^2 = \frac{1}{2\pi} \int_{-\infty}^{\infty} S_y(\omega)\, d\omega. \tag{6.8}$$

Here σ_y is the standard deviation of the substrate noise. The $6\sigma_y$ requirement for an ebeam lithography machine will be on the order of a nanometer or two.

6.2 Plant model

The plant can be modeled as a mass damper system. The state equations are written as

$$\begin{bmatrix} \dot{x} \\ \ddot{x} \end{bmatrix} = \begin{bmatrix} 0 & 1 \\ 0 & -\frac{b}{m} \end{bmatrix} \begin{bmatrix} x \\ \dot{x} \end{bmatrix} + \begin{bmatrix} 0 \\ \frac{1}{m} \end{bmatrix} F_x \tag{6.9}$$

$$\begin{bmatrix} y \end{bmatrix} = \begin{bmatrix} 1 & 0 \end{bmatrix} \begin{bmatrix} x \\ \dot{x} \end{bmatrix} \tag{6.10}$$

where m is the mass of the moving part, b is the dashpot constant due mainly to eddy current damping induced by the magnet array translating over the conductive stator bar, and y is the plant output. The transfer function, $G(s)$ for this system is given by

$$G(s) = \frac{1}{m(s + \frac{b}{m})s}. \tag{6.11}$$

The constants m and b are determined experimentally from step response data with a proportional controller. Previous measurements determined the force to current constant from vertical force sensor data. Step response data, using displacement feedback from the interferometer and closed loop proportional control, revealed the time constant and the damped natural frequency; m and b were then calculated to be 5.19 kg and 12.44 Ns/m.

6.3 Controller design

I constructed a controller composed of a lead compensator and two integrators. A single integrator eliminates the steady state errors such as those associated with proportional velocity control against the eddy current damping. The second integrator combines to also remove errors associated with acceleration in the stage trajectory. The lead compensator adds phase to the loop transmission and thus damping to

system. The controller is given by

$$G_c(s) = \frac{s+z_1}{s+p_1}\left(\frac{s+z_2}{s}\right)^2. \tag{6.12}$$

I implemented several variations of this controller and evaluated their performance during a scanning profile. The scanning profile consisted of a cubic spline fitting of the position reference such that any changes in platen acceleration occurred with constant jerk. The spline used the following parameters: jerk = .981 m/s^3, maximum acceleration = .05 g's, and maximum velocity= .03125m/s. The fitting was performed during the control routine. Because I wanted to minimize the position error during the entire profile, I placed the zeros of the two integrators to reduce the position error down to about ±100nm or about twice the position noise.

The Bode plot of the open and closed loop systems are shown in Figures 6-2 and 6-3 respectively. The desired bandwidth was set to 120Hz. In the first stage of the controller design, I just considered the lead compensator. The controller design requires the maximum phase addition to correspond to the controller bandwidth. I chose the desired phase addition to be 60^o to achieve critical damping. My initial values were based on rules of thumb. I set $\sqrt{p_1 z_1} = \omega_c$ and $p_1 = 10 \times z_1$, where ω_c is the desired controller bandwidth. The loop transmission magnitude was then adjusted to unity at ω_c. I then added two integrators and adjusted their zeros until I achieved a simulated position error during a scan of about 100nm. I used Matlab's "lsim" command in the Control System Toolbox to perform these simulations. After several iterations I completed fine tuning the poles and zeros for the controller. The continuous time controller is given by

$$G_c(s) = \frac{s+125.669}{s+2513.27}\left(\frac{s+50.2655}{s}\right)^2. \tag{6.13}$$

This continuous time controller was mapped to discrete time via Matlab's "c2dm" function with a sampling rate of 2000Hz to obtain the following discrete transfer

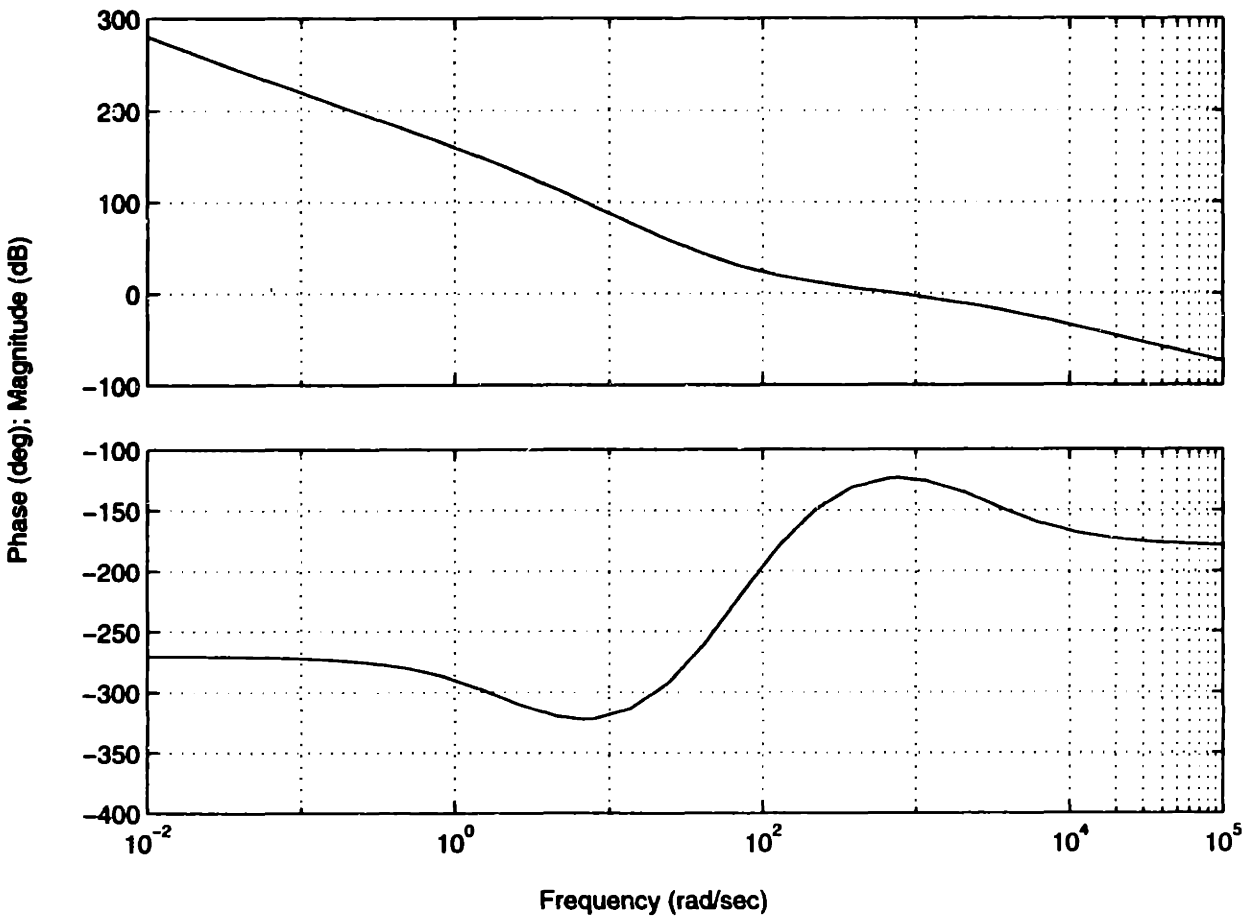

Figure 6-2: Bode plot of loop transmission

function

$$G_z(s) = \frac{1.008343e7z^3 - 2.958792e7z^2 + 2.894755e7z - 9.442837e6}{z^3 - 2.2846010z^2 + 1.569219z - .2846095}. \qquad (6.14)$$

The results of the implementation are discussed in Section 6.5.

6.4 Software

The real time software is implemented on a PC with a 200Mhz Pentium Pro processor operating under the DOS environment. The real time interrupt service routine is initiated by issuing an interrupt from the CIO-DAS1402/16 ADC board. Because this

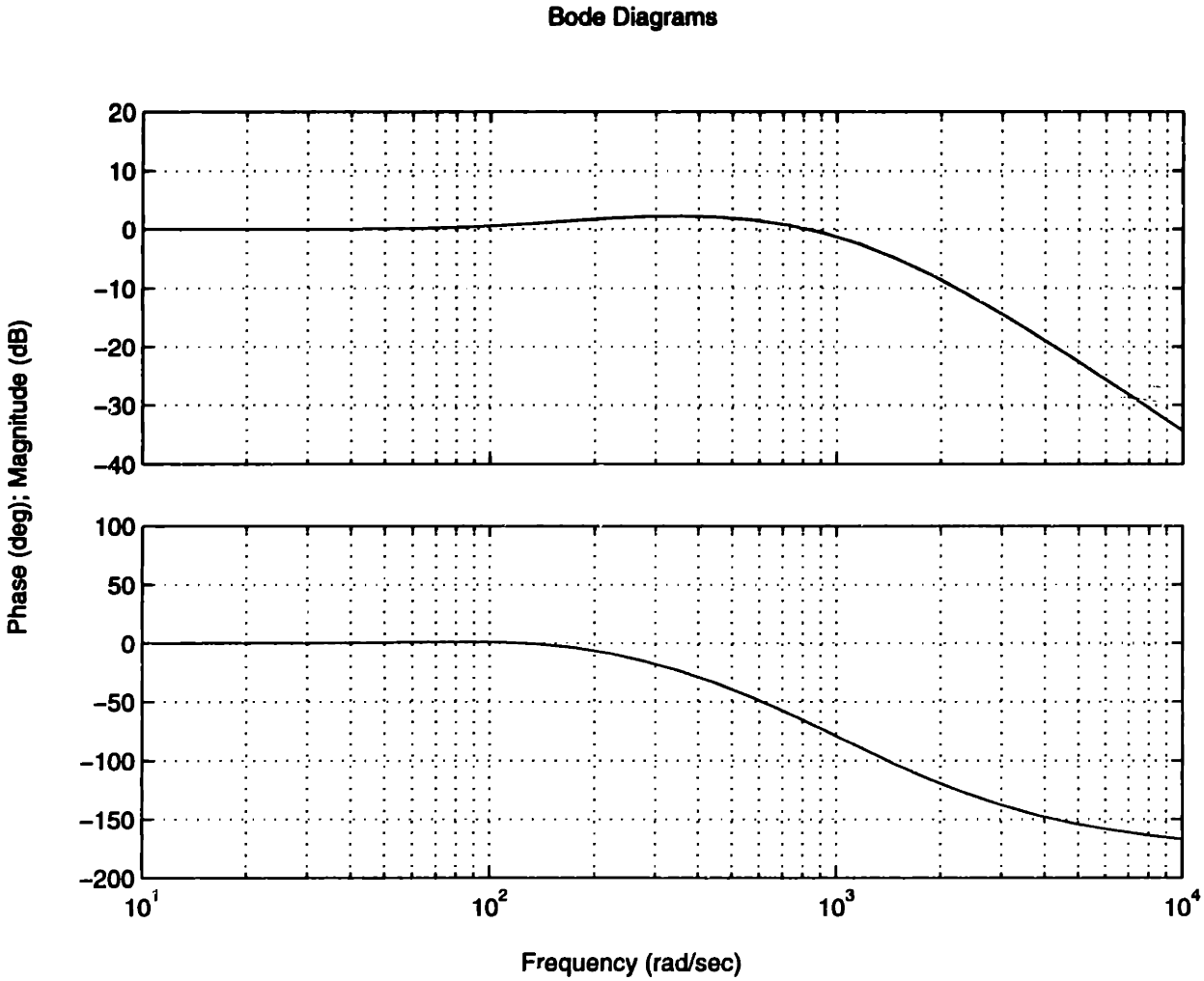

Figure 6-3: Bode plot of closed loop system

board contains a programmable counter timer, the interrupts are issued at discrete intervals. The interrupt service routine (ISR) is stored as IRQ7 on the Intel 8259 programmable interrupt controller, which is resident to the PC. For the low level programming details, [14] is a good reference. Refer to Section 5.15 for a more complete description of the system architecture.

The software was compiled with a Borland C compiler. The program performs the following functions

1. Initialize variables
2. Get and store old 8259 mask
3. Get and store address of old ISR
4. Mask level 7 interrupts
5. Set vector entry to new ISR
6. Unmask level 7 interrupts
7. Initialize CIO-DAS1402/16 ADC board
8. Command current to one phase by issuing a voltage from the CIO-DAC08/16 DAC board to one linear current amplifier
9. Set commutation phase by letting the platen hunt to an equilibrium position
10. Wait for user OK
11. Initialize HP10885A PC Axis board
12. Read platen position from the HP10885A PC Axis board and begin proportional control
13. Set the Intel 8254 counter timer chip (on the CIO-DAS1402/16 ADC board) for the desired sample time
14. Enable interrupts from CIO-DAS1402/16 ADC board

15. Interrupt service routine

    (a) Read platen position from the HP10885A PC Axis five times and convert the averaged data to a position measurement

    (b) Calculate new platen position from the profiling algorithm

    (c) Calculate controller output

    (d) Compute phase currents to correspond to the controller output

    (e) Output command voltages to the three linear current amplifiers from CIO-DAC08/16 DAC board

    (f) Read sensors from designated channels on the CIO-DAS1402/16 ADC board (for magnetometer and force sensor measurements, if specified during initialization)

    (g) Save data

    (h) Reset interrupt circuitry on board

    (i) Signal end of interrupt to master 8259 controller

16. Display data on the computer screen

17. Continue interrupt service routine until the user hits a key

18. Disable CIO-DAS1402/16 board interrupts

19. Zero the voltage output from CIO-DAC08/16 DAC board

20. Again mask level 7 interrupts

21. Reset interrupt vector

22. Reset the old 8259 mask

23. Unmask level 7 interrupts again

24. Save data to disk

6.5 Controller performance and results

The profile error, position reference, and velocity profile during a 3 cm scan is shown in Figure 6-4. The overall data fits the simulated model well. There are significant noise contributions that are revealed from discrete Fourier transform (DFT). Figure 6-5 shows the DFT of a segment of the constant velocity portion of the scan. The low frequency components are very likely due to ground vibration and ripple force of the magnetic bearing.

The largest DFT coefficient is found at 120Hz. This is probably due to the floor vibration induced by rotating machinery and/or transformers in surrounding rooms. Unfortunately, I ran out of time to trouble shoot the exact source of this noise for this thesis. However, [22] documents the DFT of the floor vibrations in the same room where I performed my experiments; significant low frequency and large 120Hz disturbances were reported. The 120Hz component is a tremendous limitation to the controller performance since the controller is not faster than it. In a real system, this disturbance would need to be removed. The DFT in Figure 6-5 also shows a peak at about 280Hz. This corresponds to the 280 Hz first natural frequency of the platen that I mentioned in Section 5.13. By reducing the bandwidth of the controller, this peak can be reduced. Another noise source to pursue is the output of the interferometer.

Figure 6-6 shows the Bode plot of the substrate to stage relative displacement given by Equation (6.1). For the purpose of argument, ω_n and ζ are set to 400 Hz and .001 respectively. The phase of the transfer function is 0^o with a gain increasing by 40 dB per decade essentially up to the natural frequency where it crosses -90°. At higher frequencies the transfer function has a gain of one with -180° phase. Thus the position noise of the platen is largely attenuated at low frequencies, with very high amplifications near the damped natural frequency. The high frequency platen noise is essentially not attenuated above ω_n, and the substrate motion is -180° out of phase with the platen. The variance of the substrate position noise can be calculated from Equation (6.8) if the platen position noise is known.

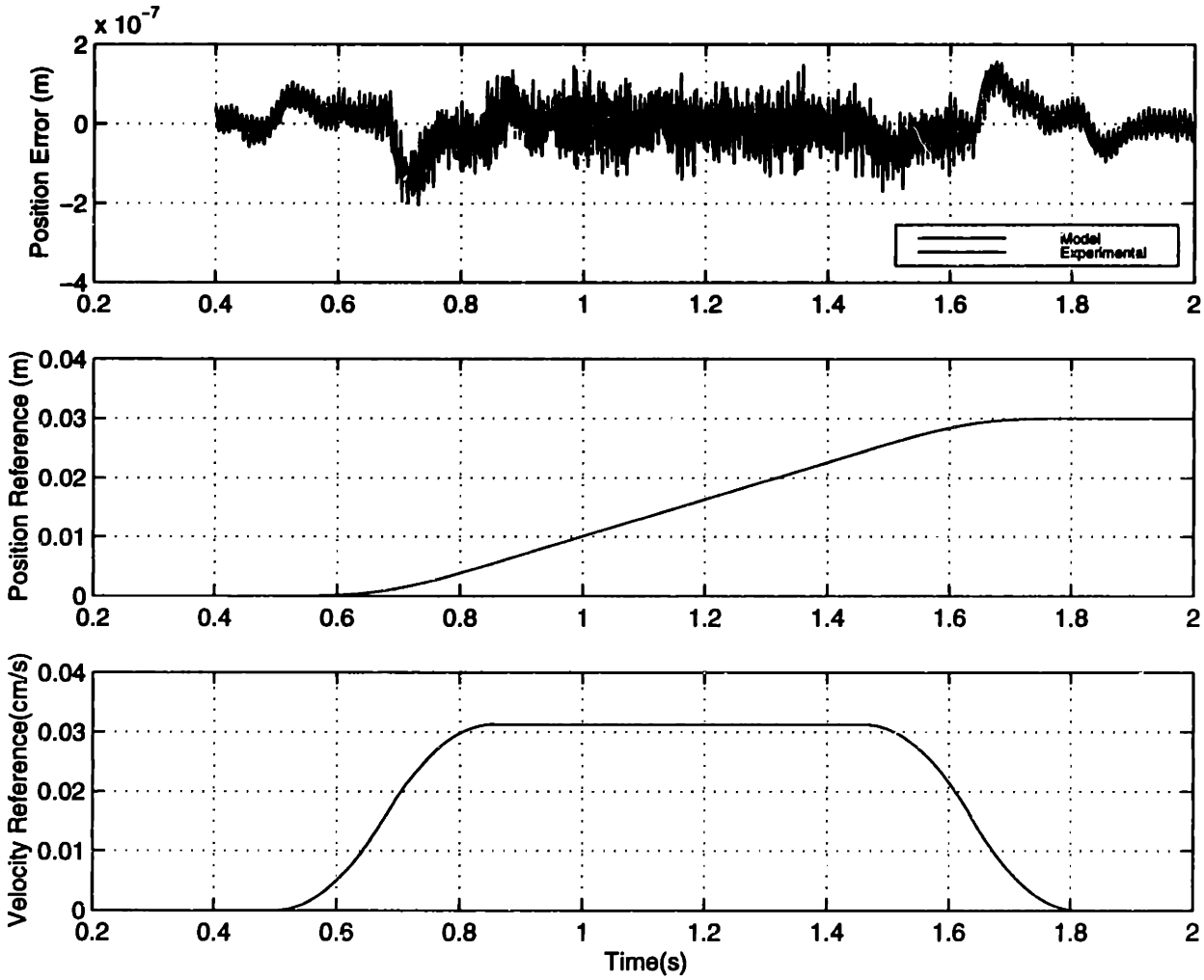

Figure 6-4: Position error during a scan for a lead lag controller

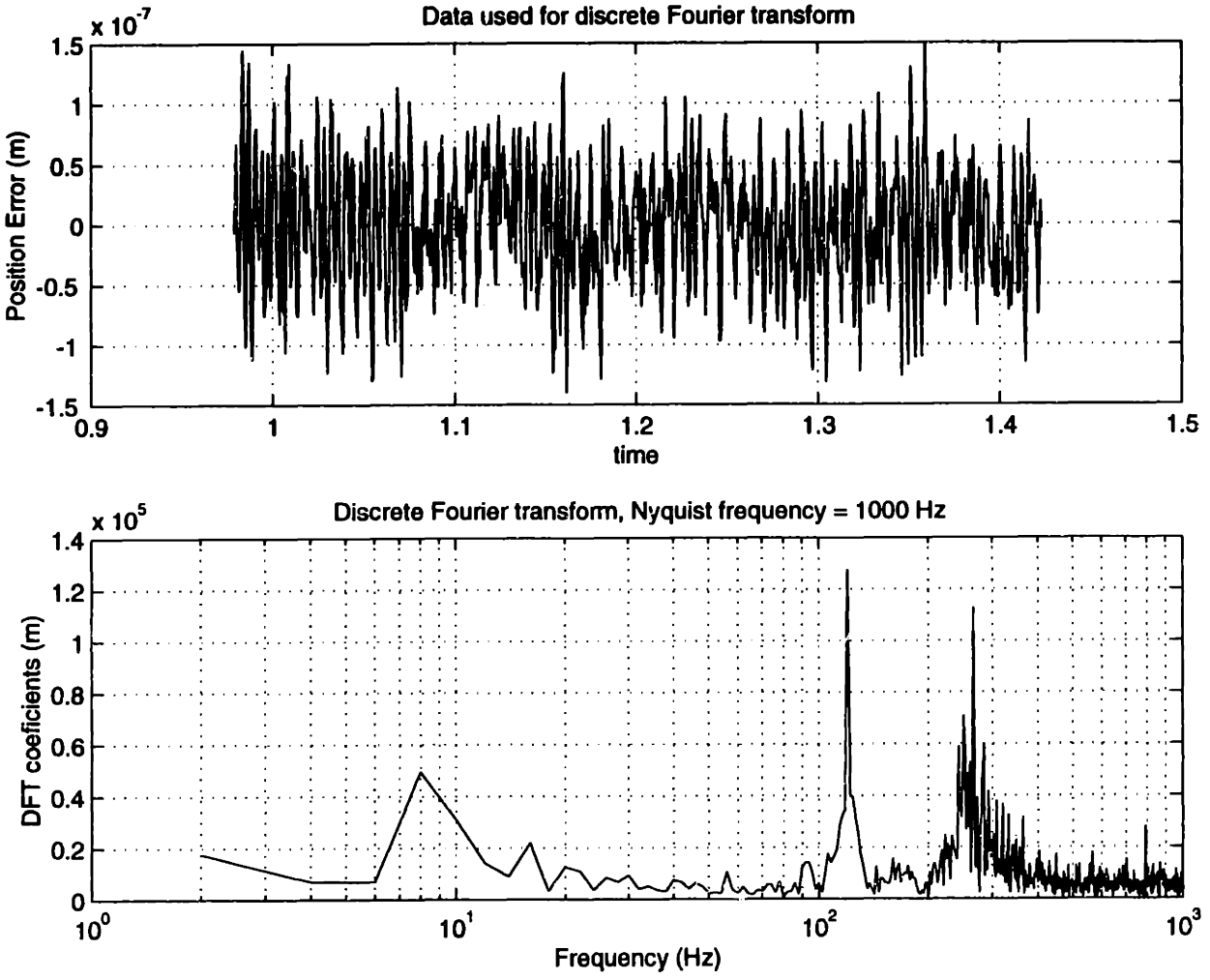

Figure 6-5: Discrete Fourier transform of position error during constant velocity profile

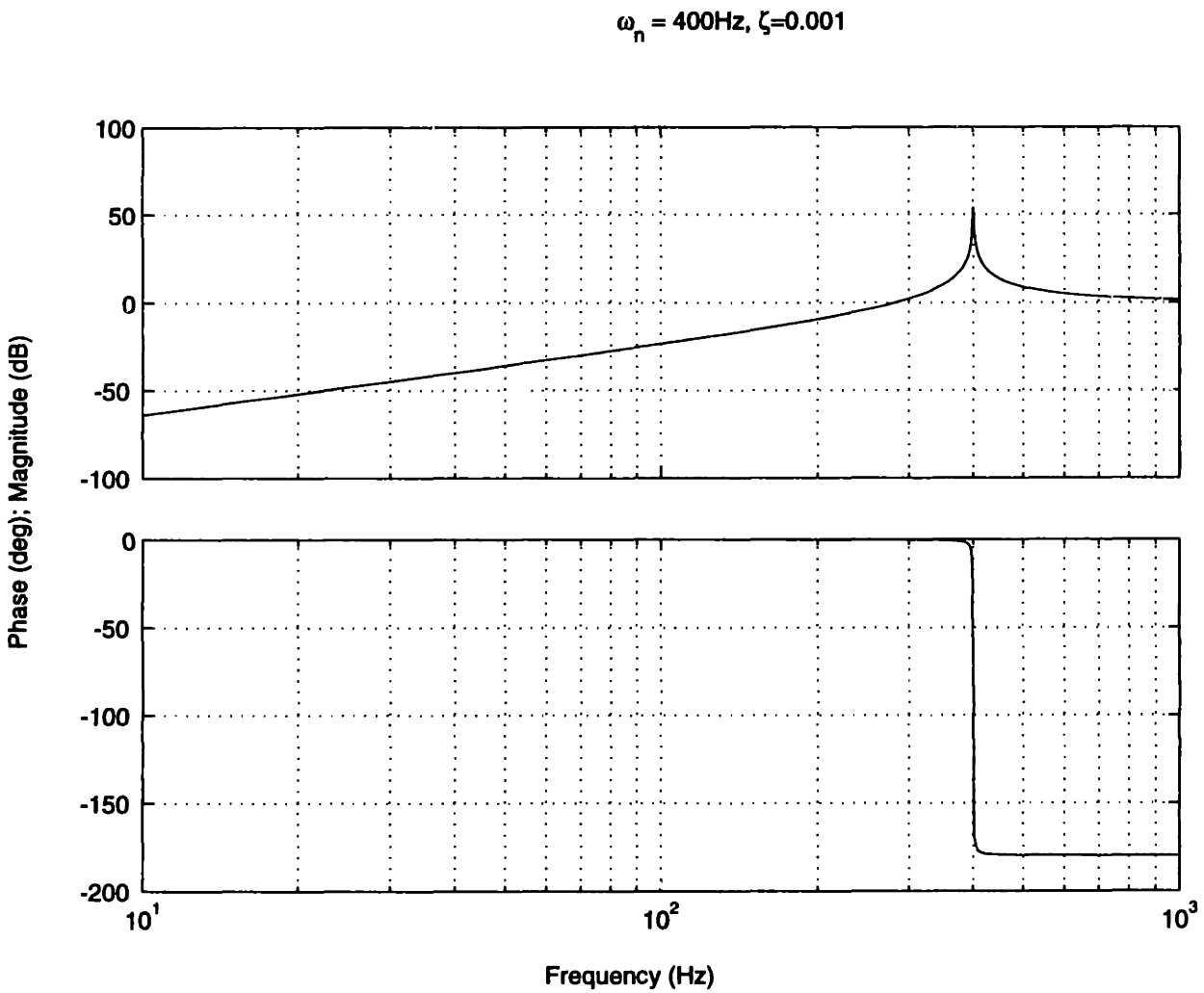

Figure 6-6: Bode plot of substrate displacement

Figure 6-7 shows the power spectrum[1] of the same data used in Figure 6-5. The substrate position noise is also shown. While the 6σ platen position noise is 300 nm, the 6σ position noise of the substrate is 3100nm as calculated from Equation (6.7) and the integral of Equation (6.8). The position noise is amplified because the substrate spectrum is amplified near the damped natural frequency. This position noise is not even close to the requirement. However, I did not make any efforts to design a position noise optimal controller. Also, the bandwidth of the controller is too high for the natural frequency of the experimental setup. Nor did I sufficiently troubleshoot the high frequency disturbances. Similarly, the controller performance was not designated as a priority for this thesis and I was unable to fully develop the controls in the time allotted. This should be an area for future study.

If in a production system, sufficient efforts are taken to reduce the noise above 100 Hz then I can just consider the power spectrum from 0 to 100Hz. The 6σ position noise from the integral of Equation (6.8) from zero to a hundred hertz is 1.3 nm. This would be satisfactory for an ebeam system. Considering that I am not using an isolation table, ideal environmental conditions, nor an optimal controller, I would expect this number is larger than what could be achieved.

Figure 6-8 shows the discrete Fourier transform of the steady state position error. This data was taken just after the scan in Figure 6-4 as indicated by the time scale. For these measurements, the platen resonance is not nearly as excited as during the constant velocity portion. In general, all the DFT coefficients above the 120 Hz spike are much smaller. Also, the low frequency components near 8Hz are smaller because of the lack of force ripple.

Figure 6-9 shows the power spectrum of the steady state data. The 6σ position noise calculated from the integral of Equation (6.8) from 0 Hz to 1000 Hz for the platen and the substrate is 150 nm and 54 nm respectively. The 6σ position noise of the substrate when just the frequencies from 0 to 100 Hz are considered is .8 nm.

The profile error during a scan with an open loop vertical force of $F_z = 10$ N is

[1]Calculated with Matlab's "psd" function. psd divided the data into overlapping sections 256 data points wide. Or in terms of Matlab help, NFFT =256.

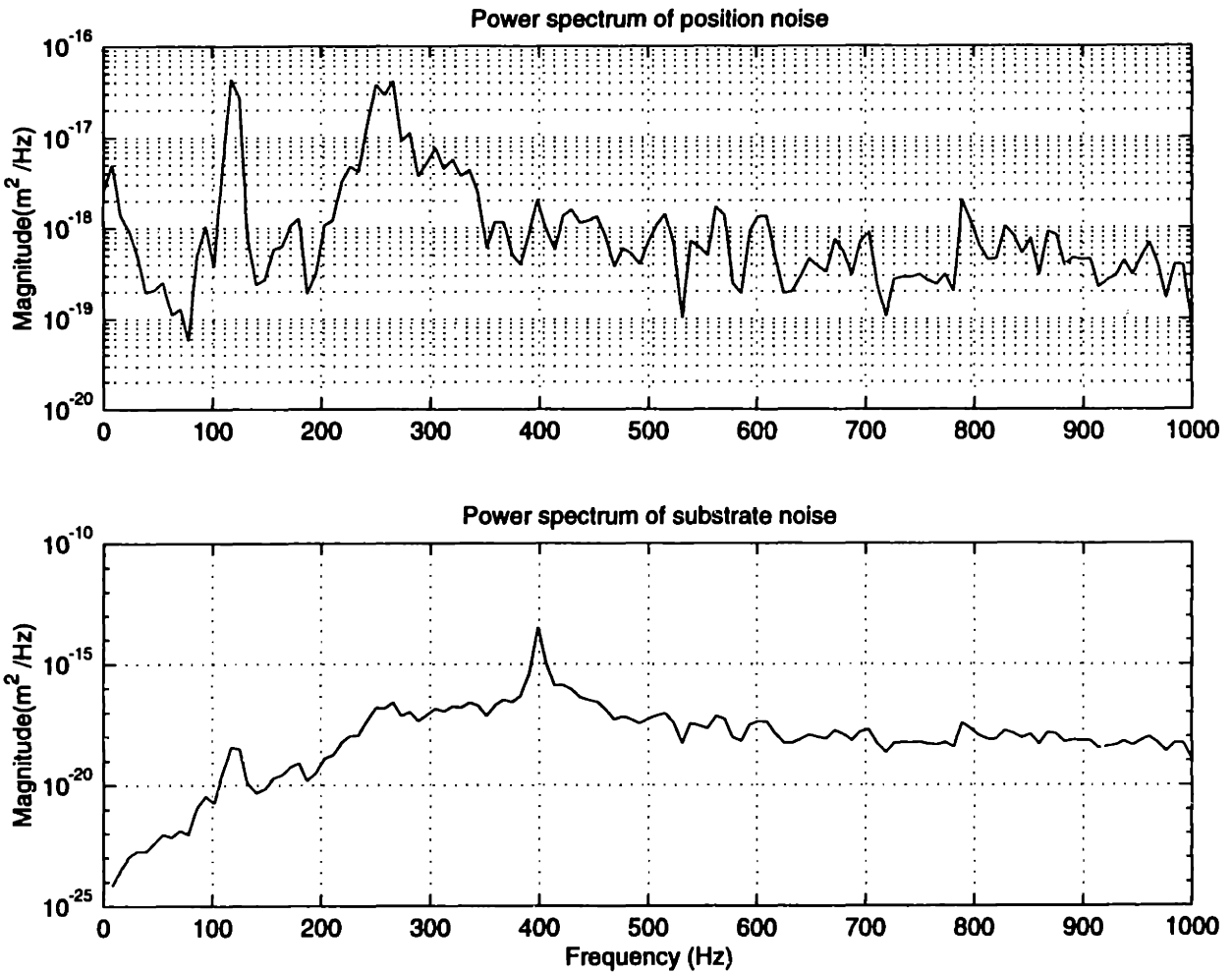

Figure 6-7: Power spectrum of platen and substrate for data from constant velocity profile

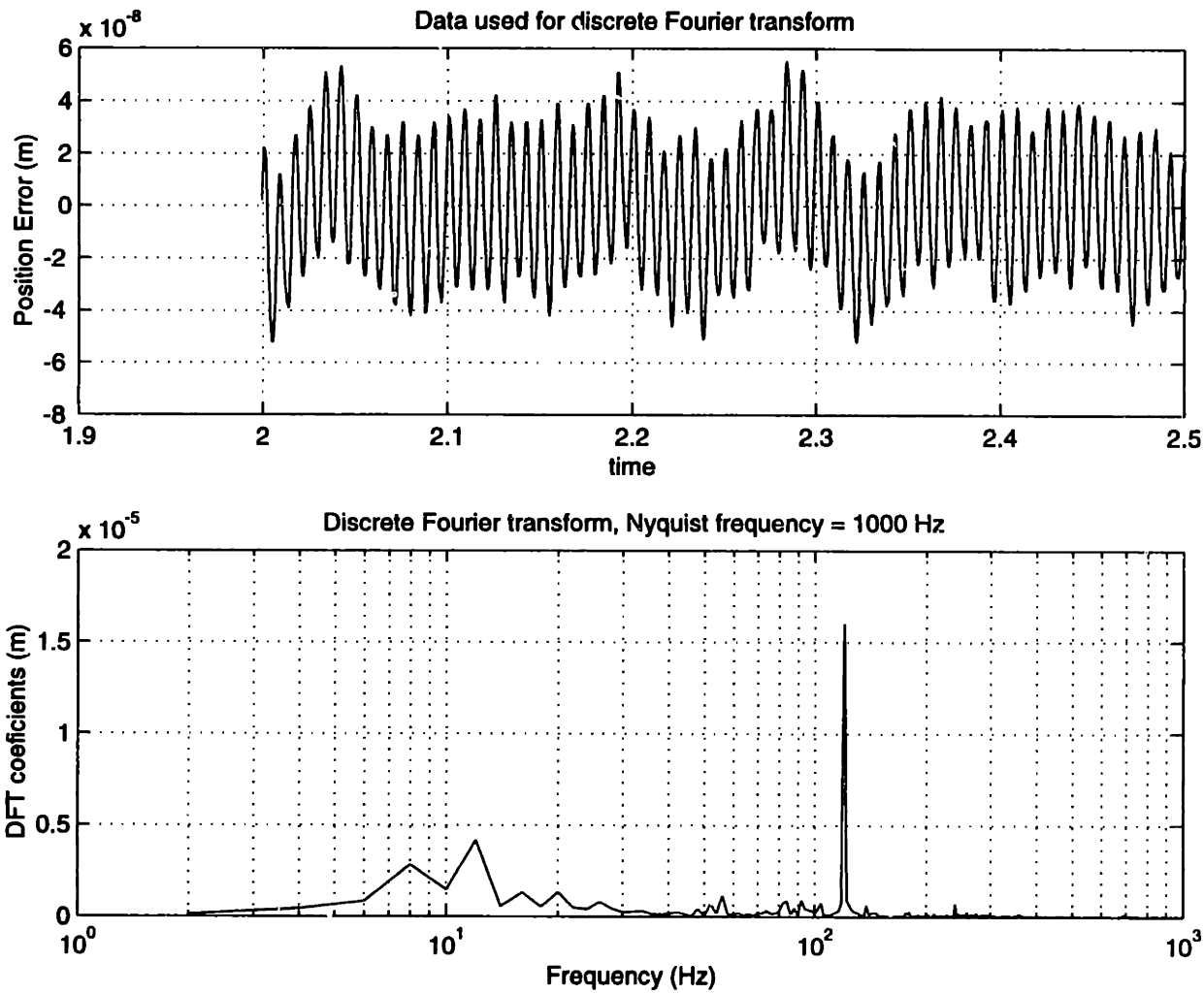

Figure 6-8: Discrete Fourier transform of position error during steady state

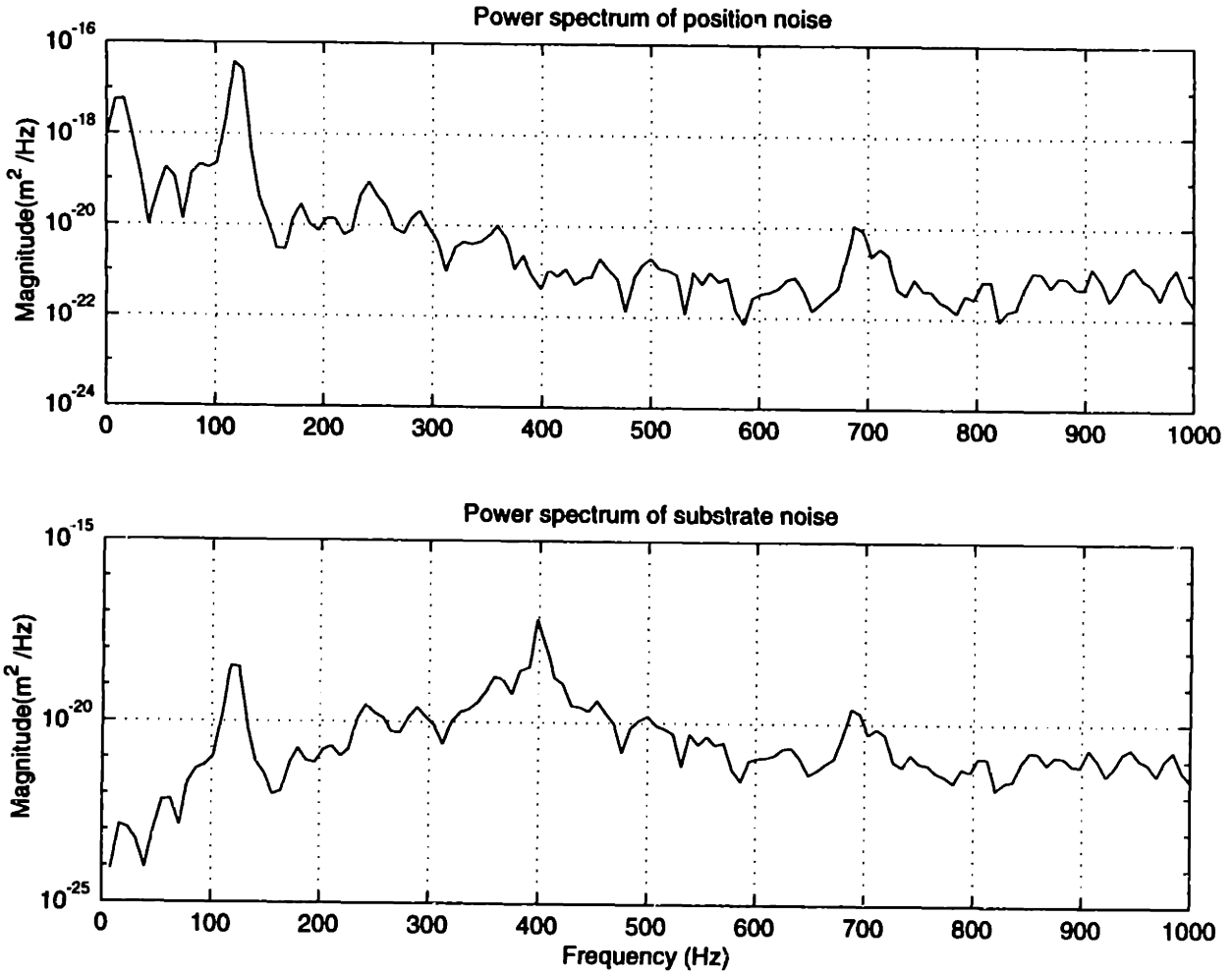

Figure 6-9: Power spectrum of platen and substrate for steady state data

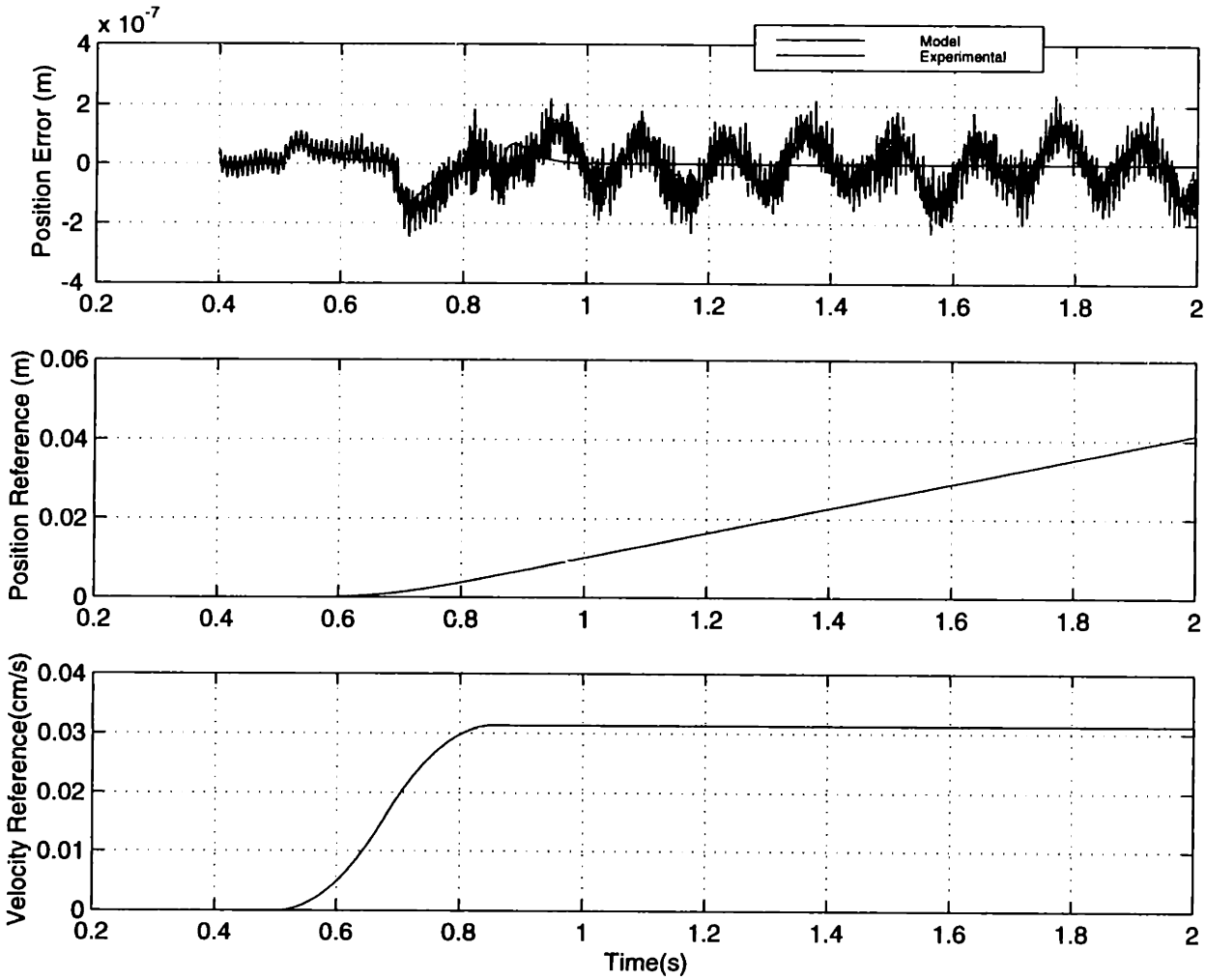

Figure 6-10: Position error during constant velocity scan with F_z=10N

shown in Figure 6-10. This figure reveals there is some coupling between the vertical and translation force components. I show the discrete Fourier transform of a portion of this data in Figure 6-11. I took efforts to window the data to correspond to the length of one spatial period. The low frequency peaks can be shown to correspond to the stator spatial period. Since the velocity of the platen is 3.125 cm/s and the period length is 2.565 cm the spatial period frequency is 1.218 Hz. The high peak at 7.3 Hz corresponds to 6 times the spatial frequency while the peak at 2.4 Hz corresponds to 2 times the spatial frequency. This cross talk can be reduced by a controller design that models the force coupling or by mapping the motor force characteristics.

Figure 6-12 shows the power spectrum of this data. The low frequency components, including the large six spatial period per second peak, are largely attenuated for

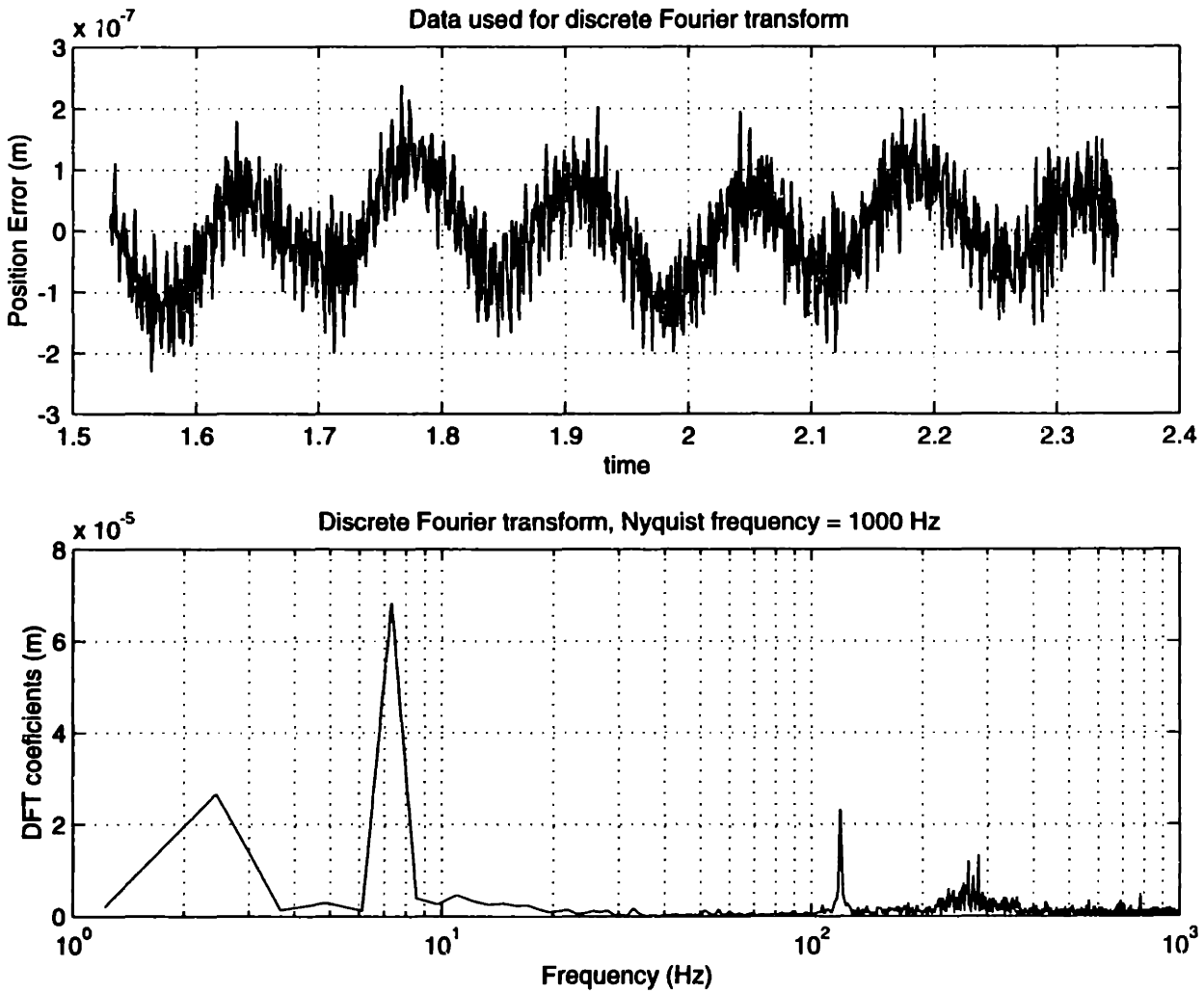

Figure 6-11: Discrete Fourier transform of position error during constant velocity profile with F_z=10N

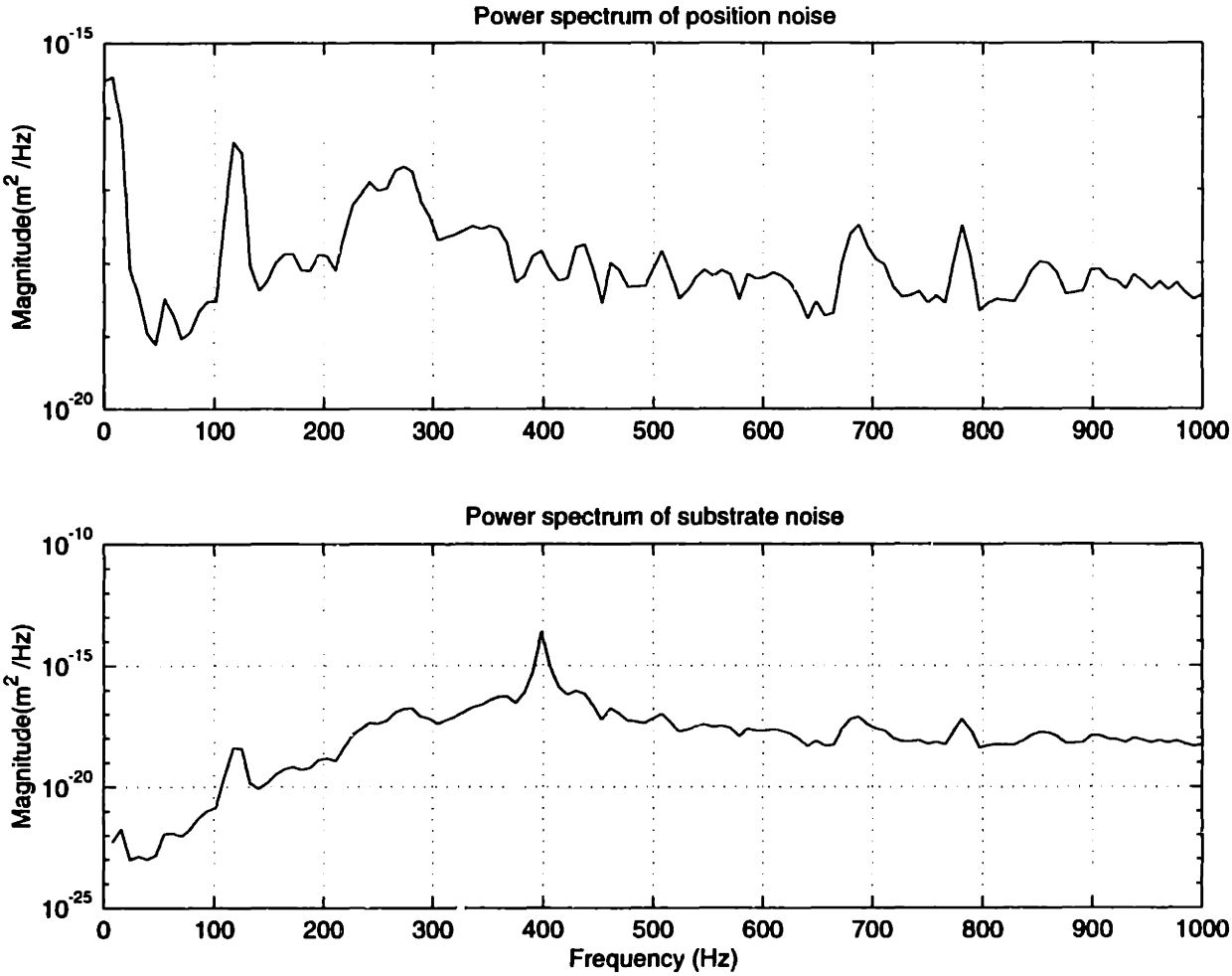

Figure 6-12: Power spectrum of platen and substrate for data from constant velocity profile with F_z=10N

the substrate power spectrum. The 6σ position noise of the platen and the substrate is 480nm and 2700nm respectively (again calculated from the integral of Equation (6.8) from 0 Hz to 1000 Hz). The 6σ position noise of the substrate when just the frequencies from 0 to 100 Hz are considered is .9nm. In the laboratory at MIT where these experiments were performed, it is known that ground vibrations vary with time. Thus, one must be careful about comparing values that strongly depend on low frequency disturbances.

While I have demonstrated submicron position control, more work needs to be performed for design and implementation of a position noise optimal controller. If time allowed, my next steps would include reducing the bandwidth of the controller

and isolating the system from ground disturbances. From the new results, I would analyze the sensor noise and disturbances, which could then be propagated through the closed loop plant in simulation. A much improved controller using appropriate filtering and estimators could then be designed.

Chapter 7

Heat transfer

7.1 Thermal stability requirement

The temperature stability requirement of the reticle is driven from the allowable thermal expansion of the glass. If a maximum length change ΔL is specified by the error budget, the allowable thermal expansion of the glass is given by

$$\Delta T = \frac{(\Delta L)}{L\alpha}. \tag{7.1}$$

Here α is the coefficient of thermal expansion. For an 8″ pattern, α=7.5×10$^{-7}/K$ (maximum for ULTE glass [34]), and an error budget of one nanometer, ΔT= 6.6mK. The stage should not cause reticle temperature drifts exceeding this value.

7.2 Thermal Current Limit of Stator

The maximum current allowed to pass through the coil is limited by the temperature rise across it. In an ebeam lithography system, the temperature of the surfaces of the stator that are exposed to vacuum would need to be maintained at the nominal room temperature. Otherwise the radiation from the stator would heat the photomask, which is equilibrated to the room temperature before entering the vacuum chamber.

Calculation of the thermal current limit requires a heat transfer analysis. A coil

Description	k [W/m/K]	C_p [J/ K/Kg]	ρ [kg/m^3]	% Area
Cotronics 132 (aluminum based potting)	8.65	1675	1160	9.3%
Copper, pure	401.00	385	8933	74.7%
Polyimide, Insulation	0.36	1214	1430	16.0%
Effective Coil Property	6.64	432	7010	100.0%

Table 7.1: Thermal properties used in coil analysis

can be modeled as a matrix of copper, insulation, and potting. I calculate an effective thermal conductivity according to the model shown in Figure 7-1. Using ANSYS Multiphysics software, I applied isothermal and adiabatic boundary conditions as shown. The adiabatic boundary is required because of symmetry and the isothermal boundary condition is an engineering approximation that assumes most of the heat flux is one dimensional at the upper and lower boundaries. By calculating the heat flow across one of the isothermal boundaries, the effective thermal conductivity $k_{eff}$is calculated as

$$k_{eff} = \frac{\sqrt{3}q'}{2\Delta T}. \tag{7.2}$$

Here q' is power flow per unit length. In the model, I assumed that $R_o/R_c = .908$, which is the ratio for 23 AWG wire with heavy build insulation [29]. The properties of the materials are shown in Table 7.1 [18, 24]. For the prototype, the potting is not the Cotronics 132 that I used for this thermal analysis. The prototype uses a resistance bondable potting that is likely to have much worse thermal conductivity than the Cotronics 132. Furthermore, since the prototype's coils were not vacuum impregnated, there are air gaps left in between the wires. To be conservative, k_{eff} for the prototype's coils can be computed using air (k_{air} =.024 J/K/kg) as the potting agent. For this case k_{eff}=1.46 J/K/kg.

For an ebeam system, the coils would very likely need to be vacuum impregnated. Moreover, the vacuum system could not tolerate the extended pump down times required to evacuate the slow leaking pockets that would be left in the coils by other

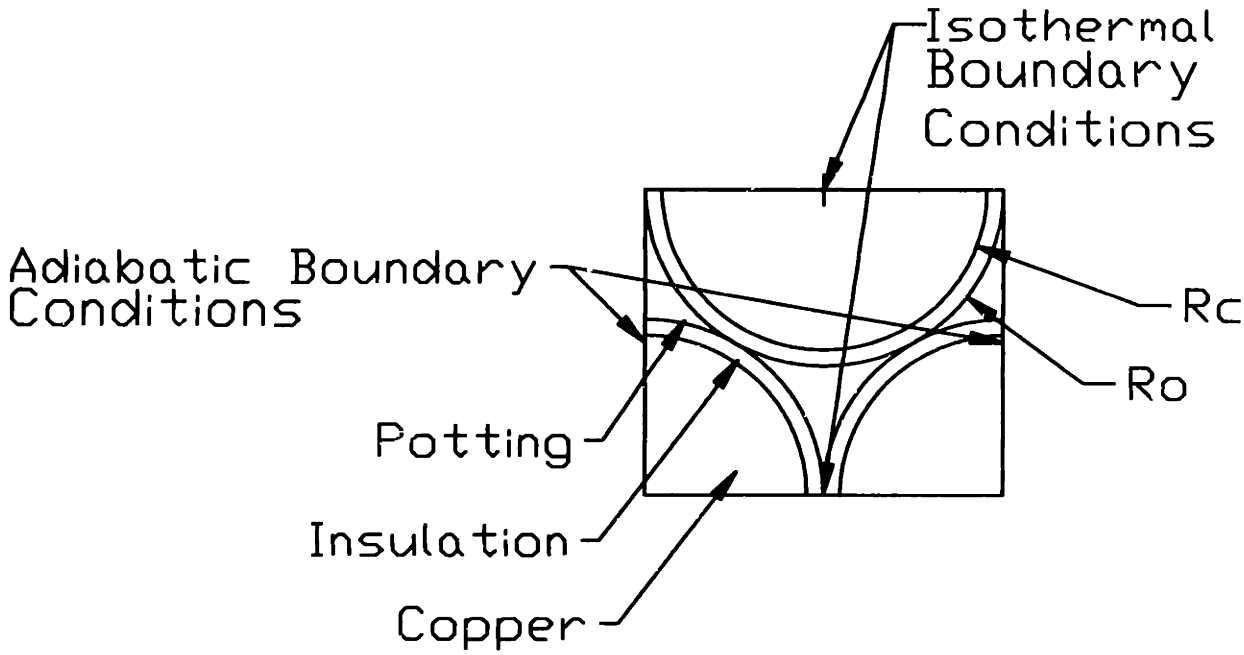

Figure 7-1: Model for coil heat transfer

potting methods. A suitable potting compound would also need to be selected based on both its thermal and vacuum properties. For the following example, I have chosen to use k_{eff} based on the Cotronics 132's thermal conductivity merely out of convenience. Furthermore, since a good potting for a real system probably won't have vastly different thermal properties, the example should provide great insight.

Since the top of the stator must be maintained at room temperature, active cooling by circulating coolant through the interior of the stator will be required. If the cooling system is designed such that the temperature change between the inlet and outlet is small, the interior of the stator can be assumed to be at a uniform temperature. Furthermore, if we neglect the edge effects, the heat transfer in the stator can be analyzed with a one dimensional model. Thus, if ΔT across the coil is specified by the cooling system's design and the outside of the coil is assumed to be adiabatic, the maximum allowable current density J_{max} is given by

$$J_{max} = \frac{\sqrt{2\sigma k_{eff}(T_{outside} - T_{inside})}}{\Gamma}. \tag{7.3}$$

Here σ is the electrical conductivity (5.60E+07 1/Ohms/m, for copper) and Γ is the

stator thickness. For example, if ΔT=10K is allowed for Γ=.2" (the prototype stator's thickness) J_{max}=1.70$\times 10^7$ A/m^2. Once the copper packing factor (74.7%) and the size of the 23AWG wire is accounted for, the allowable current amounts to 5.88 amps.

7.3 Thermal stability analysis

Power fluctuations in the stator are primarily due to the changing forces required to accelerate and decelerate the platen. The power dissipated in the stator can be derived from Equation (5.4) by taking $P = \sum I^2 R_s$ for three phase currents. R_s is the resistance a stator phase. The power dissipation is given by

$$P = \frac{3e^{\gamma z_0}}{\mu_0 \eta M G N_m} R_s \left(F_x^2 + F_z^2\right). \tag{7.4}$$

For an ebeam lithography stage the acceleration requirements are expected to be 1g in suspension and a maximum of .1g in translation. Thus, the power dissipation should vary by only 1% since only the translational acceleration varies during pattern writing.

The ebeam stage is expected to follow a velocity profile where the stage accelerates at the ends of the stage travel and rides at constant velocity for most of the range – where writing occurs. As an example, if the stage rides at 3cm/s peak velocity it takes .92 mm of travel and .061 seconds to accelerate to peak speed and decelerate to a stop. If the the stage writes 200mm long pattern stripes, the percentage of time that the stage accelerates is .9%.

To be conservative, I consider the temperature change due to velocity reversal as adiabatic. If the stator's maximum current density increases 1% from the thermal current limit calculated in Section 7.2. The temperature change can be estimated by plugging $J^2 = .01 \times J_{max}^2$ for $J_{max} = 1.70 \times 10^7 A/m^2$ and the time interval $\Delta t = .061$ seconds into the relation

$$\Delta T = \frac{\left(\frac{J}{\%\,copper\,area}\right)^2 \Delta t}{\sigma \rho C_p}. \tag{7.5}$$

This is the adiabatic temperature rise of the stator where C_p is the effective heat

capacity and ρ is the density. Using the effective coil properties from Table 7.1, ΔT becomes 1.8mK. This temperature change is insignificant considering that the reticle is allowed a temperature variation of 6.6mK. Furthermore, the temperature variations due to the acceleration and deceleration of the stage can essentially be neglected since the platen is expected to have a much higher thermal time constant compared to the frequency of stage scans.

A limitation of this model is that it neglects the periodic distribution of the currents in the stator. However, it should be sufficiently accurate, since the platen shares radiation view factors with many periods of coils. Enough averaging should occur that this estimation is valid.

It is likely that the low frequency warming of the stator will dominate the temperature changes to the stage. These temperature changes can be modeled with radiative heat transfer. I model the system according to Figure 7-2. The upper half of the boundary is the chamber temperature, designated T_c. The lower half of the boundary is the stator temperature, designated T_s. By placing the platen in the middle of the two boundaries, the view factor of the top surface of the platen with upper spherical boundary is one while the view factor of the bottom surface of the platen with bottom spherical boundary is one. The view factors of the sides of the platen are .5 with both the upper boundary and the lower boundary. I make a further assumption that the chamber and the stator are black bodies with emissivity, $\epsilon = 1$. The radiative heat transfer into the platen is given by

$$q = q_c + q_s = \epsilon A \sigma \left((T_c^4 - T_{platen}^4) + (T_s^4 - T_{platen}^4) \right). \tag{7.6}$$

Here A is the cross sectional area of the platen, σ is the Stefan Boltzman constant ($\sigma = 5.67 \times 10^{-}8 W/m^2/K^4$), and ϵ is the emissivitity of the platen. Since we are looking at small temperature ranges, linearizing this equation is a very good approximation. The heat transfer becomes

$$q = \epsilon A \sigma 8 T_o^3 \left(T_o - T_{platen} \right). \tag{7.7}$$

T_o should be assigned the average of the chamber and the stator temperature. To determine if it is valid to use the lumped capacitance method, I take the ratios of the conductive thermal resistance to the radiative thermal resistance.

$$\frac{R_{conduction}}{R_{radiation}} = \frac{L\epsilon\sigma 8T_o^3}{k}. \tag{7.8}$$

This ratio is similar to the Biot number when convection instead of radiation is the heat transfer mechanism. The characteristic length associated with the one dimensional conduction in the platen is L and k is the thermal conductivity of the platen. If I set L to the thickness of a $1/2''$ fused silica photomask, $k = 6.21$ W/m/K , $\epsilon = 1$, and $T_o = 300K$ this ratio is .03. In general, a system can be accurately modeled as a lumped capacitor if this ratio is less than .1 – so this is how I proceed.

I realize a platen for real ebeam platen will probably have a much higher thermal resistance than I am considering. However, the thermal resistance will make the photomask less sensitive to the changes in stator temperature. In fact, the platen can easily be designed with very high thermal resistances with the appropriate choice of materials and mechanical interfaces. In this case, the photomask thermal stability is limited by the chamber temperature while the stator thermal stability is a negligible issue. However, I proceed with the analysis for the stator.

The governing equation for the lumped capacitance model becomes

$$q = \epsilon A\sigma 8T_o^3 (T_o - T_{platen}) = \rho V C_p \frac{dT}{dt} \tag{7.9}$$

where V is the volume of the platen. The solution is given by

$$T_{platen} = T_o + (T_{platen,o} - T_o)e^{\frac{-(t-t_o)}{\tau}}$$
$$\text{where} \quad \tau = \frac{L\rho C_p}{8\epsilon\sigma T_o^3}. \tag{7.10}$$

Here $T_{platen,o}$ is the temperature of the platen at $i = t_o$. If the variables for the $1/2''$ fused silica photomask are used, $\tau = 3140$ seconds (52 minutes). With this long time constant the thermal control system does not need to maintain the thermal stability

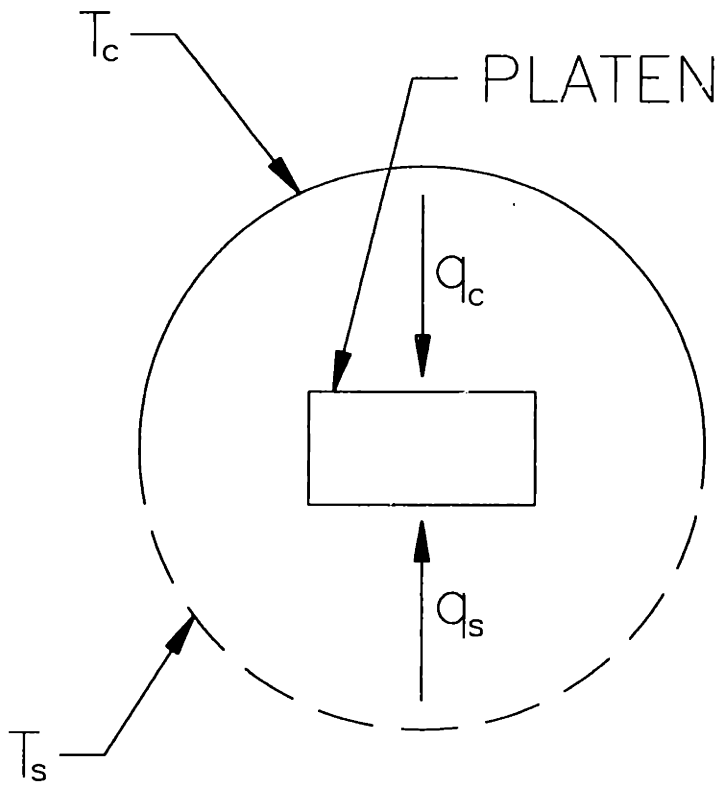

Figure 7-2: Model for radiative heat transfer

of the stator at nearly the strict requirements of the substrate. Just the low frequency stability of the stator needs to meet the strict requirements.

While the design of the thermal control system is beyond the objectives of this thesis, the thermal stability requirements of the magnetic bearing stage should be attainable with a reasonably well designed thermal control system and good temperature sensors.

Chapter 8

Conclusions

I designed, manufactured, and tested a low fringing field magnetic bearing suitable for electron beam lithography. The design is based on a synchronous motor architecture that produces forces in suspension and translation. This building block can readily be incorporated into a six degree of freedom stage with large scale planar motion and small scale focus and rotational alignments.

I formulated several stage topologies that I feel are representative of the kinematic possibilities for stages constructed from the synchronous motors. There appears to be a trade off between commutation complexity and the compactness of the footprint. In one of the stage architectures, I show it is possible to design a magnetic bearing stage with a footprint two times the travel on each side. This is the smallest footprint likely to be helpful for lithography applications and I believe it is an extremely attractive design for precision motion control in an ebeam lithography machine.

The electromagnetic field theory that I developed indicates that large field attenuation in the far field is attainable with magnetic bearings composed of opposing dipoles. I derived the theory by superposing homogeneous solutions and solving for the far field limit. Magnet and coil arrays can be constructed with very fast falling far fields, meanwhile the fields close to the array are strong and can be accurately modeled with a classical two dimensional analysis for the purpose of electromechanical properties. My theory is an essential tool that drives the design of magnet and coil arrays with low fringing fields.

I designed a magnet and coil array that implemented the analytical concepts. The prototype moves a mass of 5.2 kg and can suspend this mass with 58 W of power. The travel is over 13″ in a single degree of freedom. The design could achieve a maximum suspension force of 400 N with a vacuum impregnated stator that is constructed with the thermally conductive properties and the thermal control system that I discuss.

The experimental field measurements for the stator correspond well with a very accurate charge integration solution. Also, the multipole theory shows very good accuracy in the entire far field region of interest. The stator design achieved the far field design goal and is scalable for next generation ebeam tool requirements.

The prototype magnet array's field cancellation performance is limited by the tolerances. Monte Carlo simulations that modeled the effects of magnet and assembly tolerances corresponded very well with the experimental results. Furthermore, techniques that compensate for the tolerances must be incorporated into high performance field cancellation schemes. Although the desired fringing field magnitude for the magnet array is not achieved at present, further design and placement of additional trimming magnets will improve the performance approaching that of the theoretical array. This is an area for future work.

While my prototype magnet array can, in theory, achieve fringing fields less than ±2mG at less than six inches above the array, my investigation cites another cancelation topology that is likely to exceed this performance even with fewer cancelation superpositions. The topology is more effective because it is constructed with smaller multipole moment arms. However, its construction requires magnets that have different effective remanence. Study of practical construction methods merits further investigation.

My position control experiments for the single degree of freedom prototype shows acceptable submicron positioning accuracy during a scanning profile. At present the position noise is unacceptable for a real system. However, the noise has coherent frequencies. The disturbance vibrations are associated mainly associated with the large 120Hz component of ground vibration and the 280Hz natural frequency of the experimental setup. Due to time constraints, I was unable to implement the suggested

fixes for these coherent vibrations. Namely, the setup should be isolated from ground vibrations, the controller should have a lower cross over frequency so as to not excite the resonant frequency of the structure, and a position noise optimal controller should be designed.

Before the magnetic bearing stage technology can be implemented in a commercial system, several manufacturing and subsystem issues must be addressed. Vacuum impregnation of the coils needs to be developed. Also, selection of vacuum compatible potting with good thermal conductivity should be explored. Bonding and mechanical constraint of the magnets for high reliability during assembly and operation is another area for development. The stage for a real system will also require a thermal control system. Although my heat transfer analysis indicates that thermal stability suitable for lithography can be attained, this needs to be demonstrated.

While there is a need for further research before commercial implementation, I do not think that the remaining issues are show stoppers. More importantly, I have shown that careful design and manufacture of the novel permanent magnet array and coil array technologies yields magnetic bearing stages with negligible influence on the electron beam trajectory. Considering the performance and system level benefits, I view magnetic bearing stages as a highly promising alternative for next generation electron beam lithography.

Bibliography

[1] Manlio G. Abele. *Structures of Permanent Magnets.* John Wiley and Sons, Inc., 1993.

[2] I. Boldea. *Linear motion electromagnetic systems.* John Wiley and Sons, Inc., 1985.

[3] William Callister. *Materials Science and Engineering*, chapter 21. John Wiley and Sons, 1991.

[4] William A. Campbell and John J. Scialdone. *Outgassing Data for Selecting Spacecraft Materials, RP-1124, Rev. 3.* Addison-Wesley, 1990.

[5] Anwar Chitayat. Nanometer x–y positioning stages for scanning and stepping. *J. Vac. Sci. Technol. B*, 7(6):1412–1417, November-December 1989.

[6] D.J. Clark, J. McMurty, R. Simmons, W. D. Meisburger, and L. Veneklasen. Dynamic performance of a scanning x–y stage for automated electron beam inspection. *J. Vac. Sci. Technol. B*, 10(6):2638–2642, November-December 1992.

[7] Stephen H. Crandall, Dean C. Karnopp, Edward F. Kurtz, and David C. Pridmore-Brown. *Dynamics of Mechanical and Electromechanical Systems*, section 4.3. Krieger Publishing Company, 1982.

[8] Ruth DeJule. E-beam lithography: the debate continues. *Semiconductor International*, pages 85–92, September 1996.

[9] Etec Systems Inc., 26460 Corporate Avenue. Hayward, CA 94545. *MEBES 4500 brochure. Document A999-0212.*

[10] Gene F. Franklin, J. David Powell, and Abbas Emani-Naeini. *Feedback Control of Dynamic Systems.* Addison-Wesley, 1991.

[11] Gene F. Franklin, J. David Powell, and Michael L. Workman. *Digital Control of Dynamic Systems.* Addison-Wesley, 1994.

[12] M. Gesley. MEBES IV thermal-field emission tandem optics for electron beam lithography. *J. Vac. Sci. Technol. B*, 9(6):2949–2954, November-December 1991.

[13] Klaus Halbach. Physical and optical properties of rare earth cobalt magnets. *Nuclear Instruments and Methods*, 187:109–117, November 1981.

[14] Douglas V. Hall. *Microprocessors and Interfacing*, section 8. Glencoe/McGraw-Hill, New York, New York, second edition, 1992.

[15] H. A. Haus and J. R. Melcher. *Electromagnetic Fields and Energy.* Prentice-Hall, 1989.

[16] J. F. Hoburg. Principles of quasistatic magnetic shielding with cylindrical and spherical shields. *IEEE Transactions on Electromagnetic Compatibility*, 37(4):574+, November 1995.

[17] Satoshi Ido and Haruo Tsuyuzaki. Precision x-y stage for electron beam lithography system. *Bull. Japan Soc. of Prec. Engg.*, 18(3):267–273, September 1984.

[18] Frank P. Incropera and David P. DeWitt. *Fundamentals of Heat and Mass Transfer.* John Wiley and Sons, 1990.

[19] Won jong Kim. *Planar Magnetic Levitation.* PhD dissertation, Massachusetts Institute of Technology, Department of Electrical Engineering and Computer Science, June 1997.

[20] Rodney Kendall, Sam Doran, and Erwin Weissman. A servo guided x–y–theta stage for electron beam lithography. *J. Vac. Sci. Technol. B*, 9(6):3019–3023, November-December 1991.

[21] Eric R. Laithwaite. *A History of Linear Electric Motors.* Macmillan Education LTD, 1987.

[22] Stephen Joseph Ludwick. Control of a six degree of freedom magnetic/fluidic motion control stage. Master's thesis, Massachusetts Institute of Technology, 1996.

[23] Magnet Component Engineering, 23145 Kashiwa Court, Torrance, CA 90505. *Advanced Permanent Magnet Materials R970902.1*, 1997.

[24] Materials Engineering. *1992 Materials Selector*, December 1991.

[25] James R. Melcher. *Continuum Electromechanics.* MIT Press, 1981.

[26] Parry Moon and Domina Eberle Spencer. *Field Theory Handbook.* Springer-Verlag, 1961.

[27] Shigeo Moriyama, Tatsuo Harada, and Akihiro Takanashi. Precision x–y stage with a piezo driven fine table. *Bull. Japan Soc. of Prec. Engg.*, 22(1):13–17, March 1988.

[28] I. Mullerova and J. Fiser. Magnetic shielding of stray magnetic fields in the scanning electron microscope. *Rev. Sci. Instrum.*, 65(6):1968+, June 1994.

[29] MWS Wire Industries. *MWS Catalog*, 1995.

[30] R.J. Nielsen, J.H. Bruning, and R.M. Richman et al. Hydraulic x–y system for application in electron beam exposure systems. *J. Vac. Sci. Technol. B*, 5(1):57–60, January-February 1987.

[31] Tsuneji Rikitake. *Magnetic and Electromagnetic Shielding.* Terra Scientific Pub. Co., 1987.

[32] R. D. Schlueter and S. Marks. Three dimensional pure permanent magnet undulator design. *IEEE Transactions on Magnetics*, 32(4):2710+, July 1996.

[33] G. Schubert, U. Kirschstein, and M. Sturm. Paper supplied to me by Bernard Wallman, Leica Lithography Systems Ltd.

[34] SEMI, 805 East Middlefield Road, Mountain View, California 94043-4080. *SEMI P1-95, Specification Hard Surface Photomask Substrates*, 1995.

[35] Semiconductor Industry Association, 4300 Stevens Creek Boulevard, Suite 271, San Jose, CA 95129. *The National Technology Roadmap for Semiconductors*, 1997.

[36] David Trost. Communication with David Trost, Etec Systems Inc.

[37] David L. Trumper. *Magnetic Suspension Techniques for Precision Motion Control.* PhD dissertation, Massachusetts Institute of Technology, Department of Electrical Engineering and Computer Science, September 1990.

[38] David L. Trumper, Won jong Kim, and Mark E. Williams. Design and analysis framework for linear permanent magnet machines. *Proceedings of the IEEE IAS 29th Annual Meeting*, pages 216–223, October 1994.

[39] David L. Trumper, Won jong Kim, and Mark E. Williams. Design and analysis framework for linear permanent magnet machines. *IEEE Transactions on Industry Applications*, 32(2):371–379, March-April 1996.

[40] David L. Trumper, Mark E. Williams, and Tiep H. Nguyen. Magnet arrays for synchronous machines. *Proceedings of the IEEE IAS 28th Annual Meeting*, pages 216–223, October 1993.

[41] Haruo Tsuyuzaki, Nobuo Shimazu, and Minpei Fujinami. High speed flat guide ceramic stage for electron beam lithography. *J. Vac. Sci. Technol. B*, 4(1):280–284, January-February 1986.

[42] Herbert H. Woodson and James R. Melcher. *Electromechanical Dynamics.* Robert E. Krieger Publishing, 1968.

Appendix A

.m file for magnetic charge integration

% This .m file is the engine that solves for magnetic fields around 3D Halbach arrays by magnetic charge integration. Hx any Hy require numerical charge integration on surfaces othogonal to the x and y axes for Hx and Hy respectively. Otherwise, the charge integration is analytically exact.

Written by Paul T. Konkola

The user must define the folling parameters

magnet: magnet remanance/4/pi;

h: height of individual magnet

b: number of magnets per period of the halbach array

w: width of individual magnet

l: length (depth) of magnet or of relevant magnet

numeric: specifies number of stripes for numerical integration

xmax: number of datapoints in the x direction for a grid

ymax =xmax;

%variables used for Monte Carlo simulation of tolerance effects

Brthreesigma: three sigma value for remanence tolerance as a fraction of the nominal value for l

phithreesigma: three sigma value for phi tolerance in radians

xthreesigma: spatial tolerance in x direction (units = same as l)

ythreesigma: spatial tolerance in x direction (units = same as l)

zthreesigma: spatial tolerance in x direction (units = same as l)

x: vector of x coordinates

y: vector of y coordinates

z: vector of z coordinates

%specify magnet topology: magnet pointing down with an edge on z axis and the other edge on x>0 has zero shift; shift moves the position of this magnet by shift×w along the x axis; if just the fields for this one magnet is desired then first = 0 and last = 0; (-1)×first specifies the number of magnets to the left of this magnet; last specifies the number of magnets to the right of this magnet;

shift: see note above

first:

last:

%The fields for any of the magnet arrays or coil arrays in my thesis can be be calculated by successively applying the following algorithm and superposing the results of each application.

```
    for i = 1:b,  %Define orientation of magnets
Jxhold(i) = -sin((i - 1) * 2 * pi/b);
Jyhold(i) = -cos((i - 1) * 2 * pi/b);
end

    firstblock = fix((first+1)/b);
lastblock = fix((last)/b);
extrafirst = rem(first,b);
if first > -1,
if (rem(first,b) == 0),
extrafirst = rem(first,b) - b;
end
firstblock = fix(first/b) +1;
```

```
end
extralast = rem((last+1),b);
if rem((last+1),b) == 0,
extralast = b;
end
if last < 0,
extralast = (b + 1) + rem(last, b);
if rem(last, b) == 0,
extralast = 1;
end
lastblock = fix((last+1)/b) - 1;
end
    %set random components for Monte Carlo simulations
for n = 1:(lastblock-firstblock +2),
for m = 1:b,
%account for spatial tolerances
randomx(m,n)= randn(1)* xthreesigma/3/sqrt(1/lhold);
randomy(m,n) = randn(1)* ythreesigma/3/sqrt(1/lhold);
randomz(m,n) = randn(1)* zthreesigma/3/sqrt(1/lhold);
%account for random tolerance in remanence
Brrandom(m,n) = (1 + randn(1) * Brthreesigma/3/sqrt(1/lhold));
    %account for angular tolerance or magnetization vector
phirandom(m,n) = randn(1)*phithreesigma/3/sqrt(1/lhold);
end
end
    for i=1:xmax,
j=i;
k = i;
    tempbx = 0;
tempby = 0;
```

```
tempbz = 0;
    xhold(i) = x(i);
yhold(i) = y(i);
zhold(i) = z(i);
    for n = (firstblock-1):(lastblock),
for bb = 1:b,
DeltaX(bb) = (bb - 1) * w + b*n*w + (.5 + shift)*w;
end
    %initialize variables
beginblock = 1;
endblock = b;
    if n == (firstblock-1),
beginblock = b + 1 + extrafirst;
if extrafirst == 0,
beginblock = 1;
end
end
if n == (lastblock),
endblock = extralast;
end
    for m = beginblock:endblock,
    %account for spatial tolerances
x(i) = xhold(i) + randomx(m,(n - firstblock +2));
y(i) = yhold(i) + randomy(m,(n - firstblock +2));
z(i) = zhold(i) + randomz(m,(n - firstblock +2));
    Jx(m) = (Jxhold(m) * cos(phirandom(m,(n - firstblock + 2))) - Jyhold(m) *
sin(phirandom(m,(n - firstblock +2)))) * Brrandom(m,(n - firstblock +2));
Jy(m) = (Jxhold(m) * sin(phirandom(m,(n - firstblock + 2))) + Jyhold(m) * cos
(phirandom(m,(n - firstblock +2)))) * Brrandom(m,(n - firstblock +2));
    %HxBD needs to be numerically integrated w/ respect to y.
```

```
ytemp = y(j);
numericbx = 0;
for num = 0:numeric,
if ((num == 0) — (num == numeric)),
factor = .5;
else
factor = 1;
end

    if num == 0,
y(j) = y(j) - h/2;
else
y(j) = y(j) + h/numeric;
end

    if ((num == 0) & (num == numeric)),
factor = 1;
y(j) = ytemp;
end
    numericbx = numericbx + factor * ( -(Jx(m)*((-8*DeltaX(m) - 4*w + 8*x(i))/
(2*sqrt(4*DeltaX(m)^2 + l^2 + 4*DeltaX(m)*w + w^2 - 8 * DeltaX(m) * x(i) - 4*w*x(i)
+ 4*x(i)^2 + 4*y(j)^2 - 4*l*z(k) + 4*z(k)^2)* (l - 2*z(k) + sqrt(4*DeltaX(m)^2 + l^2 +
4*DeltaX(m)*w + w^2 - 8*DeltaX(m)*x(i) - 4*w*x(i) + 4*x(i)^2 + 4*y(j)^2 - 4*l*z(k)
+ 4*z(k)^2))) - (-8*DeltaX(m) + 4*w + 8*x(i))/ (2 * sqrt(4 * DeltaX(m)^2 + l^2
- 4*DeltaX(m)*w + w^2 - 8 * DeltaX(m)*x(i) + 4*w*x(i) + 4*x(i)^2 + 4*y(j)^2 -
4*l*z(k) + 4*z(k)^2)* (l - 2*z(k) + sqrt(4*DeltaX(m)^2 + l^2 - 4*DeltaX(m)*w + w^2
- 8 * DeltaX(m)*x(i) + 4*w*x(i) + 4*x(i)^2 + 4*y(j)^2 - 4*l*z(k) + 4*z(k)^2))) - (-
8*DeltaX(m) - 4*w + 8*x(i))/ (4*sqrt(4*DeltaX(m)^2 + l^2 + 4*DeltaX(m)*w + w^2 -
8 * DeltaX(m)*x(i) - 4*w*x(i) + 4*x(i)^2 + 4*y(j)^2 + 4*l*z(k) + 4*z(k)^2)* (-l/2 - z(k)
+ sqrt(4*DeltaX(m)^2 + l^2 + 4*DeltaX(m)*w + w^2 - 8*DeltaX(m)*x(i) - 4*w*x(i)
```

```
+ 4*x(i)^2 + 4*y(j)^2 + 4*l*z(k) + 4*z(k)^2)/2)) + (-8*DeltaX(m) + 4*w + 8*x(i))/
(4*sqrt(4*DeltaX(m)^2 + l^2 - 4*DeltaX(m)*w + w^2 - 8 * DeltaX(m)*x(i) + 4*w*x(i)
+ 4*x(i)^2 + 4*y(j)^2 + 4*l*z(k) + 4*z(k)^2)* (-l/2 - z(k) + sqrt(4*DeltaX(m)^2 + l^2 -
4*DeltaX(m)*w + w^2 - 8*DeltaX(m)*x(i) + 4*w*x(i) + 4*x(i)^2 + 4*y(j)^2 + 4*l*z(k)
+ 4*z(k)^2)/2)))) );
end
y(j) = ytemp;
    if numeric == 0,
divisions = 1;
else
divisions = numeric;
end
    %hx(i,j) = (numerical part from B and D) + (nonnumerical from A and C)
tempbx = tempbx + numericbx*h/divisions + ( Jy(m)*(log(l - 2*z(k) + sqrt( 4
* DeltaX(m)^2 + h^2 + l^2 + 4*DeltaX(m)*w + w^2 - 8*DeltaX(m)*x(i) - 4*w*x(i) +
4*x(i)^2 - 4*h*y(j) + 4*y(j)^2 - 4*l*z(k) + 4*z(k)^2)) - log(l - 2*z(k) + sqrt(4*DeltaX(m)^2
+ h^2 + l^2 - 4*DeltaX(m)*w + w^2 - 8*DeltaX(m)*x(i) + 4*w*x(i) + 4*x(i)^2 - 4*h*y(j)
+ 4*y(j)^2 - 4*l*z(k) + 4*z(k)^2)) - log(l - 2*z(k) + sqrt(4*DeltaX(m)^2 + h^2 + l^2 +
4*DeltaX(m)*w + w^2 - 8*DeltaX(m)*x(i) - 4*w*x(i) + 4*x(i)^2 + 4*h*y(j) + 4*y(j)^2 -
4*l*z(k) + 4*z(k)^2)) + log(l - 2*z(k) + sqrt(4*DeltaX(m)^2 + h^2 + l^2 - 4*DeltaX(m)*w
+ w^2 - 8*DeltaX(m)*x(i) + 4*w*x(i) + 4*x(i)^2 + 4*h*y(j) + 4*y(j)^2 - 4*l*z(k)
+ 4*z(k)^2)) - log(-l - 2*z(k) + sqrt(4*DeltaX(m)^2 + h^2 + l^2 + 4*DeltaX(m)*w
+ w^2 - 8*DeltaX(m)*x(i) - 4*w*x(i) + 4*x(i)^2 - 4*h*y(j) + 4*y(j)^2 + 4*l*z(k) +
4*z(k)^2)) + log(-l - 2*z(k) + sqrt(4*DeltaX(m)^2 + h^2 + l^2 - 4*DeltaX(m)*w +
w^2 - 8*DeltaX(m)*x(i) + 4*w*x(i) + 4*x(i)^2 - 4*h*y(j) + 4*y(j)^2 + 4*l*z(k) +
4*z(k)^2)) + log(-l - 2*z(k) + sqrt(4*DeltaX(m)^2 + h^2 + l^2 + 4*DeltaX(m)*w +
w^2 - 8*DeltaX(m)*x(i) - 4*w*x(i) + 4*x(i)^2 + 4*h*y(j) + 4*y(j)^2 + 4*l*z(k) +
4*z(k)^2)) - log(-l - 2*z(k) + sqrt(4*DeltaX(m)^2 + h^2 + l^2 - 4*DeltaX(m)*w + w^2 -
8*DeltaX(m)*x(i) + 4*w*x(i) + 4*x(i)^2 + 4*h*y(j) + 4*y(j)^2 + 4*l*z(k) + 4*z(k)^2)))
);
```

%HyAC needs to be numerically integrated w/ respect to y.

```
xtemp = x(i);
numericby = 0;
for num = 0:numeric,
if ((num == 0) — (num == numeric)),
factor = .5;
else
factor = 1;
end


   if num == 0,
x(i) = x(i) - w/2;
else
x(i) = x(i) + w/numeric;
end


   if ((num == 0) & (num == numeric)),
factor = 1;
x(i) = xtemp;
end
   numericby = numericby + factor * ( -(Jy(m)*((-4*h + 8*y(j))/ (2* sqrt( 4 *
DeltaX(m)^2 + h^2 + l^2 - 8* DeltaX(m)*x(i) + 4*x(i)^2 - 4*h*y(j) + 4*y(j)^2 - 4*l*z(k)
+ 4*z(k)^2)* (l - 2*z(k) + sqrt(4*DeltaX(m)^2 + h^2 + l^2 - 8*DeltaX(m)*x(i) + 4*x(i)^2
- 4*h*y(j) + 4*y(j)^2 - 4*l*z(k) + 4*z(k)^2))) - (4*h + 8*y(j))/ (2*sqrt(4*DeltaX(m)^2
+ h^2 + l^2 - 8*DeltaX(m)*x(i) + 4*x(i)^2 + 4*h*y(j) + 4*y(j)^2 - 4*l*z(k) + 4*z(k)^2)*
(l - 2*z(k) + sqrt(4*DeltaX(m)^2 + h^2 + l^2 - 8*DeltaX(m)*x(i) + 4*x(i)^2 + 4*h*y(j)
+ 4*y(j)^2 - 4*!*z(k) + 4*z(k)^2))) - (-4*h + 8*y(j))/ (4*sqrt(4*DeltaX(m)^2 + h^2 +
l^2 - 8*DeltaX(m)*x(i) + 4*x(i)^2 - 4*h*y(j) + 4*y(j)^2 + 4*l*z(k) + 4*z(k)^2)* (-l/2
- z(k) + sqrt(4*DeltaX(m)^2 + h^2 + l^2 - 8*DeltaX(m)*x(i) + 4*x(i)^2 - 4*h*y(j) +
```

4*y(j)^2 + 4*l*z(k) + 4*z(k)^2)/2)) + (4*h + 8*y(j))/ (4*sqrt(4*DeltaX(m)^2 + h^2 + l^2 - 8*DeltaX(m)*x(i) + 4*x(i)^2 + 4*h*y(j) + 4*y(j)^2 + 4*l*z(k) + 4*z(k)^2)* (-l/2 - z(k) + sqrt(4*DeltaX(m)^2 + h^2 + l^2 - 8*DeltaX(m)*x(i) + 4*x(i)^2 + 4*h*y(j) + 4*y(j)^2 + 4*l*z(k) + 4*z(k)^2)/2)))));

end

x(i) = xtemp;

%hy(i,j) = (numerical part from A and C) + (nonnumerical from B and D)

tempby = tempby + numericby*w/divisions + (Jx(m)*(log(l - 2*z(k) + sqrt(4 * DeltaX(m)^2 + h^2 + l^2 + 4*DeltaX(m)*w + w^2 - 8*DeltaX(m)*x(i) - 4*w*x(i) + 4*x(i)^2 - 4*h*y(j) + 4*y(j)^2 - 4*l*z(k) + 4*z(k)^2)) - log(l - 2*z(k) + sqrt(4*DeltaX(m)^2 + h^2 + l^2 - 4*DeltaX(m)*w + w^2 - 8*DeltaX(m)*x(i) + 4*w*x(i) + 4*x(i)^2 - 4*h*y(j) + 4*y(j)^2 - 4*l*z(k) + 4*z(k)^2)) - log(l - 2*z(k) + sqrt(4*DeltaX(m)^2 + h^2 + l^2 + 4*DeltaX(m)*w + w^2 - 8*DeltaX(m)*x(i) - 4*w*x(i) + 4*x(i)^2 + 4*h*y(j) + 4*y(j)^2 - 4*l*z(k) + 4*z(k)^2)) + log(l - 2*z(k) + sqrt(4*DeltaX(m)^2 + h^2 + l^2 - 4*DeltaX(m)*w + w^2 - 8*DeltaX(m)*x(i) + 4*w*x(i) + 4*x(i)^2 + 4*h*y(j) + 4*y(j)^2 - 4*l*z(k) + 4*z(k)^2)) - log(-l - 2*z(k) + sqrt(4*DeltaX(m)^2 + h^2 + l^2 + 4*DeltaX(m)*w + w^2 - 8*DeltaX(m)*x(i) - 4*w*x(i) + 4*x(i)^2 - 4*h*y(j) + 4*y(j)^2 + 4*l*z(k) + 4*z(k)^2)) + log(-l - 2*z(k) + sqrt(4*DeltaX(m)^2 + h^2 + l^2 - 4*DeltaX(m)*w + w^2 - 8*DeltaX(m)*x(i) + 4*w*x(i) + 4*x(i)^2 - 4*h*y(j) + 4*y(j)^2 + 4*l*z(k) + 4*z(k)^2)) + log(-l - 2*z(k) + sqrt(4*DeltaX(m)^2 + h^2 + l^2 + 4*DeltaX(m)*w + w^2 - 8*DeltaX(m)*x(i) - 4*w*x(i) + 4*x(i)^2 + 4*h*y(j) + 4*y(j)^2 + 4*l*z(k) + 4*z(k)^2)) - log(-l - 2*z(k) + sqrt(4*DeltaX(m)^2 + h^2 + l^2 - 4*DeltaX(m)*w + w^2 - 8*DeltaX(m)*x(i) + 4*w*x(i) + 4*x(i)^2 + 4*h*y(j) + 4*y(j)^2 + 4*l*z(k) + 4*z(k)^2))));

tempbz = tempbz + Jy(m)*(log(2*DeltaX(m) + w - 2*x(i) + sqrt(4 * DeltaX(m)^2 + h^2 + l^2 + 4*DeltaX(m)*w + w^2 - 8*DeltaX(m)*x(i) - 4*w*x(i) + 4*x(i)^2 - 4*h*y(j) + 4*y(j)^2 - 4*l*z(k) + 4*z(k)^2)) - log(2*DeltaX(m) + w - 2*x(i) + sqrt(4*DeltaX(m)^2 + h^2 + l^2 + 4*DeltaX(m)*w + w^2 - 8*DeltaX(m)*x(i) - 4*w*x(i) + 4*x(i)^2 - 4*h*y(j) + 4*y(j)^2 + 4*l*z(k) + 4*z(k)^2))) + Jx(m)*(log(h - 2*y(j) + sqrt(4*DeltaX(m)^2 + h^2 + l^2 + 4*DeltaX(m)*w + w^2 - 8*DeltaX(m)*x(i) - 4*w*x(i) + 4*x(i)^2 - 4*h*y(j)

```
+ 4*y(j)^2 - 4*l*z(k) + 4*z(k)^2)) - log(h - 2*y(j) + sqrt(4*DeltaX(m)^2 + h^2 + l^2 +
4*DeltaX(m)*w + w^2 - 8*DeltaX(m)*x(i) - 4*w*x(i) + 4*x(i)^2 - 4*h*y(j) + 4*y(j)^2
+ 4*l*z(k) + 4*z(k)^2))) - Jy(m)*(log(2*DeltaX(m) - w - 2*x(i) + sqrt(4*DeltaX(m)^2
+ h^2 + l^2 - 4*DeltaX(m)*w + w^2 - 8*DeltaX(m)*x(i) + 4*w*x(i) + 4*x(i)^2 - 4*h*y(j)
+ 4*y(j)^2 - 4*l*z(k) + 4*z(k)^2)) - log(2*DeltaX(m) - w - 2*x(i) + sqrt(4*DeltaX(m)^2
+ h^2 + l^2 - 4*DeltaX(m)*w + w^2 - 8*DeltaX(m)*x(i) + 4*w*x(i) + 4*x(i)^2 - 4*h*y(j)
+ 4*y(j)^2 + 4*l*z(k) + 4*z(k)^2))) + Jx(m)*(-log(h - 2*y(j) + sqrt(4*DeltaX(m)^2 +
h^2 + l^2 - 4*DeltaX(m)*w + w^2 - 8*DeltaX(m)*x(i) + 4*w*x(i) + 4*x(i)^2 - 4*h*y(j)
+ 4*y(j)^2 - 4*l*z(k) + 4*z(k)^2)) + log(h - 2*y(j) + sqrt(4*DeltaX(m)^2 + h^2 + l^2 -
4*DeltaX(m)*w + w^2 - 8*DeltaX(m)*x(i) + 4*w*x(i) + 4*x(i)^2 - 4*h*y(j) + 4*y(j)^2 +
4*l*z(k) + 4*z(k)^2))) + Jy(m)*(-log(2*DeltaX(m) + w - 2*x(i) + sqrt(4*DeltaX(m)^2
+ h^2 + l^2 + 4*DeltaX(m)*w + w^2 - 8*DeltaX(m)*x(i) - 4*w*x(i) + 4*x(i)^2 + 4*h*y(j)
+ 4*y(j)^2 - 4*l*z(k) + 4*z(k)^2)) + log(2*DeltaX(m) + w - 2*x(i) + sqrt(4*DeltaX(m)^2
+ h^2 + l^2 + 4*DeltaX(m)*w + w^2 - 8*DeltaX(m)*x(i) - 4*w*x(i) + 4*x(i)^2 + 4*h*y(j)
+ 4*y(j)^2 + 4*l*z(k) + 4*z(k)^2))) - Jx(m)*(log(-h - 2*y(j) + sqrt(4*DeltaX(m)^2 +
h^2 + l^2 + 4*DeltaX(m)*w + w^2 - 8*DeltaX(m)*x(i) - 4*w*x(i) + 4*x(i)^2 + 4*h*y(j)
+ 4*y(j)^2 - 4*l*z(k) + 4*z(k)^2)) - log(-h - 2*y(j) + sqrt(4*DeltaX(m)^2 + h^2 + l^2 +
4*DeltaX(m)*w + w^2 - 8*DeltaX(m)*x(i) - 4*w*x(i) + 4*x(i)^2 + 4*h*y(j) + 4*y(j)^2
+ 4*l*z(k) + 4*z(k)^2))) - Jy(m)*(-log(2*DeltaX(m) - w - 2*x(i) + sqrt(4*DeltaX(m)^2
+ h^2 + l^2 - 4*DeltaX(m)*w + w^2 - 8*DeltaX(m)*x(i) + 4*w*x(i) + 4*x(i)^2 + 4*h*y(j)
+ 4*y(j)^2 - 4*l*z(k) + 4*z(k)^2)) + log(2*DeltaX(m) - w - 2*x(i) + sqrt(4*DeltaX(m)^2
+ h^2 + l^2 - 4*DeltaX(m)*w + w^2 - 8*DeltaX(m)*x(i) + 4*w*x(i) + 4*x(i)^2 + 4*h*y(j)
+ 4*y(j)^2 + 4*l*z(k) + 4*z(k)^2))) - Jx(m)*(-log(-h - 2*y(j) + sqrt(4*DeltaX(m)^2 +
h^2 + l^2 - 4*DeltaX(m)*w + w^2 - 8*DeltaX(m)*x(i) + 4*w*x(i) + 4*x(i)^2 + 4*h*y(j)
+ 4*y(j)^2 - 4*l*z(k) + 4*z(k)^2)) + log(-h - 2*y(j) + sqrt(4*DeltaX(m)^2 + h^2 + l^2 -
4*DeltaX(m)*w + w^2 - 8*DeltaX(m)*x(i) + 4*w*x(i) + 4*x(i)^2 + 4*h*y(j) + 4*y(j)^2
+ 4*l*z(k) + 4*z(k)^2)));
end
end

    Bx(i) = magnet * tempbx;
```

```
By(i) = magnet * tempby;
Bz(i) = magnet * tempbz;
Bxy(i) = sqrt(Bx(i)^2 + By(i)^2);
end
end
```

%reset old parameters succesive applications of this program can use the original position values

```
for i=1:xmax,
x(i) = xhold(i);
y(i) = yhold(i);
z(i) = zhold(i);
end
```